

Advanced Technologies in Earth Sciences

Michael Weber
Ute Münch *Editors*

Tomography of the Earth's Crust: From Geophysical Sounding to Real- Time Monitoring

GEOTECHNOLOGIEN
Science Report No. 21



GEOTECHNOLOGIEN



Springer

Advanced Technologies in Earth Sciences

Series editors

Ute Münch, Potsdam, Germany

Ludwig Stroink, Potsdam, Germany

Volker Mosbrugger, Frankfurt, Germany

Gerold Wefer, Bremen, Germany

For further volumes:

<http://www.springer.com/series/8384>

Michael Weber · Ute Münch
Editors

Tomography of the Earth's Crust: From Geophysical Sounding to Real-Time Monitoring

GEOTECHNOLOGIEN Science
Report No. 21

 Springer

Editors

Michael Weber
Department of Physics of the Earth
GFZ, German Research Centre for
Geosciences
Potsdam
Germany

Ute Münch
Coordination Office
GEOTECHNOLOGIEN
Potsdam
Germany

ISSN 2190-1635

ISSN 2190-1643 (electronic)

ISBN 978-3-319-04204-6

ISBN 978-3-319-04205-3 (eBook)

DOI 10.1007/978-3-319-04205-3

Springer Cham Heidelberg New York Dordrecht London

Library of Congress Control Number: 2013958388

© Springer International Publishing Switzerland 2014

This work is subject to copyright. All rights are reserved by the Publisher, whether the whole or part of the material is concerned, specifically the rights of translation, reprinting, reuse of illustrations, recitation, broadcasting, reproduction on microfilms or in any other physical way, and transmission or information storage and retrieval, electronic adaptation, computer software, or by similar or dissimilar methodology now known or hereafter developed. Exempted from this legal reservation are brief excerpts in connection with reviews or scholarly analysis or material supplied specifically for the purpose of being entered and executed on a computer system, for exclusive use by the purchaser of the work. Duplication of this publication or parts thereof is permitted only under the provisions of the Copyright Law of the Publisher's location, in its current version, and permission for use must always be obtained from Springer. Permissions for use may be obtained through RightsLink at the Copyright Clearance Center. Violations are liable to prosecution under the respective Copyright Law. The use of general descriptive names, registered names, trademarks, service marks, etc. in this publication does not imply, even in the absence of a specific statement, that such names are exempt from the relevant protective laws and regulations and therefore free for general use.

While the advice and information in this book are believed to be true and accurate at the date of publication, neither the authors nor the editors nor the publisher can accept any legal responsibility for any errors or omissions that may be made. The publisher makes no warranty, express or implied, with respect to the material contained herein.

Printed on acid-free paper

Springer is part of Springer Science+Business Media (www.springer.com)

Foreword

Advanced Technologies in Earth Sciences is based in the German Geoscientific Research and Development Program “GEOTECHNOLOGIEN” funded by the Federal Ministry of Education and Research (BMBF) and the German Research Foundation (DFG).

This program comprises a nationwide network of transdisciplinary research projects and incorporates numerous universities, nonuniversity research institutions and companies. The books in this series deal with research results from different innovative geoscientific research areas, interlinking a broad spectrum of disciplines with a view to documenting System Earth as a whole, including its various subsystems and cycles. The research topics are predefined to meet scientific, sociopolitical, and economic demands for the future.

Ute Münch
Ludwig Stroink
Volker Mosbrugger
Gerold Wefer

Preface

The zone near the surface of our planet is the interface between geo-, bio-, hydro-, and atmosphere and the basis for our daily life. Water, natural resources (salt, ore, oil, and gas) and energy, for example heat, are exploited from this zone. Increasingly, waste and other material will be stored underground. We do not only use the surface for infrastructure but rather we increasingly expand construction to the subsurface for example relocating traffic to tunnels.

Suitable exploration and monitoring technologies are therefore of enormous importance to mitigate danger and damages in this economically and ecologically sensitive area. High resolution time-dependent images are necessary to derive crucial information about the subsurface. Thus, there is an urgent need for technologies and methods which enable high-resolution imaging of structures and processes in the subsoil on different spatial and time scales. The objective of this research topic was therefore the refinement of tomographic methods and their application to geological processes.

Despite methodical progress, especially in mathematical and numerical geophysics during the last few years, like the real-time data acquisition and evaluation in addition to computer-aided visualization programs, various methods are often still used independently due to economical reasons. However, the concerted combination and the enhancement of different methods allow new prospecting strategies.

The research work on the topic of “Tomography of the Earth’s Crust: From Geophysical Sounding to Real-Time Monitoring” has focused on the development of cross-scale multiparameter methods and their technological application together with the development of innovative field techniques. Seismic wave field inversion theory, diffusion and potential methods were developed and optimized with respect to cost and benefit aspects.

This volume summarizes the scientific results of nine interdisciplinary joint projects funded by the German Federal Ministry of Education and Research in the framework of the Research and Development Program GEOTECHNOLOGIEN.

Highlights and innovations presented cover many length scales and involve targets ranging from applications in the laboratory, to ground water surveys of heterogeneous aquifer, geotechnical applications like tunnel excavation, coal mine and CO₂ monitoring and the imaging and monitoring of tectonic and societally relevant objects as active faults and volcanoes.

To study these objects, the authors use the full spectrum of geophysical methods (ultrasonics, seismic and seismology, electromagnetics, gravity, and airborne) in combination with new methods like seismic interferometry, diffuse wave field theory and full-wave-form inversion in 3D and partially also in 4D.

To make the results and implementations available to a broader community as well as to end-users, unique knowledge-based platforms were developed in terms of computer code, benchmark data, technical definitions, and recommendations via a web portal.

Ute Münch
Head of the GEOTECHNOLOGIEN coordination office

Michael Weber
Director of Department “Physics of the Earth”
German Research Centre for Geosciences, GFZ

Contents

1 Broadband Electrical Impedance Tomography for Subsurface Characterization Using Improved Corrections of Electromagnetic Coupling and Spectral Regularization	1
Andreas Kemna, Johan A. Huisman, Egon Zimmermann, Roland Martin, Yulong Zhao, Andrea Treichel, Adrian Flores Orozco and Thomas Fechner	
2 Towards an Integrative Inversion and Interpretation of Airborne and Terrestrial Data	21
Hans-Jürgen Götze, Martin Afanasjew, Michael Alvers, Liliana Barrio-Alvers, Ralph-Uwe Börner, Christian Brandes, Rudolf Eröss, Peter Menzel, Uwe Meyer, Mathias Scheunert, Bernhard Siemon, Klaus Spitzer, Dominik Steinmetz, Johannes Stoll, Gupta Sudha, Bülent Tezkan, Angelika Ullmann and Jutta Winsemann	
3 MIIC: Monitoring and Imaging Based on Interferometric Concepts	43
Christoph Sens-Schönfelder, Hortencia Flores-Estrella, Martina Gassenmeier, Michael Korn, Florian Köllner, Claus Milkereit, Ernst Niederleithinger, Stefano Parolai, Marco Pilz, Eraldo Pomponi, Andreas Schuck, Katja Thiemann and Jürgen Völkel	
4 The MINE Project: Monitoring Induced Seismicity in a German Coal Mine	63
Simone Cesca, Francesco Grigoli, Ali Tolga Şen, Samira Maghsoudi, Torsten Dahm and Thomas Meier	

5	Three-Dimensional Multi-Scale and Multi-Method Inversion to Determine the Electrical Conductivity Distribution of the Subsurface (Multi-EM)	83
	Oliver Ritter, Klaus Spitzer, Martin Afanasjew, Michael Becken, Ralph-Uwe Börner, Felix Eckhofer, Michael Eiermann, Oliver G. Ernst, Alexander Grayver, Jens Klump, Naser Meqbel, Christian Nittinger, Jan Thaler, Ute Weckmann and Julia Weißflog	
6	MuSaWa: Multi-Scale S-Wave Tomography for Exploration and Risk Assessment of Development Sites	95
	Hendrik Paasche, Michael Rumpf, Agostiny M. Lontsi, Jörg Hausmann, Katrin Hannemann, Thomas Fechner, Matthias Ohrnberger, Ulrike Werban, Jens Tronicke, Frank Krüger and Peter Dietrich	
7	Seismic Tomography and Monitoring in Underground Structures: Developments in the Freiberg Reiche Zeche Underground Lab (Freiberg, Germany) and Their Application in Underground Construction (SOUND)	115
	Stefan Lüth, Thomas Bohlen, Rüdiger Giese, Sven Heider, Silke Hock, Stefan Jetschny, Ulrich Polom, Sonja Wadas and Aissa Rechlin	
8	Toolbox for Applied Seismic Tomography	135
	Thomas Forbriger, Michael Auras, Filiz Bilgili, Thomas Bohlen, Simone Butzer, Sandra Christen, Luigia Cristiano, Wolfgang Friederich, Rüdiger Giese, Lisa Groos, Heiner Igel, Florian Köllner, Rolf Krompholz, Stefan Lüth, Stefan Mauerberger, Thomas Meier, Ilaria Mosca, Dirk Niehoff, Heike Richter, Martin Schäfer, Andreas Schuck, Florian Schumacher, Karin Sigloch, Mario Vormbaum and Frank Wuttke	
9	Tomographic Methods in Hydrogeology	157
	Olaf A. Cirpka, Carsten Leven, Ronnie Schwede, Kennedy Doro, Peter Bastian, Olaf Ippisch, Ole Klein and Arno Patzelt	

Chapter 1

Broadband Electrical Impedance Tomography for Subsurface Characterization Using Improved Corrections of Electromagnetic Coupling and Spectral Regularization

Andreas Kemna, Johan A. Huisman, Egon Zimmermann, Roland Martin, Yulong Zhao, Andrea Treichel, Adrian Flores Orozco and Thomas Fechner

Abstract The low-frequency complex electrical conductivity in the mHz to kHz range has been shown to enable an improved textural, hydraulic, and biogeochemical characterization of the subsurface using electrical impedance spectroscopy (EIS) methods. Principally, these results can be transferred to the field using electrical impedance tomography (EIT). However, the required accuracy of 1 mrad in the phase measurements is difficult to achieve for a broad frequency bandwidth because of electromagnetic (EM) coupling effects at high frequencies and the lack of inversion schemes that consider the spectral nature of the complex electrical conductivity. Here, we overcome these deficiencies by (i) extending the standard spatial-smoothness constraint in EIT to the frequency dimension, thus enforcing smooth spectral signatures, and (ii) implementing an advanced EM coupling removal procedure using a newly formulated forward electrical model and calibration measurements. Both methodological advances are independently validated, and the improved imaging capability of the overall methodology with respect to spectral electrical properties is demonstrated using borehole EIT measurements in a heterogeneous aquifer. The developed procedures represent a significant step forward towards broadband EIT, allowing transferring the considerable diagnostic potential of EIS in the mHz to kHz

A. Kemna (✉) · R. Martin · A. Flores Orozco
Geodynamics/Geophysics, Steinmann Institute, University of Bonn, Meckenheimer
Allee 176, 53115 Bonn, Germany
e-mail: kemna@geo.uni-bonn.de

J. A. Huisman · A. Treichel
Forschungszentrum Jülich GmbH, Institute for Bio- and Geosciences – Agrosphere (IBG 3),
52425 Jülich, Germany

E. Zimmermann · Y. Zhao
Forschungszentrum Jülich GmbH, Central Institute for Engineering, Electronics, and Analytics –
Electronic systems (ZEA 2), 52425 Jülich, Germany

T. Fechner
Geotomographie GmbH, Am Tonnenberg 18, 56567 Neuwied, Germany

range to geophysical imaging applications at the field scale for improved subsurface characterization.

1.1 Introduction

Spectral induced polarization (SIP), also known as electrical impedance spectroscopy (EIS), is a geophysical method to measure the frequency-dependent complex electrical conductivity of soils, sediments, and rocks in the mHz to kHz range. In the absence of electronically conducting minerals, the real part of the complex electrical conductivity is a measure of ionic conduction in the water-filled pores and along water-mineral interfaces. The imaginary part of the complex conductivity is a measure of ionic polarization in response to an external electric field associated with electrically charged mineral surfaces and constrictions in the pore space (e.g., Leroy et al. 2008; Revil 2013). EIS can be implemented in a tomographic framework (e.g., Kemna et al. 2000), and is then commonly referred to as electrical impedance tomography (EIT).

In the last decades, EIS and EIT have been increasingly used in a wide range of applications, including lithological and textural characterization (e.g., Vanhala 1997; Slater and Lesmes 2002), direct estimation of hydraulic conductivity (e.g., Kemna et al. 2004; Binley et al. 2005; Revil and Florsch 2010), delineation of contaminant plumes (e.g., Kemna et al. 2004; Flores Orozco et al. 2012a), and monitoring of biogeochemical processes associated with contaminant remediation (e.g., Williams et al. 2009; Flores Orozco et al. 2013). The potential of EIS measurements for these applications has been clearly demonstrated in laboratory studies. It arises from the fact that the complex conductivity is directly affected by pore space geometry, pore fluid chemistry, and mineral surface properties. However, it is currently still difficult to fully capitalize on the recognized diagnostic capabilities of EIS measurements in EIT field applications (Kemna et al. 2012).

A first difficulty that currently limits the value of EIT measurements is that existing EIT inversion approaches treat all frequencies independently. This may lead to inconsistent imaging results that do not adequately capture the smooth and relatively weak frequency dependence of the complex electrical conductivity that has been reported in most studies dealing with the electrical properties of soils, sediments, and rocks.

A second reason why currently EIT is not able to deliver its full potential is related to the required high accuracy of 1 mrad in the phase measurements over a broad frequency range, extending from mHz to kHz. In recent years, considerable progress has been made with respect to understanding, quantifying, and correcting different error sources present in laboratory EIS and EIT measurements above 10 Hz (Zimmermann et al. 2008a, b). Despite this instrumental progress, it is still not possible to achieve such a high accuracy for a broad frequency bandwidth in EIT field applications. This is related to electromagnetic (EM) coupling effects that considerably affect EIT measurements at frequencies above ~ 10 Hz (e.g., Madden

and Cantwell 1967). This EM coupling is mainly caused by capacitive and inductive coupling between the electrical wires or between the wires and the soil and is thus inherent to field EIT measurements.

Within this context, the project ‘4D Spectral Electrical Impedance Tomography—a diagnostic imaging tool for the characterization of subsurface structures and processes (4DEIT)’ was formulated. The main aims of this project were threefold. A first aim was to extend the standard spatial-smoothness constraint in EIT to the frequency dimension in order to obtain consistent imaging results across multiple frequencies. The developed approach was implemented in an existing EIT inversion code and validated using laboratory EIT measurements. A second aim was to develop correction procedures for inductive and capacitive coupling in EIT measurements made with multi-electrode chains. Controlled test measurements in a water-filled container were used for initial validation of the correction procedures and to determine the maximum expected accuracy that can be achieved using EIT field measurements of the complex electrical conductivity. A final aim was to evaluate these methodological advances using borehole EIT measurements made in the heterogeneous aquifer of the Krauthausen test site. In the following, we report on the main scientific findings of the 4DEIT project.

1.2 Inversion Methodology

1.2.1 EIT Inversion Approach

Electrical impedance tomography involves the inversion of a set of transfer impedances, Z , measured on an array of electrodes using a series of individual four-electrode configurations, into a distribution of complex resistivity, $\rho = |\rho| e^{j\phi}$ (with resistivity magnitude $|\rho|$, resistivity phase ϕ , and imaginary unit $j^2 = -1$), or complex electrical conductivity $\sigma = |\sigma| e^{-j\phi} = \sigma' + i\sigma''$ (with conductivity magnitude $|\sigma| = 1/|\rho|$, conductivity phase $-\phi$, real part of conductivity σ' , and imaginary part of conductivity σ'').

We here build upon the finite-element based, smoothness-constraint inversion code by Kemna (2000), in which log-transformed impedances are used as data and log-transformed complex conductivities (of lumped finite-element cells) as parameters to account for the large range of resistance values in typical EIT data sets and of resistivity values for earth materials, respectively. For standard single-frequency, i.e., non-spectral, applications, the algorithm follows a standard Gauss-Newton procedure for non-linear inverse problems and iteratively minimizes an objective function, $\Psi(\mathbf{m})$, composed of the measures of data misfit and spatial model roughness, with both terms being balanced by a regularization parameter λ :

$$\Psi(\mathbf{m}) = \|\mathbf{W}[\mathbf{d} - \mathbf{f}(\mathbf{m})]\|^2 + \lambda \|\mathbf{R}\mathbf{m}\|^2, \quad (1.1)$$

where \mathbf{d} is the data vector, \mathbf{m} the model vector, $\mathbf{f}(\mathbf{m})$ the operator of the finite-element forward model, \mathbf{W} a data weighting matrix, and \mathbf{R} a (real-valued) matrix evaluating the (first-order) spatial roughness of \mathbf{m} . Under the assumption that the data errors are uncorrelated and normally distributed, \mathbf{W} is a diagonal matrix, with its entries in this study being estimated from the analysis of impedance data pairs measured in normal and reciprocal configurations (Koestel et al. 2008; Flores Orozco et al. 2012b). At each iteration step, a univariate search is performed to find the optimum value of the regularization parameter λ which locally minimizes the data misfit. The model update, $\Delta\mathbf{m}$, is calculated from solving the linear system of equations

$$\left[\mathbf{J}^H \mathbf{W}^H \mathbf{W} \mathbf{J} + \lambda \mathbf{R}^T \mathbf{R} \right] \Delta\mathbf{m} = \mathbf{J}^H \mathbf{W}^H \mathbf{W} [\mathbf{d} - \mathbf{f}(\mathbf{m})] - \lambda \mathbf{R}^T \mathbf{R} \mathbf{m}, \quad (1.2)$$

where \mathbf{J} is the Jacobian matrix computed for the given model \mathbf{m} , H denotes the Hermitian (complex conjugate transpose), and T the transpose matrix. The iteration process is stopped when the root-mean-square data-misfit value reaches the value of 1 for a maximum possible λ , yielding the smoothest spatial distribution explaining the data.

1.2.2 EIT Inversion with Spatio-Spectral Regularization

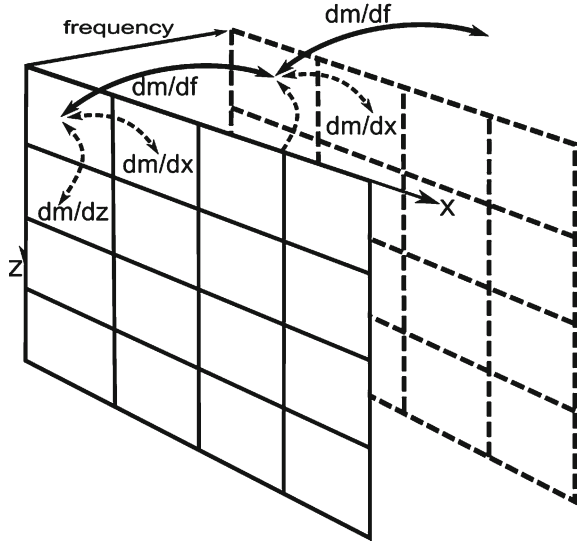
Current complex conductivity (or complex resistivity) imaging approaches are limited to the inversion of single-frequency data (e.g., Kemna et al. 2004; Blaschek et al. 2008), or the independent inversion of multi-frequency data sets (e.g., Kemna et al. 2000; Flores Orozco et al. 2012a, 2013). Such an approach limits the characterization capabilities of EIT because there is no control on the spectral behavior in the inversion procedure, resulting in considerable ill-posedness with respect to the retrieval of spectral characteristics. In order to overcome this deficiency, we implemented an extended EIT inversion scheme with full spatio-spectral regularization for the simultaneous inversion of multi-frequency impedance data sets by adding an additional smoothness constraint with respect to the spectral dimension.

Let \mathbf{m}_f , \mathbf{d}_f , \mathbf{J}_f , and \mathbf{W}_f denote the extended model vector, the data vector, the Jacobian matrix, and the data weighting matrix, respectively, that contain all model vectors \mathbf{m}_i , data vectors \mathbf{d}_i , Jacobian matrices \mathbf{J}_i , and data weighting matrices \mathbf{W}_i for N measurement frequencies ($i = 1, \dots, N$):

$$\mathbf{m}_f = \begin{pmatrix} \mathbf{m}_1 \\ \vdots \\ \mathbf{m}_N \end{pmatrix}, \quad \mathbf{d}_f = \begin{pmatrix} \mathbf{d}_1 \\ \vdots \\ \mathbf{d}_N \end{pmatrix}, \quad \mathbf{J}_f = \begin{pmatrix} \mathbf{J}_1 & & \\ & \ddots & \\ & & \mathbf{J}_N \end{pmatrix}, \quad \mathbf{W}_f = \begin{pmatrix} \mathbf{W}_1 & & \\ & \ddots & \\ & & \mathbf{W}_N \end{pmatrix}. \quad (1.3)$$

Note that \mathbf{J}_f and \mathbf{W}_f are block diagonal matrices. For simultaneously inverting the data \mathbf{d}_f we solve the extended linear system of equations

Fig. 1.1 Spatio-spectral regularization scheme implemented in the multi-frequency EIT inversion. The indicated planes represent the spatial model parameterization (lumped finite-element cells in the x,z -plane) at two successive frequencies (f). In addition to its adjacent neighbors in space, each model parameter is coupled to its adjacent “spectral” neighbor (same location in space, but for next frequency)



$$\left[\mathbf{J}_f^H \mathbf{W}_f^H \mathbf{W}_f \mathbf{J}_f + \lambda \mathbf{R}_f^T \mathbf{R}_f \right] \Delta \mathbf{m}_f = \mathbf{J}_f^H \mathbf{W}_f^H \mathbf{W}_f [\mathbf{d}_f - \mathbf{f}_f(\mathbf{m}_f)] - \lambda \mathbf{R}_f^T \mathbf{R}_f \mathbf{m}_f, \quad (1.4)$$

with correspondingly extended forward model response \mathbf{f}_f and model update $\Delta \mathbf{m}_f$, where spatio-spectral smoothing is realized by an extended model roughness matrix, \mathbf{R}_f , given by

$$\mathbf{R}_f = \begin{pmatrix} \mathbf{R}_1 & 0 & \dots & 0 \\ 0 & \mathbf{R}_2 & \ddots & \vdots \\ \vdots & \ddots & \ddots & 0 \\ 0 & \dots & 0 & \mathbf{R}_N \end{pmatrix} + \lambda_f \begin{pmatrix} -1 & 0 & \dots & 0 & 1 & 0 & \dots & 0 \\ 0 & \ddots & \ddots & \vdots & \ddots & \ddots & \ddots & \vdots \\ \vdots & \ddots & -1 & 0 & \dots & 0 & 1 & 0 \\ 0 & \dots & 0 & -1 & \ddots & \vdots & \ddots & 1 \end{pmatrix}. \quad (1.5)$$

In Eq.(1.5), \mathbf{R}_i denote the spatial roughness matrices (generally identical for all measurement frequencies), and the second matrix on the right-hand side contains non-zero entries only at the diagonal element and at one off-diagonal element that correspond to the model parameters at the same location in space but for two successive frequencies (Fig. 1.1). Here, the values -1 and 1 are only indicative; actually the true spectral gradient of the model with respect to log frequency is implemented. The spectral regularization strength in the inversion can be adjusted with the additional regularization parameter λ_f .

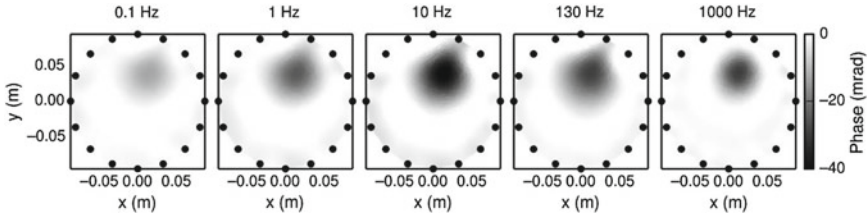


Fig. 1.2 EIT phase images of a cylindrical copper target in a water-filled cylindrical tank at five selected measurement frequencies computed with spatio-spectral regularization. *Black dots* indicate position of electrodes used for data acquisition

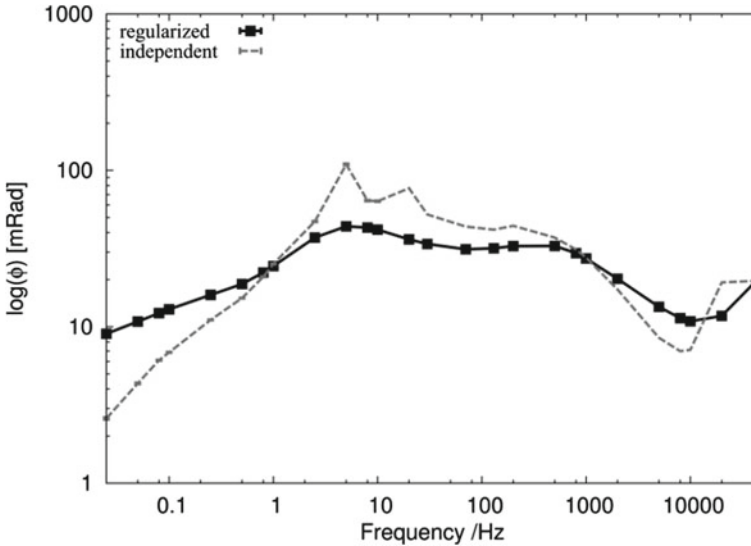


Fig. 1.3 Recovered phase spectrum at the center of the copper target (cf. Fig. 1.2) using independent single-frequency inversions (*dashed grey curve*) and the new multi-frequency inversion with spectral regularization (*solid black curve*)

1.2.3 Validation Using a Physical Tank Model

In order to compare single-frequency inversions with inversion results obtained with additional spectral regularization, EIT measurements were made on a copper cylinder positioned within a water-filled cylindrical tank using the laboratory EIT system described in Zimmermann et al. (2008b). The copper target can easily be identified by the high phase values in the reconstructed images (Fig. 1.2). The phase spectrum extracted from the EIT images at the center of the copper target reveals rather erratic spectral variations, especially in the frequency range between 1 and 100 Hz, where highest polarization is observed for the single-frequency inversions (Fig. 1.3). This reflects the inherent ill-posedness of a non-spectrally regularized inversion approach

with respect to the recovery of spectral variations. With the new spatio-spectral regularization approach, the inverted spectral phase values show a more consistent, smoothly varying behavior, in agreement with the typical dispersion characteristics of electrical relaxation processes. It is clear that the choice of the regularization parameter λ_f in Eq. 1.5 controls the amount of spectral smoothing, and future studies will need to establish methods to determine the most appropriate values of λ_f .

1.3 Inductive and Capacitive Coupling Effects: Modeling and EIT Data Correction

1.3.1 Design of EIT Field System and Borehole Electrode Chains

In order to image the spectral phase response of low-polarizable soils and rocks, spectral EIT measurements with high phase accuracy in a broad frequency range are needed. It is challenging to design EIT data acquisition to achieve such a high accuracy, especially in the high frequency range (100 Hz to 45 kHz). Previous work focused on the development of a laboratory spectral-EIT measurement system with sufficient accuracy (Zimmermann et al. 2008b). On the basis of this laboratory system, a prototype for spectral EIT data acquisition at the field scale was realized (Zimmermann et al. 2010; Zimmermann 2011). Both systems have a modular design with active electrode modules consisting of integrated amplifiers for electric potential measurements and integrated switches for current injection. To achieve the required high accuracy, the developed EIT systems rely on model-based correction methods to minimize the remaining errors of the system. The errors that have been corrected in such a manner are related to amplification, signal drift, and propagation delay of the signal due to the long cables, amongst other error sources.

For borehole EIT measurements, electrode chains and logging tools have recently been developed and constructed. The borehole chains consist of eight active electrode modules with an electrode spacing of 100 cm, whereas the borehole logging tool consists of four electrode modules with an electrode spacing of 16.2 cm. For the electrical connection of the active electrode modules to the EIT data acquisition system, a 25 m long shielded multicore cable is used in both cases (Zhao et al. 2013).

1.3.2 Electromagnetic Coupling

The necessary use of long cables in the design of borehole electrode chains introduces additional errors in the phase measurements due to electromagnetic coupling effects; these effects can be separated in (i) inductive coupling between the long electric loops for current injection and potential measurement, and (ii) capacitive coupling between the cable and the electrically conductive environment. Both types

of coupling currently limit the upper frequency for accurate EIT measurements to the tens of Hz range. The phase errors due to electromagnetically induced eddy currents in the subsurface are small in relation to these two effects and can be neglected for the application considered here.

The inductive coupling using two borehole chains can be divided into two cases: (i) coupling within one electrode chain and (ii) coupling between two different electrode chains. In the first case, the electrical wires in a single multicore cable are close together and this leads to strong inductive coupling. It is important to note that the strength of this coupling depends only on the design of the multicore cable and not on the cable layout during field measurements. In the second case, the coupling is weaker due to the larger separation between the electrical wires. However, the strength of the coupling depends on the position of the multicore cable layout during field measurements, which must therefore be determined or controlled in order to allow adequate corrections for inductive coupling. However, the cable separations only need to be known with cm accuracy. In summary, a configuration with current injection and voltage measurement in one borehole belongs to the first case, and a configuration with current injection in one borehole and voltage measurement in a second borehole belongs to the second case. All other configurations can be obtained by superpositioning of these two types.

Here, we present correction methods for inductive coupling in one multicore cable and capacitive coupling between the borehole chains and the subsurface. The correction of inductive coupling in one cable is a complicated task because the separation between the wires needs to be known with an accuracy better than 0.1 mm. In addition, the inductive coupling is also influenced by eddy currents in the outer shielding of the chain.

1.3.3 Correction Methodology

Inductive coupling leads to a parasitic additive imaginary part in the measured transfer impedances. Typically, a wide range of four-electrode configurations is used to measure the electrical impedance of the subsurface. This electrical transfer impedance Z_M is the ratio of the measured voltage U_M between two potential electrodes and the injected current I_I between two excitation electrodes. Each electrode is connected with one wire which is parallel to the other wires in the case of current injection and voltage measurement in one borehole (Fig. 1.4). The active elements in the electrode modules can be neglected for the consideration of the inductive effects.

Due to the inductive coupling between the two wire pairs, an additional voltage U_{II} in loop II is induced from the injected current I_I in loop I (Fig. 1.4). This means that the injected current leads to an impedance Z_S of the subsurface and the unwanted induced impedance Z_{IC} . This results in the total measured transfer impedance

$$Z_M = Z_S + Z_{IC} = Z_S + j\omega M. \quad (1.6)$$

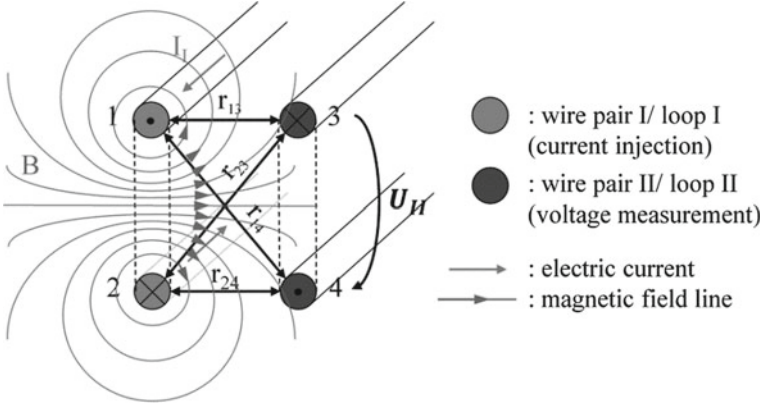


Fig. 1.4 Mutual induction between two parallel electrical wire pairs (from Zhao et al. 2013)

This equation shows that the error due to inductive coupling can be removed by subtracting the coupling impedance Z_{IC} , which is the mutual inductance M multiplied by the imaginary unit j and the angular frequency ω , from the measured transfer impedance.

In order to determine the exact coupling impedances, we have evaluated several approaches. In a first approach, we tried to determine the values based on the geometry of the multicore cable. However, it is not possible to determine the wire positions within the multicore cable with the required accuracy. In addition, eddy currents in the electrical shield have a big influence on the impedance in the kHz frequency range. Therefore, this approach was abandoned. In an alternative approach, we measured the mutual inductance for all possible electrode configurations (Zhao et al. 2013). This is cumbersome and time-consuming for practical use. To overcome this practical problem, the latest calibration method relies on a pole-pole matrix

$$\mathbf{P} = \begin{bmatrix} \mathbf{A} & \mathbf{B} \\ \mathbf{C} & \mathbf{D} \end{bmatrix}, \quad (1.7)$$

with coupling impedances derived from pole-pole calibration measurements. The matrix \mathbf{A} contains the coupling impedances between the wires of the first borehole chain, and the matrix \mathbf{D} contains the coupling impedances between the wires of the second borehole chain. The matrices \mathbf{B} and \mathbf{C} contain the coupling impedances between the wires of different borehole chains. The strength of these couplings depends on the position of the multicore cable layout during field measurements and can be calculated using equations provided in Sunde (1968). This calculation is not treated here. In the future, we will also consider this case of coupling.

In order to obtain the coupling impedances in one borehole chain (matrices \mathbf{A} and \mathbf{D}) using pole-pole (i.e., ground-based) current injection and voltage measurements, all electrodes of the chain are short-circuited and connected to the ground of the

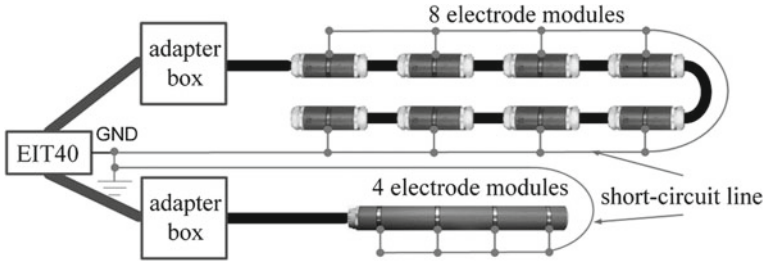


Fig. 1.5 Pole-pole measurement for electrode chain with eight ring electrodes and 25m long multicore cable, and the logging tool with four electrodes

EIT system (Fig. 1.5). Then, the current is injected at one electrode and the induced voltages are measured at all other electrodes. This measurement is repeated for all electrodes of the chain.

The coupling impedances $Z_{m,n}$ of the pole-pole matrices **A** and **D** are the quotients of the measured induced voltages U_n and the injected currents I_m . In the case of chains with eight electrodes, there are 56 (8×7) measured impedances. The diagonal elements are zero. This yields 8×8 -matrices for **A** and **D**. With the full matrix **P**, the coupling impedance between two arbitrary wire pairs can be calculated using

$$Z_{ABMN} = (Z_{BN} - Z_{AN}) - (Z_{BM} - Z_{AM}), \quad (1.8)$$

where A and B are the numbers of current electrodes and M and N are the numbers of potential electrodes.

Using this approach, we are able to correct impedance measurements for any electrode configuration in a single borehole and later for all configurations. Instead of 840 measurements for all possible configurations in one chain with eight electrodes, only 56 measurements are necessary using this newly developed pole-pole calibration. There are additional additive impedances from the short-circuit wire (Fig. 1.5) that need to be corrected with additional measurements. This issue has not been resolved yet, and needs additional attention.

The parasitic current due to the potential differences between the subsurface and the outer shield of the multicore cable (i.e., capacitive coupling) is the second source of phase errors. The outer shield of the multicore cable is used to shield the inner wires from the environment and is therefore connected with system ground (zero potential). The potential distribution in the subsurface is the wanted result of the current injection. These potential differences to the shield cause uncontrolled parasitic currents across the insulator of the multicore cable. An a-priori calculation of the parasitic currents is not possible, because the potential distribution in the subsurface depends on the unknown electrical conductivity distribution.

In order to consider these capacitive coupling effects, the admittances of discrete capacitances of cable segments are integrated in the finite-element based electrical forward model. The developed method results in a linear system of equations

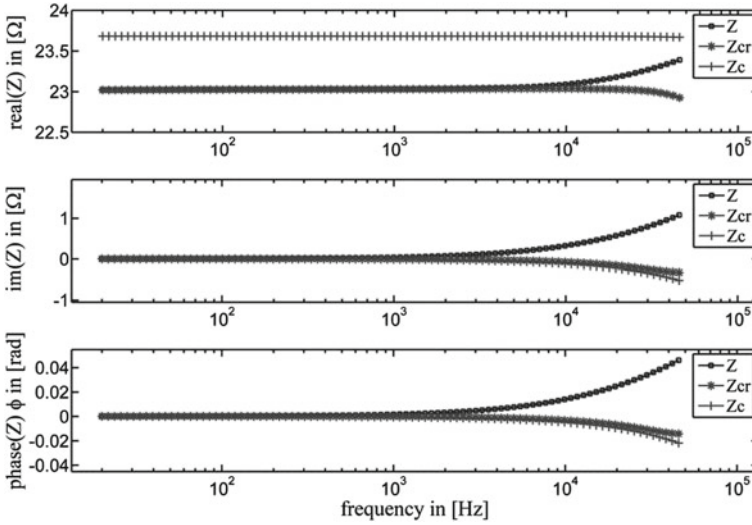


Fig. 1.6 Spectrum of original measured transfer impedances Z , inductive coupling-corrected data Z_{cr} , and modeled data Z_c

$$[\mathbf{Y}_S + \mathbf{Y}_C] \mathbf{U} = \mathbf{I}, \quad (1.9)$$

where \mathbf{U} is the potential and \mathbf{I} the injected current at the nodes of the finite-element modeling mesh. The electrical conductivity distribution in the subsurface is considered within the admittance matrix \mathbf{Y}_S and the admittances of the cable segments are considered with the new matrix \mathbf{Y}_C . The capacities for each node where a capacitance is integrated are calculated on the basis of the outer diameter, the length of the cable segment and the thickness and the permittivity of the insulator. For more details about this modeling we refer to Zimmermann (2011) and Zhao et al. (2013).

1.3.4 Validation of Correction Procedures

The correction methods for inductive and capacitive coupling were verified with a borehole logging tool placed vertically in the center of a water-filled container. The modeled transfer impedance Z_c for a current injection at the outer two electrodes and a voltage measurement between the inner two electrodes of the logging tool can be compared with the measured impedance Z and the impedance Z_{cr} after correction of the inductive coupling (Fig. 1.6). The impedance spectra show an excellent agreement for the imaginary part and the phase angle of the modeled transfer impedances Z_c and the corrected impedance Z_{cr} . The small deviation in the real part is related to geometry errors in the finite-element modeling (e.g., inaccurate electrode positions).

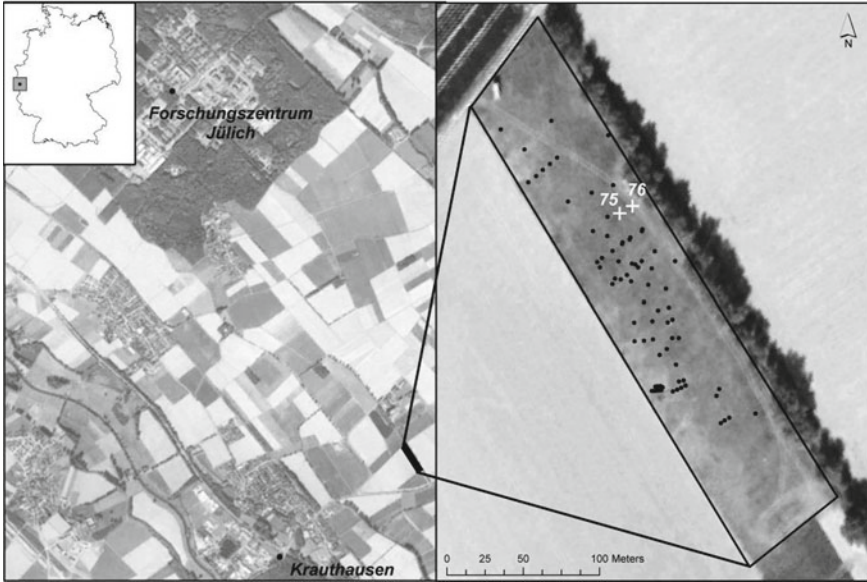


Fig. 1.7 Location of the Krauthausen test site close to the Forschungszentrum Jülich in the Western part of Germany (*left*) and position of monitoring wells, including boreholes 75 and 76, at the site (*right*)

This result shows that a phase accuracy of 1 mrad at 10kHz can be achieved under controlled conditions after accounting for inductive and capacitive coupling effects.

1.4 Field Validation

1.4.1 Krauthausen Test Site

The developed inversion procedure and the correction procedures for inductive and capacitive coupling effects were evaluated by means of borehole EIT measurements at the Krauthausen test site. This test site is situated approximately 10 km northwest of the city of Düren and 6 km southeast of the Forschungszentrum Jülich GmbH, Germany (Fig. 1.7). The upper aquifer is composed of sandy Quaternary deposits with variable gravel content. On top of this aquifer, there is a silty soil layer, and the base of the aquifer consists of silt and clay layers at a variable depth ranging from 11 to 13 m below the surface. The site is equipped with 76, 10–11 m deep observation wells that are screened from 3 m depth downwards (Fig. 1.7).

The hydrogeological characteristics of this test site have been investigated in great detail. Döring (1997) estimated that the geometric mean and variance of the

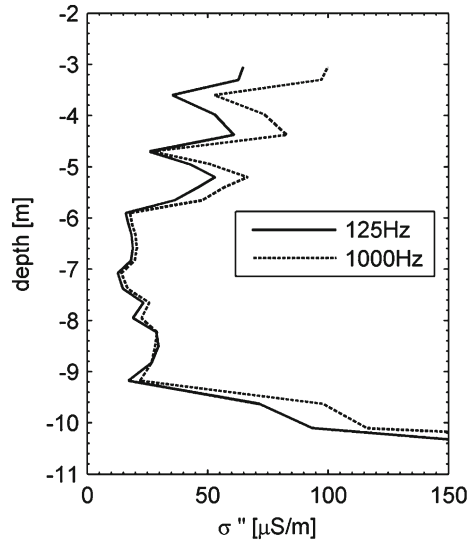
hydraulic conductivity of the aquifer were 0.0013 ms^{-1} and 1.3 (variance of log transformed hydraulic conductivity), respectively. The spatial correlation lengths in the horizontal and vertical directions were determined to be 6.7 m and 0.37 m using cone-penetration tests (Tillmann et al. 2008). The mean porosity is 26 % with a standard deviation of 6 % (Vereecken et al. 2000). The Krauthausen test site has also been the focus of several studies dealing with the application of electrical resistivity tomography to derive hydrologically relevant aquifer properties (e.g., Kemna et al. 2002; Vanderborght et al. 2005; Müller et al. 2010).

1.4.2 Reference EIS Measurements

During drilling and installation of borehole 76 in 2006, aquifer material was collected and visually separated according to layering. This resulted in 29 samples of sediment from a depth range between 1.90 and 10.55 m. After sample collection, the sediment was air-dried and stored for further analysis. The complex electrical conductivity of these samples was determined using an impedance spectrometer that allows accurate EIS measurements for a broad frequency range from 1 mHz to 1 kHz (Zimmermann et al. 2008a). For this, we used a sample holder with a height of 36 cm and a diameter of 6 cm. Two sintered bronze plates were used as current electrodes at the top and bottom of the sample holder, and two ceramic electrodes following the design of Breede et al. (2011) were used as potential electrodes. Before the samples were packed, gravel larger than 1 cm in diameter was removed by sieving. We used the wet-packing method described in Breede et al. (2011) using a CaCl_2 solution with an electrical conductivity of about 0.08 S m^{-1} , which corresponds with the electrical conductivity of the groundwater at the site.

Values of σ'' determined using EIS measurements on repacked samples are provided for two frequencies as a function of depth in Fig. 1.8. According to these measurements, roughly three different layers can be recognized. In the top of the aquifer from 3 to 5 m below surface, σ'' is relatively high and somewhat dependent on frequency. The stronger polarization at 1 kHz as compared to 125 Hz is an indication that the higher σ'' is related to relatively high clay contents in this part of the aquifer. At a depth of 6–7 m below surface, there is a layer with low σ'' values, and in the lowest part of the aquifer, σ'' starts to increase again. There are several issues that complicate a direct transfer of these laboratory EIS measurements to the field, such as the increase in σ' because of the drying and repacking of the laboratory samples and the removal of the gravel fraction before EIS measurements. Nevertheless, we expect that the general pattern and the approximate range of σ'' values should be accurately reproduced by the EIT field measurements.

Fig. 1.8 Imaginary part of the electrical conductivity at 125 Hz (*solid curve*) and 1 kHz (*dashed curve*) as a function of depth obtained from laboratory EIS measurements on repacked Krauthausen sediment samples (without gravel fraction) from borehole 76



1.4.3 EIT Data Acquisition

EIT measurements were made between boreholes 75 and 76 at the Krauthausen test site using borehole electrode chains as described above in each borehole. The groundwater table was located 2.5 m below the surface at the time of the measurements. The uppermost electrode of both electrode chains was placed at a depth of 2.7 m. There were eight electrodes with a separation of 1 m, which means that the deepest electrode of both chains was placed at 9.7 m depth. For current injection, we used all possible electrode configurations for “skip-0” (1–2, 2–3, ..., 9–10, etc.), “skip-2” (1–4, 2–5, etc.), “skip-4” (1–6, 2–7, 3–8), and some configurations for “skip-5” (1–7, 2–8) and “skip-6” (1–8). For the voltage measurements, we used the same electrode pairs except those including current electrodes (e.g., 1–2 4–7, 2–3 1–4, 1–7 2–3), and the corresponding reciprocal measurements (e.g., 4–7 1–2, 1–4 2–3, 2–3 1–7). Prior to the inversion, we corrected the inductive coupling effects by determining $j\omega M$ (Eq. 1.6) for all electrode configurations within a single borehole with the calibration method outlined above. Cross-hole electrode configurations that were known to be hardly affected by inductive coupling were also considered. The remaining cross-hole electrode configurations were not yet considered.

1.4.4 EIT Imaging Results

The EIT field measurements were inverted using two approaches. Initially, only measurements in borehole 76 were considered in an inversion assuming a horizontally

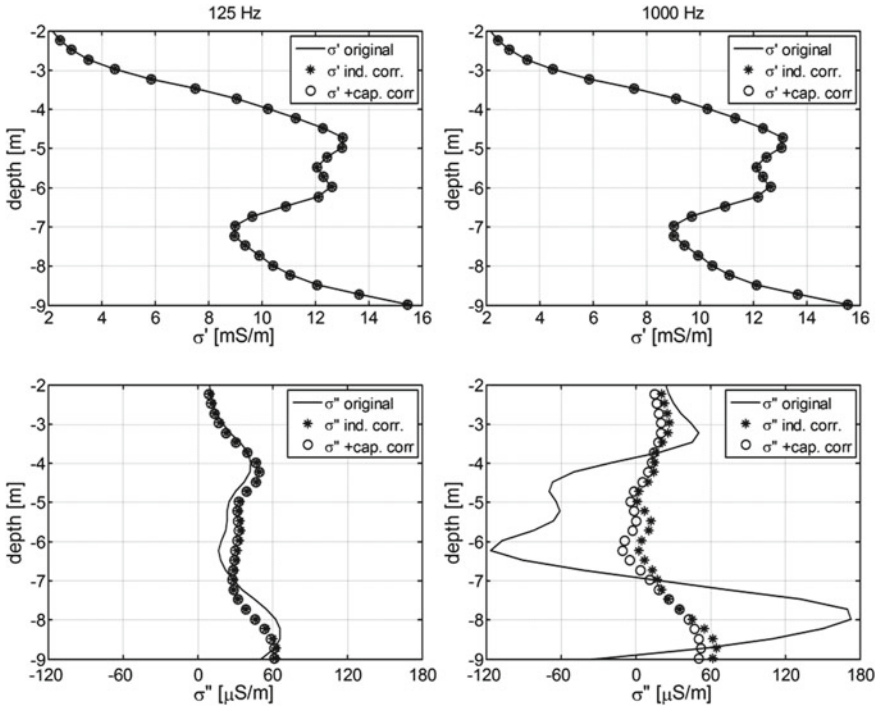


Fig. 1.9 Depth profiles of real (*top*) and imaginary (*bottom*) conductivity at 125 Hz (*left*) and 1 kHz (*right*) as obtained from EIT measurements in borehole 76 at the Krauthausen test site, with (*open symbols*) and without (*solid curves*) corrections for inductive and capacitive coupling, using a 1D inversion scheme

layered subsurface (1D inversion). This inversion involves an axisymmetric 2D forward modeling problem. The corresponding 2D finite-element modeling, however, is a simple extension of 2D finite-element modeling in terms of Cartesian coordinates where the contribution of each element to the finite-element matrix is multiplied by $2 \pi r$, with r being the radial distance of the element's centroid from the symmetry axis (see, e.g., Kwon and Bang 1997). We also considered capacitive coupling in the axisymmetric 2D forward modeling using the approach outlined above. In particular, we considered two kinds of capacitances. The first one is the frequency-dependent capacitance between the cable isolation and the soil. This capacitance was obtained from the dimensions of the electrode chain and was estimated to be as high as 11,000 pF in the low-frequency range. The second type of capacitance is the input capacitance at the electrode amplifier, which was found to be 40 pF (Zhao et al. 2013). We modified the modeling tools presented in detail in Zimmermann (2011) to simulate such axisymmetric modeling domains with additional capacitances.

The results of this 1D inversion approach for the complex conductivity distribution with depth are shown in Fig. 1.9 for EIT measurements made at 125 Hz and 1 kHz in borehole 76. In a first step, raw EIT measurements were inverted. Especially at 1 kHz,

this resulted in relatively strong variations of σ'' with depth that are not in agreement with the reference EIS measurements (cf. Fig. 1.8). Physically implausible negative values of σ'' are also observed at 1 kHz. After correction of the EIT measurements for inductive coupling effects, the inversion was repeated. The inversions of the data corrected for inductive coupling yield much less variation of σ'' with depth, and physically implausible negative values are not present (Fig. 1.9). The effect of the correction for inductive coupling is much stronger at 1 kHz than at 125 Hz. In parts of the profile, the difference between the corrected and uncorrected σ'' values is as large as $100 \mu\text{S m}^{-1}$, corresponding to phase differences up to ~ 12 mrad. Although this difference is much smaller at 125 Hz, the corrections still amount to $10\text{--}20 \mu\text{S m}^{-1}$ ($\sim 1\text{--}2$ mrad) in parts of the profile. In a final step, the corrected EIT data were inverted using the forward model with integrated capacitances. The effect of this correction for capacitive coupling is clearly apparent at 1 kHz, but it is of secondary importance compared with the correction for inductive coupling. Finally, Fig. 1.9 also shows that σ' is not significantly affected by the correction for inductive and capacitive coupling effects.

The 1D inversion results after correction for inductive and capacitive coupling effects (Fig. 1.9) correspond reasonably well with the laboratory EIS measurements (Fig. 1.8). The general pattern of σ'' is consistent between the two frequencies. The approximately three layers with different σ'' values can also be recognized in the 1D inversion result for the corrected data. The additional decrease of σ'' in the top of the aquifer visible in the inverted depth profile is associated with unsaturated soil above the groundwater table that is not reflected in the laboratory EIS measurements on saturated samples. However, it is also apparent that the accuracy of the corrections can still be improved at 1 kHz. For example, σ'' is still slightly negative in the depth range between 5 and 7 m. We attribute this to additional additive impedances in the calibration measurements that have not yet been considered in the pole-pole matrix used to correct for inductive coupling.

Our second inversion approach is based on a two-dimensional, frequency-dependent parameterization of complex electrical conductivity and uses the spatio-spectral regularization outlined above. It thus represents a 3D inverse problem and involves 2.5D forward modeling (3D source in 2D space, see Kemna 2000 for details) for each considered frequency. The inverted data sets comprise EIT measurements in both boreholes. Data errors were quantified following the approaches of Koestel et al. (2008) and Flores Orozco et al. (2012b). Because it is not straightforward to implement the correction approach for capacitive coupling in the 2.5D forward model, due to the inherent Fourier transform with respect to the strike direction of the assumed 2D spatial distribution, this correction has not yet been considered in the inversion. However, the previous analysis (Fig. 1.9) clearly showed that inductive coupling effects are much stronger and thus their correction is more important for accurate cross-borehole EIT imaging.

The EIT complex conductivity imaging results obtained at 2 Hz, where coupling effects are not yet significant and thus inverted images for data with and without inductive corrections are virtually identical, are shown in Fig. 1.10. The images reveal a general layering as in agreement with the corresponding lab data as well as the 1D

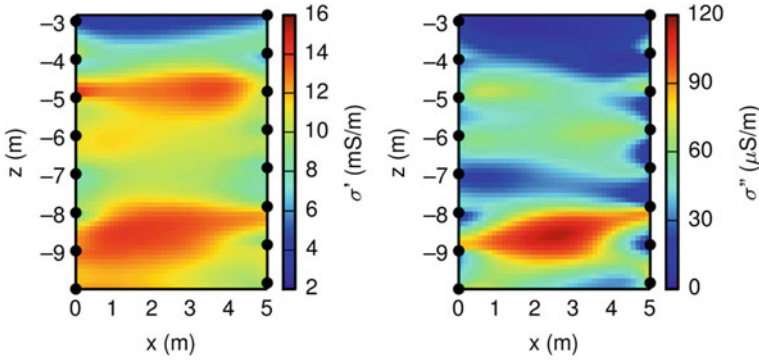


Fig. 1.10 Images of real (*left*) and imaginary (*right*) conductivity at 2 Hz as obtained from EIT measurements in boreholes 75 and 76 at the Krauthausen test site. Black dots indicate position of electrodes in borehole 75 (*left side of the images*) and 76 (*right side of the images*)

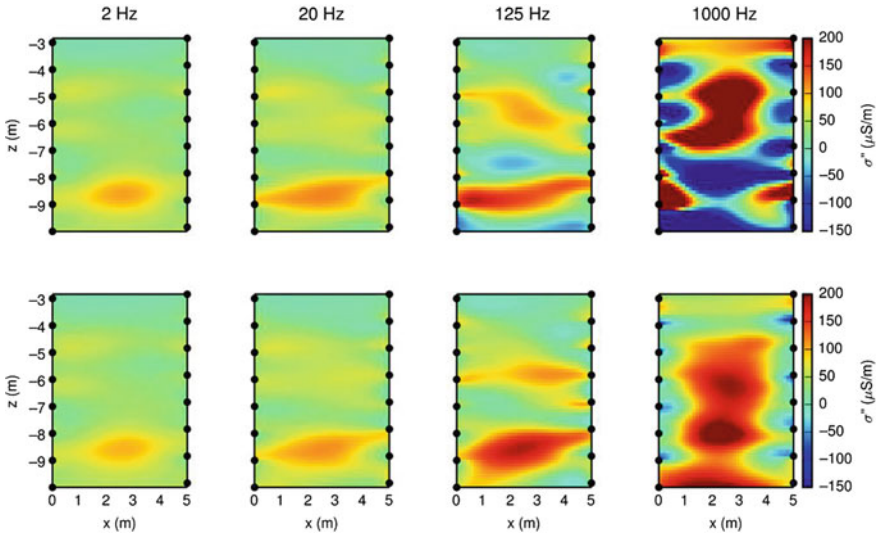


Fig. 1.11 Images of imaginary conductivity at selected frequencies obtained from multi-frequency EIT measurements in boreholes 75 and 76, without (*top panel*) and with (*bottom panel*) corrections for inductive coupling, using the newly developed inversion scheme with spatio-spectral regularization. Black dots indicate position of electrodes (cf. Fig. 1.10)

inversion results (cf. Figs. 1.8 and 1.9). Given the much larger number of measurements taken into account here, a higher vertical resolution is obtained than with the 1D inversion, which is likely to explain the differences with respect to vertical variability and contrast in the recovered values, in particular for the imaginary conductivity σ'' . When inspecting the σ'' images obtained at higher frequencies (Fig. 1.11), the distorting effect of the inductive coupling in the data becomes evident. Inverting the corrected data yields consistent images with a relatively smooth, steady increase of

the imaginary conductivity with frequency in the polarizable sediment layers, as also observed in the laboratory measurements (Fig. 1.8), while without the inductive data correction the images exhibit erratic patterns, with physically meaningless negative values, at frequencies above 100Hz. As already outlined when discussing the 1D inversion results, we expect that there is still room for improving the data correction procedures and thus the achievable image quality, especially for frequencies above 100Hz.

1.5 Conclusions and Outlook

In the 4DEIT project, we have successfully increased the power of spectral EIT technology by developing (i) a new method for spectral regularization in multi-frequency EIT inversion, and (ii) correction procedures for capacitive and inductive coupling in borehole EIT measurements using multi-electrode chains. Spectral regularization was found to provide spectrally smoother changes in the complex electrical conductivity that are more consistent with the typical electrical relaxation behavior of soils, sediments, and rocks. In ideal test conditions, the developed correction methods for inductive and capacitive coupling resulted in an accuracy of 0.8 mrad at 10kHz. Borehole EIT measurements in a heterogeneous aquifer confirmed that EIT measurements above 50Hz were indeed considerably affected by inductive and capacitive coupling effects, as indicated by excessively large and partly physically implausible values for the imaginary part of the electrical conductivity. Application of the newly developed correction procedures showed that inductive coupling effects were considerably stronger than capacitive coupling effects in borehole EIT measurements. After correction, EIT inversion results corresponded reasonably well with the expected range of complex conductivity values derived from laboratory EIS measurements. However, it was also apparent that there is still room to improve the correction methods for inductive coupling, and we are currently in the process of extending the pole-pole matrix used for data correction with additional additive capacitances that have so far not been considered.

We conclude that with the methodological improvements achieved in this project, broadband EIT has become a feasible technology for field-scale surveys, in particular those involving boreholes. In the near future, we hope to transfer the considerable diagnostic potential of broadband electrical spectroscopy with respect to textural, hydraulic, and biogeochemical soil and rock properties to geophysical imaging applications, thus enabling a breakthrough in the spatially highly resolved characterization and diagnosis of subsurface lithology, hydrogeology, and biogeochemistry at depth scales ranging from 1 to 100 m.

Acknowledgments The 4DEIT project was funded by the German Ministry of Education and Research (BMBF) in the framework of the R&D Program GEOTECHNOLOGIEN (Grants 03G0743A, 03G0743B, 03G0743C).

References

- Binley AM, Slater LD, Fukes M, Cassiani G (2005) The relationship between frequency dependent electrical resistivity and hydraulic properties of saturated and unsaturated sandstone. *Water Resour Res* 41:W12417
- Blaschek R, Hördt A, Kemna A (2008) A new sensitivity-controlled focusing regularization scheme for the inversion of induced polarization data based on the minimum gradient support. *Geophysics* 73:F45–F54
- Breede K, Kemna A, Esser O, Zimmermann E, Vereecken H, Huisman JA (2011) Joint measurement setup for determining spectral induced polarization and soil hydraulic properties. *Vadose Zone J* 10:716–726
- Döring U (1997) Transport der reaktiven Stoffe Eosin, Uranin und Lithium in einem heterogenen Grundwasserleiter. Ph.D. thesis, University of Kiel, Germany
- Flores Orozco A, Kemna A, Oberdörster C, Zschornack L, Leven C, Dietrich P, Weiss H (2012a) Delineation of subsurface hydrocarbon contamination at a former hydrogenation plant using spectral induced polarization imaging. *J Cont Hydrol* 136(137):131–144
- Flores Orozco A, Kemna A, Zimmermann E (2012b) Data error quantification in spectral induced polarization imaging. *Geophysics* 77:E227–E237
- Flores Orozco A, Williams KH, Kemna A (2013) Time-lapse spectral induced polarization imaging of stimulated uranium bioremediation. *Near Surf Geophys* 11:531–544
- Kemna A (2000) Tomographic inversion of complex resistivity—theory and application. Ph.D. thesis, Ruhr-University of Bochum, Germany
- Kemna A, Binley A, Ramirez A, Daily W (2000) Complex resistivity tomography for environmental applications. *Chem Eng J* 77:11–18
- Kemna A, Vanderborght J, Kulesa B, Vereecken H (2002) Imaging and characterisation of subsurface solute transport using electrical resistivity tomography (ERT) and equivalent transport models. *J Hydrol* 267:125–146
- Kemna A, Binley A, Slater L (2004) Crosshole IP imaging for engineering and environmental applications. *Geophysics* 69:97–107
- Kemna A, Binley A, Cassiani G, Niederleithinger E, Revil A, Slater L, Williams KH, Haegel F-H, Hördt A, Kruschwitz S, Leroux V, Titov K, Zimmermann E (2012) An overview of the spectral induced polarization method for near-surface applications. *Near Surf Geophys* 10:453–468
- Koestel J, Kemna A, Javaux M, Binley A, Vereecken H (2008) Quantitative imaging of solute transport in an unsaturated and undisturbed soil monolith with 3-D ERT and TDR. *Water Resour Res* 44:W12411
- Kwon YW, Bang H (1997) The finite element method using MATLAB. Florida, Boca Raton
- Leroy P, Revil A, Kemna A, Cosenza P, Ghorbani A (2008) Complex conductivity of water-saturated packs of glass beads. *J Colloid Interface Sci* 321(1):103–117
- Madden TR, Cantwell T (1967) Induced polarization, a review. In: Hansen DA, Heinrichs WE Jr, Holmer RC, MacDougall RE, Rogers GR, Sumner JS, Ward SH (eds) *Society of exploration geophysicists' mining geophysics, vol II*. pp 373–400
- Müller K, Vanderborght J, Englert A, Kemna A, Rings J, Huisman JA, Vereecken H (2010) Imaging and characterization of solute transport during two tracer tests in a shallow aquifer using electrical resistivity tomography and multilevel groundwater samplers. *Water Resour Res* 46:W03502
- Revil A, Florsch N (2010) Determination of permeability from spectral induced polarization in granular media. *Geophys J Int* 181:1480–1498
- Revil A (2013) On charge accumulations in heterogeneous porous materials under the influence of an electrical field. *Geophysics* 78(4):D271–D291
- Slater LD, Lesmes D (2002) IP interpretation in environmental investigations. *Geophysics* 67:77–88
- Sunde ED (1968) *Earth conduction effects in transmission systems*. Dover Publications, New York
- Tillmann A, Englert A, Nyari Z, Fejes I, Vanderborght J, Vereecken H (2008) Characterization of subsoil heterogeneity, estimation of grain size distribution and hydraulic conductivity at the Krauthausen test site using cone penetration test. *J Contam Hydrol* 95:57–75

- Vanderborght J, Kemna A, Hardelauf H, Vereecken H (2005) Potential of electrical resistivity tomography to infer aquifer transport characteristics from tracer studies: a synthetic case study. *Water Resour Res* 41:W06013
- Vanhala H (1997) Mapping oil-contaminated sand and till with the spectral induced polarization (SIP) method. *Geophys Prospect* 45:303–326
- Vereecken H, Döring U, Hardelauf H, Jaekel U, Hashagen U, Neuendorf O, Schwarze H, Seidemann R (2000) Analysis of solute transport in a heterogeneous aquifer: the Krauthausen field experiment. *J Contam Hydrol* 45(3–4):329–358
- Williams KH, Kemna A, Wilkins MJ, Druhan J, Arntzen E, N’Guessan AL, Long PE, Hubbard SS, Banfield JF (2009) Geophysical monitoring of coupled microbial and geochemical processes during stimulated subsurface bioremediation. *Environ Sci Technol* 43:6717–6723
- Zhao Y, Zimmermann E, Huisman JA, Treichel A, Wolters B, van Waasen S, Kemna A (2013) Broadband EIT borehole measurements with high phase accuracy using numerical corrections of electromagnetic coupling effects. *Meas Sci Tech* 24(8):085005
- Zimmermann E, Kemna A, Berwix J, Glaas W, Munch HM, Huisman JA (2008a) A high-accuracy impedance spectrometer for measuring sediments with low polarizability. *Meas Sci Tech* 19:105603
- Zimmermann E, Kemna A, Berwix J, Glaas W, Vereecken H (2008b) EIT measurement system with high phase accuracy for the imaging of spectral induced polarization properties of soils and sediments. *Meas Sci Tech* 19:094010
- Zimmermann E, Huisman JA, Kemna A, Berwix J, Glaas W, Meier H, Wolters B, Esser O (2010) Advanced electrical impedance tomography system with high phase accuracy. In: *Proceedings of the 6th World Congress on industrial process tomography (WCIPT6)*, Beijing, China, pp 583–591, 6–9 Sept 2010
- Zimmermann E (2011) *Phasengenaue Impedanzspektroskopie und -tomographie für geophysikalische Anwendungen*. Ph.D. thesis, University of Bonn, Germany

Chapter 2

Towards an Integrative Inversion and Interpretation of Airborne and Terrestrial Data

Hans-Jürgen Götze, Martin Afanasjew, Michael Alvers, Liliana Barrio-Alvers, Ralph-Uwe Börner, Christian Brandes, Rudolf Eröss, Peter Menzel, Uwe Meyer, Mathias Scheunert, Bernhard Siemon, Klaus Spitzer, Dominik Steinmetz, Johannes Stoll, Gupta Sudha, Bülent Tezkan, Angelika Ullmann and Jutta Winsemann

Abstract The aim of the joint research project is to generate information from airborne geophysical measurements that are properly transferred from physically quantitative descriptions of the subsurface (electrical conductivities, densities, susceptibilities) into spatial structures and information matching the understanding of end-users: geologists, hydrogeologists, engineers and others. We suggest new types of inversion, which are integrated in the interactive workflow to support typical trial and error approaches of inverse and forward EM and gravity/magnetic field modelling for 1D and 3D cases. Subsequently, we combine resistivity and density models with geological 3D subsurface models. The integrated workflow minimizes uncertainties

H.-J. Götze (✉) · P. Menzel
Institut für Geowissenschaften, Christian-Albrechts-Universität Kiel, Kiel, Germany
e-mail: hajo@geophysik.uni-kiel.de

U. Meyer · B. Siemon · A. Ullmann
Abteilung Grundwasser und Boden, Bundesanstalt für Geowissenschaften und Rohstoffe,
Hannover, Germany

R. Eröss · G. Sudha · B. Tezkan
Institut für Geophysik und Meteorologie, Universität zu Köln, Cologne, Germany

J. Stoll
Mobile Geophysical Technologies, Celle, Germany

R.-U. Börner · M. Scheunert · K. Spitzer
Institut für Geophysik und Geoinformatik, TU Bergakademie Freiberg, Freiberg, Germany

M. Afanasjew
Institut für Numerische Mathematik und Optimierung, TU Bergakademie Freiberg,
Freiberg, Germany

M. Alvers
Transinsight GmbH Dresden, Dresden, Germany

C. Brandes · D. Steinmetz · J. Winsemann
Institut für Geologie, Leibniz Universität Hannover, Hannover, Germany

L. Barrio-Alvers
Biotechnologie Zentrum, Technische Universität Dresden, Dresden, Germany

in the interpretation of geophysical data and allows a significantly improved and fast interpretation and imaging of the 3D subsurface architecture. The results of the AIDA project demonstrate that combined 3D geological and geophysical models enable a much better reconstruction of the subterraneous space. AIDA stands for “From Airborne Data Inversion to In-Depth Analysis” and is part of the R&D program: Tomography of the Earth’s Crust—From Geophysical Sounding to Real-Time Monitoring.

2.1 Introduction

The rising competition in land use especially between water economy, agriculture, forestry, building material economy and other industries often lead to irreversible deterioration in the water and soil system (e.g. salinization and degradation) due to over-exploitation which results in a long term damage of natural resources. Spatial surveys of the subsurface structure and physical parameters by airborne geophysical measurements and subsequent ground geophysical surveys target exemplary at two test sites (Cuxhaven and Rhüden, Fig. 2.1) enabling to gain the needed additional knowledge. The complementary use of airborne and ground geophysics, the validation, assimilation and improvement of current results by inversion techniques and plausibility tests helped us to respond to the following key questions: (1) Which algorithms are useful to describe structural settings of the usable subsurface by user specific characteristics as e.g. water volume, layer thicknesses, porosities. (2) What are the physical relations of observed parameters (electrical conductivities, magnetic susceptibilities, densities, etc.) to geological strata? (3) How can we deduce characteristics or parameters from the observations which describe near subsurface structures (e.g. groundwater systems, their charge, discharge and recharge, vulnerabilities and other quantities)?

The six partners of the AIDA project (AIDA: From Airborne Data Inversion to In-Depth Analysis) developed new and expanded existing inversion strategies to improve structural parameter information on different space and time scales and tested them for a multi-parameter inversion applying interactive graphic tools. A primary goal was also to solve comparable society related problems (as salinization, erosion, contamination, degradation etc.) in regions within Germany by generalization of project results. Modelling results from the different projects are still based on very heterogeneous modelling software and philosophies. We harmonized results for comparison, validation and synoptic visualization (Sect. 2.7). Validation and definition of geological units were based on 3D-subsurface models of electrical resistivity, borehole logs, gravity/magnetics and seismic models as constraints. A GOCAD[®] model of the tunnel valley is used as constrain for geophysical-modelling in appropriate software.

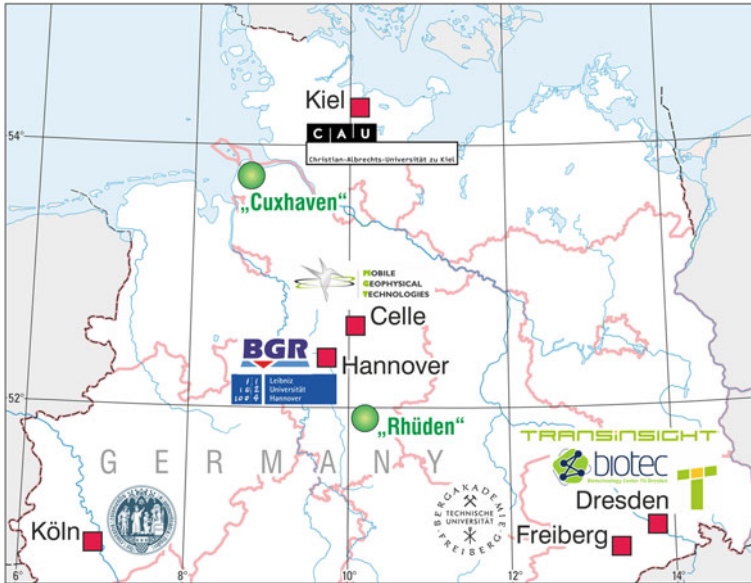


Fig. 2.1 Location map of AIDA partners and their research areas: the Cuxhaven subglacial tunnel valley in the North and the Lutter anticline near Rhüden in the center

2.2 Data Bases

We selected three areas to test our recently developed algorithms and the work flow. Two areas are located in the Central European Basin System (CEBS). The basin developed in the Permian as a rift basin (Littke et al. 2008). The up to 10 km thick basin fill comprises Lower Permian to Neogene continental and marine deposits. During the Pleistocene the CEBS was affected by repeated glaciations and transgressed by the Scandinavian ice sheets. Two test sites were chosen, the Cuxhaven subglacial tunnel valley and its Neogene host sediments and a salt anticline (Lutter anticline) in the northwestern part of the Harz foreland plus a third location in Switzerland.

Cuxhaven tunnel valley

The Cuxhaven tunnel valley is located in northwestern Germany, between Cuxhaven and Bremerhaven (Fig. 2.1). This area is characterized by the occurrence of numerous Middle Pleistocene subglacial tunnel valleys, which are deeply incised into Neogene and Palaeogene marginal marine deposits. These tunnel valleys are often important groundwater reservoirs and have a complex fill, reflecting repeated cut-and fill processes. The Cuxhaven tunnel valley is about 350 m deep and 1–2 km wide. The lower fill consists of interbedded gravel, sand and silt, deposited by meltwater. In the upper part fine-grained glacio-lacustrine deposits (Lauenburg clay complex) and interglacial marine Holsteinian deposits occur. During the subsequent Saalian glaciation an up to 40 m thick terminal moraine formed that consists

of meltwater deposits and till, flanked by younger Eemian and Holocene intertidal and salt marsh sediments. The data base includes airborne electromagnetics (AEM), comprising both frequency-domain helicopter-borne electromagnetic data (HEM) and time-domain helicopter-borne electromagnetic data (SkyTEM), helicopter-borne magnetic (HMG) and radiometric (HRD) measurements, ground-based continuous vertical electrical soundings (CVES), time-domain electromagnetics (TEM), direct current (DC), 2D reflection seismic profiles, gravimetric data sets and borehole logs were made available.

Lutter anticline (Rhüden)

The Lutter anticline lies within the Harz foreland area, 10 km northeast of Rhüden (Fig. 2.1). It represents a salt-cored anticline that formed during the Cretaceous contraction phase of the CEBS. The broad anticline trends NNE-SSW, is approximately 5 km wide and composed of Mesozoic sedimentary rocks. The data base includes an airborne survey comprising HEM, HMG and HRD and ground based gravity data.

Neuchâtel (Swiss)

The suitability of the test area (an electric cable and a pipeline) was proven by preceding geophysical investigations performed by subproject 1. It was chosen due to the vicinity to Luzern, where *Aeroscout* has its office and strong known anomalies occur. The VLF-method is sensitive for lateral conductivity changes. The prominent anomalies ensured a strong signal, this way, despite all kind of different noise and problems that may occur in a pilot project area, we ensured that the first UAS-VLF survey was able to resolve the anomalies.

2.3 Aero-Ground Inversion

One of the central project objectives was the combination of an unmanned aerial system (UAS) with the very low frequency (VLF) method. It will help to bridge the gap between conventional aero- and terrestrial geophysics. An UAS is capable of navigating precisely and is therefore suited for geophysical measurements flying with low and constant velocity at low altitudes across areas of interest. The strength of the VLF method is the ability to quickly map areas. In March 2012 a first experiment UAS-VLF measurements were conducted with a prototype system on a test area close to Neuchâtel in Switzerland (N 47.025, E 7.016). This system consists of a three-component electromagnetic sensor and a data logger deployed on an unmanned helicopter (Fig. 2.2). To receive comparable data ground based VLF and UAS-VLF measurements were carried out. Time series of the H_x , H_y and H_z components were processed to derive the transfer functions. The measurements of both methods clearly indicate the location of the anomalies. A data example of the survey is shown in Fig. 2.3. The relation of the horizontal and vertical magnetic field components $H_z(f) = A(f) \cdot H_x(f) + B(f) \cdot H_y(f)$ is used to derive the magnetic transfer function $A(f) = H_z(f) \cdot H_x(f)$.

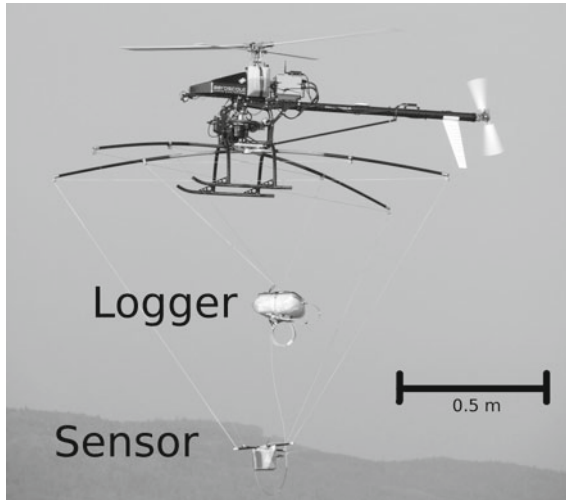


Fig. 2.2 The UAS-VLF-system with the logger and sensor hanging on the suspension. The especially developed suspension satisfies numerous functions. It mitigates oscillations, rotations and vibrations of the sensor and the logger and, additionally, helps to reduce torques caused by the devices (onto the helicopter). A reasonable compromise between low noise and flight stability had to be found. Additionally, the logger and the sensor went through a weight reduction process

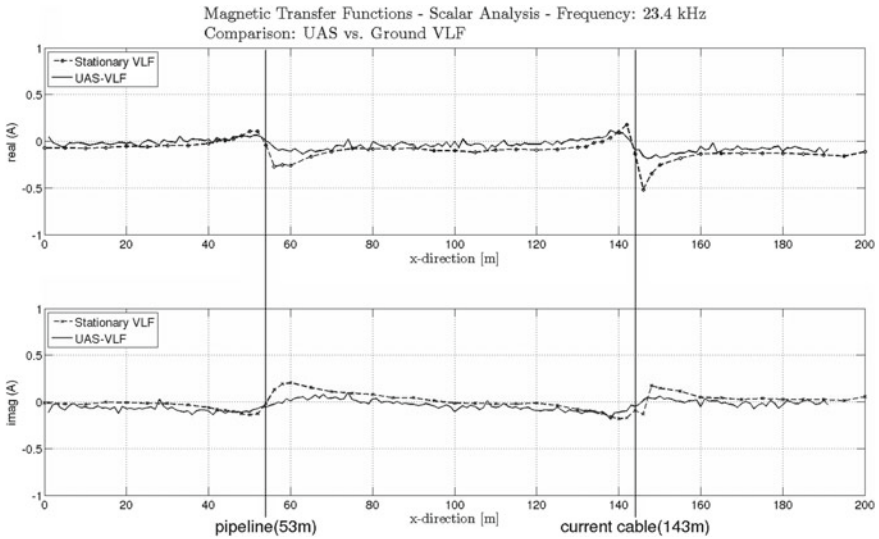


Fig. 2.3 Scalar analysis and comparison of the stationary ground and UAS-VLF measurements of the A component of the magnetic transfer function along a common transect. The real (*top*) and imaginary part (*bottom*) of the magnetic transfer functions is shown along the profile distance in meters. The 23.4 kHz frequency is utilized

As expected, the amplitudes of the ground based VLF measurements are bigger and the transfer function is less noisy compared to the UAS-VLF measurements. Nevertheless, the anomalies (inflection points) are clearly visible for both methods and their locations could successfully be detected by the UAS-VLF and ground based VLF measurements. The time series were analyzed by the scalar as well bivariate methods. For more details see Eröss et al. (2013).

The accuracy of model parameters for inversion was improved at shallow and greater depths. HEM, TEM and RMT measurements have been combined by using a 1D joint inversion methodology. To obtain this, the data sets, the model functions and the Jacobian matrices of these methods are combined to acquire only one set of model parameters as described below.

$$\mathbf{d} = \begin{pmatrix} \mathbf{d}_1(RMT) \\ \mathbf{d}_2(HEM) \\ \mathbf{d}_3(TEM) \end{pmatrix}, \mathbf{J} = \begin{pmatrix} \mathbf{J}_1(RMT) \\ \mathbf{J}_2(HEM) \\ \mathbf{J}_3(TEM) \end{pmatrix}, \mathbf{f} = \begin{pmatrix} \mathbf{f}_1(RMT) \\ \mathbf{f}_2(HEM) \\ \mathbf{f}_3(TEM) \end{pmatrix}, \quad (2.1)$$

where \mathbf{d} is the measured data vector and \mathbf{f} is the computed response that correspond to the logarithms of in-phase and quadrature components, induced voltages, and apparent resistivities and phases for HEM, TEM and RMT data, respectively. \mathbf{J} is the Jacobian matrix containing the parameter sensitivities, i.e. the derivatives of the functional \mathbf{f} with respect to the model parameters \mathbf{m} . The objective of the joint inversion of three different electromagnetic methods is to explore the Earths subsurface from shallow to deep structures. This has led us to construct a matrix whose elements are based on the selected method and corresponding model parameter. The newly developed algorithm functions as follows:

1. Choose maximum and minimum value of depth of investigations, for all the methods used, following Spies (1989). Out of these, four depths of investigation indices will be used, which are $d_{max}(RMT)$, $d_{min}(HEM)$, $d_{max}(HEM)$ and $d_{min}(TEM)$. Where $d_{max}(RMT)$ is the maximum depth down to which RMT can resolve well. Consequently, $d_{min}(HEM)$ and $d_{max}(HEM)$ are the minimum and maximum depths which HEM can resolve well. Similarly, $d_{min}(TEM)$ is the minimum depth above which TEM cannot resolve earth structures sufficiently.
2. Choose a starting model.
3. Derive model parameter weighting matrix \mathbf{W}_m : If $d_i \geq d_{max}(RMT)$; elements of the weighting matrix for the model parameters of the layers below i th layer will be given less weight, however, for the i th layer and layers above i th layer will get 100% weight for RMT. Here, d_i is the depth of the bottom of the i th layer. Similarly, weighting elements are calculated for TEM and HEM methods.
4. The data weighting matrix, \mathbf{W}_d , containing the data errors/noise is also multiplied to the elements of the Jacobian of the joint inversion matrix. To nullify the effect of the number of data points of a particular data set in joint inversion, the Jacobian is multiplied with the square root of the ratio of total number of data points in all the methods to the number of data points in the particular method.

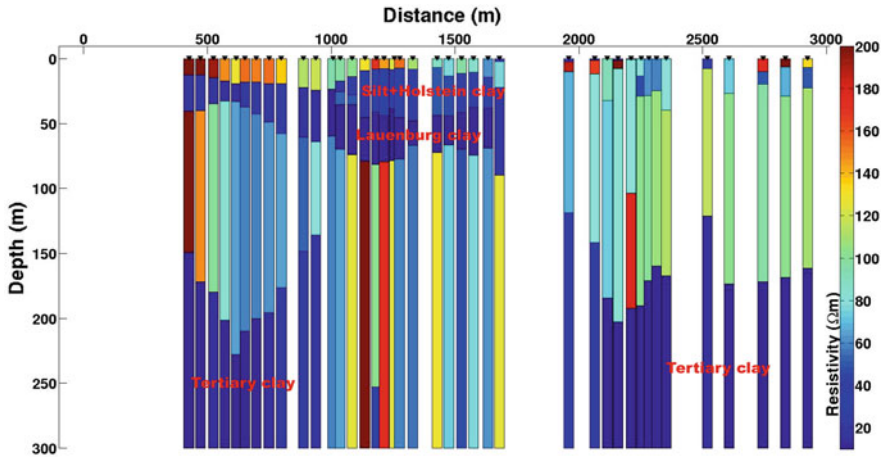


Fig. 2.4 The 1D Marquardt weighted-joint interpreted models for RMT, HEM and TEM data

5. This matrix is multiplied to the Jacobian matrix of the joint inversion and then inverted. Therefore, the resultant sensitivity matrix for weighted-joint inversion becomes

$$\mathbf{J}_w = \mathbf{W}_d \mathbf{J} \mathbf{W}_m \sqrt{\frac{\sum N}{N}}, \quad (2.2)$$

where $\sum N$ is the sum of the number of data points of all methods and N is the number of data points in a particular method.

6. The weighting matrix \mathbf{W}_m is updated after every iteration according to the new model obtained after each iteration and the inversion continues.

We used the Levenberg-Marquardt (Levenberg 1944; Marquardt 1963) inversion method, which provided damped least square solution by adding constant multiplier (β) as

$$\Delta \mathbf{m} = (\mathbf{J}_w^T \mathbf{J}_w + \beta^2 \mathbf{I})^{-1} \mathbf{J}_w^T \mathbf{y}. \quad (2.3)$$

where $\mathbf{y} = \mathbf{d} - \mathbf{f}$ is the difference between the measured data vector (\mathbf{d}) and the computed response (\mathbf{f}) at each iteration.

We have applied the weighted-joint inversion methodology on the Cuxhaven tunnel valley. Figure 2.4 illustrates the 1D Marquardt weighed-joint inversion models. The Marquardt models indicate a three to five layer geological structure. In the central part, i.e. in the valley, five layer structures have been observed, however, on the east and west side of the valley it can be explained with a four layer structure. The Marquardt weighted-joint inversion models infer the boundaries of the Holsteinian, Lauenburg clay complex and underlying fine-grained Neogene deposits. However, the base of the Paleogene is not resolved. It has been found that the results are consistently improved in all cases for the weighted-joint inversion.

2.4 Model Coupling HEM 1D+

HEM data sets are used for both geophysical and geological modelling, e.g. for groundwater or mineral exploration. As a standard procedure, the multi-frequency HEM data are inverted to resistivity-depth models using 1D inversion methods. Since the footprint of the HEM system is rather small and smooth conductivity structures are close to 1D settings, this is a valid approach. Furthermore, our “advanced 1D inversion” methods improve 1D inversion results by taking neighbouring data points and additional information from further geophysical measurements into account (Siemon et al. 2009). However, areas of higher dimensionality (anomalies) are not recovered correctly by 1D inversion procedures and require multi-dimensional modelling. Cox et al. (2012) developed a smooth 3D inversion for airborne electromagnetic data using a moving footprint technique. Accurate multi-dimensional inversion of HEM data of an entire survey, however, is still not state of the art.

Our idea is to combine 1D and 3D inversion of HEM data (Ullmann et al. 2013b). We restrict the 3D inversion to areas of strong anomalies only. The challenging task is, besides 3D inversion itself, to define those areas where 1D inversion is not able to produce acceptable resistivity models. A newly developed search algorithm (Ullmann et al. 2013a) is used to identify areas of higher dimensionality in HEM data sets. As the quantity to be measured in HEM, the secondary magnetic field, is strongly dependent on altitude variations it cannot be used directly as input for the search algorithm. Therefore, the secondary fields are transformed to apparent resistivities which are much less dependent on altitude variations. For each frequency 2D grids of the logarithmic apparent resistivities are produced using natural neighbour interpolation. The cell size is chosen of the order of a quarter of the line spacing. The search algorithm, consisting of several image processing methods, is then applied to the apparent resistivity grids. The results are added up to use all information about existing anomalies together coming from different depths, i.e. different frequencies (Fig. 2.5 left). The identified anomalies are sorted in five different classes (‘2D’, ‘3D circular’, ‘3D oval’, ‘3D elongate’, ‘chaotic’). In two steps, the region-based shape descriptors compactness, eccentricity, elongation, and deficit of convexity are grouped to the corresponding classes using the k-means algorithm. The anomalies are divided into 2D and 3D structures, in which the 3D structures are differentiated into circular, oval, or elongated shapes. The class ‘chaotic’ contains big anomalies consisting likely of overlapping single anomalies induced by different bodies in or on the subsurface (Fig. 2.5 centre). The classification results are used for optimised 3D model set-up.

A certain area containing the anomaly of interest is defined based on the result of the search algorithm (Fig. 2.5 right). In this region the HEM data have to be modelled in 3D. The corresponding HEM data are extracted for 3D inversion. Outside the anomalous region, the HEM data are inverted to resistivity-depth models using a standard 1D inversion method based on a starting model derived from apparent resistivities and centroid depth values. The anomalous HEM data are inverted to a 3D resistivity model applying a newly developed inversion scheme (Scheunert

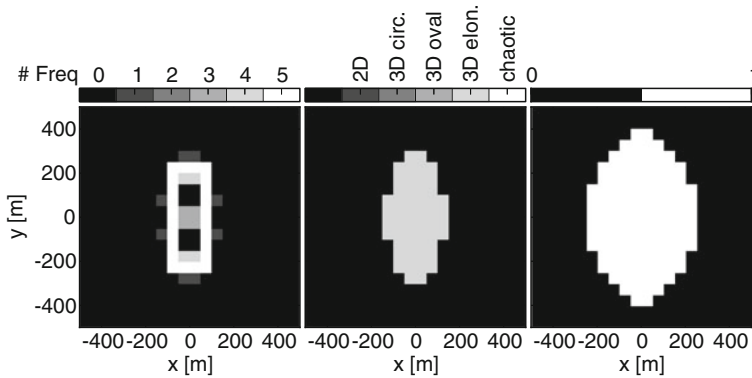


Fig. 2.5 Location and number of frequencies where anomalies were detected (*left*) and the classification scheme of detected anomalies (*centre*). Resulting anomalous region necessary for 3D inversion (*right*)

et al. 2013). The 3D inversion is carried out for a finite difference discretization using the given 1D background. Finally, the 3D inversion model (Fig. 2.6b and c) of the anomalous region can be integrated into the quasi 1D background (Fig. 2.6a). The integration of the resulting 3D models requires that the layered background coincides with the quasi 1D environment outside the anomalous region. This is generally not the case except for some small isolated structures. Therefore, the data sets have to be transformed to a 1D background (normal field transform) and, after 3D inversion, back-transformed to the originally environment. Figure 2.6d shows the resulting 1D/3D inversion model. The combination of 1D and 3D inversion of HEM data is demonstrated on synthetic HEM data derived from a 3D resistivity model (Fig. 2.7) as published by Siemon et al. (2009).

2.5 HEM 3D Inversion

Based on the precedent localisation of the entire HEM survey to those parts which are actually affected by an expected 3D anomaly (Sect. 2.4) we have developed an inversion scheme capable of revealing those anomalous conductivity structures. The approach exploits a priori information, given by a state-of-the-art laterally constrained 1D inversion. We reformulate the 3D boundary value problem of the total electric field E in terms of the secondary electric field E_{sec}

$$E = E_{\text{pri}} + E_{\text{sec}}, \quad (2.4)$$

$$\nabla \times \nabla \times E_{\text{sec}} + i\omega\mu_0\sigma E_{\text{sec}} = -i\omega\mu_0(\sigma - \sigma_{\text{pri}})E_{\text{pri}} \quad \text{in } \Omega, \quad (2.5)$$

$$n \times E_{\text{sec}} = 0 \quad \text{on } \partial\Omega, \quad (2.6)$$

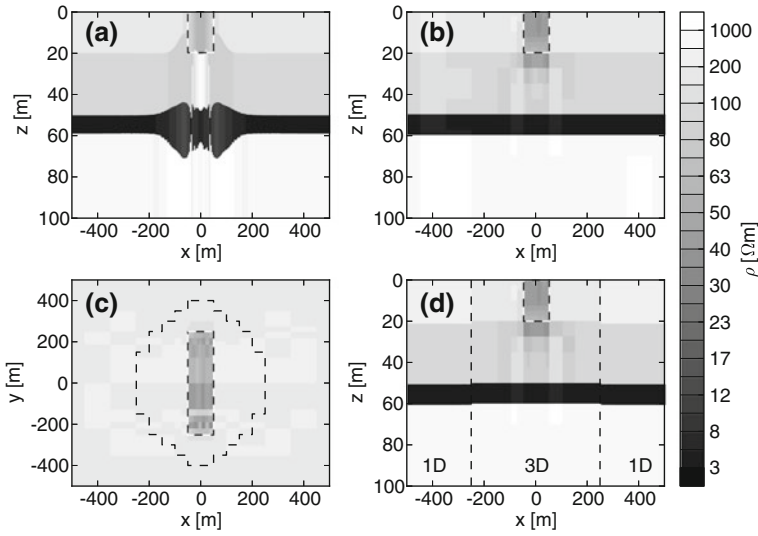


Fig. 2.6 1D (a) and 3D (b) inversion results along a profile across the model centre. *Top view* on the 3D inversion model (c) and combination of 1D and 3D inversion results (d) from a and b. The *dashed black-and-white line* shows the location of the cube. The *dashed black line* indicates the border of the previously defined area

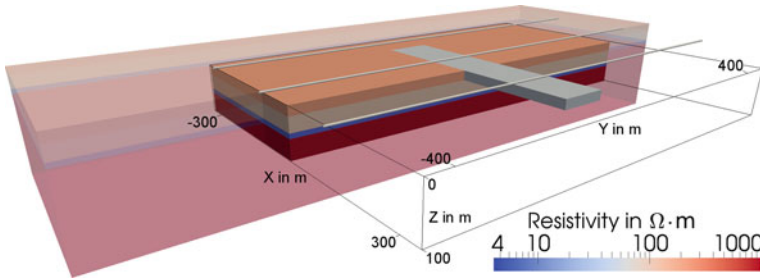


Fig. 2.7 Sketch of the model domain excluding the air layer and about half of its front-facing part. The semi-transparent part hints at the full size of the model (1200 m × 1800 m × 350 m) where a rectangular block (500 m × 100 m × 20 m with 50 Ω · m) is embedded in a horizontally layered half-space (layer depths 20 m; 30 m; 10 m; 190 m with 200 Ω · m; 100 Ω · m; 5 Ω · m and 1000 Ω · m from top to bottom). The black outline indicates the bounds of the active region. Survey profiles are indicated by the white tubes

where E_{pri} is the analytical primary electric field of a vertical magnetic dipole located in air. Furthermore we denote by ω the angular frequency, μ_0 the vacuum permeability, σ the total conductivity, and σ_{pri} the conductivity of the background model, respectively. We employ both finite difference and finite element methods to transform the continuous boundary value problem into a system of linear equations

$$A(\boldsymbol{\sigma}) u_{\text{sec}} = -A(\boldsymbol{\sigma}) u_{\text{pri}} + A(\boldsymbol{\sigma}_{\text{pri}}) u_{\text{pri}} = b, \quad (2.7)$$

with u_{sec} the secondary and u_{pri} the primary field solution of the discretised forward problem. The resulting system subsequently yields expressions for the gradient and approximate Hessian of the minimisation problem (sensitivity equations). Resulting from the unique transmitter-receiver coil configuration of the HEM problem, an explicit representation of the Jacobian matrix is used. To handle the sensitivity-related quantities, a tensor-based problem formulation is exploited. For solving the inverse problem, we apply a Gauss-Newton method with a Tikhonov-type regularisation term

$$\frac{1}{2} \underbrace{\|d^{\text{obs}} - d(m)\|_2^2}_{\text{data misfit}} + \frac{\lambda}{2} \underbrace{\|W(m - m_{\text{ref}})\|_2^2}_{\text{model roughness}} \rightarrow \min_m, \quad (2.8)$$

$$m := \log \boldsymbol{\sigma}, \quad (2.9)$$

where we aim at finding a model parameter distribution m such that both the difference between measured data d^{obs} and predicted data from the forward solution $d(m)$ for a given model parameter set as well as the parameter roughness are minimal. For the latter we consider the action of the model weighting matrix W on the difference between the model parameter vector and a reference model m_{ref} , i.e. the known background model. The model roughness itself is weighted by the regularisation parameter λ . Therefore, the predicted data is identified by

$$d(m) = Q[A^{-1}(m)b + u_{\text{pri}}]. \quad (2.10)$$

Here Q denotes the measurement operator, capable of extracting the total fields at distinct receiver sites from the discrete field components within the computational domain. The derived linear least squares problem is solved with Krylov subspace methods, such as LSQR, that are able to deal with the inherent ill-conditioning (Hestenes and Stiefel 1952; Paige and Saunders 1982). We further include two types of implicit regularisation schemes that simultaneously reduce the amount of model parameters and the computational cost. Based on the cumulative sensitivities (footprint) for the survey setup and the background resistivity known a priori, we define an active region as part of the parameterisation of the inverse problem where changes of m are explicitly allowed. Additionally we utilise a coarse parameter grid that is the starting point for an (adaptively) refined modeling forward grid. For numerical simulations and inversion studies we used a synthetic model (Siemon et al. 2009) that is shown in Fig. 2.7. We aim at reconstructing the electrical resistivity distribution of $M = 33,600$ parameter cells of the active region. The data points are distributed over three parallel profile lines. The line spacing is 200 m. Along the profiles, data is sampled every 4 m. The height of the transmitter-receiver pair above ground is $h = 30$ m. Samples of the vertical magnetic field have been collected for five frequencies. The synthetic data set comprises $N = 3765$ data points. Figure 2.8 shows a reconstruction of the conductivity distribution obtained from an inversion

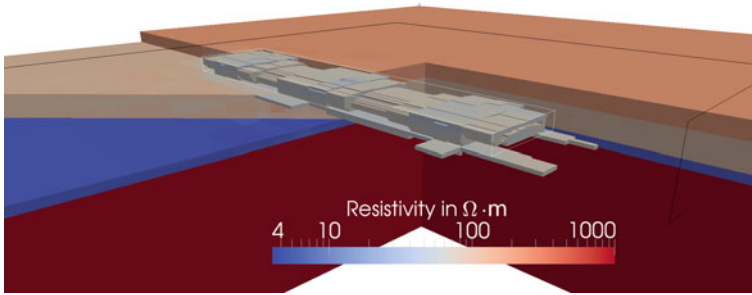


Fig. 2.8 Inversion result: Spatial distribution of the electrical resistivity. For scale and orientation refer to Fig. 2.7

of synthetic data. The final model shows an overall good agreement with the true model. After 20 Gauss-Newton iterations, the relative data residual has dropped to $1.9 \cdot 10^{-4}$. Furthermore, a smooth transition between the active and inactive region of the model is obtained due to an appropriate boundary condition imposed for the discretised model regularisation operator.

2.6 Potential Fields, Evolutionary Algorithms and Data Evaluation

In this paragraph we focus on two different tasks firstly on 3D inverse and forward modelling by evolution strategy for inversion of potential field data and secondly resampling of mass data.

We developed an interactive optimization-approach capable of combining manual modelling with automated covariance-matrix-adoption-evolution-strategy (CMA-ES, Ostermeier et al. 1994) geometry optimization. We focussed on the aspects of user-interactions supported by constrained and topology-conserving methods. In realistic geophysical models the number of geometry-describing triangles is often in the order of several hundreds of thousands. If triangles get small, the probability of incorrect and topology-destroying cross-overs increases with time. Unfortunately a destroyed topology cannot be formulated by a smooth penalty. The model is either valid or not. If it is not valid it has to be discarded. This fact leads quickly to an under-representation of good (valid) solutions, which implies that CMA-ES cannot adapt to the “landscape of the quality function” as desired. The optimization process slows down and most often stops completely. CMA-ES is strong in terms of global convergence and flexible in terms of adoption to the (local) quality function. This is achieved by learning a mutation-distribution on the fly. The method can deal with high-dimensional, highly scaled parameter spaces and fast convergence is achieved on a variety of typical test cases. But CMA-ES cannot guarantee topology-conservation of the models during optimization. There are two solutions

to the problem. (1) “re-injection”, where the strategy can actively be taught what a correct solution is or better would be: For example the parameter can be set (back) to—or short before—the constraining limit of the parameter and then be re-injected to the CMA-ES. This method is extremely computing intense and re-injection is not fully developed in terms of numerical stability. (2) Our idea to achieve topology conservation is to manipulate the space—which hosts the model—instead of the model itself (Alvers 1998). This can be achieved by a new paradigm where topology is preserved intrinsically. The basic idea is to change the size of grid elements (element legs) and make sure that (a) the legs are always greater than zero and (b) the element stays convex. The model behind must be sampled with high resolution as a prerequisite to always preserve topology. The idea is, to deform the models surrounding space. Thus, the model is optimized indirectly through its bent, entrapping space. In that way the model will be deformed while topology is intrinsically conserved. The model to be optimized is meshed with a regular grid in two dimensions, with e.g. tetrahedron grid in 3D. Then the grid (= containing space) is changed in such a way that the geometry of the model becomes optimal with respect to the quality function. Figure 2.9 illustrates the idea. Any grid modification is only performed along the edges of a grid element, which must not become zero-length (or negative) because the grid would touch (or even intersect) itself and the topology of the grid and therefore the topology of the model behind would be again destroyed. Model parameters are shifted to the length of the grid sides/legs. Now the coarse and fine grids control the possible geometry-resolution and therefore the number of optimization parameters. The beauty of this approach is that the user has full control and is not directly confronted with a highly resolved model with a huge number of triangles. In the 3D case the handles used to distort the room are defined in a cube or on tetrahedrons. The resolution of the cube can also be adjusted such that model updates can be either more focused or may affect a larger area. This is obviously useful to switch between detailed work and more regional model updates. More regional updates in the deeper parts of the model are also useful because the user gets immediate feedback on the model changes. This method is generic and can be applied to polyhedral models, voxel models and hybrid models (Schmidt et al. 2011). Inversion is typically done in batch where constraints are defined beforehand and then after a few minutes or hours a model fitting the data and constraints is generated. Quite often these models fit the data but appear to be unrealistic and the constraints are changed in order to improve the solution. Constraints can be entered directly (for example the maximum depth of an interface) or implemented indirectly (for example in the regularization). True geological constraints are difficult to implement because of their complexity.

Many data sets in geosciences contain extreme large amount of data. The high point density of these data sets often causes problems for processing and visualization. For efficient numeric handling, diverse resampling techniques are used to ease the data for better computation performance. Most common resampling methods usually reduce either highly resolved gridded data regularly or interpolate dense scattered 3D points on a coarse point grid. Because of parameter independency and interpolation, these methods cause a high loss of information. To avoid this problem, the presented “CIDRe” framework was developed (CIDRe: “Constrained Indicator

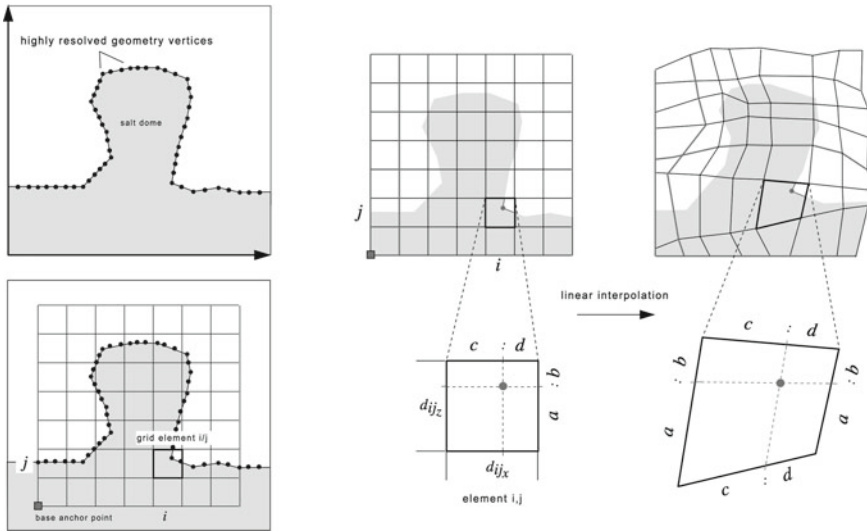


Fig. 2.9 *Left* A geological structure (salt dome) is meshed with a grid. *Right* The grid deformation is performed on grid legs and the model is interpolated linearly

Data Resampling”). The framework gets use of an irregular resampling method to improve handling, visualization and exchangeability of data and results. The new resampling algorithm uses the given data-parameters as resampling constraints (e.g. elevation, measured gravity or apparent resistivity). Accordingly the resampling chooses points, which are essentially important for the data set and rejects points with low additional information. Interpolation is not needed for resampling, so this method causes much lower errors than regular or interpolating resampling methods with similar resampling rates, in particular for data with strongly varying parameter distributions.

To demonstrate the achieved resampling results, the “CIDRe”—framework was applied on real HEM data (Siemon et al. 2004), that were used for inversion of observations in Sects. 2.3–2.5 and as constraints for geological modelling in Sect. 2.7. The resampling result is shown in Fig. 2.10, the parameter “apparent resistivity” ρ_a , inverted for the secondary field measured with a frequency of 385 Hz, was chosen as resampling constrain.

2.7 Model Development and Evaluation

One of the primary goals was the integration and assimilation of the results of the AIDA project partners in the framework of its examinations of plausibility and visualization of modelling and inversion. Here we will provide a priori conditions for structural model design as it results from 1D and 3D HEM-inversion.

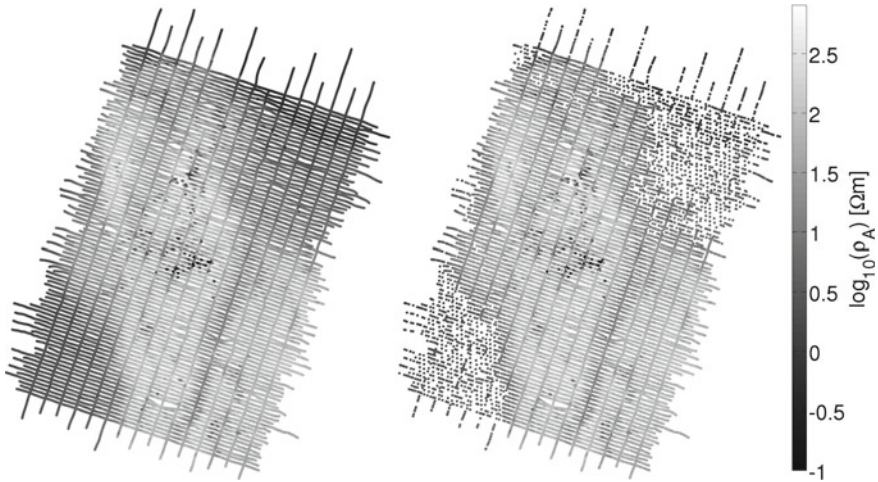


Fig. 2.10 Original (*left*) and resampled (*right*) ρ_a data. The resampling result achieves an average difference of 0.19 % to original parameter distribution for a resampling rate of 22.3 %

The aim of the joint project is an improved user oriented interpretation of combined 3D inversion and modelling of near subsurface data derived from airborne and ground-based geophysics. This was achieved by the development of an integrated workflow and new 3D modelling approaches, based on the integration of different geophysical, sedimentological, and petrophysical data. The main task was to combine geophysical and geological data sets to provide more realistic 3D subsurface models. In general, the ambiguity of geological, hydrogeological and geophysical data can lead to uncertainties in the resulting subsurface models. These uncertainties are caused by (1) limited data coverage (boreholes, seismic profiles, electromagnetic); (2) the limited vertical and lateral resolution of airborne electromagnetics (HEM and SkyTEM) and (3) the correlation of geophysical and lithological/hydrogeological properties (e.g. Burschil et al. 2012; Klimke et al. 2013). The workflow in Fig. 2.11 was established to reduce these uncertainties: First, pre-existing geophysical and geological data sets were used to build independent 3D subsurface models. The geological 3D subsurface models were constructed based on borehole data and 2D seismic reflection profiles. In a next step, the 1D AEM inversion results were utilized to construct a 3D resistivity grid model of the subsurface. To achieve this, we constructed a regular spaced grid and integrated the 1D AEM inversion results and subsequently analyzed the data by means of geostatistical methods such as nearest neighbour, discrete smooth interpolation algorithm and kriging. The best results were achieved by kriging. The advantage of this procedure is that it provides a fast selection of three-dimensional objects with specific resistivity ranges and therefore provides a rough estimate about the depositional architecture. To test the accuracy of the 3D resistivity model we calibrated it with seismic facies and lithological logs. The general correlation of grain size classes and resistivity values allows for a rough

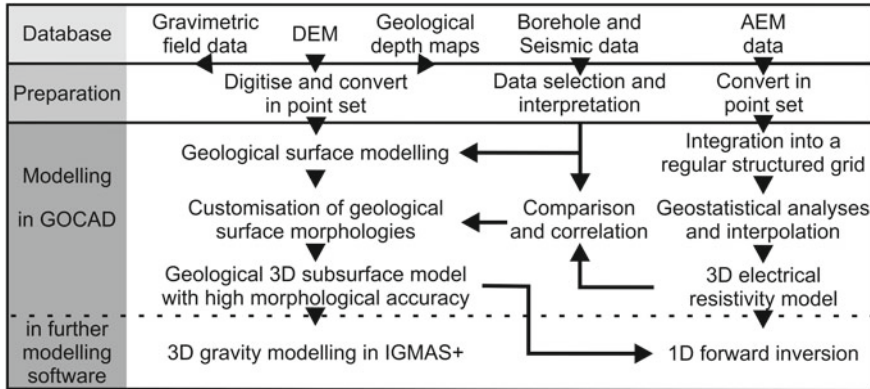


Fig. 2.11 Workflow for geological evaluation of geophysical models from different subprojects of the AIDA research partners

correlation of airborne electromagnetic data and lithology. However, the effect of overlapping resistivity values with different grain size classes may result in a misinterpretation of the lithology. The correlation between seismic facies, reflector patterns and AEM data enables the reconstruction of larger scale architectural elements and bounding surfaces. Resistivity images probably also allow the detection of fracture and fault systems. Open fractures may act as fluid conduits and therefore are characterized by a higher water content and hence a resistivity pattern that differs from the surrounding rocks. Subsequently, the 3D resistivity model and the 3D subsurface model were integrated and the initial parameters and boundary conditions of the geological model were adjusted. In the final step, 3D subsurface models were validated by comparing AEM forward modelling results based on these geological models with measured AEM results to identify remaining uncertainties. Additionally the models were used as input for 3D gravity modelling in IGMAS+. Therefore interfaces between IGMAS+ and GOCAD[®] and/or other user software in the AIDA project has to be developed and implemented.

An interface infrastructure was implemented for data exchange, processing and visualization to support the integration of particular results. This improvement consists of separate scripts, tools and applications and additionally integrates the “CIDRe”-framework, which was already introduced in Sect. 2.6. For purposes documented below, interfaces for Tsurf-data (GOCAD[®]) and IGMAS+ XML-data were provided. The 3D geological model geometry for the Cuxhaven tunnel valley (Sect. 2.2) will be validated later by the synthetic gravity effect, calculated by gravity forward modelling.

Closed polyhedral subsurface geometries were extracted as Tsurf-objects. These geometries were represented by triangulated hulls for each stratigraphic unit, which can be imported to the gravity forward modelling software IGMAS+ (Schmidt et al. 2011). Topographic geometry parts with elevation above 0 m are removed.

Additionally, model boundaries are extended by 15-fold model extension in each direction to avoid computational edge effects.

In IGMAS+ for each triangulated body hull a “body” object is assigned to this geometry to encapsulate the geophysical subsurface parameters, e.g. density. The parameter set is assumed to be constant for the entire body geometry. Earlier studies already showed that the gravity signal of the infilled masses of a tunnel valley varies between $-0.3 * 10^{-5} \frac{m}{s^2}$ (Rumpel et al. 2009) and $0.3 * 10^{-5} \frac{m}{s^2}$ (Gabriel et al. 2003). The anomalies depend on the different densities of the infill. Stronger anomaly differences in mentioned studies are associated with the density values of the parametrization of the “Lauenburg Clay Complex (LCC)” (Rumpel et al. 2009). It varies between densities of $1813 \frac{kg}{m^3}$ and $1996 \frac{kg}{m^3}$ (Gabriel et al. 2003). From this we concluded, that the negative gravity anomaly interpreted by Rumpel et al. (2009) is mainly associated with rather low LCC densities. Generally we are in agreement with Rumpel et al. (2009) and Gabriel et al. (2003) that the tunnel valley fill is characterized by higher densities than the surrounding Neogene host sediments. Therefore, the gravity effect of the Lauenburg Clay Complex may mask the gravity anomalies of the basal coarse-grained tunnel valley fill.

According to these results, the geological architecture can be regarded as plausible. The LCCs density remains rather uncertain: gravity forward modelling suggests a density value of some $1900 \pm 20 \frac{kg}{m^3}$ for the LCC.

2.8 Discussion of Results

The AIDA results demonstrate that combined 3D geological and geophysical models enable a much better reconstruction of the subsurface architecture. The combination of an unmanned aerial system (UAS) with the very low frequency (VLF) method was successfully tested. Areas with low data coverage can be interpolated based on AEM data, if the correlation of resistivity values and lithology is known. In general the penetration depth is controlled by the lithology and their conductivity. SkyTEM data have a higher penetration depth (up to 300 m) but a lower vertical and lateral resolution, restricting the visualization of smaller-scale geological features. In contrast, the HEM method provides a much higher vertical and lateral resolution, but a lower depth penetration of up to 150 m.

New methods were developed and tested for the interpretation of AEM data, which mainly based on 3D modelling approaches. (1) In particular we used 1D AEM inversion results and applied a new 3D resistivity gridding procedure based on geo-statistical analyses and interpolation techniques to create continuous 3D resistivity grid models. This integrated workflow minimizes uncertainties in the interpretation of AEM data and allows for a significantly improved interpretation and imaging of the 3D subsurface. (2) The limits in the lateral and vertical resolution may lead to a diffuse reconstruction of thin-bedded sand/mud couplets, smaller-scale architectural elements and bounding surfaces, shown by Jørgensen et al. (2003), Viezzoli et al. (2008), Christensen et al. (2009) and Klimke et al. (2013). (3) The effect of

overlapping resistivity values with different grain size classes, as well as the effect of salt or fresh Water in saturated sediments may result in a misinterpretation of the lithology (Burschil et al. 2012; Klimke et al. 2013). (4) Anthropogenic noise effects in the AEM data can hinder a proper geological interpretation. Several new studies focus on the determination and elimination of these noise effects and their minimization (e.g. Tølbøll 2007; Siemon et al. 2011).

In order to enhance the model accuracy airborne and ground-based measurements (e.g. HEM, RMT and TEM) can be combined by joint inversion.

Automatic detection and handling of conductivity anomalies for in- and output routines were developed and tested; they enable to restrict 3D modelling only into areas where 3D modelling is really necessary. In all other cases a 1D inversion scheme is suggested. The user interface HEM1D+ controls all modelling interactions.

Inversion is typically done in batch where constraints are defined beforehand and then after a few minutes or hours a model fit of data and constraints is generated. Quite often these models fit the data but appear to be unrealistic and the constraints are changed in order to improve the solution. Constraints can be entered directly (for example the maximum depth of an interface) or implemented indirectly (for example in the regularization). True geological constraints are difficult to implement because of their complexity.

We developed a new novel weighted 1D weighted-joint inversion algorithm for the TEM, RMT and HEM data which was first of all tested by synthetic data and was then applied on a field data set. The weighted-joint Marquardt inversion models clearly infer the boundaries of the Lauenburg and Holsteinian clay complex in the common test area. To recover the spatial distribution of electrical conductivities from HEM data sets a 3D inversion scheme was developed, implemented and successfully applied. The inverse problem is solved using a Gauss-Newton approach. A novel method to evaluate and store the Jacobian leads to a noticeable reduction of computational effort. Together with state-of-the-art regularization techniques, the improved efficiency yields a substantial progress in the field of EM inversion methods. Based on the precedent localization of the entire HEM survey to those parts which are actually affected by an expected 3D anomaly we have developed an inversion scheme capable of revealing those anomalous conductivity structures. The approach exploits a priori information, given by a state-of-the-art laterally constrained 1D inversion.

A new scheme of inversion was developed during the runtime of the project. It is integrated in the interactive workflow to support typical trial and error approaches. Instead of alter a geological interface manually the user can kick off a (topology-conserving) inversion in a focused area, watch the inversion progress on the screen and interrupt in case the solution becomes geologically unrealistic. One can then wind a few steps back, change parameters of the inversion (e.g. change the selected region or change constraints) and start over. Thus the user always stays in control of the inversion process.

Problems arise from the spatial consistency of different geometries used in different software. They concern the geometrical GOCAD[®] and density modelling software (IGMAS+): triangulated hulls for each subsurface region have to be consistently closed, which means that each triangle edge of the hull mesh has to be shared

by two triangles in an opposite direction. This requirement is needed for correct gravity calculation in IGMAS+ (Schmidt et al. 2011) but not for GOCAD[®]. Therefore, each GOCAD-mesh has to be checked for geometrical consistency before it can be inserted in IGMAS+ for forward modelling. Further limitations are related to material parameters. The stratigraphic units can be detected by apparent resistivities and not always by densities. Toward this end the given geometry of the geological model does not represent subsurface densities. However, we demonstrated that the geological model cause a gravity field which fits published data.

2.9 Conclusions and Future Tasks

We provide fast and accurate methods for integrated 3D models of the subsurface both for geometry and parameters by resistivity grid modelling by the interpolation of 1D AEM inversion data and 3D forward modelling of terrestrial (gravity) data. The comparison of our integrated models with 1D AEM inversion results (Sect. 2.7) shows a significant improvement of the interpretation of AEM data and thus an improved reconstruction of the 3D subsurface architecture. AIDA project partners mostly achieved the primarily addressed goals. The handling of 3D models is restricted to models which were calculated (a) by forward modelling techniques and (b) inverted models based on synthetic data. Intensive collaboration within the AIDA project focussed on subprojects which directly got use of HEM, TEM and RMT data e.g. in the test area of Cuxhaven tunnel valley by both 1D inversion results and in-output interfaces of synthetic HEM data and/or models. As a result, a workflow was developed which recovers a 3D conductivity structure from subsets of large HEM data sets. These subsets have been reliably identified by research described in Sect. 2.4 on the basis of an anomaly detection algorithm. The 3D conductivity models obtained by the application of a 3D inversion (refer to Sect. 2.5) which have later been successfully merged with the original model based on local 1D inversions. The integration of borehole, seismic and AEM data into a Gocad model led to highly accurate geological 3D subsurface models at both test sites and proved the consistency of electrical resistivity models. A combination with density modelling was much more difficult because reliable information for both Bouguer gravity field and densities are still missing in the area of the Cuxhaven tunnel valley. The geological model did not really fit the measured gravity field. More generally we conclude from the intensive disciplinary collaboration that interactive geophysical modelling is tedious and very complex. Automated methods must at least support the experts and the connected problems are severe. The usage of automated optimization methods is problematic in case many solutions need to be rejected because of the model becoming inconsistent. However, the combined strategy of interactive optimization and space warping, instead of moving the corner points of the geometry directly, eased this problem.

We developed and suggest a couple of new inversion schemes, which are integrated in the interactive workflow to support geological interpretation. However, uncertainties in the integrated interpretation of AEM and ground data remain, mainly caused

by limitation related to their lateral and vertical resolution, anthropogenic noise effects, effects of overlapping resistivity values with varying grain size classes and pore water characteristics. Future work should focus on the determination and elimination of these uncertainties and their minimization. We will emphasize the need for highly-developed numerical regularization techniques such as the total variation regularization which employ jump-preserving features that might be necessary when appropriate geological a priori data is available. However, in conventional inversion procedures, constraining boundary conditions are assigned to “points” and topologically incorrect models are rejected. This often leads to problems like “extinction” of good individuals/solutions due to rather “small errors”. Human experts can often—but not always—keep topology through their knowledge about possible geological structures and their developments. To teach this to algorithms is impossible. Artificial neural networks (e.g. Gunnink et al. 2012) and sequential indicator simulations (e.g. Bosch et al. 2009) might be interesting in future to distinguish between different lithologies, parameter contrasts and depositional architecture of the subsurface. The developed algorithms still need more optimization towards intensive tests with real world data.

Acknowledgments The AIDA-Verbundprojekt is part of the support program GEOTECHNOLOGIEN of the BMBF: “Tomography of the Earth’s Crust—From Geophysical Sounding to Real-Time Monitoring”. We appreciate the financial support of our project by the BMBF and its administration by the Projektträger Jülich.

References

- Alvers MR (1998) Zur Anwendung von Optimierungsstrategien auf Potentialfeldmodelle. PhD thesis, FU Berlin (SFB 267), Berliner Geowissenschaftliche Abhandlungen, Reihe B, Band 28, Berlin, 108 Seiten.
- Bosch JHA, Bakker MAJ, Gunnink JL, Paap BF (2009) Airborne electromagnetic measurements as basis for a 3D geological model of an Elsterian incision. *Zeitschrift der deutschen Gesellschaft für Geowissenschaften* 160(3):249–258
- Burschil T, Scheer W, Kirsch R, Wiederhold H (2012) Compiling geophysical and geological information into a 3D model of the glacially-affected island of Föhr. *Hydrol Earth Syst Sci* 16:3485–3498
- Christensen NB, Reid JE, Halkjær M (2009) Fast, laterally smooth inversion of airborne time-domain electromagnetic data. *Near Surf Geophys* 7:599–612
- Cox LH, Wilson GA, Zhdanov MS (2012) 3D inversion of airborne electromagnetic data. *Geophysics* 77(4):WB59–WB69
- Eröss RB, Stoll JB, Tezkan B (2013) Three-component VLF using an unmanned aerial system as sensor platform. *First Break* 31(7):33–41
- Gabriel G, Kirsch R, Siemon B, Wiederhold H (2003) Geophysical investigation of buried Pleistocene subglacial valleys in Northern Germany. *J Appl Geophys* 53:159–180
- Gunnink JL, Bosch JHA, Siemon B, Roth B, Auken E (2012) Combining ground-based and airborne EM through artificial neural networks for modelling hydrogeological units under saline groundwater conditions. *Hydrol Earth Syst Sci* 16:3061–3074
- Hestenes RM, Stiefel E (1952) Methods of conjugate gradients for solving linear systems. *J Res Nat Bur Stan* 49(6):409–436

- Jørgensen F, Lykke-Anderson H, Sanderson PBE, Auken E, Nørmark E (2003) Geophysical investigations of buried Quaternary valleys in Denmark: an integrated application of transient electromagnetic soundings, reflection seismic surveys and exploratory drillings. *J Appl Geophys* 53:215–228
- Klimke J, Wiederhold H, Winsemann J, Ertl G, Elbracht J (2013) Three-dimensional mapping of Quaternary sediments improved by airborne electromagnetics in the case of the Quakenbrück Basin, Northern Germany. *Zeitschrift der deutschen Gesellschaft für Geowissenschaften* 164(2):369–384
- Levenberg K (1944) A method for the solution of certain non-linear problems in least squares. *Q Appl Math* 2:164–168
- Littke R, Bayer U, Gajewski G, Nelskamp S (2008) Dynamics of complex intracontinental basins. The example of the Central European Basin System. Springer, Heidelberg, p 519
- Marquardt DW (1963) An algorithm for least-squares estimation of non-linear parameters. *SIAM J Appl Math* 11:431–441
- Ostermeier A, Gawelezyk A, Hansen N (1994) A derandomized approach to self-adaptation of evolution, strategies. *Evol Comput* 2(4):369–380
- Paige CC, Saunders MA (1982) LSQR: an algorithm for sparse linear equations and sparse least squares. *ACM Trans Math Softw* 8(1):43–71
- Rumpel HM, Binot F, Gabriel G, Siemon B, Steuer A, Wiederhold H (2009) The benefit of geophysical data for hydrological 3D modelling—an example using the Cuxhaven buried valley. *Zeitung der deutschen Gesellschaft für Geowissenschaften* 160(3):259–269
- Scheunert M, Afanasjew M, Börner RU, Einermann M, Ernst OG, Spitzer K (2013) 3D inversion of helicopter electromagnetic data. In: 5th international symposium on three-dimensional electromagnetics, Sapporo, Japan, Extended Abstract, p 4
- Schmidt S, Plonka C, Götze HJ, Lahmeyer B (2011) Hybrid modelling of gravity, gravity gradients and magnetic fields. *Geophys Prospect* 59(6):1046–1051
- Siemon B, Eberle DG, Binot F (2004) Helicopter-borne electromagnetic investigation of coastal aquifers in north-west germany. *Zeitschrift für Geologische Wissenschaften* 32(5/6):385–395
- Siemon B, Auken E, Christiansen AV (2009) Laterally constrained inversion of helicopter-borne frequency-domain electromagnetic data. *J Appl Geophys* 67(3):259–268
- Siemon B, Steuer A, Ullmann A, Vasterling M, Voß W (2011) Application of frequency-domain helicopter-borne electromagnetics for groundwater exploration in urban areas. *Phys Chem Earth, Parts A/B/C* 36(16):1373–1385
- Spies BR (1989) Depth of investigation in electromagnetic sounding methods. *Geophysics* 54:872–888
- Tølbøll RJ (2007) The application of frequency-domain helicopter-borne electromagnetic methods to hydrogeological investigations in Denmark. PhD thesis, Department of Earth Sciences, University of Aarhus, Denmark
- Ullmann A, Siemon B, Miensopust M (2013a) Automatic detection and classification of induction anomalies in helicopter-borne electromagnetic data sets. In: 5th international symposium on three-dimensional electromagnetics, Sapporo, Japan, Extended Abstract, p 4
- Ullmann A, Siemon B, Scheunert M, Afanasjew M, Börner RU, Spitzer K, Miensopust M, (2013b) Combined 1D and 3D inversion of helicopter-borne electromagnetic data. In: Near surface geoscience, (2013) Bochum, Extended Abstract, Germany, p 5
- Viezzioli A, Christiansen AV, Sørensen K (2008) Quasi-3D modelling of airborne TEM data by spatially constrained inversion. *Geophysics* 73(3):F105–F113

Chapter 3

MIIC: Monitoring and Imaging Based on Interferometric Concepts

Christoph Sens-Schönfelder, Hortencia Flores-Estrella, Martina Gassenmeier, Michael Korn, Florian Köllner, Claus Milkereit, Ernst Niederleithinger, Stefano Parolai, Marco Pilz, Eraldo Pomponi, Andreas Schuck, Katja Thiemann and Jürgen Völkel

Abstract The capability of seismic interferometry to create virtual sources at receiver sites from records of ambient seismic noise is used for seismic monitoring and tomography of different targets. We present hardware developed specifically for the needs of seismic data acquisition in the context of monitoring and ambient noise tomography. Digitizers are capable of continuous recording and real time wireless data transmission in self organizing meshes to allow for robust telemetry in difficult circumstances such as cities or landslides that may cause the loss of stations. A software tool is described that implements required processing and analysis procedures for the interferometric processing. We have applied the novel 3D ambient noise surface wave tomography approach to the Issyk-Ata fault in Kyrgyzstan. It shows that seismic interferometry can successfully be used for structural investigations on length scales of only 100 m. The method uses 3D sensitivity kernels for a single-step inversion of phase velocity dispersion curves for subsurface S-wave velocity structure and incorporates topography. We recover lateral differences in sediment velocities and an offset of the bedrock depth across the fault. Applications of interferometric monitoring to the geological CO₂ storage test site in Ketzin (Germany) and to the Piton de la Fournaise volcano (La Reunion island) emphasize the value

C. Sens-Schönfelder (✉) · M. Gassenmeier · C. Milkereit · S. Parolai · M. Pilz
Helmholtz Centre Potsdam, GFZ German Research Centre for Geosciences, Telegrafenberg,
14473 Potsdam, Germany
e-mail: sens-schoenfelder@gfz-postdam.de

H. Flores-Estrella · M. Korn · E. Pomponi
Leipzig University, Institute for Geophysics and Geology, Talstrasse 35, 04103 Leipzig, Germany

F. Köllner · A. Schuck
GGL Geophysics and Geotechnics Leipzig GmbH, Bautzner Str. 67, 04347 Leipzig, Germany

E. Niederleithinger
BAM Federal Institute for Materials Research and Testing, Unter den Eichen 87, 12205
Berlin, Germany

K. Thiemann · J. Völkel
K-UTECH AG Salt Technologies, Am Petersenschacht 7, 99706 Sondershausen, Germany

of this approach. At Ketzin site we identify variations of the subsurface velocities that are correlated with changes in the ground water level and mask potential signals from the reservoir depth. At Piton de la Fournaise volcano, seismic velocity changes are linked to volcanic processes as shown by comparison with surface displacement and seismicity that are typically used to characterize volcanic activity. We observe a clear distinction between phases of inflation prior to eruptions and deflation during periods of quiescence.

3.1 Introduction

For the realization of interferometric time series analyses, the utilization of coherent phase information in complex wave fields is essential. In the context of elastic waves and, in particular, for the extraction of phase velocities from ambient noise, the first seismological application making use of this idea was presented by Aki (1957). He proposed to deduce information about the subsurface from the spatial correlation of the noise field, which is assumed to be random due to distributed and uncorrelated sources continuously exciting elastic waves. In contrast to this spatial correlation, Poupinet et al. (1984) demonstrated that the complex scattered wave field recorded after an excitation of elastic waves in a heterogeneous medium such as the earth's crust shows temporal correlation as well. The noise's correlation properties are controlled by the propagation medium regardless of the wave field's complexity, and if the medium is stationary, the waveforms will be, too. This allows to monitor changes in the subsurface by comparing waveforms recorded at different times.

These investigations established the basic concepts of what is now referred to as seismic interferometry (Curtis et al. 2006). However, to boost the development of applications using the spatial and temporal coherence of complex wave fields like noise and seismic coda, it took another essential finding: Only the experimental observation—and later also the mathematical confirmation—that the impulse response or Green's function of the elastic medium can be retrieved directly from diffuse wave fields increased the interest in such signals and accelerated research.

Focusing on the use of seismic interferometry for the investigation of the subsurface, the MIIC project (Monitoring and Imaging based on Interferometric Concepts) as part of the GEOTECHNOLOGIEN program contributes to this development. Special attention is given to the transfer and application on different length scales ranging from centimeters in laboratory over geotechnical scales to even kilometers in seismological applications. According to the project's structure, this article is organized in three parts, whereof the first describes technical developments of hard- and software. In the second part, we concentrate on imaging applications employing seismic interferometry to obtain high-resolution structural information about the subsurface. The third and last part is devoted to monitoring, where the permanent presence of seismic noise is used to continuously follow the evolution of the target medium.

The library behind this interface uses the core functions of the ObsPy toolbox (Megies et al. (2011), <https://github.com/obspy>) for data import and handling of raw seismological data. It contains functions for the typical routines of data pre-processing such as sign-bit normalization or spectral whitening. Cross-correlation which usually is the most CPU-time consuming part of the processing is implemented as a multi-process routine that optionally uses multiple cores of the system. A new data structure is defined for cross-correlations, which holds meta-information of the two participating stations, about the original data as well as information that are specific to the correlation.

Assessing temporal variations requires a further data structure: a set of correlations from a single station pair generated from the noise that was recorded at different times—a correlation matrix. A specific module is dedicated to the processing of this data structure. It implements filtering, trimming, normalization, smoothing and functions to estimate temporal variations of the correlation functions such as apparent stretching due to changes in the subsurface velocity and shifting of the correlation functions as a consequence of clock drifts.

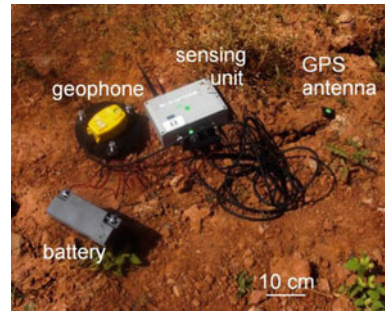
Results can be visualized directly or exported into image files. To facilitate the interface with other software for further analysis or visualization the data structures can be saved into MatLab® files. The documentation is available at <http://theo1.geo.uni-leipzig.de/docs>.

3.2.2 Seismic Sensors for Continuous Recording with Wireless Real Time Access

To meet the specific requirements of the application of interferometric concepts for data acquisition optimized instruments, being low-cost and allowing for near real-time data transmission and continuous recording, have been developed in the project. The instruments are based on the SOSEWIN system, originally developed by the Helmholtz-Zentrum Potsdam - Deutsches GeoForschungsZentrum (GFZ) and Humboldt University of Berlin (see Fleming et al. 2009 and Fig. 3.2).

This system employs advances in various technologies to incorporate off-the-shelf sensors with processing and communications components into low-cost seismic sensing units that are linked by advanced, robust and rapid communications routing and network organizational protocols appropriate for wireless mesh networks. The reduced cost of the instruments (less than one tenth of a standard instrument) allows creating dense, self-organizing and decentralized seismic imaging and monitoring networks of up to hundreds of nodes. In particular, its self-organizing capability, allows the system to adapt continuously to changing circumstances, i.e., the addition/removal/malfunctioning of nodes and interference in communications due to local (and possibly time-varying) phenomena. This is particularly important for monitoring purposes since some of the sections of the network might be lost following landslides, earthquakes, etc.

Fig. 3.2 Field use of the wireless sensing unit (top right) connected with one 4.5 Hz Geophone. During 2D array seismic noise measurements, which generally involve period of recording of few hours, the necessary energy can be provided by small 17 Ah batteries (bottom left)



Moreover, each sensing unit also has the capacity to measure other environmental parameters (temperature, humidity, etc.). This allows to obtain also detailed images of environmental impacts. At the same time, the stations also create a wireless mesh network by which the data required for efficient interferometric monitoring and imaging can be transmitted via WiFi to a computer that belongs to the network. This is different from standard seismological equipment and allows a preliminary analysis of the data directly in the field.

Therefore, the system can provide real-time information for use in seismic 3D imaging and 4D monitoring of changes in the subsoil conditions, environmental parameters as well as soil-structure interactions. Due to their lower cost the much higher instrumental density means that analysis tools can rely more on real data and less on interpolation schemes. This is particularly important since the system functionality can be extended also to early warning (e.g. activation of landslides after earthquakes).

3.3 Shear-Wave Velocity Imaging of Complex Shallow Structures

The shear wave velocity v_s is a key parameter related to the assessment of the local amplification of ground motion and is most commonly used in engineering seismology. Within this context, shear wave velocity values can be measured in situ by means of various invasive (borehole) or non-invasive (shear wave refraction and reflection studies) techniques. Although these techniques provide accurate and well resolved values of v_s they suffer from several drawbacks, such as increasing costs with required depth or only pointwise estimates.

In recent years, passive seismic techniques have received considerable attention and have become increasingly attractive in a broad range of seismological disciplines on different scales (e.g. Bonnefoy-Claudet et al. 2006). This kind of techniques are generally low cost and carried out with instruments that are easy to deploy, and are not bound to any active sources. The success of these applications is explained by the fact that passive methods are based on surface waves, which are by far the strongest waves excited in the seismic noise wave field.

Among the passive methods seismic interferometry has particularly become popular in a variety of applications in the recent years (see reviews by Campillo 2006; Curtis et al. 2006 among many others). One of the most intriguing applications of the method, shown both theoretically and experimentally, is that a random wavefield has correlations, which, on average, take the form of the Green's function of the media (e.g. Rickett and Claerbout 1999; Lobkis and Weaver 2001; Weaver and Lobkis 2001; Snieder 2004). Between pairs of receivers, the Green's function can be extracted from cross-correlations of ambient noise recorded at both receivers, allowing an estimate of the propagation delay between the stations. So far, such travel time measurements of Rayleigh waves reconstructed from seismic noise have mainly been used at lower frequencies to produce high-resolution images on continental and regional scales whereas only very few studies exist so far showing the applicability of the method for higher frequencies on the local scale (Chávez-García and Luzón 2005; Brenguier et al. 2007; Picozzi et al. 2009).

Here we introduce a new method for a one-step tomographic inversion scheme for obtaining 3D shear-wave velocity models. The method, which also works in complex environments with significant topography, is based on the micro-array recordings of seismic noise (i.e. the deployment of a number of 10–20 stations distributed over the area of interest) for a few hours. Thereon, Rayleigh wave phase velocities have to be determined for each interstation ray path, e.g. based on the frequency domain SPAC technique of Aki (1957). Therefore we make use of the possibility to substitute an average over time of the correlation in the frequency domain between two stations for a fixed interstation distance instead of the azimuthal average of the correlation required by SPAC (Weaver and Lobkis 2004). The basic idea of this hypothesis is that the average of the cross-correlation between two stations for a long enough time window averages all the different directions of the waves composing the microtremors, i.e., a single station pair can be seen as being equivalent for an azimuthal average of many station pairs with the same interstation distance. In this context, Curtis and Halliday (2010) clearly highlight the importance of a suitable distribution of noise sources in all directions around the station pair of interest.

In order to confirm this, for a one line profile we have used seismic noise records excited by a non-synchronized source, such as a person jumping, near the first receiver of the profile. With the cross-correlation of these records (using the first receiver as reference) we obtain seismic sections that are comparable to those from standard active source data, showing the reliability of high frequency seismic noise interferometry.

With these seismic sections we calculate frequency (ω)—slowness (p) transforms following Forbriger (2003). In Fig. 3.3 we show the (ω , p)-spectrum obtained for the seismic section obtained from the cross-correlations of the non-synchronized noise and for the active source seismic section. The most prominent signals in these figures correspond to the fundamental mode of Rayleigh waves. Additionally, both spectra show high slowness values (around 5 s km^{-1}) for low frequencies (10 Hz) which might be due to a shallow water table that can cause a different depth for the shallow velocity changes for P and S-waves. For the two kinds of sources the emergence of

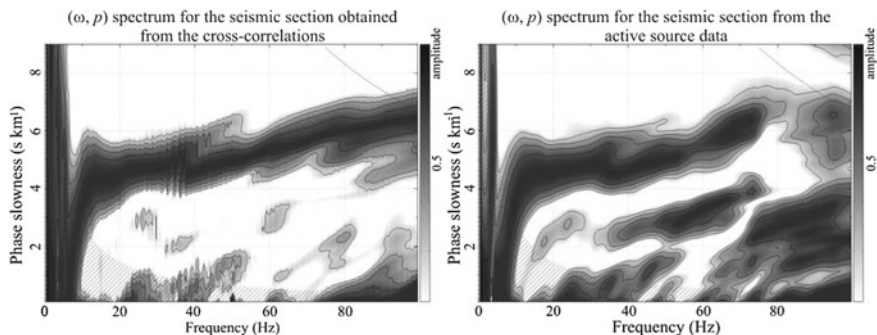


Fig. 3.3 (ω, p) spectra for a line profile (34, 5 m long) for two sets of data. *Left* for the seismic section obtained from the cross-correlations of the non-synchronized noise. *Right* for the seismic section of the active source data. Both sources were located next to the first receiver. The *grey scale* indicates the modulus of the complex wave field obtained by the transform

potential osculation points that indicate the presence of different modes with similar slowness is visible at around 30 Hz.

The main difference between these spectra is the emergence of the first higher mode of surface waves in the transformation of the active source data (35–75 Hz and 2.5–3.7 s km^{-1}), which is not visible in the spectrum of the interferometric signal. This might be due to the fact that with the cross-correlation of records with multiple modes spurious events are generated losing information about higher modes (Halliday and Curtis 2008).

From these results we can confirm that even if the majority of sources are clustered in a narrow azimuthal range (a person jumping near the first receiver of a line profile) the travel time information is stable, providing enough energy coming from the remaining azimuthal sectors (Derode et al. 2003).

Using seismic noise recorded by an instrumental array we can determine the travel times for all ray paths between the sensors. The first step of data processing consists of preparing the waveform data from each individual station. Since our interest lies in detecting local variations in v_s for the shallowest part of the subsurface and since the distances of the array only span a range of some meters to around one hundred meters, we are strongly interested in high frequency noise (higher than a few Hz) where Rayleigh waves are prevalent.

Therefore, a suitable high-pass filter should be applied to the data aiming to improve the signal-to-noise ratio for the high-frequency range of interest, and to oppress the influence of large-amplitude low-frequency signals that tend to obscure noise signals. After preparing the time series, one-bit normalized data were used to calculate the cross-correlations for all interstation pairs, following Campillo and Paul (2003) and Bensen et al. (2007). The calculated cross-correlations are stacked for all selected frequencies and for each pair of receivers to improve the signal-to-noise ratio (Bensen et al. 2007). Finally, the travel times between all stations are calculated from the estimated phase velocities using the known distances between sensors.

Although the ray path is velocity dependent, meaning that travel time inversion is a non-linear problem, deviations of the paths from a straight line will be sufficiently small. Therefore, a bias of a few percent can be tolerated to keep the solution linear, and the medium of interest can be subdivided into a reasonable number of smaller cells so that the problem can be expressed in a simple discrete matrix form.

Starting from a homogeneous 3D velocity model for the entire medium of interest, an iterative procedure using singular value decomposition, for minimizing the misfit between the observed and theoretical travel times, can be adopted (Picozzi et al. 2009; Pilz et al. 2012, 2013). In particular, the measured slowness along each ray path contains information about the underlying structure to depths corresponding to approximately one-third to one-half the wavelength of each frequency (Foti et al. 2009).

To account for the fact that shallow blocks are sampled more intensely than deeper ones, we introduce a further constraint on the solution which weights the data depending on the number, length, orientation, and vertical penetration depth of each ray path segment crossing each cell. When running the inversion procedure the weights for all cells, and accordingly the velocity vectors, are updated after each iteration step until a reasonable compromise between the reduction of the rms error between the observations and the predictions and the norm of the solution is reached. Finally, the updated slowness s is used to calculate the 3D shear wave velocity structure using the relation with the Rayleigh wave slowness by $v_s = (0.92s)^{-1}$.

As an example Fig. 3.4 shows the inversion results of the array recordings obtained after 500 iterations across the Issyk-Ata fault in Kyrgyzstan, a moderately dipping thrust to reverse fault defining the northern deformation front for the central Tien Shan between $\sim 74^\circ\text{E}$ and $\sim 75^\circ\text{E}$ longitude. A clear difference in S-wave velocity is observed, contrasting the northern and the southern parts of the studied area and running in an east-west direction parallel to the fault. The transition zone is rather sharp, spanning only some tens of meters. A distinct low-velocity wedge in the uppermost part of the northern section of the studied area can be identified (reddish color in Fig. 3.4) which might be caused by fault scarp weathering and present-day detritus which had slid off from the rock terrace. In this interpretation, formation of the colluvial wedge would represent multiple faulting events with a total displacement of around 10 m.

The estimated absolute v_s values are robust and compatible with the findings of previous studies for similar material in Bishkek (Parolai et al. 2010). Below the low-velocity deposits the material can be interpreted as late Pleistocene and Holocene terraces whereas Pliocene conglomerates with dense carbonate cement with gravel stones form the high velocity bluish part in the south (Korjenkov et al. 2012, Fig. 3.4). Remarkably, this novel approach has identified two parallel fault structures, one lowering the Tertiary by nearly 30 m, and the other lowering the top of the Tertiary strata to greater, but unresolved, depths to the north.

This means that, based on the correlation of seismic noise recordings and using a limited number of seismic stations and recording times of several tens of minutes, detailed images of the local subsoil structure can be obtained even under pronounced topographic conditions. In contrast to information gained from traditional

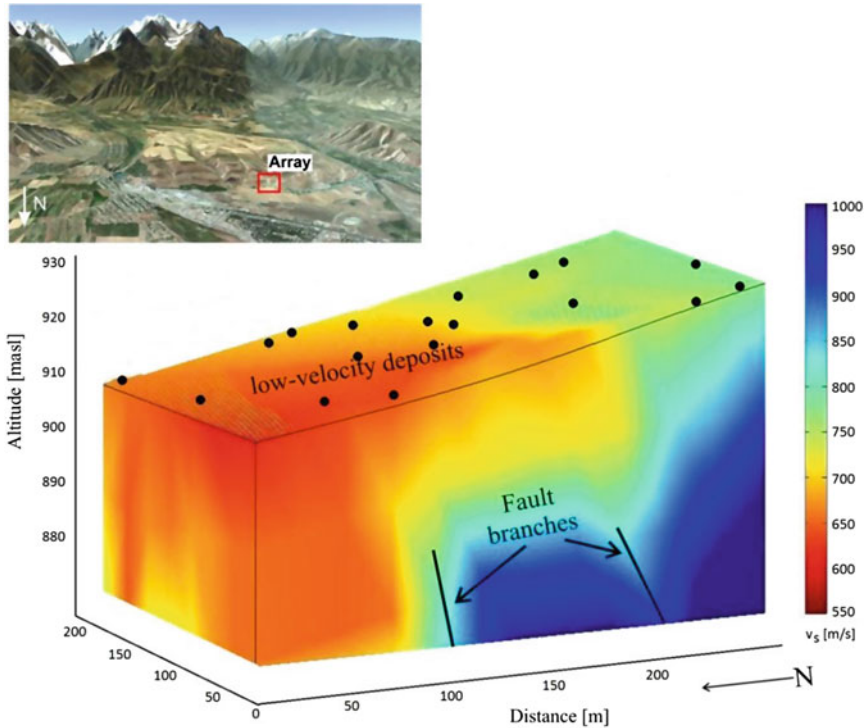


Fig. 3.4 *Top* Satellite image showing the southern outskirts of Bishkek facing the Ala-Too range. The topography is exaggerated by a factor of two. Location of the array measurement is indicated. Google Earth, © 2012, CNS Spot Image © 2012, Digital Globe © 2012. *Bottom* Inversion results of measurements on the Issyk-Ata fault obtained after 500 iterations. The topography is amplified about 3 times. The *dots* represent locations of the sensors

2D trench excavation, such seismic imaging methods can add an extra dimension and a deeper perspective. The presented technique is particularly advantageous since it can return useful information about the heterogeneous subsurface structure and structural changes therein in complex environments across seismic faults or areas prone to landslides almost in real time even if earthquakes do not occur. Such information about the S-wave velocity distribution is difficult to acquire with traditional methods, simply analyzing the ambient noise field by the means described here can serve as a reliable and economical alternative.

3.4 The Monitoring of Seismic Velocity Variations with Ambient Seismic Noise

As shown in the previous section, the concepts of seismic interferometry allow to obtain information about subsurface structure from records of ambient seismic noise. Furthermore, the permanent presence of this signal also allows to investigate dynamic

processes that alter the elastic properties of the subsurface. The above described methodology can be used to monitor temporal variations in the medium with high spatial resolution by repeated imaging if the wave speed variations caused by changes in the mechanical characteristics of the subsurface material exceed a few percent (the uncertainty of the velocity estimates). While this, together with the necessary length of acquired seismic noise signal, is particularly suitable for engineering applications, other approaches can be considered when the velocity changes in geological materials that are caused by natural processes like deformation in volcanoes or co-seismic stress changes in fault zones are of smaller amplitude.

When high temporal resolution at large spatial scale is required or when subtle temporal variations of the order of a fraction of a percent are to be investigated Coda Wave Interferometry, CWI (Poupinet et al. 1984; Snieder et al. 2002; Sens-Schönfelder and Wegler 2006) is a more appropriated approach. However, the higher and excellent accuracy of velocity change estimates below 0.1 % is obtained by using multiply scattered coda waves with unknown propagation paths. This uncertainty causes a degradation of spatial resolution.

Two important properties of this method are of relevance: firstly, coda waves reconstructed from seismic noise are not as sensitive as direct waves to changes of the noise properties e.g. its dominant direction. Secondly the long propagation time of coda waves allows for amplification of small velocity changes to significant time shifts which increases the accuracy but lowers the spatial resolution.

The concept of applying coda wave interferometry to noise correlation functions is discussed in Sens-Schönfelder and Wegler (2011). Here we discuss applications to seismic monitoring at the CO₂ storage test site in Ketzin (Germany) and present an approach to image changes of seismic velocities at Piton de la Fournaise Volcano on La Reunion Island (France).

3.4.1 Monitoring Subsurface Changes at the CO₂ Storage Test Site in Ketzin

Regarding the potential risk of unwanted migration of carbon dioxide and the expense of active seismic investigations, we test the feasibility of monitoring a CO₂-storage-testsite in Ketzin (Brandenburg, Germany) with CWI.

Since June 2008, supercritical CO₂ is injected in an anticlinal saline aquifer of about 80m thickness, the Stuttgart Formation, at a depth of approximately 650m (Fig. 3.5a). With a nearly constant injection rate, more than 60.000 tons of CO₂ have been injected from 2008 until the beginning of 2012, which is a relatively small amount, compared to other offshore injection sites.

3D time-lapse monitoring between 2005 and 2011 (Ivanova et al. 2012) indicates an asymmetric CO₂ plume, with an extension of 250m in N-S direction and about 350m in the E-W direction, with larger quantities of CO₂ in the western part.

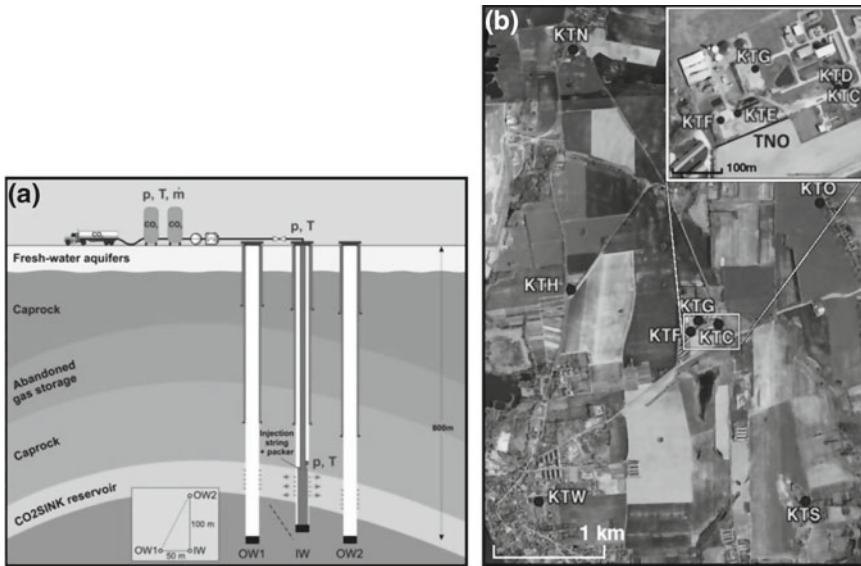


Fig. 3.5 **a** Scheme of CO₂ injection in a saline aquifer at 650m depth (<http://www.co2sink.org/techinfo/injection.htm>). **b** Station-map of Ketzin with close-up of the injection site

We operated a seismic network around the test-site from May 2008 (before the start of the injection) until June 2010, consisting of three-component Guralp seismometers with a sampling rate of 100 Hz. During February 2011 the network was re-equipped, extended and operated until February 2012. The number of receivers in the network was increased from 5 (in 2008) up to 10 receivers (in 2011) in distances from tens of meters up to a few kilometers around the injection site (Fig. 3.5b).

To retrieve estimates of the Green's functions between the seismic stations, pairwise cross-correlation of one hour long segments was applied after rotation of the horizontal components into R- (parallel to inter station azimuth) and to T- coordinates (perpendicular to inter station azimuth), followed by the usual preprocessing (trend removal, down sampling, 1 bit normalization). The cross-correlations are asymmetric and dominated by a phase traveling with about 300 m/s, which is consistent with Rayleigh waves propagating in the shallow sediments (Fig. 3.6a).

We analyzed the correlation functions for possible velocity changes using the stretching method of Sens-Schönfelder and Wegler (2006). Due to the fact that the long term average injection rate is almost constant, we expect a monotonic decrease of seismic velocities. We observe velocity variations with all station and component combinations that show a cyclic behavior of approximately one year period, which cannot be caused by the CO₂ injection (Fig. 3.7a).

In order to characterize the depth distribution of the velocity changes, we analyzed moving time windows after the direct arrival with a velocity of 300 m/s. The analysis in the frequency range of 1.5–3 Hz showed that the amplitude of the annual velocity

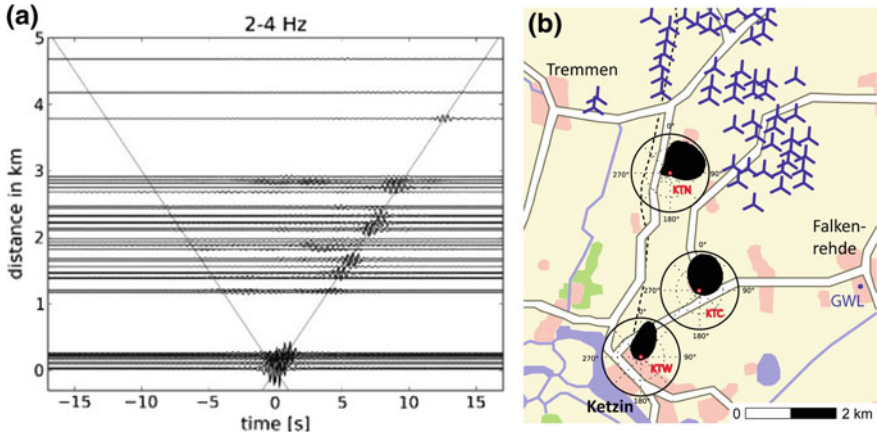


Fig. 3.6 **a** Time distance section of cross-correlations at 2–4 Hz, a velocity of 300 m/s is indicated with lines. **b** Map of the Ketzin area with histograms of measured noise directions pointing towards a wind park (at 2–2, 4 Hz, <http://www.havelland-flaeming.de>)

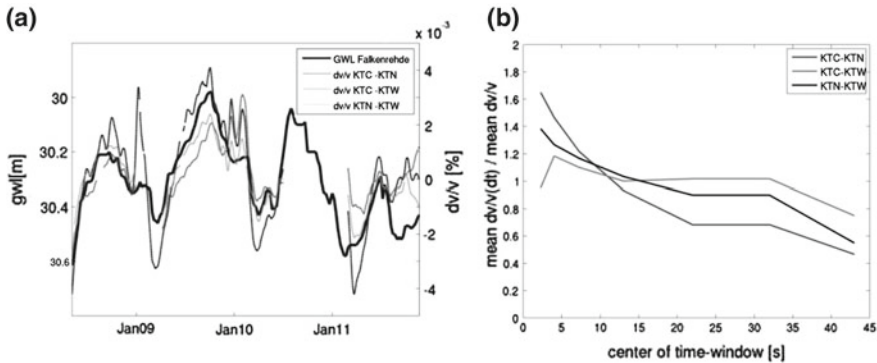


Fig. 3.7 **a** Ground water level and mean velocity change averaged over all time-windows and components for three station combinations at 1, 5–3 Hz. **b** Lapse time dependence of the velocity changes as the ratio of velocity change at a particular time-window to mean velocity change

variations decreases in time windows in later parts of the coda (Fig. 3.7b). As shown by Obermann et al. (2013) such a GWL observation can be explained with velocity changes that occur in the shallow subsurface. As the changes are periodic and shallow, we suspect a meteorological influence. A comparison of the velocity changes to ground water level (GWL) measurements in a well in Falkenrehde, which is approximately 3, 5 km north-west of the injection site, shows a clear correlation between the phases of the velocity changes and the GWL (Fig. 3.7a).

To exclude the possibility that variations of the noise source locations, that might also show an annual periodicity, cause the apparent velocity variations, we analyzed the prominent direction of the noise. Under the assumption of a dominance of Rayleigh waves on the vertical component, which was confirmed in several tests,

we calculated the backazimuth of the dominant propagation direction by maximizing the coherence between the Hilbert transform of the vertical component and the horizontal component rotated to point in the noise direction. The analysis showed a good stability of the noise direction, and therefore excludes the noise-field itself as a cause for the velocity variations.

The observed directions of the noise measured at KTC, KTN and KTW point in the direction of a wind park, whereby the distribution for KTW, which is furthest away, is more narrow as the distribution for KTC and KTN, which are closer to the wind park and thus show a broader distribution of azimuths of incident wave field (Fig. 3.6b). This distribution is stable throughout the analyzed period.

We can thus confirm that the observed periodic velocity variations are not related to modifications in the noise sources distribution but caused by changes in the GWL. These periodic variations mask potential signals of material changes at the reservoir depths.

3.4.2 *Velocity Monitoring at Piton de la Fournaise Volcano*

Piton de la Fournaise Volcano on La Reunion Island (France) in the Indian Ocean was one of the first places where the concept of monitoring temporal variations of the seismic velocity with noise correlation functions was applied. It is one of the most active volcanoes on Earth with usually more than one basaltic eruption per year.

During the period from mid-1999 until end of 2000 Brenguier et al. (2008) observed long term variations of the seismic velocities with unknown origin that are interrupted by short term drops before eruptions. Based on this temporal coincidence Brenguier et al. (2008) suggested to use the velocity variations as an indicator for upcoming eruptions. Here we use a densified network to investigate the relation between the spatial distribution of velocity changes and different processes affecting the volcano.

In 2009 the seismometer network at Piton de la Fournaise was densified by the UnderVolc research program (Brenguier et al. 2012). The seismic network is indicated in Fig. 3.9 by green dots together with the GPS network operated by the Observatoire volcanologique du Piton de la Fournaise that we use as one indicator of the volcanic activity.

We calculate noise correlation functions as described above and estimate velocity changes from their coda for all available station pairs. This results in 210 curves of velocity changes that represent the dynamics of the volcano. The variations of the velocity are not homogeneously distributed in space as measurements show a clear systematic depending on the participating stations. To infer the spatial distribution of velocity changes we have to make an assumption about the spatial sensitivity of the measurements. We therefore assume that coda waves propagate in the multiple scattering regime which concentrates the sensitivity around the stations. Under this assumption we invert the velocity changes measured at station pairs for changes at the location of individual stations. Figure 3.8 shows these station-wise velocity changes

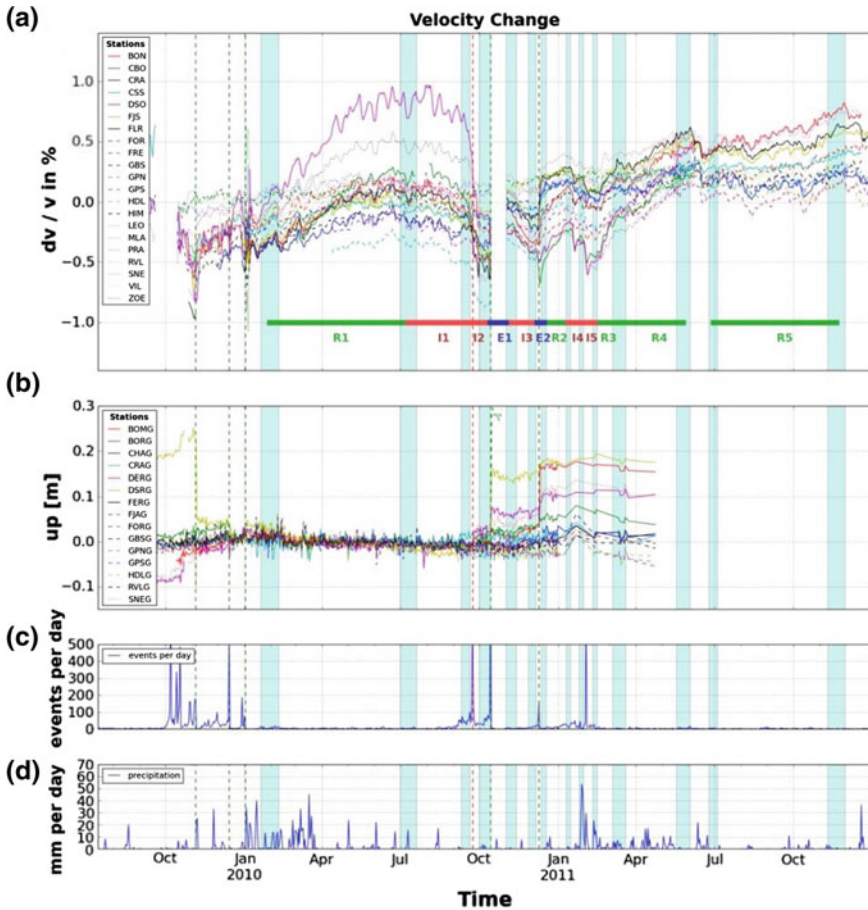


Fig. 3.8 **a** Velocity changes at the seismic stations. **b** Upward component of the surface deformation. **c** Daily number of seismic events in the summit area. **d** Precipitation. Vertical green lines indicate eruptions; red line indicates a documented intrusion. Vertical bars indicate the periods of stable velocities used for averaging. Horizontal lines show the intervals where velocity changes are mapped

together with the upward component of surface deformation, summit seismicity, and precipitation rate (Huffman et al. 2001).

Common dynamics in the data shown in Fig. 3.8 is easily identified by means of the seismicity. Seismic crises exceeding more than 100 events per day are always reflected by abrupt deformation and velocity changes. During seismically quiet periods deformations show slow subsidence accompanied by a mostly steady velocity increase with an exception in the third quarter of 2010. A relation with precipitation cannot be established.

To map the spatial variability of the velocity changes we assume spatial continuity and interpolate linearly between estimates at the station locations. Here we focus on

two time intervals, I2 and R1 (Fig. 3.8) for which the distributions of velocity changes are shown in Fig. 3.9a and b, respectively.

Figure 3.9 shows maps of the velocity changes for two periods with clearly different types of processes. The first example (Fig. 3.9a) shows the time interval that includes the dyke intrusion on September 23, 2010 (I2 in Fig. 3.8). The intrusion was accompanied by a seismic crisis and caused surface deformation detected by the GPS network. It was also observed as a characteristic low frequency tilt signal at a neighboring seismic broad band station (Roult et al. 2012). Seismic velocities decreased during the intrusion by up to 0.4%. While the outer part of the volcano remains at almost constant velocity the decrease concentrates around the summit area. Surface deformation during this time interval shows expansion and uplift around the summit.

The second example (Fig. 3.9b) shows the velocity changes that occurred between February and July, 2010 (R1 in Fig. 3.8). This is a period of quiescence that followed on intensive activity to the end of 2009 in which three eruptions occurred in two months. During this period there was no seismic activity at the summit and surface deformation indicates a steady but subtle deflation. Similarly, the seismic velocities show a constant steady increase. Geographically this increase is again focused around the summit area. Changes associated with eruptions are spatially heterogeneous but involve large scale velocity increase in the northern part of the volcano.

The two examples shown above are characteristic for the type of the dominant process. In our data set there are different episodes that are most likely associated with magmatic intrusions. These are the periods I3 preceding an eruption in December 2010 and the periods I4 and I5 that coincide with a seismic crisis in February 2011 (Fig. 3.8). All of them show a velocity decrease with a similar spatial distribution but variable amplitude to period I2 depicted in Fig. 3.9a. Also the remaining periods of quiescence indicated as R2-4 in Fig. 3.8 show the same pattern as period R1—a velocity increase concentrated around the summit.

Based on these characteristic changes of velocities our observations help to assess the state of activity of the volcano. The change in the velocity trend in July 2010 can for example be interpreted as a preparatory signal of the dyke intrusion in September. This occurred prior to any clear signal in the deformation time series. Also the interval between the eruptions in October and December can clearly be identified as affected by inflation rather than quiescence on the basis of the velocity changes indicating an increasing probability for an eruption that eventually occurred in December.

3.5 Summary

In the previous sections we described the two approaches followed in the MIIC-project to obtain a dynamic tomographic record of the subsurface that not only images the seismic velocity structure but also monitors its changes.

In Sect. 3.3 we described our newly developed technique to investigate the velocity distribution on an engineering scale from ambient seismic noise records using frequencies higher than a few Hz. The algorithm is very efficient as it performs a

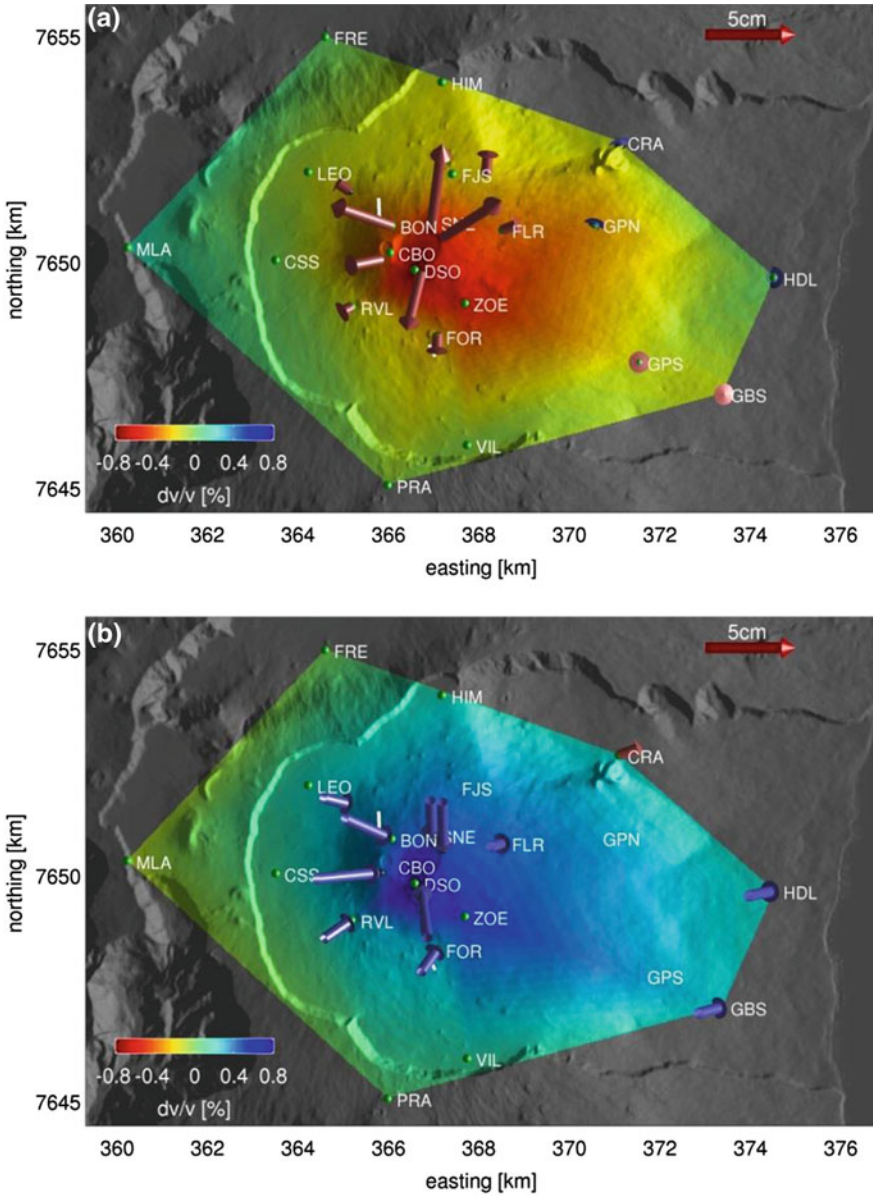


Fig. 3.9 Distribution of velocity changes for two time intervals. *Green dots* represent seismic stations. *Arrows* denote surface deformation. *Red (blue) arrows* indicate uplift (subsidence) and point away (towards) the station. **a** Changes associated with the dyke intrusion in September 2010 (I2 in Fig. 3.8). **b** Gradual changes during a quiet period in 2010 (R1 in Fig. 3.8)

3D inversion directly on dispersion curves without a detour via velocity maps. We obtained high quality 3D images of subsurface structures along an active fault and on a landslide in central Asia. These applications demonstrate the possibility to use interferometric concepts for imaging on a spatial scale of several hundred meters.

As the required recording durations in this frequency range are of the order of several hours we are able to monitor velocity changes on a time scale below one day with high spatial resolution just by repeated tomographic inversions. This reaches the target of a dynamic tomography from the imaging side.

The complementary approach starting from noise based monitoring of scattered wave fields is described in Sect. 3.4. The application to the CO₂ storage test site illustrates the high precision that can be achieved by interferometry and allows to detect relative variations of seismic velocities of about 0.1 %. At Piton de la Fournaise volcano we show how information about the spatial distribution of the velocity changes can be obtained also from scattered wave fields. The resulting maps illustrate how the volcanic processes influence the seismic velocities. This way we obtain information about the dynamics of the volcano that is complementary to more conventional measurements such as seismicity and surface deformation. It demonstrates the success of augmenting the noise based monitoring with spatial resolution to obtain a dynamic tomography.

Acknowledgments The project MIIC is part of the R&D-Programme GEOTECHNOLOGIEN. It is funded by the German Ministry of Education and Research (BMBF), Grants/ Förderkennzeichen of sub-projects 03G0736A, 03G0736B, 03G0736C, 03G0736D, 03G0757A.

Data from Piton de la Fournaise was kindly provided by the UnderVolc project and the Observatoire volcanologique du Piton de la Fournaise.

References

- Aki K (1957) Space and time spectra of stationary stochastic waves, with a special reference to microtremors. *Bull Earthq Res Inst Tokyo Univ* 24:415–457
- Bensen GD, Ritzwoller MH, Barmin MP, Levshin AL, Lin F, Moschetti MP, Shapiro NM, Yang Y (2007) Processing seismic ambient noise data to obtain reliable broad-band surface wave dispersion measurements. *Geophys J Int* 169:1239–1260
- Bonnefoy-Claudet S, Cotton F, Bard PY (2006) The nature of noise wavefield and its applications for site effects studies: a literature review. *Earth-Sci Rev* 79:205–227
- Brenguier F, Shapiro NM, Campillo M, Nercessian A, Ferrazzini V (2007) 3D surface wave tomography of the Piton de la Fournaise volcano using seismic noise correlations. *Geophys Res Lett* 34:L02305. doi:10.1029/2006GL028586
- Brenguier F, Shapiro NM, Campillo M, Ferrazzini V, Duputel Z, Coutant O, Nercessian A (2008) Towards forecasting volcanic eruptions using seismic noise. *Nat Geosci* 1:126–130
- Brenguier F, Kowalski P, Staudacher T, Ferrazzini V, Lauret F, Boissier P, Di Muro A (2012) First results from the underVolc high resolution seismic and GPS network deployed on Piton de la Fournaise volcano. *Seismol Res Lett* 83:97–102
- Campillo M, Paul A (2003) Long-range correlations in the diffuse seismic coda. *Science* 299:547–549
- Campillo M (2006) Phase and correlation in ‘random’ seismic fields and the reconstruction of the green function. *Pure Appl Geophys* 163:475–502

- Curtis A, Gerstoft P, Sato H, Snieder R, Wapenaar K (2006) Seismic interferometry—turning noise into signal. *Lead Edge* 25:1082–1092
- Curtis A, Halliday D (2010) Source-receiver wave field interferometry. *Phys Rev E* 81:1–10
- Chávez-García FJ, Luzón F (2005) On the correlation of seismic microtremors. *J Geophys Res* 110:B11313. doi:[10.1029/2005JB003671](https://doi.org/10.1029/2005JB003671)
- Derode A, Larose E, Tanter M, de Rosny J, Tourin A, Campillo M, Fink M (2003) Recovering the Green's function from field-field correlations in an open scattering medium (L). *J Acoust Soc Am* 113:2973–2976
- Fleming K, Picozzi M, Milkereit C, Kuhnlenz F, Lichtblau B, Fischer J, Zulfikar C, Özel O (2009) SAFER and EDIM working groups: the self-organizing seismic early warning information network (SOSEWIN). *Seismol Res Lett* 80(5):755–771
- Forbriger T (2003) Inversion of shallow seismic wavefields. I. Wavefield transformation. *Geophys J Int* 153:719–734
- Foti S, Comina C, Boiero D, Socco LV (2009) Non uniqueness in surface wave inversion and consequences on seismic site response analyses. *Soil Dyn Earthq Eng* 29:982–993
- Halliday D, Curtis A (2008) Seismic interferometry, surface waves and source distribution. *Geophys J Int* 175:1067–1087
- Huffman GJ, Adler RF, Morrissey M, Bolvin DT, Curtis S, Joyce R, McGavock B, Susskind J (2001) Global precipitation at one-degree daily resolution from multi-satellite observations. *J Hydrometeorol* 2:36–50
- Ivanova A, Kashubin A, Juhojuntti N, Kummerow J, Hennings J, Juhlin C, Lüth S, Ivandic M (2012) Monitoring and volumetric estimation of injected CO₂ using 4D seismic, petrophysical data, core measurements and well logging: a case study at Ketzin, Germany. *Geophys Prospect* 60(5):957–973
- Korjenkov AM, Kolchenko VA, Rott PG, Abdieva SV (2012) Strong mediaeval earthquakes in the Chuy basin, Kyrgyzstan. *Geotectonics* 46:303–314
- Lobkis OI, Weaver RL (2001) On the emergence of the Green's function in the correlations of a diffuse field. *J Acous Soc Am* 110:3011–3017
- Megies T, Beyreuther M, Barsch R, Krischer L, Wassermann J (2011) ObsPy-What can it do for data centers and observatories? *Ann Geophys* 54:47–58
- Obermann A, Planes T, Larose E, Sens-Schönfelder C, Campillo M (2013) Depth sensitivity of seismic coda waves to velocity perturbations in an elastic heterogeneous medium. *Geophys J Int* 194(1):372–382
- Parolai S, Orunbayev S, Bindi D, Strollo A, Usupayev S, Picozzi M, Di Giacomo D, Augliera P, D'Alema E, Milkereit C, Moldobekov B, Zschau J (2010) Site effect assessment in Bishkek (Kyrgyzstan) using earthquake and noise recording data. *Bull Seismol Soc Am* 100(6):3068–3082
- Picozzi M, Parolai S, Bindi D, Strollo A (2009) Characterization of shallow geology by high-frequency seismic noise tomography. *Geophys J Int* 176:164–174
- Pilz M, Parolai S, Picozzi M, Bindi D (2012) Three-dimensional shear wave velocity imaging by ambient seismic noise tomography. *Geophys J Int* 189:501–512
- Pilz M, Parolai S, Bindi D (2013) 3D passive imaging of complex seismic fault systems: evidence of surface traces of the Issyk-Ata fault (Kyrgyzstan). *Geophys J Int* 194:1955–1965. doi:[10.1093/gji/ggt214](https://doi.org/10.1093/gji/ggt214)
- Poupinet G, Ellsworth W, Frechet J (1984) Monitoring velocity variations in the crust using earthquake doublets: an application to the calaveras fault, California. *J Geophys Res* 89(4):5719–5731
- Rickett J, Claerbout J (1999) Acoustic daylight imaging via spectral factorization: Helioseismology and reservoir monitoring. *Lead Edge* 18:957–960
- Roult G, Peltier A, Taisne B, Staudacher T, Ferrazzini V, Di Muro A (2012) A new comprehensive classification of the Piton de la Fournaise activity spanning the 1985–2010 period. Search and analysis of short-term precursors from a broad-band seismological station. *J Volcanol Geoth Res* 241–242:78–104
- Sens-Schönfelder C, Wegler U (2006) Passive image interferometry and seasonal variations of seismic velocities at Merapi Volcano, Indonesia. *Geophys Res Lett* 33(21):1–5

- Sens-Schönfelder C, Wegler U (2011) Passive image interferometry for monitoring crustal changes with ambient seismic noise. *C R Geosci* 343:639–651
- Snieder R, Grêt A, Douma H, Scales J (2002) Coda wave interferometry for estimating nonlinear behavior in seismic velocity. *Science* 295(5563):2253–5
- Snieder R (2004) Extracting the Green's function from the correlation of coda waves: a derivation based on stationary phase. *Phys Rev E* 69:046610-1–046610-8
- Weaver RL, Lobkis OI (2001) Ultrasonics without a source: thermal fluctuation correlations at MHz frequencies. *Phys Rev Lett* 87:134301-1–134301-4
- Weaver RL, Lobkis OI (2004) Diffuse fields in open systems and the emergence of the greens function. *J Acoust Soc Am* 116:2731–2734

Chapter 4

The MINE Project: Monitoring Induced Seismicity in a German Coal Mine

Simone Cesca, Francesco Grigoli, Ali Tolga Şen, Samira Maghsoudi, Torsten Dahm and Thomas Meier

Abstract During the last three years, the MINE project has developed and successfully applied seismological tools, addressing different aspects of the monitoring of mining environments, as dynamic local-scale systems. The human interaction with the shallow underground mining environment, can lead to rock mass weakening or locally induce stress perturbations. As a consequence, triggered or induced seismicity is often observed at mines, potentially posing a risk to miners and infrastructures. This work illustrates a number of recently developed seismological techniques, based on the analysis of full waveforms, which target the problem of detection, location, and characterization of mining-induced seismicity. The proposed methodologies are here discussed through their application to a 14-months coal mining dataset, affecting the region of Hamm, Ruhr, Germany. An automated full-waveform detection and location technique is first used to generate a seismic catalog. A full moment tensor amplitude spectra technique is then adapted for the analysis of induced seismicity, leading to the inversion of more than 1000 focal mechanisms. Finally, a new developed clustering algorithm is used to automatically classify source types, and to track their temporal evolution. The combined application of the methods developed within the MINE project could successfully characterise the mining-induced seismicity and its spatio-temporal variation. Our methods are suitable for automated analysis, and can be easily adopted for mining monitoring purposes in other locations, and with different network geometries.

S. Cesca (✉) · F. Grigoli · A. T. Şen · S. Maghsoudi · T. Dahm
Institute of Earth and Environmental Sciences, University of Potsdam, Potsdam, Germany
e-mail: cesca@gfz-potsdam.de

S. Cesca · T. Dahm
GFZ German Research Centre for Geosciences, Potsdam, Germany

T. Meier
Institute of Geosciences, Christian-Albrechts-University of Kiel, Kiel, Germany

4.1 Introduction

Mining environments are dynamic systems characterized by a strong human interaction with the underground environment and a significant temporal evolution of the mining system. A variety of human activity are carried out in mines, including blasting, cutting, drilling and mass shifting. These geomechanical operations affect the mine geometry and can induce local stress perturbations. Mining activities can therefore induce or trigger significant seismicity, including induced events along weakened regions or pre-existing faults, rockfalls and collapses, which pose a risk to miners, infrastructures and can affect the population living in the mining environment surrounding.

The MINE project aimed to develop seismological tools, able to improve the monitoring and imaging of mining environments. In particular, the development of specific techniques making use of full waveforms and the analysis of continuous signals was supported in our project, to enhance and improve previously available methods and monitoring tools, which mostly only focused on triggered signals.

In this work, we demonstrate the performance of different selected methodologies developed within the MINE project with a common benchmark dataset, relative to coal mining induced seismicity occurring in the Ruhr region. This work specifically focuses on addressing the problems of seismic source location, seismic source inversion and seismic source classification in mines.

4.2 A Coal Mining Dataset from the Ruhr Region, Germany

Coal mining in the Ruhr region, North Rhine-Westphalia, Germany, has been performed for centuries since early 13th century. The coal deposit spreads between the Lippe and Ruhr river. Geologically, the region is characterized by the presence of different coal-bearing layers from the upper Carboniferous period. These strata comprise sandstone and claystone layers with distributed coal seams. This structure has an overall thickness of approximately 6,000 m. The coal seams reach the surface in a strip along the Ruhr river and dip downwards toward North. The thickness of the coal layers ranges up to few meters. It is thinner for deeper layers, it increases up to 3–4 % workable seam between the Witten and Bochum strata (approximately between 2,000 and 4,000 m depth) and then drop again in the younger, upper stratas of the Upper Carboniferous (Drozdowski 1993; Coldewey and Semrau 1994). According to Coldewey and Semrau (1994), the total thickness of the carbon layers is approximately 70 m, when only considering the first 3,000 m depth structure.

Induced seismicity in the Ruhr region has been monitored by the Ruhr University Bochum since 1983 (Bischoff et al. 2010). In this report, we focus on the investigation of induced seismicity following longwall coal mining in the Hamm Heringen region, which is located at the Eastern edge of the Ruhr region. The process of longwall consists in the repeated mining and removal of single ore slices. The mining activity

processed at depths between 700 and 1,500 m below the free surface. The size of the slices removed by the longwall mining had dimensions up to 300 m in height and 1,000 m in length. The thickness of the coal seams was about 2 m (Bischoff et al. 2010). The stope advanced with an average velocity of about 100 m/month. The mining region is considered tectonically inactive and all observed seismicity assumed to be induced or triggered by mining operations. The region close to the town of Hamm was continuously monitored by the HAMNET network, a local network running from June 2006 to July 2007. Along the time of the network deployment, longwall mining was mostly performed between August 2006 and April 2007. The network consists of 15 surface sensors: 9 short-period (Mark L- 4C-3D, 1 Hz) and 6 broadband stations (5 Gralp CMG, 60 s; 1 Trillium 40, 40 s), covering a region of about $2 \times 3.5 \text{ km}^2$. Thanks to this local network, more than 7,500 events could be detected and located during the monitoring interval (Bischoff et al. 2010). The dataset includes 7,337 local events at the mining area (51.64–51.67 Lat N, 7.72–7.76 Lon E) in Hamm Heringen (Bischoff et al. 2010). Epicenters are distributed across a region of $4 \times 3 \text{ km}^2$, and about 90% are located close to the longwall area. Hypocentral estimations (manual picking, based on P arrival time inversion) indicate source depths between 500 and 1,500 m. The average source depth is at about 1,000 m, which is approximately 100 m above the average mining level. Earthquake magnitudes range between $M_L - 1.7$ and 2.0. The epicentral and depth distribution of the events shows a clear relation with the mining process. The average hypocentral depth is 1,000 m, just above the mining level. The epicenters indicate that induced seismicity migrate according to the advance of the mining face, which proceeded from WSW toward ENE. The number of events increased during the mining activity and reduced again after the mining stopped. Finally the frequency-magnitude distribution (FMD) does not follow the Gutenberg-Richter law and shows a peculiar bimodal distribution, often observed in other mining environments.

The large number of events and the good quality of seismic waveforms provide an optimal dataset to test the potential of full waveform based methodologies developed within the framework of the MINE project.

4.3 Location of Mining Induced Seismicity

4.3.1 Full Waveform Automated Location Methodology

Microseismic monitoring operations are nowadays a common practice in many industrial applications, from oil and gas hydrofracking operations to mining stability monitoring. Such applications generally require fully automatic and noise robust methods to locate microseismic events. In order to locate the mining induced seismicity occurred in the Ruhr coal mine (Germany) we applied here the fully automated location method based on waveform coherence analysis proposed by Grigoli et al. (2013).

The method relies on the use of the Short-Term-Average/Long-term_Average (STA/LTA) traces of both the P and S characteristic functions obtained by three component seismic traces. The P and S characteristic functions correspond to the vertical and the horizontal energy traces respectively. The STA/LTA of these functions are then used as input data of the automated location procedure. Finally, in order to locate a seismic event, the space of possible locations is scanned and the STA/LTA traces of both P and S characteristic functions are stacked along travel time surfaces corresponding to the selected hypocenter. Iterating this procedure on a three-dimensional grid we retrieve a multidimensional matrix whose absolute maximum corresponds to the coordinates of the seismic event. The flow chart in Fig. 4.1 illustrates how location is performed by using this method.

4.3.2 Location of Coal Mining Induced Events in the Ruhr Region, Germany

Seismicity in the Ruhr region is mainly due to coal mining operations. Since 1983 mining induced seismicity has continuously been monitored by the Ruhr University Bochum. We consider here about 13 months of data from the temporary network, HAMNET, which was deployed from July 2006 to July 2007 to monitor and analyze seismicity induced by the mining operations close to the town of Hamm. The network consisted of 15 stations, including both short-period and 6 broadband velocity sensors, deployed at the surface, within a region of about $3 \times 2 \text{ km}^2$ (Fig. 4.2).

The sampling rate of available waveform was 200 Hz. With this setup, and using a standard STA/LTA detection algorithm, Bischoff et al. (2010) identified more than 7000 events along a time period of about 13 months in the years 2006–2007. Source location was performed by the inversion of manual picked P first onsets, based on the assumption of a homogeneous halfspace velocity model ($V_P = 3880 \text{ m/s}$). Estimated M_L magnitudes range between -2.0 and 2.0 . Here we automatically located a subset of this dataset, composed by 391 events with magnitudes above $M_L 0.5$. Figure 4.3 shows a sample ($M_L = 1$, occurred on October 4th, 2006 at 13.50.30 GMT) of the waveform recorded at few selected stations.

The automated location procedures is here applied to cut velocity waveforms. Traces start a few seconds before the event trigger and have a length of about 16 S. We located 391 seismic events by stacking the chosen characteristic functions along both P and S arrival times. In order to show the quality of our results we compared the coherence matrices obtained using different velocity models. Figure 4.4 shows a comparison between: (a) coherence matrices computed considering both P and S arrival times and an homogeneous velocity model, (b) coherence matrices computed considering both P and S arrival times with a layered velocity model. The adoption of the layered model significantly improves the quality of our results (this result is confirmed by the analysis of the full dataset): the coherence values at the hypothetical hypocenters are larger for the layered model and related uncertainties are smaller (Grigoli et al. 2013).

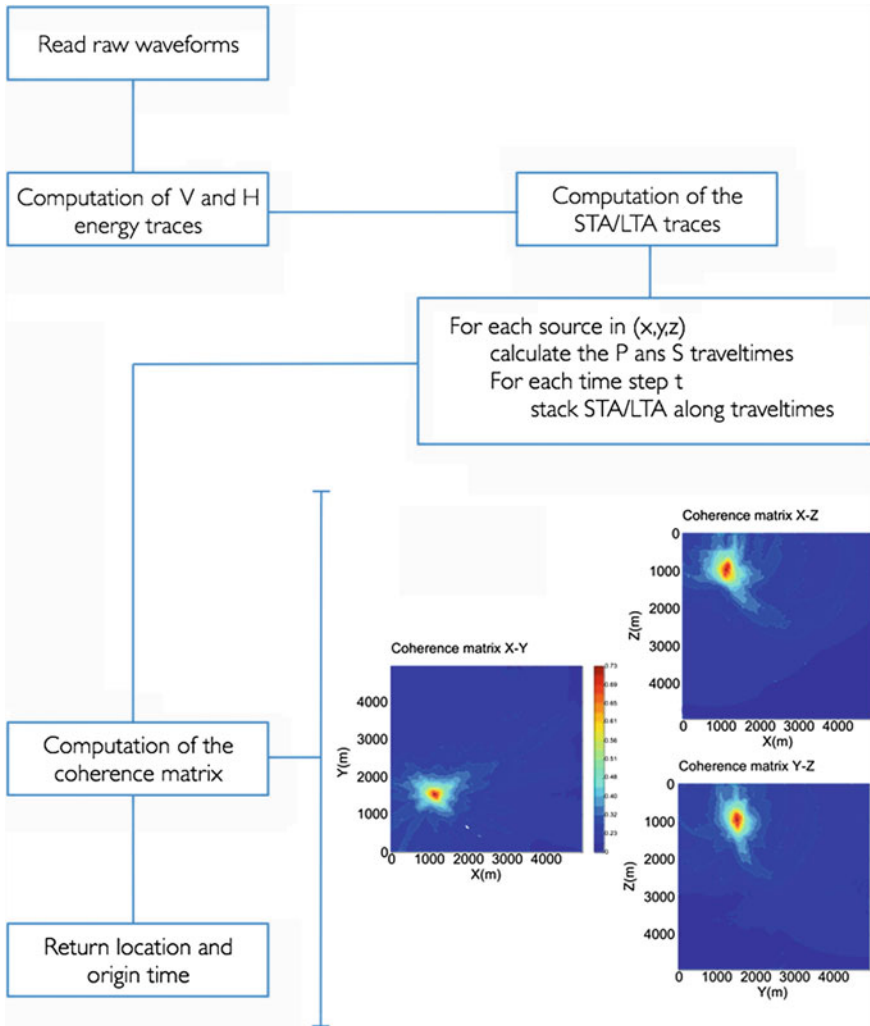


Fig. 4.1 Flow diagram of the location algorithm (after Grigoli et al. 2013). Coherence matrix XY is obtained by projecting, for each X–Y, its maximum along Z (coherence matrices XZ and YZ are obtained in a similar way)

Events locations cluster in the region of active mining with distances up to 500 m from the panel (Fig. 4.2a, b, c). Only three events are located at further distance. Results indicate a good agreement between both locations, with more than 90% of the events within 200m from the manually located sources. Automated locations obtained using the waveform stacking approach are more clustered in depth than locations retrieved manually and in better agreement with the mining level depth. For each location, uncertainties have been estimated perturbing 25 times the length

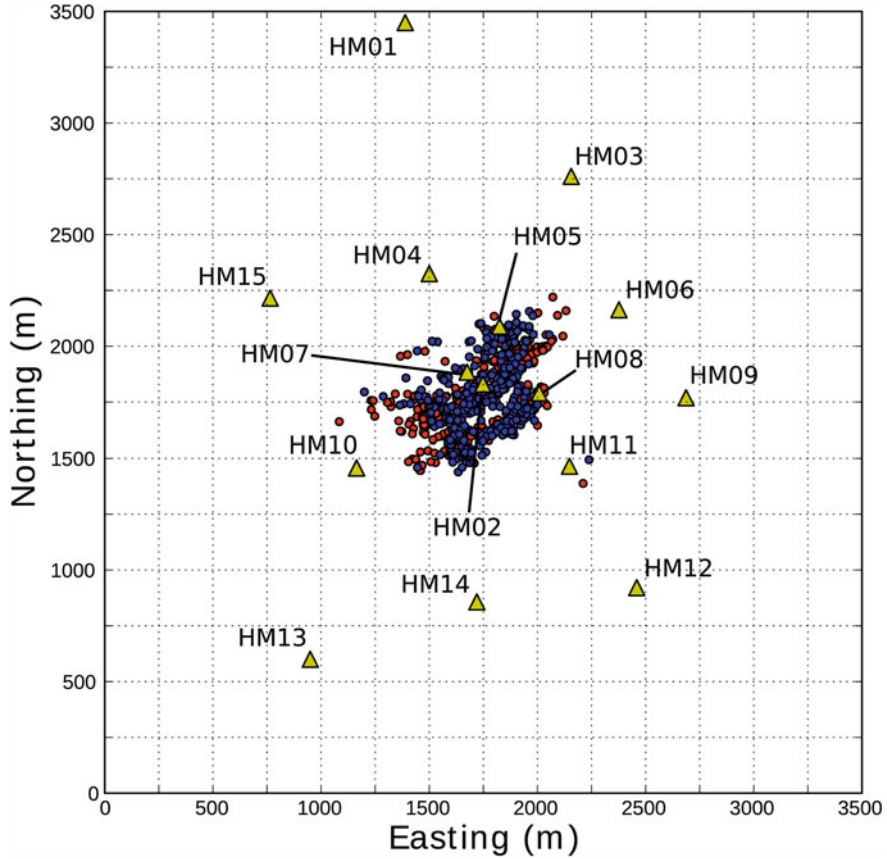


Fig. 4.2 Geometry of the network and location results for all 391 seismic events (*blue dots*) and comparison with results obtained using a manual location procedure (*red dots*). The reference point $(x, y) = (0, 0)$ corresponds to $x = 3411193$ and $y = 5723463$ in the Gauss-Krüger system (after Grigoli et al. 2013)

of the short and long time windows (the short time window has random length in the range 0.1–0.3 s, the long time window is 2 times longer), about 90 % of the events have uncertainties of about 50 m for epicentral coordinates and about 100 m for depth.

4.4 Source Inversion

If the location procedure timely provides important information on the spatial distribution of the induced seismicity, source inversion techniques can be used to infer information on the energy release, the type of rupture processes, the orientation of active faults or on the presence of tensile failure and isotropic sources, which are

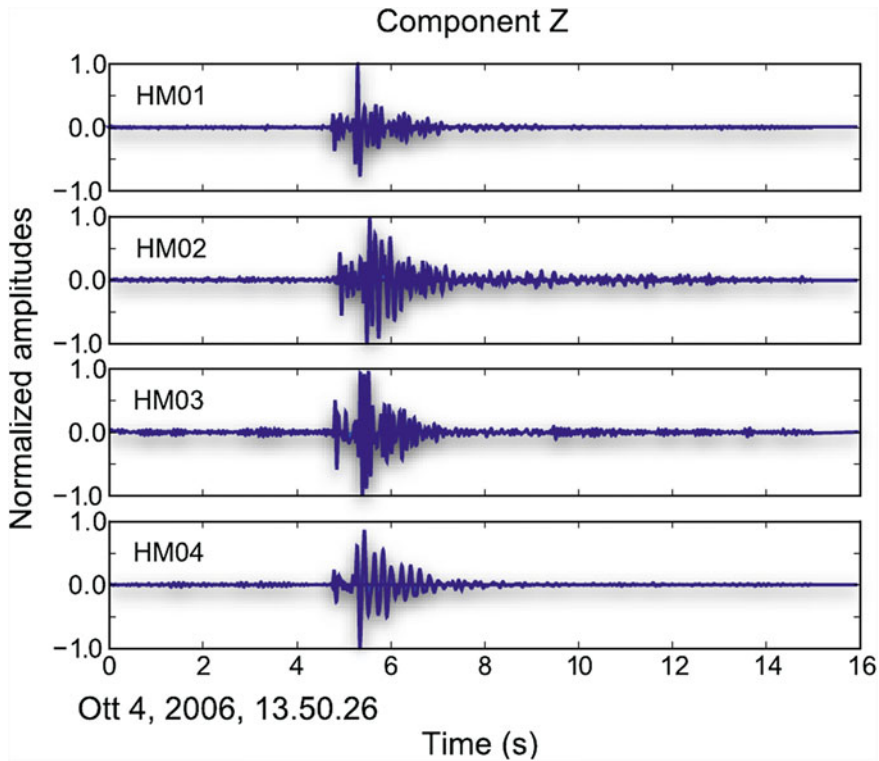


Fig. 4.3 Vertical component velocity traces of a microseismic event occurred on October 4th, 2006 at 13.50.30 GMT, recorded by four station of the network (after Grigoli et al. 2013)

important to better understand the ongoing fracturing processes and to assess the stability of the mining environments. The MINE project has adapted seismological source inversion techniques formerly developed for regional and teleseismic applications, in order to study weak induced seismicity at a small scale.

4.4.1 Methodology

The implementation of an automated source inversion algorithm for a mining environment was realized through the adoption of the Kiwi tools (Heimann 2011) and their extension to small-scale and full moment tensors. This software was successfully applied to study seismic sources of moderate and large earthquakes at local and regional distances (Cesca et al. 2010; Buforn et al. 2011; Cesca et al. 2013a; Custodio et al. 2012), and tested for automated routines (Domingues et al. 2012). However, it was never routinely applied before to small events in near-field distances with magnitude below M_w 3.5. The Kiwi tools now allow synthetic seismograms generation

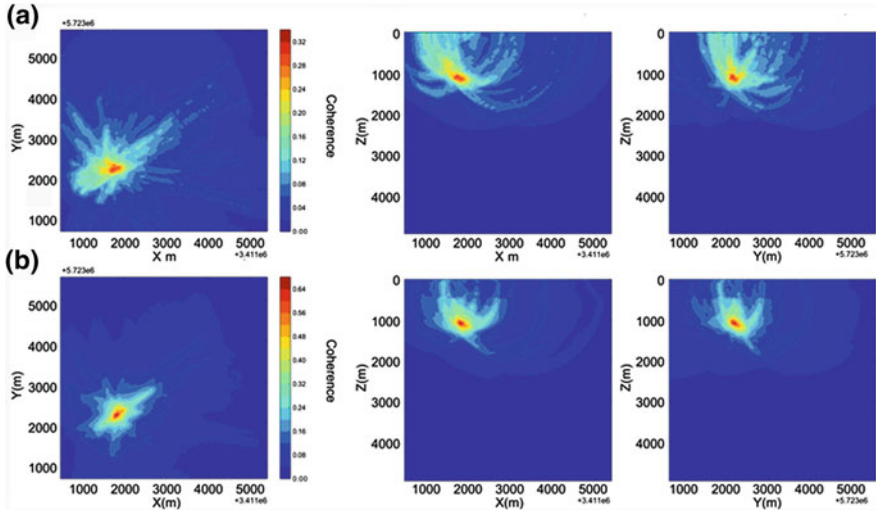


Fig. 4.4 Coherence matrices obtained by stacking the STA/LTA traces using: **a** P and S arrival times for an homogeneous velocity model and **b** P and S arrival times for a layered velocity model. Coherence matrix XY is obtained by projecting, for each X-Y, its maximum along Z (coherence matrices XZ and YZ are obtained in a similar way). Coherence values are represented in color scale. Coordinates are in the Gauss-Krieger system (after Grigoli et al. 2013)

and source inversions, both for DC, full MT and different kinematic models, and require pre-calculated Greens functions (GFs), which are stored in structured databases. GFs have been generated for two different layered model using a reflectivity method.

The inversion is performed in different steps, which output is shown in Fig. 4.5. The initial point source inversion relies on the information available through the seismic catalogue compiled by the Ruhr University Bochum, including the hypocentral location and a first, rough magnitude estimation. This information is used to set up a dense range of starting configurations for the point source parameters (strike, dip, rake, moment, depth). The first inversion step adopts a double couple (DC) point source model and perform the inversion in the frequency domain, fitting amplitude spectra of unrotated full waveforms. Since the inversion is non linear, the inversion is iteratively repeated for all starting configurations. A Levenberg-Marquardt approach is used to minimize the ℓ^2 norm misfit from each starting model. As a result, four possible configurations of the fault plane angles (strike, dip, rake; 4 configurations due to intrinsic fault-auxiliary plane and focal mechanism polarity ambiguities), the centroid depth, the scalar moment and the magnitude are resolved. The fit of amplitude spectra is preferred for the inversion, because it does not require a precise trace alignment and it is less dependent on the accuracy of the velocity model. Data and synthetics are tapered in the time domain and a bandpass filter is applied in the frequency domain. The best DC model, as well as other possible non-DC models is chosen as starting models for the following amplitude spectra inversion step, where

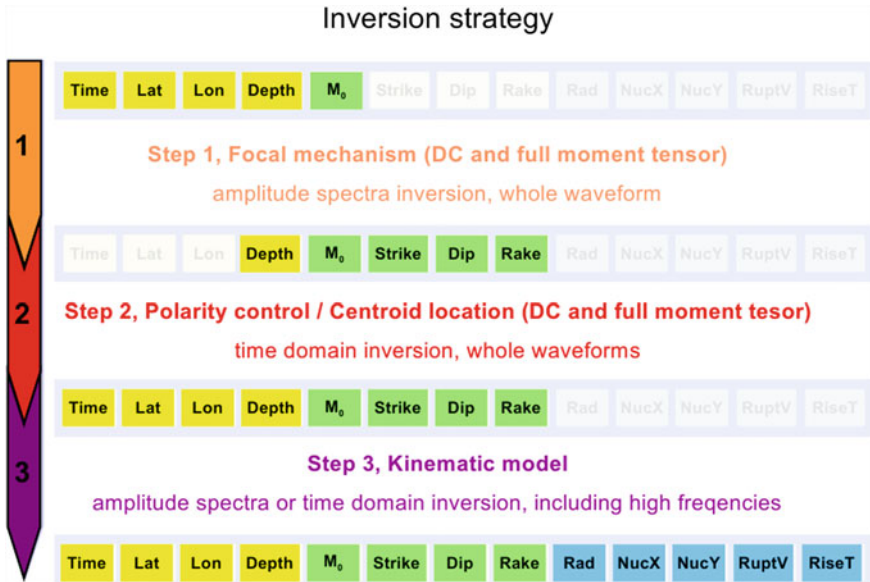


Fig. 4.5 The sketch illustrates the output of the different steps of the inversion process: DC focal mechanism and fit of amplitude spectra are obtained after inversion step 1a, full MT focal mechanism and fit of amplitude spectra after inversion step 1b, DC and full MT focal mechanism with correct polarities are obtained by fitting displacement waveforms in the time domain (results include the decomposition of the full MT into DC, CLVD and isotropic components), and finally, finite rupture model (including information on plane orientation, size, and directivity patterns) are derived by the fit of high-frequency amplitude spectra after inversion step 3

a full moment tensor point source model is assumed. The waveforms processing steps and inversion approach remain unchanged, so that the new misfit estimation can be directly compared with the DC one. The full moment tensor is decomposed into double couple (DC), compensated linear vector dipole (CLVD) and isotropic (ISO) components. Then, the focal mechanism polarity is determined, by comparing synthetic displacement traces for both polarities with the observed waveforms. A grid search for possible centroid locations and centroid times, around the starting values is also performed. At the end of this stage, all point source parameters are derived. As a last step, a kinematic source inversion may be carried out. This is challenging for weak earthquakes in a mine, as the inversion requires the modeling of high-frequency radiation (e.g. up to 10Hz or more), with a simplified velocity model. Therefore results are only briefly discussed here. For the finite source inversion we adopt the centroid location, focal mechanism and scalar moment according to the point source inversion results, and test a limited range of possible extended source models: circular vs. line models, different fault plane orientations, rupture sizes (between 10 and 350 m radius), and rupture propagation modes (including unilateral and bilateral ruptures). The inversion is performed again by fitting amplitude spectra and repeated for 2 frequency ranges, from 1 Hz up to 10 and 20 Hz respectively.

4.4.2 Source Parameters of Coal Mining Induced Events

The automated application of the method to all 3371 events, all those with magnitude above $M_L - 0.5$, is interpreted only for a subset of the best 1169 solutions. The selection of best solutions was done on the base of low misfit values and sufficient number of available data. DC and full MT results are summarized in Fig. 4.6 and 4.7, adapted after Sen et al. (2013). Results show that most events repeatedly show similar focal mechanisms, characterized by normal faulting (90% of the events between -110° and -70°) and with a steeper fault plane (in most cases dipping between 50° and 65°) and a sub-horizontal one. Focal mechanisms can be further classified upon their strike angle. The distribution of strike angles highlights different families of events, with strike angles of about 70° , 160° , 250° and 310° . This finding can be easier discussed in Fig. 4.6, where the number of events is plotted along strike-dip, strike-rake and dip-rake diagrams, and where families of events with similar focal mechanisms can be better identified. The strike angles of the clusters are fitting with the orientation of the mining walls and stope, which are here indicated by dashed lines. The bottom side of Fig. 4.6 illustrates the temporal evolution of the spatial (Fig. 4.6b) and magnitude (Fig. 4.6c) distributions within each cluster. Specific patterns characterize different clusters, in terms of the temporal, spatial and magnitude distributions of seismic events. Clusters 1 and 4 are more localized in space and time and mostly occur at the beginning and end of the study period, and at the SW and NE edge of the panel, respectively. Events of cluster 2 take place during the whole time frame and epicenters are spread in a larger region. The magnitude distributions (Fig. 4.3c) tell that largest events ($M_W > 1$) have mechanisms associated to clusters 3 and 4.

Full moment tensor inversions were performed for the same dataset (1169 events); results are illustrated in Fig. 4.7. To discuss full MT results we perform its decomposition and plot DC, CLVD and ISO components on a source-type diagram (Hudson et al. 1989). For most events the DC component dominates the deviatoric term (DC is larger than CLVD). The distribution of CLVDs resemble the patterns observed also for natural events. For example, see Cesca et al. 2013a, who discussed the distribution of spurious CLVD terms resulting from the limitation of the modeling approach (e.g. because of noisy data or poor knowledge of the velocity model). This would at first suggest CLVD components are spurious terms, only retrieved because of an approximated description of the velocity model, or an unfavorable network geometry. However, the distributions of DC and ISO components provide a different image: most of the events show relevant isotropic components, which can account for up to 50% of the energy release. Note that for tectonic earthquakes, the isotropic component is often significantly larger than values obtained in synthetic tests. The center of the source-type plot is underpopulated, indicating few pure DC events, whereas most events are characterized by a combination of shear and tensile cracks. In most cases (more than 60%) we observe opening cracks (combination of positive ISO and positive CLVD) rather than closing ones (negative ISO, negative CLVD, about 30%). This clear predominance seems quite reliable, despite the polarity resolution

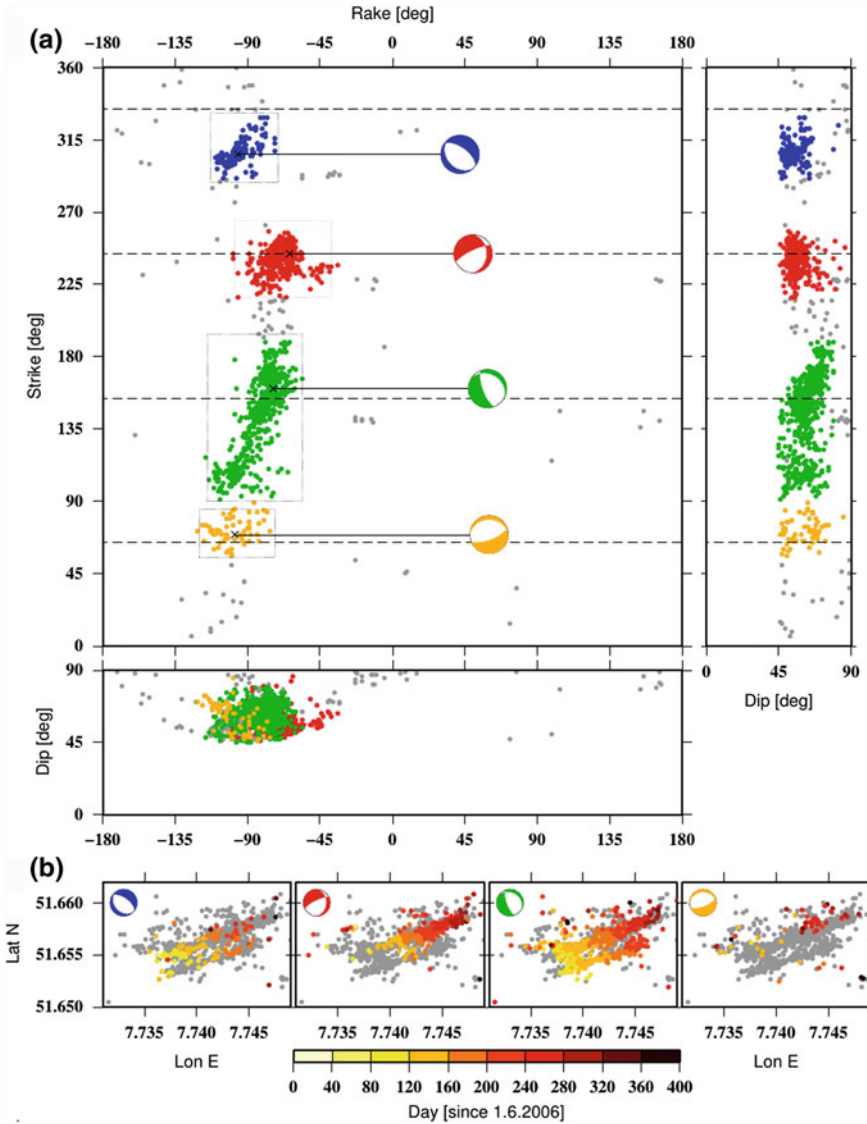


Fig. 4.6 Spatial, temporal and magnitude distribution of different focal mechanism families (after Sen et al. 2013). **a** The number of events along strike-rake, dip-rake and strike-dip plots highlights four clusters (*dotted squares*) of events with similar DC focal mechanisms (*colored focal spheres*). Clusters show similar normal faulting, but different strike orientations, which are consistent with the orientation of mining walls (*dashed lines*). **b** Spatiotemporal distribution of the four clusters

problem highlighted by the jack-knife test. Only in few cases (less than 10%), we have ambiguous ISO and CLVD signs.

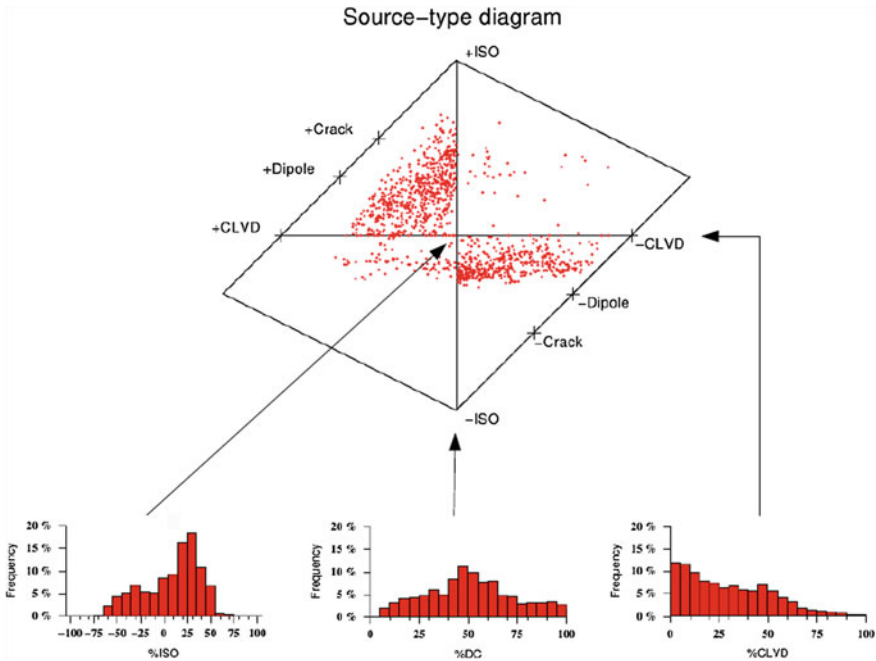


Fig. 4.7 Distribution of full MT solution (after Sen et al. 2013). *Left* distribution of decomposed terms (DC, CLVD, ISO) after full MT inversion. *Right* source type plots are shown for each single event (black circles)

From spectral analysis of a random events subset, corner frequencies were estimated approximatively between 3 and 15 Hz, for magnitudes between M_W 1.0 and 1.8, suggesting that the failures occur with a slow rupture velocity (Kwiatek et al. 2011). Based on these findings, a preliminar kinematic inversion was carried out assuming a rupture velocity of about 1.4 km/s (0.7 times the S wave velocity at the source depth, as estimated from the local layered velocity model). Kinematic source model inversion was then carried out for 158 events, all events with $M_L \geq 1.0$ and with a reliable point source solution. For the range of considered magnitudes and the spectral analysis, the inversion with frequencies up to 10 and 20 Hz should have the potential to resolve finite source parameters, at least for largest events. However, in most cases (84% for 1–10 Hz, 57% for 1–20 Hz) the best finite source solutions have the smallest tested size, which make them equivalent to a point source (the discretized extended source model is composed by a single point source). For the remaining cases, when a larger size is found (in general a radius of 25 m), sub-vertical fault planes are preferred to sub-horizontal ones (a result consistently found for both tested frequency ranges). No clear directivity pattern was resolved.

4.5 Focal Mechanism Clustering

Source inversion results for single events or a limited number of earthquakes can be easily evaluated to discuss the fault geometry or to invert for local stresses, the automated analysis of large moment tensor catalogues require the setup of specific tools. These analysis should be able to automatically recognise the most dominant source characteristics of the target seismicity, identify families of events with similar focal mechanisms, and share the earthquake catalogue according to the chosen classification. We show here how clustering techniques can be used to this purpose. Data clustering is the task of automatically classifying a set of objects into classes, known as clusters, which are group of objects similar among them.

4.5.1 Focal Mechanism Clustering Methodology

Clustering requires the choice of a metric, which is used to evaluate the similarity among different objects to be classified. In this case, the objects to be classified will be focal mechanisms or moment tensors. Different distances among moment tensors have been considered in the past, e.g. by Kagan (1991, 1992), Willemann (1993), Tape & Tape (2012) and Cesca et al. (2013b). The Kagan angle approach was proposed by Kagan (1991, 1992) to describe the difference among pure DC source models. It has the beauty to be intuitive as one DC model can be obviously transformed into another DC models through rotations. Using a quaternion convention, a single rotation is sufficient to transform any DC model into another one, and the rotation angle, also known as Kagan angle, can be used to define the metrics. The other considered metrics, such as ℓ^1 , ℓ^2 or cosine distance are useful to compare full moment tensor mechanisms (as well as deviatoric ones), including pure DC cases. Once the reference metric is chosen, the distance is typically normalized so that it range among the values 0 (equal objects) and 1 (maximal dissimilarity).

Several techniques have been proposed in the last decades. They may lead to different clustering results depending on adopted algorithms and parametrizations. We adopt here a density-based clustering approach, DBSCAN (Ester et al. 1996). Density-based clustering identify clusters from densely populated areas (in moment tensor space) of the dataset. DBSCAN is, in particular, based on the concept of density reachability. According to this approach, an event B pertains to the same cluster of event A, if it can be reached from A, through a chain of densely populated regions. The shape of each cluster is thus controlled by a drop in the density at its edges. Two parameters define the performance of DBSCAN: a threshold value ε defines the maximal distance at which a target event is considered directly reachable from a starting event, while N_{\min} is a measure of the density of a given region, defined as the minimum number of the events which have to be situated within the distance range. N_{\min} is also a constraint for the minimal size of a cluster. If A is surrounded by more than N_{\min} target events, they are part of the same cluster, and point A defined as a

core point in the cluster. The cluster is then enhanced applying the same approach to previous target events, until the new target events are located in sparse regions, and have too few reachable events. These last points are identified as edge points of the cluster. Points in sparse region of the dataset may have too few neighbours and therefore will not be associated to any cluster, but considered as noise, a desirable quality in presence of outliers. Among DBSCAN qualities, we can cite its concept of noise, its stability against the catalogue sorting, and the non-predefined number of clusters. The weakest aspect of DBSCAN is its poor resolution power in case of close clusters. As well as all other clustering techniques, the DBSCAN performance is strongly linked to the choice of the parameters (in this case N_{\min} and ϵ), which remain subjective and which can strongly affect the number and size of detected clusters.

4.5.2 Focal Mechanism Clustering Analysis and Monitoring Applications

To illustrate possible applications of moment tensor clustering, we consider the HAMNET mining induced microseismic dataset, and the DC and full MT solutions obtained by Sen et al. 2013 and discussed in the previous paragraphs. Two clustering approaches are considered, for which a complete description is given in Cesca et al. (2013b). When dealing with the DC catalogue, we use the Kagan angle distance clustering, whereas for the full MT catalogue, we adopt a weighted cosine-distance approach, where weights are defined for each moment tensor component as the reciprocal of the related uncertainty. For both applications the DBSCAN parameters are fixed to $N_{\min} = 10$ and $\epsilon = 0.90$. A discussion on the effects of a variation of these parameters is given in Cesca et al. (2013b).

Results of the DC are illustrated in the top panels of Figs. 4.8 and 4.9: five main clusters are identified. Their focal mechanisms are better discussed in the bottom side of the figure. Cluster 1 (303 events) and 5 (14 events) are relatively similar among them and their normal faulting focal mechanisms striking in direction NE-SW and N-S, with one plane commonly striking parallel to the panel wall (about N 60° E); the smaller Cluster 5 has a more relevant oblique component. Cluster 2 (358 events), 3 (76 events) and 4 (117 events) also have similar features, striking sub-parallel to the panel sides; the steeper plane of clusters 2 and 3 dip toward SW, and toward NE for cluster 4. Finally, 301 events are considered as noise.

A second application to the full MT catalogue was performed using a weighted cosine distance, according to Cesca et al. (2013b) and results are illustrated in Figs. 4.8 and 4.9 (bottom panels). Only three clusters are found: cluster 1 and 2 are largest, with 317 and 466 events respectively, with the smallest clusters 3 similar to cluster 2. 368 focal mechanisms are not assigned to any cluster and considered as noise. The bottom plot of Fig. 4.9 show the source type diagram representation (Hudson et al. 1989), and highlights how the two main identified clusters are characterized

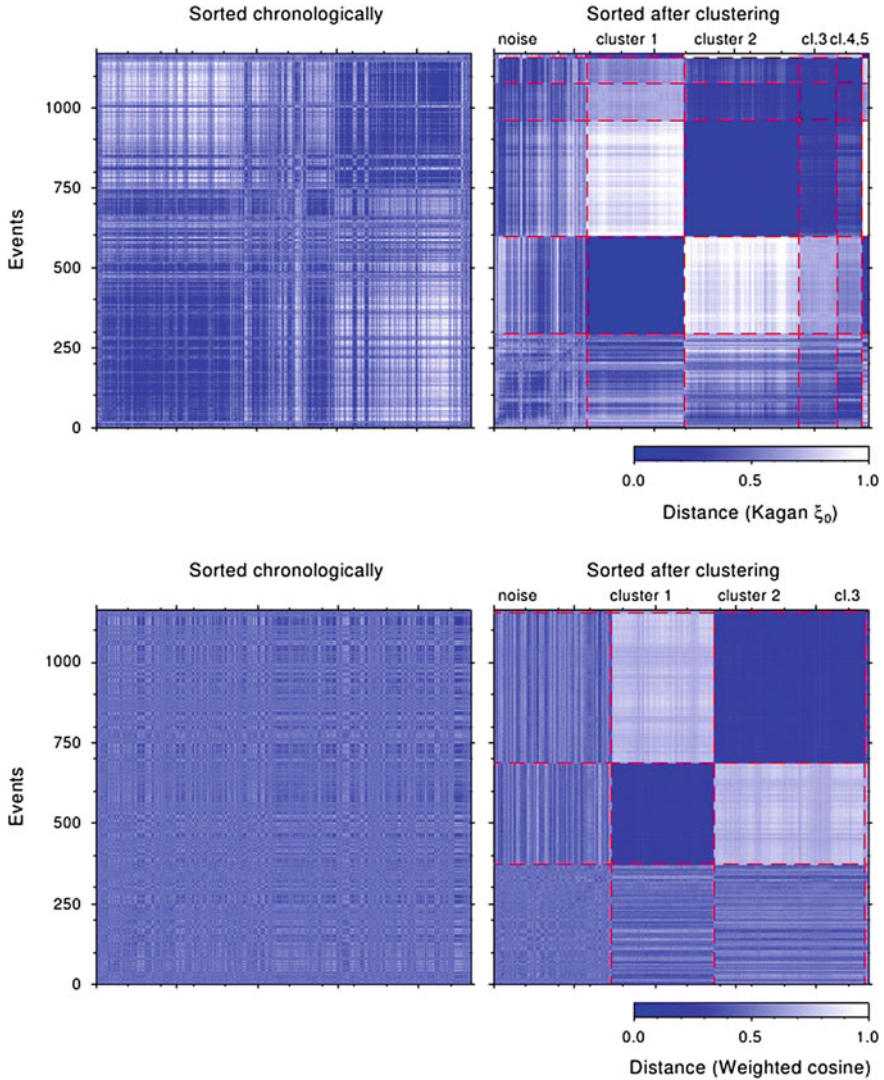


Fig. 4.8 Results of DC and MT clustering of a coal mining induced dataset, Ruhr, Germany (after Cesca et al. 2013b). Similarity matrices are shown before (left) and after (right) clustering for the DC (top) and full MT (bottom) clustering. Red dashed lines indicate noise events and identified clusters

by full moment tensor with similar decomposition and includes events with variable orientation of the DC component. Only the third, smallest cluster, which is more compact, contains events with similar decomposition and similar DC mechanism (the steeper plane has a strike of about 330° , making this DC term comparable with cluster 3 in the DC approach).

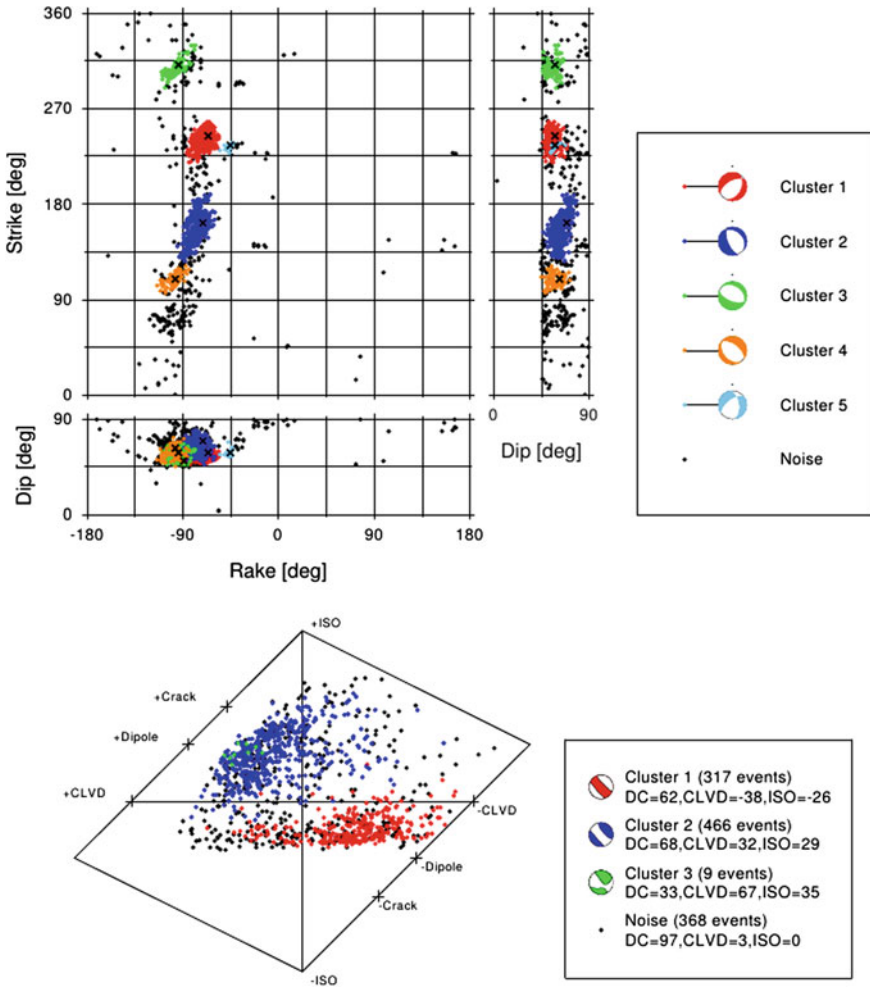


Fig. 4.9 Results of DC (*top*) and full MT (*bottom*) clustering of a coal mining induced dataset, Ruhr, Germany (after Cesca et al. 2013b). *Top* strike, dip and rake parameters are plotted (*bottom left*) along strike-dip, rake-dip and strike-rake diagrams, according to the color legend on the *bottom right*. Mean focal mechanisms are plotted with the same color scale. *Bottom* full MT source models are plotted using a source-type diagram, according to the color legend on the *bottom right* (where mean values for the MT decomposition are given for each cluster)

In the following we show how the source clustering method can be used for mining monitoring purposes. Using its application to the DC catalogue for the Hamm region, we simulate the temporal evolution of the catalogue. Since the moment tensor inversion is performed within 3 min and clustering of a catalogue of about 1000 events within 1 min on a single processor, the clustering application can work in near-real time. In terms of the warning time required to detect the appearance of

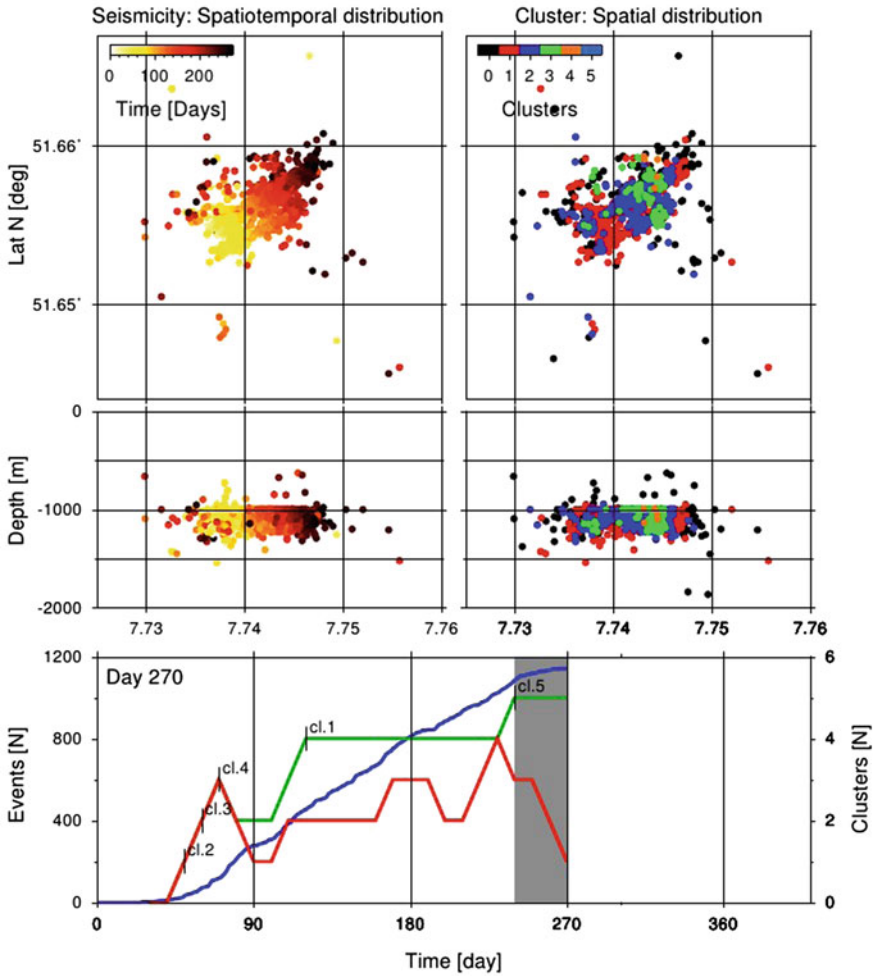


Fig. 4.10 Snapshot (day 270 since July 14, 2006) of the seismicity monitoring framework, simulating the continuous monitoring applied to the Ruhr DC catalogue. *Top* plots illustrate the spatiotemporal evolution of seismicity and clusters. The *bottom* panel illustrates the evolution of the number of detected clusters (*thick red and green lines*) and the cumulative number of event (*thick blue line*), as a function of time. The clustering is repeated every 10 days, after a first learning period of 30 days. The *red curve* is obtained considering only the seismicity recorded in the preceding 30 days, the *green curve* using all events until the running day. *Thin black lines* and cluster labels denote the appearance of clusters for the cumulative seismicity approach (*green line*)

a new cluster, these computation times may be negligible for many applications. More often, the warning time will be controlled by the seismicity rate and the N_{min} parameter. Infact, a new cluster will only be detected when a sufficient number of events with a new common, focal mechanism have been identified. Before this time, they are identified as noise, and might only be detected looking at the noise rate,

an option which is not discussed here. The monitoring starts here after a learning period of 30 days, which is needed to have a sufficient number of earthquakes focal mechanism solutions. The clustering analysis is routinely repeated (here every 10 days) considering either the whole seismic catalogue until the current date, which we refer as cumulative seismicity approach, or only the events of a previous period (here 30 days), which we refer as time window approach. The number and characteristics of the clusters are iteratively updated. A change in the cluster mean values or the appearance/disappearance of a new cluster can be used as a warning signal and trigger more detailed source analysis and an update of the hazard assessment.

The cumulative seismicity approach (Fig. 4.10 bottom, green line) is suited to monitor the overall seismicity: the number of events increases with time while the clustering approach becomes more stable. The time window approach (Fig. 4.10 bottom, red line) may be less stable during periods of weaker activity, but it can also be used to detect the disappearance or weakening of previously active clusters. Results are illustrated in Fig. 4.10, where a snapshot (at day 270) of the monitoring framework is shown.

4.6 Conclusions

We presented here an application of different automated, full waveform based methodologies of mining seismology, which can be used to monitor mining environments, characterize induced seismicity and image the spatiotemporal evolution of fracturing processes. The application to a coal mining dataset from the Ruhr region, Germany, illustrate how these techniques can be combined within a monitoring framework, quickly providing important information, which is helpful to update the hazard assessment in the mine. In particular, the discussed methodologies can be used to infer the origin time and location of the induced seismic events, their magnitude, to provide earthquake source models, to assess the presence of shear and tensile crack components, to automatically classify focal mechanisms and to detect the appearance, disappearance, and seismic rate changes of specific rupture processes.

Acknowledgments We are thankful to the Ruhr University Bochum and to all researchers involved in the installation and handling of the local network, for monitoring and providing access to data used in this study. This work has been funded by the project MINE. The project MINE is part of the R&D-Programme GEOTECHNOLOGIEN, The MINE project is funded by the German Ministry of Education and Research (BMBF), Grant of project BMBF03G0737.

References

- Bischoff M, Cete A, Fritschen R, Meier T (2010) Coal mining induced seismicity in the Ruhr area, Germany. *Pure Appl Geophys* 167:63–75. doi:[10.1007/s00024-009-0001-8](https://doi.org/10.1007/s00024-009-0001-8)
- Bufo E, Pro C, Cesca S, Udias A, Del Fresno C (2011) The 2010 Granada, Spain, deep earthquake. *Bull Seismol Soc Am* 101:2418–2430. doi:[10.1785/0120110022](https://doi.org/10.1785/0120110022)

- Cesca S, Heimann S, Stammer K, Dahm T (2010) Automated point and kinematic source inversion at regional distances. *J Geophys Res* 115(24):B06304. doi:[10.1029/2009JB006450](https://doi.org/10.1029/2009JB006450)
- Cesca S, Rohr A, Dahm T (2013a) Discrimination of induced seismicity by full moment 592 tensor inversion and decomposition. *J Seismol* 17(1):147–163. doi:[10.1007/s10950-012-9305-8](https://doi.org/10.1007/s10950-012-9305-8)
- Cesca S, Sen AT, Dahm T (2013b) Seismicity monitoring by cluster analysis of moment tensors. *Geophys J Int* (submitted)
- Coldewey WG, Semrau L (1994) Mine water in the Ruhr area (Federal Republic of Germany). In: INWA Proceedings 1994
- Custodio S, Cesca S, Heimann S (2012) Application to the 2007 Mw 5.9 Horseshoe Abyssal Plain, offshore SW Iberia, earthquake. *Bull Seismol Soc Am* 102:361–376. doi:[10.1785/0120110125](https://doi.org/10.1785/0120110125)
- Domingues A, Custodio S, Cesca S (2012) Waveform inversion of small to moderate earthquakes located offshore southwest Iberia. *J Int Geophys*. doi:[10.1093/gji/ggs010](https://doi.org/10.1093/gji/ggs010)
- Drozdowski G (1993) The Ruhr coal basin (Germany): structural evolution of an autochthonous foreland basin. *Int J Coal Geol* 23:231–250
- Ester M, Kriegel H-P, Sander J, Xu X (1996) A density-based algorithm for discovering clusters in large spatial databases with noise. In Simoudis E, Han J, Fayyad UM (eds) Proceedings of the second international conference on knowledge discovery and data mining. AAAI Press, Menlo Park, pp 226–231, ISBN 1-57735-004-9
- Grigoli F, Cesca S, Vassallo M, Dahm T (2013) Automated seismic event location by travel-time stacking: an application to mining induced seismicity. *Seismol Res Lett* 84(4):666–677. doi:[10.1785/0220120191](https://doi.org/10.1785/0220120191)
- Heimann S (2011) A robust method to estimate kinematic earthquake source parameters, PhD Thesis, University of Hamburg
- Hudson JA, Pearce RG, Rogers RM (1989) Source type plot for inversion of the moment tensor. *J Geophys Res* 94(B1):765–774. doi:[10.1029/JB094iB01p00765](https://doi.org/10.1029/JB094iB01p00765)
- Kagan YY (1991) 3-D rotation of double-couple earthquake sources. *Geophys J Int* 106:709–716
- Kagan YY (1992) Correlation of earthquake focal mechanisms. *Geophys J Int* 110:305–320
- Kwiatak G, Plenkers K, Dresen G (2011) Source parameters of picoseismicity recorded at Mponeng deep gold mine, South Africa: implications for scaling relations. *Bull Seismol Soc Am* 101(6):2592–2608
- Sen AT, Cesca S, Bischoff M, Meier T, Dahm T (2013) Automated full moment tensor inversion of coal mining induced seismicity. *Geophys J Int*. doi:[10.1093/gji/ggt300](https://doi.org/10.1093/gji/ggt300)
- Tape W, Tape C (2012) Angle between principal axis triples. *Geophys J Int* 191:813–831. doi:[10.1111/j.1365-246X.2012.05658.x](https://doi.org/10.1111/j.1365-246X.2012.05658.x)
- Willemann RJ (1993) Cluster analysis of seismic moment tensor orientations. *Geophys J Int* 115:617–634

Chapter 5

Three-Dimensional Multi-Scale and Multi-Method Inversion to Determine the Electrical Conductivity Distribution of the Subsurface (Multi-EM)

Oliver Ritter, Klaus Spitzer, Martin Afanasjew, Michael Becken, Ralph-Uwe Börner, Felix Eckhofer, Michael Eiermann, Oliver G. Ernst, Alexander Grayver, Jens Klump, Naser Meqbel, Christian Nittinger, Jan Thaler, Ute Weckmann and Julia Weißflog

Abstract Combining different electromagnetic (EM) methods in joint inversion approaches can enhance the overall resolution power. Every method is associated with a particular sensitivity pattern. By assembling complementary patterns, subsurface imaging becomes more complete and reliable. We describe different paths to obtain multi-EM inversions. First, a joint inversion approach using finite difference forward operators is outlined that formulates the problem of minimizing the objective function using different weights for each individual method. Then we address a sequential approach using finite element methods on unstructured grids to cycle through the different EM methods iteratively. Both methods are based on a traditional parametrization using piecewise constant model parameters which may be inefficient when describing the usually rather coarse models. Therefore, we investigate wavelet-based model representations as an alternative.

O. Ritter · A. Grayver · J. Klump · N. Meqbel · J. Thaler · U. Weckmann
Helmholtz Centre Potsdam GFZ German Research Centre for Geosciences, Potsdam, Germany

K. Spitzer (✉) · M. Afanasjew · R.-U. Börner · J. Weißflog
Institute of Geophysics and Geoinformatics, TU Bergakademie Freiberg, Freiberg, Germany
e-mail: klaus.spitzer@geophysik.tu-freiberg.de

M. Becken · C. Nittinger
Institute of Geophysics, University of Münster, Münster, Germany

F. Eckhofer · M. Eiermann · O. G. Ernst · M. Afanasjew
Institute of Numerical Analysis and Optimization, TU Bergakademie Freiberg, Freiberg, Germany

O.G. Ernst
Department of Mathematics, TU Chemnitz, Chemnitz, Germany

5.1 Introduction

Geophysical methods are applied to investigate the Earth's interior. We obtain models of the Earth by imaging physical parameters such as density, electrical conductivity, or elastic properties using a variety of techniques. Here, we consider geophysical methods exploiting electric currents generated by electromagnetic (EM) induction or galvanic coupling to sense the electrical conductivity structure at depth. During the last years, these techniques have experienced rapid development for exploration purposes of the drillable subsurface. For instance, active controlled-source electromagnetic (CSEM) techniques are now frequently used together with seismic techniques to characterize resistive hydrocarbon reservoirs in offshore petroleum exploration. Deep saline aquifers exhibit high electrical conductivities and constitute one of the prime targets for electrical imaging methods, making these techniques one of the most important geophysical tools to characterize target horizons for CO₂ storage or geothermal reservoirs.

We attempt to enhance the reconstruction capabilities of geoelectric potential field and electromagnetic diffusion methods covering a wide range of scales from boreholes to regional and lithospheric dimensions. To reach these goals, we have developed an interdisciplinary concept integrating working groups from applied and numerical geophysics, information technology and numerical mathematics.

At first, we describe a joint inversion approach that uses data misfit and regularization in one objective function with different weights for each method. The implementation is based on the existing inversion framework ModEM by Egbert and Kelbert (2012) and Meqbel (2009) and incorporates CSEM, magnetotellurics (MT), and direct current (DC) (Spitzer 1995) finite difference (FD) forward operators. The parametrization is based on rectangular blocks. The second approach uses unstructured tetrahedral meshes for both the finite element forward (FE) operator and the parametrization. Rectangular grids are easy to construct and handle, but they are incapable of discretizing more complicated geometries such as steep surface topography or known subsurface structures like mining galleries. Keeping this in mind, we restrict ourselves here, however, to very simple geometries to make our results comparable.

A final section deals with a new method to parameterize the model in a more efficient way using wavelets. The idea behind is to compress the information describing coarse model structures by using a limited subset of wavelet coefficients. Inverting for these coefficients yields a less underdetermined problem and, thus, a potentially less biased solution.

5.2 Finite Difference Approach

In this section, we describe a joint inversion of the MT, CSEM and DC data using FD operators. The EM methods under consideration differ in their sensitivities towards resistive and conductive structures as well as in their exploration depths. While the

MT method generally resolves conductive structures up to depths of the Earth's upper mantle, CSEM and DC resistivity methods are sensitive to resistive layers in the uppermost crust. Thus, a proper weighting between different EM data sets is essential for a joint inversion. Here we present recently developed weighting schemes used for joint inversion of MT, CSEM and DC resistivity data. In addition, inverting multi-EM methods jointly requires the different forward modeling codes to be implemented in a common framework. For this purpose, we made use of the EM modular system ModEM of Egbert and Kelbert (2012) which uses the parallelization schemes described by Meqbel (2009). This package was initially developed to invert only MT data. For our joint inversion approach, we extended ModEM to include the forward modeling operators of CSEM using a secondary field formulation with a 1D analytic solution of Key (2009) and a DC resistivity solver by Spitzer (1995). All three solvers are capable of handling a three-dimensional distribution of electrical conductivity in the subsurface. Our proposed joint inversion scheme is based mainly on weighting the individual components of the total data gradient after each model update. Norms of each data residual are used to assess how much weight the individual components of the total data gradient must be given to result in a homogeneous contribution of all data sets to the inverse solution.

To demonstrate the efficiency of the proposed weighting schemes and to explore the contribution of each method we used synthetic data sets computed from a 3D synthetic model consisting of a shallow resistive thin block and a conductive and resistive larger block further below (Fig. 5.1a). These structures are embedded in a homogeneous background resistivity of $10 \Omega\text{m}$. To demonstrate the resolution power of the MT and CSEM methods, we first inverted these two data sets separately. When fitting only the MT data, the inversion result in Fig. 5.1b shows that the conductive block is well resolved while the shallow and the deeper resistivity blocks are barely seen. In contrary, fitting the CSEM data separately results in a model in which the shallow thin resistive block is better resolved while only the tops of the deeper conductive and resistive blocks are imaged. As a next step, we inverted the MT and CSEM data jointly to test the new weighting scheme.

Figure 5.1d shows that combining MT and CSEM data and using an appropriate weighting results in a better image of the shallow thin resistive block as well as the deeper resistive and conductive blocks. The DC resistivity data are collected along three (synthetic) boreholes penetrating to a depth of about 700m. Joint inversion of CSEM and DC resistivity data results in a more accurate reconstruction of the resistivity of the shallow thin block and a better definition of its lower and upper edges (Fig. 5.1e). In the last inversion experiment, we inverted all three data sets (MT, CSEM and DC resistivity) jointly. The model in Fig. 5.1f clearly demonstrates that joint 3D inversion is feasible. More importantly it shows, that a combination of these three methods results in a much better image of the subsurface than what can be achieved with any of the individual methods.

An additional thread of our developments on the basis of FD involves a fully distributed parallel three-dimensional CSEM inversion algorithm (Grayver et al. 2013). Ideas presented in Streich (2009) were further elaborated and incorporated into this new code. The inversion algorithm is based on Gauss-Newton minimization

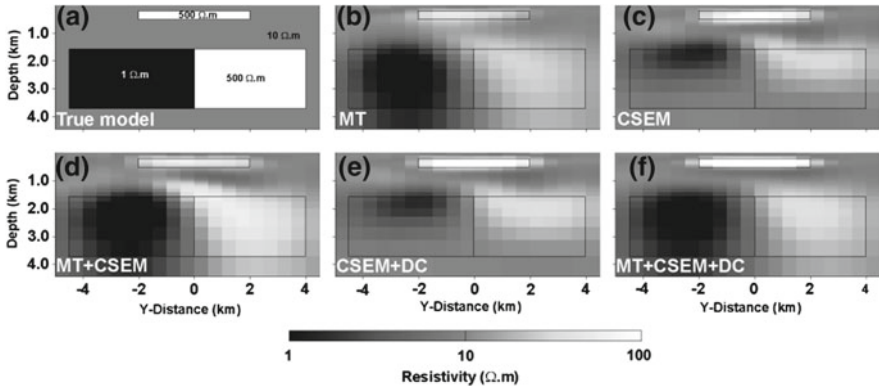


Fig. 5.1 **a** Cross section (y-axis) through a 3D model used to compute the synthetic data. **b** and **c** show inversion results when fitting MT and CSEM data separately. **d–e** show joint 3D inversion results using the new weighting scheme **d** MT and CSEM, **e** CSEM and DC resistivity and **f** MT, CSEM and DC resistivity data. The inversion model in **f** resembles most closely the structures of the original model shown in **a**

and uses a parallel distributed direct-solver for FD forward modeling. The forward modeling implements efficient routines to handle realistic source geometries accurately (Streich and Becken 2011). This inversion scheme has been used to invert real CSEM data collected across the Ketzin CO₂ storage formation, 15 km west of Berlin (Grayver 2013). Figure 5.2 shows resistivities obtained from the 3D inversion along the receiver line. The image contains several prominent conductive and resistive horizontally continuous structures that also appeared nearly identically for different inversion setups. The regional geology is well constrained, with an anticline structure of sediments overlying a salt pillow (Förster et al. 2009). The top of the anticline is at a depth of approximately 2 km near the center of our survey line. The electrical conductivity structures recovered by 3D CSEM inversion correlate well with the main geological units (Klapperer et al. 2011).

5.3 Finite Element Approach

The joint inversion schemes introduced above are based on classical FD forward operators using structured grids, which are limited with respect to discretizing complex structures such as topography, bathymetry or generally curved objects. As a part of Multi-EM we have therefore developed 3D forward modeling and inversion schemes based on FE on unstructured tetrahedral grids. These approaches allow for an easy incorporation of complicated, more realistic model geometries, which are encountered in the geosciences. A further major difference to the inversion concept described above is the sequential mode of cycling through the individual inversion of each EM method using the output of the previous scheme as the reference model

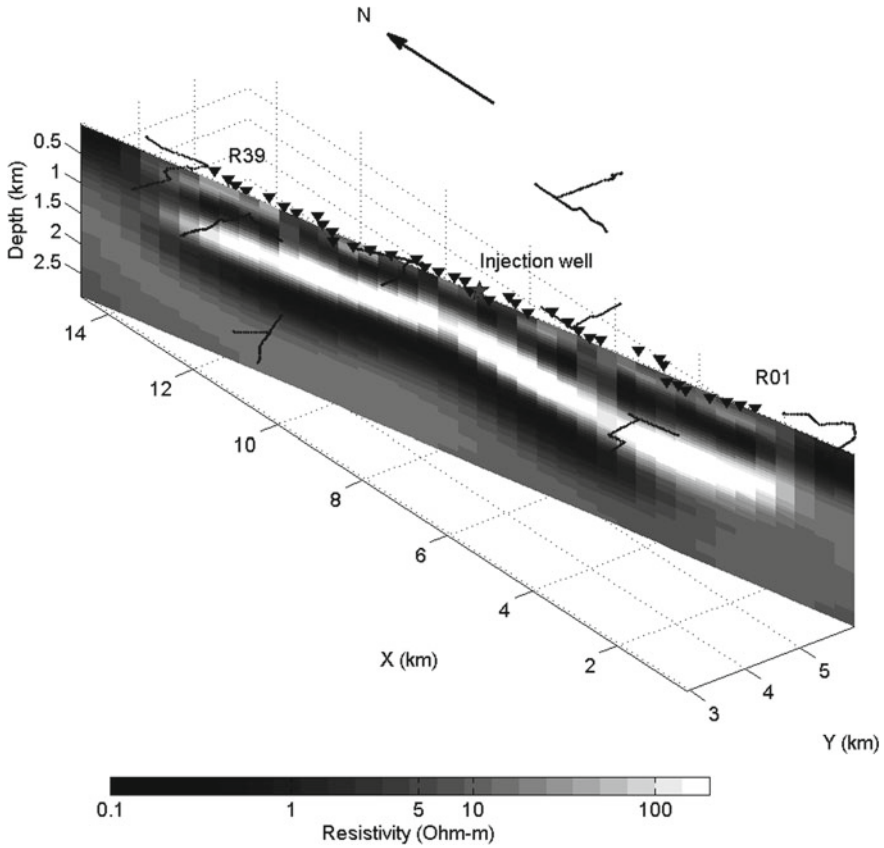


Fig. 5.2 Vertical section extracted from the 3D inversion model along the receiver line. Lines and triangles indicate transmitters and receivers, respectively. The star shows the position of the CO₂ injection well

for the following one. In this way, we do not have to determine the full set of regularization parameters all at once which is a major difficulty due to their inherent uncertainty. In order to achieve a solid and unified software base for our FE methods, we have implemented all new forward and inverse operators in MATLAB. The resulting code is modularized and the interfaces between model geometry, grid generator and inverse operator are being standardized so that the individual EM method may conveniently access the model and pass the inversion output over to the subsequent program. The EM methods we are reporting on are DC and TEM. However, FE solutions for CSEM and MT (Franke-Börner et al. 2012) are near completion ultimately providing the capability of joint inversion of all four EM methods.

The DC resistivity code by Weißflog et al. (2012) enables us to model complex topography and to extract the derivatives, which are crucial for the inversion while retaining full control over the assembly process of the system matrix. For simplicity,

we apply a regularized Gauss-Newton method. To stabilize the inversion procedure and provide additional information to avoid ambiguities, a suitable regularization strategy is necessary. As our inversion approach is based on a FE discretization of the equation of continuity using a piecewise constant representation of the conductivity model, a regularization operator is required that is applicable to piecewise constant model parameters on unstructured grids. We have therefore implemented a smoothness regularization by (Schwarzach and Haber 2013) in which the penalty function measures the norm of a weak gradient of the conductivity field. The latter is evaluated using duality techniques with $H(\text{div})$ -conforming Raviart-Thomas vector elements of lowest order.

For solving the 3D transient electromagnetic (TEM) problem we have developed two different approaches. Both use Nédélec finite elements to discretize the spatial part of the curl-curl equation for the electric field. In the first method, the time evolution of electromagnetic fields is propagated forward in time, whereas in the latter the Fourier components of these fields are computed for a suitable set of frequencies, which are then transformed numerically into the time domain. Each of these methods is numerically challenging if not, as in the case of explicit time stepping, prohibitively expensive. We have therefore employed rational Krylov subspace techniques (RKST) to reduce the numerical costs both in the time and the frequency domain. In the time domain, RKST are used in conjunction with a geometric multigrid method to solve the resulting linear system of ordinary differential equations. In this way, the initial electric field is advanced to only a small set of selected times of interest (Afanasjew et al. 2013). In the frequency domain, RKST are applied as a model reduction technique where the resulting system matrix is projected onto a low-dimensional subspace retaining the information of the main eigenvalues (Börner et al. 2013).

In the following experiments we limit ourselves to two dimensions. However, the methodology applies to 3D scenarios in the same manner. To demonstrate the advantage of a joint TEM/DC approach and showcase the respective properties of the different methods, the model (Fig. 5.3a) consists of two smaller bodies of high conductivity close to the surface and a larger structure of high resistivity buried at greater depth within a $100 \Omega\text{m}$ background. First, the synthetic data for TEM and DC were independently calculated on different grids. Then the inversion process was started for TEM and DC using a homogeneous reference model on a common inversion mesh (i.e., parametrization) resulting in inverse models displayed in Fig. 5.3b, c, respectively. It is easy to see that the TEM configuration (with receivers located between -200 m and $+200\text{ m}$ and two sources on the surface) is not able to resolve the deeper structure while being able to distinguish the two shallow bodies quite clearly. Our DC setup is a pole-pole configuration with four sources on the Earth's surface and one borehole source at a depth of 350 m . The receivers are located along the surface between $\pm 600\text{ m}$. The DC inversion reconstructs the large structure at depth while failing to separate the smaller objects to our satisfaction. Figure 5.3d shows the DC inversion result using the same configuration as described above and the TEM solution (Fig. 5.3b) as the reference model. Combining the individual resolution properties of these two methods yields a better image of the two conductive blocks as well as of the resistive body at greater depth.

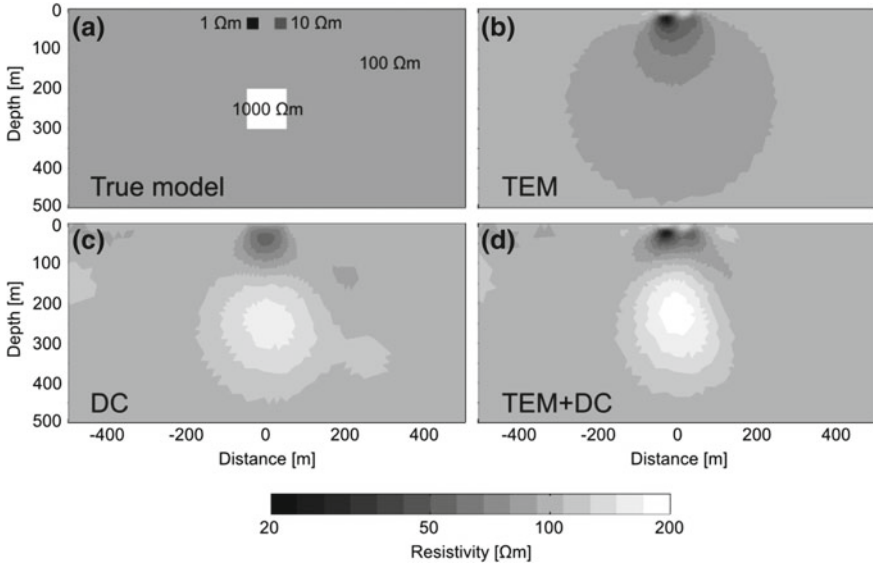


Fig. 5.3 **a** The true model used to compute the synthetic data. **b** and **c** are the inversion results for only TEM and DC data, respectively. **d** Using the TEM solution as the reference model, we then inverted the DC resistivity data to obtain a joint inversion result, which recovers the three anomalous bodies well

5.4 Sparse Inversion in Wavelet Domain

The preceding inversion examples relied on a parametrization of the subsurface into disjoint blocks of piecewise constant resistivity. In such bases, complex structures are most conveniently represented by using a large number of small model blocks to allow for the needed degree of detail and flexibility to describe the resistivity distribution. This approach introduces a large solution null-space, and the commonly applied smoothing regularization techniques result in heavily biased model estimates.

Here, we investigate alternative bases to represent resistivity that allow for a sparse representation of the resistivity distribution. The term sparse is used here to indicate that the model is described with as little as possible non-zero coefficients. Sparse image recovery has in the last years become a rapidly developing field in compressed sensing, and has proven particularly successful in medical imaging. Here, we apply these concepts for the first time to electromagnetic geophysical imaging problems by transforming the resistivity image into wavelet domain and estimating the significant wavelet coefficients.

A wavelet multi-resolution basis admits the approximation of a function with different levels of details on various scales. Because many of the details contained in images are unimportant, the corresponding coefficients can be threshold from the decomposition in order to obtain a compressed version of the original image. We attempt to exploit these compression capabilities of wavelets in the framework of the

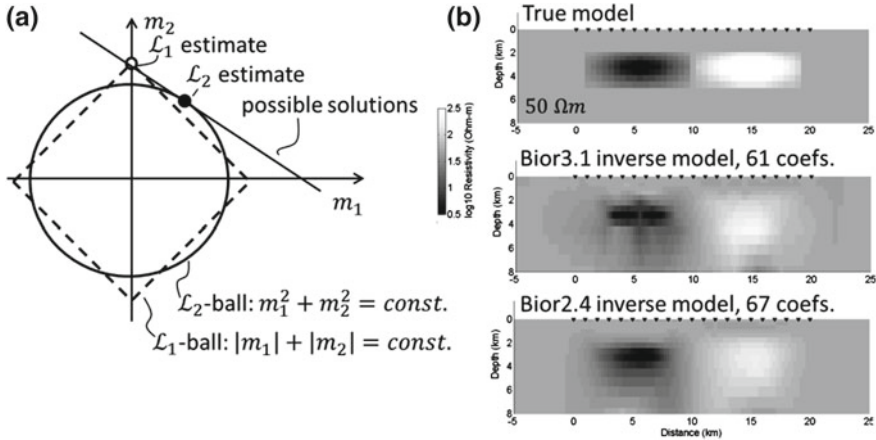


Fig. 5.4 Sparse Inversion. **a** Solution simplicity, expressed in the L2 and L1 norms of model parameters for a simple two-parameter problem. Among all possible solutions (*solid line*), the objective of minimal L1 norm yields a sparse solution (open dot, with $m_1 = 0$), whereas the minimal L2 norm is found for a smooth solution with $m_1 \approx m_2$. Figure modified after Loris et al. (2007). **b** Inversion examples for a two-blob model. True model (*upper panel*) used to generate synthetic data and db4 (*middle panel*) and bior2.2 (*lower panel*) inversion models that fit the data to within their randomly generated errors. Both inversion models require only a fraction of non-zero coefficients when compared to standard block parametrizations

inverse magnetotelluric problem. We formulate the following objective: determine the few non-zero wavelet coefficients which are required to represent a model that can explain the observed data. Accordingly, the approach falls into the class of sparsity-constrained inversion schemes. These schemes minimize the combination of the data misfit in a least squares (L2) sense and of a model coefficient norm in a L1 sense (L1-L2 minimization). The minimal L1 coefficient norm renders the solution sparse, in contrast to an L2 norm minimization that renders the solution smooth (cf. Fig. 5.4a).

The minimization of a L1-L2 objective is problematic, because the function is non-convex and non-differentiable. We applied a primal-dual-interior point method which has shown to be efficient for L1-L2-norm minimization (Borsic and Adler 2012). The algorithm inverts for a differentiable approximation of the L1-norm. The formulation seeks to minimize the gap between a primal and a dual objective function and is iteratively solved for with a Newton method.

The appearance of sparse wavelet models is dependent on the particular choice of wavelets. We have focused on smooth wavelets that result in smooth resistivity models, similar to those generated with the notably different smoothing regularized inversion scheme. However, only a fraction of coefficients is required to represent the model. Figure 5.4b depicts, as an example, inversion models estimated from synthetically generated, noise-contaminated data using a five-level db4 (middle panel) and bior2.2 wavelet representation (lower panel). The true model used to generate the data is depicted in the upper panel. We find that about 60 wavelet coefficients are sufficient to describe a model that fits the data.

For the example in the Fig. 5.4, the forward solutions were obtained with a FE approach (Lee et al. 2009) that solves the induction problem for the uncompressed resistivity distribution reconstructed from the wavelet representation. Rectangular elements were employed. The wavelet sensitivities were evaluated by projecting the space domain sensitivities into wavelet domain.

Our results demonstrate that over-parametrization of the model region can be eliminated by projecting the model domain into a sparsifying basis. This proposed approach results in an alternative class of models by invoking sparsity based regularization; it may furthermore yield computational benefits provided that sparsity could be exploited in the evaluation of the Jacobian. Our approach could also be beneficial for model appraisal when evaluating resolution and covariances for a limited set of coefficients.

5.5 Conclusions

This project has given us the possibility to explore various strategies of joining different EM methods in common inversion schemes. The outcome is clear: combining two or more EM techniques in a complementary way may enhance the ability to reconstruct subsurface conductivity structures. However, the way to achieve this aim is multifaceted. The existing inversion framework ModEM offers a practical environment to rapidly incorporate existing forward modeling software. With respect to the inversion strategy the main problem is the determination of a set of regularization parameters all at the same time. We have therefore begun to investigate a sequential mode where the inversion result of one method serves as a reference model for the next. Using synthetic models, both approaches have demonstrated that the combination of EM methods may produce enhanced images of the subsurface compared to individual inversions.

Moreover, we have learned in the course of the project that mixing FD and FE approaches is unrewarding because the strengths of each approach are diminished. Whereas the FD method takes advantage of its simplicity, the sparsity of the resulting system matrix and the relatively small efforts of administering rectangular Cartesian grids, the FE method stands out due to its enormous flexibility with respect to adapting any given geometry using unstructured meshes. At first glance, FD might be the method of choice if it comes to inversion because the structures to be reconstructed are initially not known and, thus, grid adaptivity does not play an important role. However, given topography, subsurface structures as caves or voids, and a-priori information from, e.g., seismics may put high requirements on the future inversion software. The price to pay is the increased administrative effort for FE.

We have also acquired first experiences with alternative model parametrization techniques in the wavelet domain. We apply for the first time compressed sensing concepts to the inversion of magnetotelluric data and recover a sparse solution by minimizing a mixed L1-L2 norm objective function.

Finally, we have extensively used massively distributed computations for 3D inversions. In fact, working with real-world problems and in general with large model domains and comprehensive data sets requires adequate computer hardware that continuously offers an increasing number of computing cores, at least for the foreseeable, middle-term future. High-performance computing on a moderate or large number of nodes goes therefore hand in hand with innovative mathematical and numerical concepts. Thus, this project marks a starting point for a wide variety of further research efforts in EM inversion based on the research results at hand.

References

- Afanasjew M, Börner R-U, Eiermann M, Ernst OG, Spitzer K (2013) Efficient three-dimensional time domain TEM simulation using finite elements, a nonlocal boundary condition, multigrid, and rational Krylov subspace methods. In: Extended Abstract, Proceedings 5th international symposium on three-dimensional electromagnetics, Sapporo, Japan, 7–9 May 2013, p 4
- Börner R-U, Ernst OG, Güttel S (2013) Three-dimensional transient electromagnetic simulation using rational Krylov subspace projection methods. In: Extended Abstract, Proceedings 5th international symposium on three-dimensional electromagnetics, Sapporo, Japan, 7–9 May 2013, p 4
- Borsic A, Adler A (2012) A primal-dual interior-point framework for using L1 and L2 norm on the data and regularization terms of inverse problems. *Inverse Prob* 28:095011
- Egbert GD, Kelbert A (2012) Computational recipes for electromagnetic inverse problems. *Geophys J Int* 189:251–267
- Förster A, Giese R, Juhlin C, Norden B, Springer N (2009) The geology of the CO2SINK site: from regional scale to laboratory scale. *Energy Procedia* 1:2911–2918
- Franke-Börner A, Börner R-U, Spitzer K (2012) On the efficient formulation of the MT boundary value problem for 3D finite element simulation. In: Expanded Abstract, Proceedings 21st international workshop on electromagnetic induction in the earth, Darwin, Australia, 25–31 Jul 2012, p 4
- Grayver AV, Streich R, Ritter O (2013) Three-dimensional parallel distributed inversion of CSEM data using a direct forward solver. *Geophys J Int* 193(3):1432–1446. doi:10.1093/gji/ggt055
- Grayver AV (2013) Three-dimensional controlled-source electromagnetic inversion using modern computational concepts. PhD Thesis, FU Berlin
- Klapperer S, Moeck L, Norden B (2011) Regional 3D geological modelling and stress field analysis at the CO2 storage site of Ketzin, Germany. *Geoth Resour Counc Trans* 35(1):419–424
- Key K (2009) 1D inversion of multicomponent, multifrequency marine CSEM data: methodology and synthetic studies for resolving thin resistive layers. *Geophysics* 74:F9–F20
- Lee SK, Kim HJ, Song Y (2009) MT2DInvMatlab—a program in MATLAB and FORTRAN for two-dimensional magnetotelluric inversion. *Comput Geosci* 36:1722–1734
- Loris I, Nolet G, Daubechies I, Dahlen FA (2007) Tomographic inversion using 11-norm regularization. *Geophys J Int* 170:359–370
- Meqbel NMM (2009) The electrical conductivity structure of the Dead Sea Basin derived from 2D and 3D inversion of magnetotelluric data. PhD Thesis, Free University of Berlin
- Schwarzbach C, Haber E (2013) Finite element based inversion for time-harmonic electromagnetic problems. *Geophys J Int* 193:615–663
- Spitzer K (1995) A 3D finite difference algorithm for DC resistivity modeling using conjugate gradient methods. *Geophys J Int* 123:903–914
- Streich R (2009) 3D finite-difference frequency-domain modeling of controlled-source electromagnetic data: direct solution and optimization for high accuracy. *Geophysics* 74(5):F95–F105

- Streich R, Becken M (2011) Electromagnetic fields generated by finite-length wire sources: comparison with point dipole solutions. *Geophys Prospect* 59(2):361–374
- Weißflog J, Eckhofer F, Börner R-U, Eiermann M, Ernst O, Spitzer K (2012) 3D DC resistivity FE modeling and inversion in view of a parallelised Multi-EM inversion approach. In: Extended Abstract, Proceedings 21st electromagnetic induction workshop, Darwin, Australia, 25–31 Aug 2012, p 4

Chapter 6

MuSaWa: Multi-Scale S-wave Tomography for Exploration and Risk Assessment of Development Sites

Hendrik Paasche, Michael Rumpf, Agostiny M. Lontsi, Jörg Hausmann, Katrin Hannemann, Thomas Fechner, Matthias Ohrnberger, Ulrike Werban, Jens Tronicke, Frank Krüger and Peter Dietrich

Abstract Near surface seismic imaging bears a high potential to enhance geotechnical site characterization. We highlight recent advances made in S-wave tomography for characterizing near surface unconsolidated sediments. This comprises progress in experimental setup and acquisition technology for local scale S-wave tomography. We discuss the development of mobile seismic crosshole tomography solely building on temporary installations realized by direct push technology as well as a modular borehole geophone chain suitable for operation in shallow and slim near surface boreholes. These technical developments are accompanied by progress in geophysical model generation, i.e., fully non-linear inversion strategies suitable for routine application and model uncertainty appraisal. We link S-wave and P-wave tomographic models to geotechnical target parameters and evaluate recent developments made for high resolution ground-truthing using direct push technology for geotechnical and stratigraphic analyses. To be able to provide improved regional scale seismic properties we advanced the Rayleigh wave based imaging of S-wave velocity variations using diffusive wavefield theory for modeling the full microtremor H/V spectral ratio for receivers at the surface and in depth.

H. Paasche (✉) · J. Hausmann · U. Werban · P. Dietrich
Department Monitoring and Exploration Technologies, UFZ Helmholtz Centre for Environmental Research, Permoser Str. 15, 04318 Leipzig, Germany
e-mail: hendrik.paasche@ufz.de

M. Rumpf · A. M. Lontsi · K. Hannemann · M. Ohrnberger · J. Tronicke · F. Krüger
Institute of Earth and Environmental Sciences, University of Potsdam, K.-Liebknecht-Str. 24-25, 14476 Potsdam, Germany

T. Fechner
Geotomographie GmbH, Am Tonnenberg 18, 56567 Neuwied, Germany

6.1 Introduction

Modern human civilization requires a high mobility of their individuals and merchandise traffics. This requires substantial effort in improving or extending transportation infrastructure and pathways above, on, and below the Earth's surface. Planning and construction of new transportation pathways or buildings, such as bridges, or renovation of existing infrastructure requires communication and collaboration between initiators, consultants, and constructors. Earth scientists, in particular geophysicists and geotechnical engineers, have an important role in this process by providing spatial information about relevant characteristics of the construction ground. Ideally, such a geotechnical characterization of the ground should go beyond a deterministic assessment of subsurface states and conditions as it is routinely done nowadays. Instead, a probabilistic geotechnical risk assessment of envisaged construction and development sites would allow for improved decision making with regard to constructional safety of planned infrastructure.

Depths of interest in geotechnical surveys of development sites may vary according to the geotechnical issue to be addressed. Typical extents range from a few meters to more than 100 m. Traditionally, geotechnical surveying and analysis tools are used at selected locations to gain information about the subsurface (e.g., Lunne et al. 1997; Fahay 1998; Atkinson 2000). State of the art methodologies comprise drilling and core analyses, borehole logging or heavy load tests, and dynamic probing. Such laterally sparse exploration techniques provide detailed 1D information about parameter variations with depth. However, surveys solely relying on 1D exploration techniques are likely to fail when it comes to the characterization of spatially highly heterogeneous near surface sediments.

Geophysical tomographic imaging techniques (e.g., Lehmann 2007) offer the capability to visualize physical parameter variations in heterogeneous subsurface environments in one, two, or three dimensions. Due to physical reasons, seismic methods are particularly suitable for investigating construction grounds and their mechanical properties (e.g., Robertson et al. 1995; Dietrich and Leven 2006). In the past, almost exclusively seismic P-wave tomography has been used for high resolution local-scale exploration of development sites. The geotechnical benefits resulting from P-wave velocity information are rather limited. Additional knowledge about the spatial variation of S-wave velocities is required to derive spatial geotechnical parameter distributions relevant for engineering applications, such as shear strength or Poisson's ratio. A key objective of our work was therefore the enhancement of S-wave tomography for aiming on routine and efficient application of seismic S-wave tomography for high resolution exploration of construction ground.

In addition to improved local scale geotechnical exploration strategies, reliable methodologies for regional geotechnical ground and risk assessment are desired. Traditionally, this is done by performing passive seismic experiments employing receiver arrays placed at selected locations within the survey area. The use of seismic ambient noise (SAN) has proven to be a valuable tool for subsurface characterization. However, the combination of active and passive seismic surface wave experiments is not

routinely done up to now. Employment of seismic 3D arrays realized by commonly used three-component (3C) borehole and surface-planted geophones is expected to overcome some limitations of the classical dispersion analysis. Additionally, SAN tomography bears the potential to image S-wave velocity variations in the subsurface over larger regions. Within the MuSaWa project, we focused on advancing the Rayleigh wave based imaging of S-wave velocity variations using diffusive wave-field theory for modeling the full microtremor H/V spectral ratio for receivers at the surface and in depth.

Acquisition of geotechnical parameters is required for reliable ground truthing of geophysical tomograms and deduced geotechnical properties. In this context direct push (DP) technology offers an innovative approach for site investigation. DP probes allow for *in situ* recording of high resolution depth profiles for geotechnical, hydrological, or geophysical exploration of near surface sediments. In MuSaWa, we employed DP technology for high resolution analysis of sediment stratigraphy and geotechnical properties to support geophysical tomography interpretation. Additionally, within the frame of MuSaWa the high mobility of DP technology has been appealing to develop new acquisition techniques for high resolution P- and S-wave crosshole tomography carried out independently from permanently installed boreholes.

Furthermore, to improve acquisition efficiency of seismic tomography utilizing borehole recording systems, we developed a multi-station borehole acquisition system. Technological development has been done in parallel to field measurements. The new system has been employed in some field experiments using three 3C borehole geophones suitable to record P- and S-wave energy arriving at each receiver station.

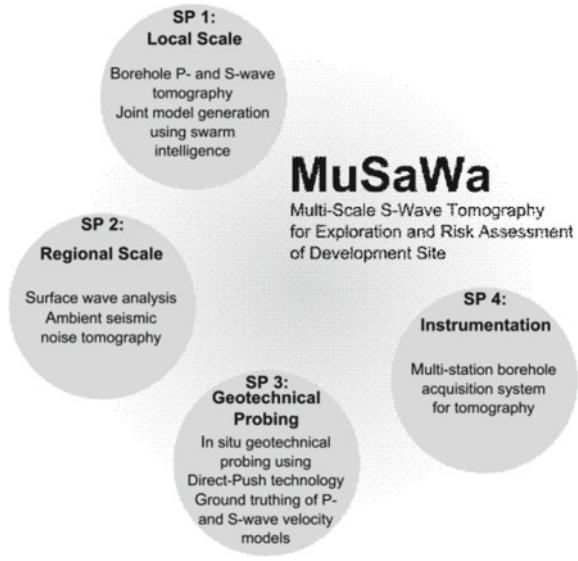
MuSaWa is a collaboration project with partners from the University of Potsdam, the Helmholtz Centre for Environmental Research—UFZ, Leipzig, and Geotomographie GmbH, Neuwied (Paasche et al. 2011). MuSaWa comprises four subprojects (SP; Fig. 6.1) addressing issues related to local and regional scale S-wave tomography, DP technology for seismic and geotechnical validation, and instrumentation advancement for efficient S-wave energy recording in boreholes, respectively. In the following, we highlight recent achievements resulting from the research work carried out in the MuSaWa project.

6.2 SP 1: S-wave Tomography—the Local Scale

6.2.1 Mobile Acquisition of Crosshole Tomographic Data

To improve the acquisition of seismic data for geotechnical site assessments and to overcome the limitations of stationary boreholes, we tested in close cooperation with SP 3 (see Sect. 6.3) the feasibility and applicability of an efficient and mobile acquisition strategy. In this strategy, sources and receivers have been deployed in

Fig. 6.1 Graphical sketch of the MuSaWa project. Major research goals of the four subprojects (SP) are listed



two differently sized steel rods installed using a sonic drill system (source rod, inner diameter of 7.7 cm) and a conventional DP system (receiver rod, inner diameter of 6.67 cm), respectively. As source we have used a commercial electrodynamic borehole impactor source (manufactured by Geotomographie GmbH, Neuwied), which is designed to generate horizontally polarized S-waves. However, this source generates high frequency P-waves as well. As receiver we have used a 3C borehole geophone pneumatically attached to the installed steel rod. Initial tests of this mobile acquisition system have shown that the steel rods are not capable of transmitting enough energy from the source into the surrounding ground and into the receiver rod. Especially no P-wave energy could be detected. To be able to detect P-wave and S-wave energy, we slotted the steel rods in the vicinity of the source and the receiver locations. To prevent fine-grained material to be washed into the steel rods, we sealed the slots with synthetic resin. Figure 6.2a shows a receiver gather recorded at our test site in Taucha, Germany, using steel rods without slots. S-wave energy is clearly visible whereas P-wave energy cannot be recognized. Figure 6.2b shows a receiver gather recorded using slotted steel rods for sources and receivers at the same test site. S-wave energy is clearly visible again. Although the amplitudes of P-wave arrivals are small compared to the S-waves, P-wave arrivals can be recognized and a comparison of both receiver gathers shows the improvement using the slotted source and receiver rods.

Using this mobile acquisition system based on DP and sonic drill technology with slotted source and receiver rods we were able to successfully perform several simple crosshole seismic experiments at the MuSaWa test site of Löbnitz with borehole spacings of 10 m. Figure 6.2c shows a data example of these experiments. Data quality allows for reliable determination of first-cycle onsets for P-wave and S-wave energy.

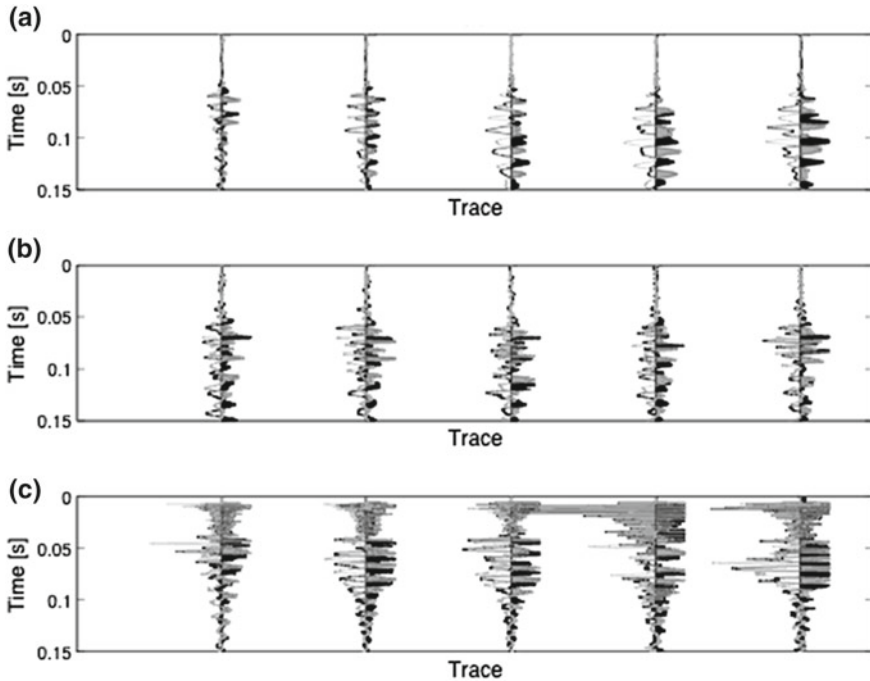


Fig. 6.2 **a** Receiver gather recorded with the mobile acquisition systems using steel rods without any modification at the test site in Taucha, Germany. S-wave energy is clearly visible whereas P-wave energy cannot be recognized. **b** Receiver gather recorded with the mobile acquisition systems using slotted steel rods at the test site in Taucha, Germany. S-wave and P-wave energy are visible, although P-wave amplitudes are quite small compared to those of the S-waves. **c** Receiver gather recorded with the mobile acquisition systems using slotted steel rods at the test site in Löbnitz, Germany. S-wave and P-wave first onset traveltimes are clearly visible

6.2.2 Fully Non-linear Joint Inversion of Tomographic Data

Usually traveltimes data sets covering the same subsurface area are inverted separately. However, joint inversion of such co-located data sets helps to reduce uncertainties and ambiguities in data analysis and interpretation. Commonly linearized inversion techniques (e.g., local search optimization methods) are used to reconstruct velocity fields iteratively. Initialization and constraints set in these techniques (e.g., initial model, enforced model smoothness) usually have a critical impact on the outcome of the inversion. To overcome the limitations of local search optimization methods, various global optimization methods have been proposed to invert seismic traveltimes data (e.g., Boschetti et al. 1996; Weber 2000). A fundamental advantage of such global optimization methods is the independency of the inversion result from the chosen initial models. Furthermore, they provide the possibility to explore the model solution space globally resulting in an ensemble of plausible solutions explaining the

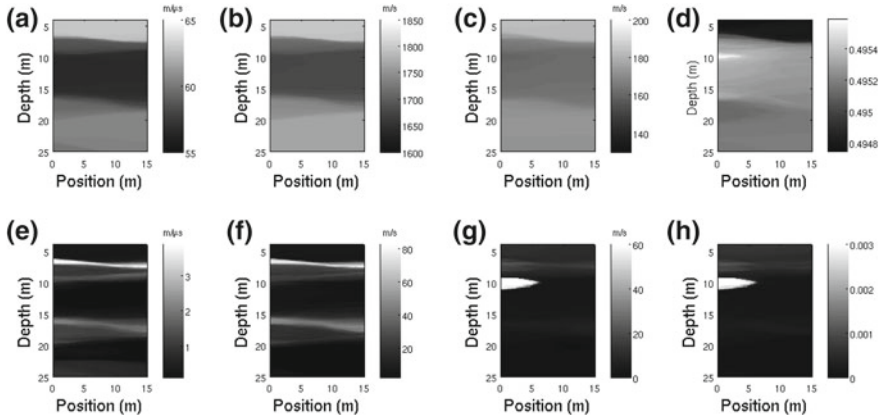


Fig. 6.3 Results of PSO based joint inversion in terms of median velocity models and further derived geotechnical parameters illustrated by median models and interquartile ranges of a final model ensemble of 125 acceptable solutions. **a** GPR median model, **b** P-wave median model, **c** S-wave median model, **d** Poisson's ratio median model computed using the whole velocity model ensemble, **e** GPR interquartile range model, **f** P-wave interquartile range model, **g** S-wave interquartile range model, **h** Poisson's ratio interquartile range model computed using the whole velocity model ensemble

data equally well. This allows for quantitative model reconstruction ambiguity and resolution appraisal (Sen and Stoffa 1995; Vasco et al. 1996). We have developed a global inversion approach (Tronicke et al. 2011, 2012; Paasche and Tronicke 2013) to jointly invert different crosshole traveltimes data sets. Our approach is based on particle swarm optimization (PSO), a global optimization technique first introduced by Kennedy and Eberhart (1995).

We demonstrate our global joint inversion approach by jointly inverting tomographic crosshole P-wave, S-wave and GPR traveltimes acquired at a well-constrained test site in Horstwalde, Northern Germany. Figure 6.3 illustrates the results of the joint inversion of P-wave, S-wave, and GPR traveltimes in terms of median and interquartile range models of an ensemble of acceptable solutions comprising 125 models. All models explain the data equally well. A clear stratification is observable in the resulting velocity models. The interquartile range is an appropriate measure to describe the spread of the underlying velocity distributions. This robust statistical measure can be used to illustrate the uncertainties in the final model ensemble. The interquartile range models show the same stratification and give us the possibility to detect areas where we have lower confidence in the final reconstructed velocity values (areas with high interquartile ranges), and which therefore might be excluded from further interpretations. These areas coincide largely with major layer boundaries.

Under the assumption that appropriate, site specific petrophysical relations linking the seismic and electromagnetic wave propagation velocities and further geotechnical parameters of interest can be formulated, these final models and their uncertainty information can be used to aid and improve geotechnical site assessment. In

particular, this would allow for quantification of errors and uncertainties in derived geotechnical parameter models. This is exemplarily illustrated in Fig. 6.3d, h for Poisson's ratio as geotechnical parameter determined from the whole ensemble of 125 P- and S-wave velocity models. Figure 6.3d shows the corresponding median model. The uncertainty information for Poisson's ratio is illustrated in Fig. 6.3h in the form of the interquartile range model.

6.3 SP 2: S-Wave Tomography—the Regional Scale

6.3.1 Test Sites, Geological Setting and Data

Experiments have been conducted at three sites; two in Germany and one in Greece. The first is in Horstwalde, located approximately 50 km south of Berlin. The second site is located close to Löbnitz, northern Saxony. At both sites the subsurface is mainly composed of quaternary sediment deposits (Lontsi et al. 2013). The very shallow subsurface down to 15 m is well known from previous geophysical investigation both in Horstwalde (e.g., Rumpf and Tronicke 2014) and in Löbnitz (e.g., Hausmann et al. 2013b). Active and passive seismic surface wave experiments have been carried out at the above mentioned sites. A 5 kg sledge hammer source and 4.5 Hz vertical geophones were used in the active experiment. Lennartz LE-3D 1 and 5 s sensors are used for the passive experiment. The third site is the Mygdonia basin in north-eastern Greece. The basin is a Neogene graben structure with significant seismic activity along distinct normal fault patterns (Hannemann et al. 2013).

6.3.2 Full H/V (f, z) Inversion

The inversion of geophysical observables for structural properties requires a model which can well explain the data and correlates with the geological formation. For the inversion of the microtremor H/V spectra, three fundamental assumptions have been made. First, we assume that the derived H/V observation curves originate purely from surface waves (Rayleigh and Love in given proportion). Second, we use a pure Rayleigh wave forward model and perform a polarization analysis on the H/V observation prior to inversion and, finally, we consider a complete modelling of the microtremor directional energy density and the inversion of the full H/V for the medium properties. The latter is more realistic as it considers energy contribution from all wave types. The theory of the microtremor H/V spectral method based on the imaginary part of the Green's function can be found in Sanchez-Sesma et al. (2011).

The full inversion is performed for frequencies of up to 10 Hz on the H/V spectral ratio computed at the test site in Horstwalde. Here, 3C borehole data are available at 12, 34, and 41 m depths, together with data recorded using a sensor at the surface.

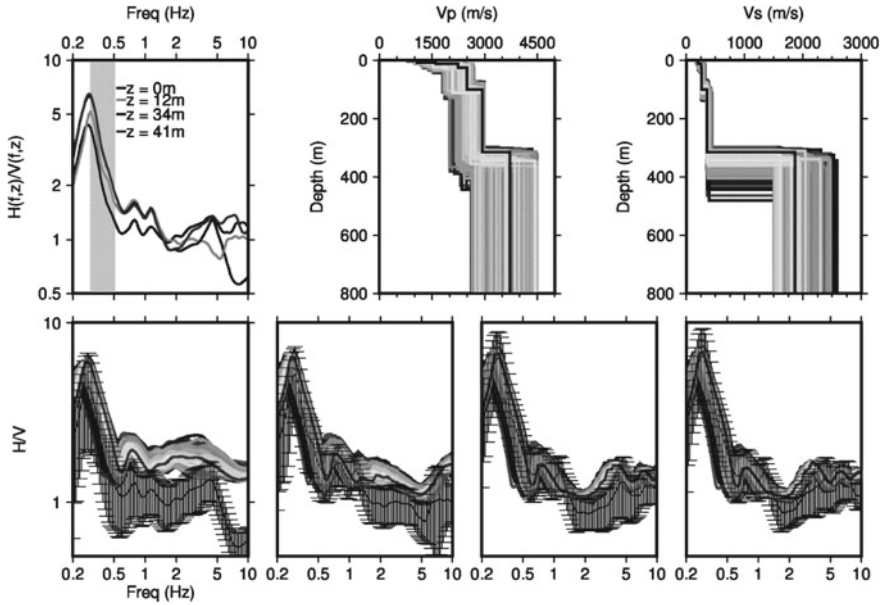


Fig. 6.4 Full H/V inversion for receivers at depth using weights (0.25, 0.25, 0.25, 0.25). The narrow grey band between 0.3 and 0.5 Hz shows the routinely inverted H/V frequency band

Inversion results (Fig. 6.4) using the neighbourhood algorithm (Wathelet 2008) and an equal weighting coefficient of 1/4 show that for frequencies between 0.1 and 1 Hz, we have good fitting of the H/V spectral curve. The overall fit of the H/V spectral shape is also observed at high frequencies for receivers at depth. The total sediment thickness is estimated to be 300 m. The general trend and fitting of the observed H/V spectral curve over a broad frequency range shows that the new theory could well be used as a standalone technique for subsurface characterization.

6.3.3 Dispersion Analysis of Active and Passive Seismic Surface Wave Data

We applied the slant stack f-k method also known as Multi-channel Analysis of Surface Waves (MASW; Park et al. 1999) to active data for determining the dispersion characteristic of the surface waves. The f-k analysis is also applied to the raw and to the cross-correlated passive data. The latter is known as interferometric MASW (IMASW; O'Connell and Turner 2011). Dispersion curves for active seismic are obtained for frequency ranging from 10 to 25 Hz.

We apply the cross-correlation to all pairs of stations in Löbnitz following the processing steps described by (Bensen et al. 2007). Daily cross-correlation Green's

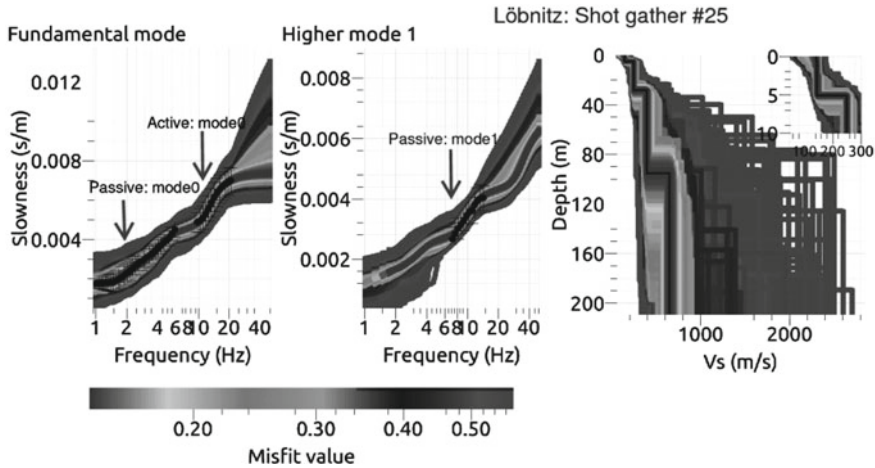


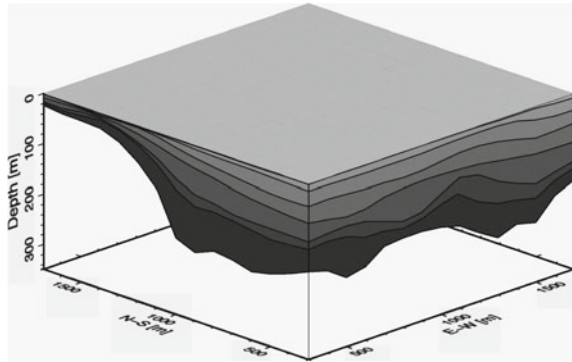
Fig. 6.5 Inversion results of active and passive seismic phase velocity dispersion curves

Function (CGF) are then stacked. Assuming a dominantly 1D medium this allows creating a virtual shot gather by sorting the CGF according to inter-station distance. We then equivalently use the MASW technique on the rearranged CGF. The dispersion analysis is performed on both the causal and acausal part and shows directivity in the signal propagation. In this study, picked dispersion curves present a high signal to noise ratio in the frequency range from 1 to 6 Hz for the fundamental mode and 6–15 Hz for the first higher mode. The picked dispersion curves are combined and inverted for the 1D Vs profile (Fig. 6.5).

6.3.4 Combined Inversion of Full Microtremor $H/V(f, z)$ Spectral Curve and Phase Velocity

We have used a non-redundant linear array configuration of six Lennartz LE-3D 1 s sensors recording at 200 Hz sampling rate over a maximum aperture of 1760 m installed at the test site in Horstwalde. Following the principle ideas of seismic interferometry we also computed long term average cross-correlation for all 15 resulting receiver pairs along the line. Assuming the equivalence of the cross-correlations with inter-station Green's functions we created a virtual linear co-array configuration with approximately 100 m inter-station spacing that allows processing the data similar to active MASW recordings. Two modes are identified with exploitable frequency range and sufficiently high signal to noise ratio between 0.3–4 Hz and 0.8–1.7 Hz for the fundamental and first higher mode, respectively. Under the assumption of a mainly horizontally layered 1D structure we further use the result of single station H/V analysis at each recording instrument at depth together with the dispersion curves to

Fig. 6.6 3D S-wave velocity model for the Mygdonian basin derived from seismic ambient noise tomography. The northern part is characterized by a shallow sediment cover dipping down to 200 m thickness in the south



invert for the S-wave velocity profile. This joint inversion advantageously uses the newly presented full microtremor theory as forward model.

6.3.5 Surface Wave Tomography in the Mygdonian Basin, Thessaloniki, Greece

At the test site in north eastern Greece, SAN were conducted by installing a permanent circular array with an aperture of 2000 m and a temporary inner circular array with 900 m aperture. The temporarily inner geometry was rotated during the SAN campaign. Both, day's and night's recordings were considered. We aim at testing the applicability of the surface wave traveltome tomography method on moderate scales and at deriving the 3D geological structure. We applied the cross-correlation technique on all receiver pairs. To the resulting CGF the multiple filter technique is applied for obtaining the Rayleigh wave group traveltome. A surface wave tomographic method that involves the use of approximate Fresnel volumes and inter-frequency smoothing constrains is used to invert the obtained traveltome data set (Hannemann et al. 2013). Dispersion curves at selected nodes are obtained and further inverted for the 3D velocity model of the basin (Fig. 6.6).

6.4 SP 3: Direct Push Based Seismic and Geotechnical Measurements

6.4.1 State of the Art

The static penetration test (also called cone penetration testing—CPT) is used for *in situ* determination of cone resistance, sleeve friction, and pore water pressure of unconsolidated sediments. These specific values enable the estimation of subsoil

lithology and the evaluation of geotechnical parameters (e.g., Lunne et al. 1997; Robertson 1990). CPT soundings are a standard DP based methodology. Considering new developments in DP technologies, *in situ*-obtained soil color was recognized as a promising novel approach for geotechnical site characterization. This DP technology can provide proxy information about the layer structure related to mineral composition and chemical state in the saturated and unsaturated zone. However, an appropriate method for processing of such data is still required.

Furthermore DP technology offers the possibility to drive a seismic P-wave source into the ground without the need for permanent installations. This has demonstrated to be a feasible method for near surface 2D determination of seismic velocity (Paasche et al. 2009).

Regarding the S-wave based 2D seismic tomography, the technical requirements of an efficient source as well as of receiver arrays practicable for DP installations have not been available for a long time (see Sect. 6.5). The application of S-wave sources and receivers practicable for DP technologies represent a current challenge extending the field of operation and the flexibility of S-wave tomography.

Besides technical issues, uncertainties exist regarding the quantitative evaluation of geotechnical parameters from seismic tomography. While seismic velocities can be determined by inversion of P- and S-wave traveltimes, there has been no quantitative evaluation tool to check the validity of seismic velocities. The consideration of *a priori* information of ground properties provided by DP technology should help to better quantify both seismic velocities and geotechnical parameters.

6.4.2 Objectives

In the frame of the overall objects of the MuSaWa project, SP 3 strives to design, further improve, and evaluate DP based measuring concepts for tomographic S-wave seismic surveys, and to deduce parameter correlations for geotechnical validation. Hence, the project work focuses in detail on (a) developing efficient and practicable geometries for acquisition of S-wave tomographic data in cooperation with SP 1; (b) optimizing post-processing and interpretation approaches of *in situ*-measuring DP-technologies, especially soil color measurements, for enhanced understanding and comparison with seismic parameters (which is needed for parameterization in SP 1 and SP 2); (c) improving the knowledge of correlations between seismic and geotechnical parameters analyzing available data; (d) evaluating measuring concepts and methods by means of field studies; and (e) acquiring *in situ* geotechnical parameters (e.g., by CPT).

6.4.3 Research Results

Within SP 3, routines for handling DP based high resolution soil color data were developed. We calculated color surrogates (e.g., chroma, brightness, etc.) and tested

(i) a moving window analysis using a smoothed mean, (ii) a cluster algorithm, and (iii) wavelet filtering for smoothing soil color data to extract depth-related information. We compared these results with CPT measurements and soil sampling logs, showing that they corresponded well with each other. We found influences of soil moisture on the brightness of the soil comparing soil moisture data and lab-samples to color logs. Soil color could be used as an indicator of *in situ* soil moisture patterns, imaging e.g., the capillary fringe and/or small-scale variations of soil moisture changes (due to high resolution measurement methods employed), which cause a decrease in luminosity. We could also successfully delineate zones of opposite chemical states (oxidative/reductive) by interpreting the occurrence of reddish and grey colors. From 1D interpretation, we were able to analyze this variation in two dimensions (cross section). Hence, *in situ*-obtained color information allowed a reliable interpretation of on-site subsurface features, such as layers. Our approach leads to an increase of information about the geological set-up providing a new understanding of soil colors as a technically reliable parameter (Hausmann et al. 2013a).

Additionally, we applied different geophysical and DP methods for geotechnical characterization of near surface sediments in view of their potential as construction ground (Fig. 6.7). A set of DP driven soundings provided high resolution vertical information, which was required for ground-truthing. In particular, we applied electrical resistivity logging, cone penetration testing, and sonic core sampling. Integrating these data with 2D geophysical methods (e.g., multi-channel analysis of surface waves (Steinel et al. 2013), electrical resistivity tomography, ground penetrating radar) improved the resulting spatial interpolation of sparse geotechnical information (Hausmann et al. 2013b). The joint interpretation of these methods allowed a characterization of the subsurface' structure. These information is essential for a detailed and reliable interpretation of the seismic results (see Sect. 6.2) and are used as site-specific knowledge for the parameterization of non-linear global inversion in SP 1 (see Sect. 6.2).

We extended the multi-offset (MO) reversed vertical seismic profiling (RVSP) tomography method (Paasche et al. 2009) by developing a mobile crosshole seismic tomographic approach enable highly flexible and economic near surface seismic P- and S-wave tomography. DP sonic drilling technology for temporary installation of steel rods was used for hosting seismic sources and/or receivers for mobile crosshole surveys (Fig. 6.8). The steel rods are sliced and sealed with synthetic resin or silicone to avoid backfill. Mobile DP devices provide the flexibility to easily access different locations and investigation depths. The results demonstrate the potential of mobile P- and S-wave tomography to be a routine application for local-scale development site exploration. The technique offered as well the possibility for measurements with the new modular multi-station borehole acquisition system, which was developed by SP 4 (see Sect. 6.5) for a combined P- and S-wave tomography using commercial seismic sources.

The subprojects results comprise spatial distributions of geotechnical parameters by joint interpretation of data sets from DP-technologies and traditional geophysical methods. Additionally we developed a new DP based mobile crosshole tomography for joint acquisition of P- and S-waves.

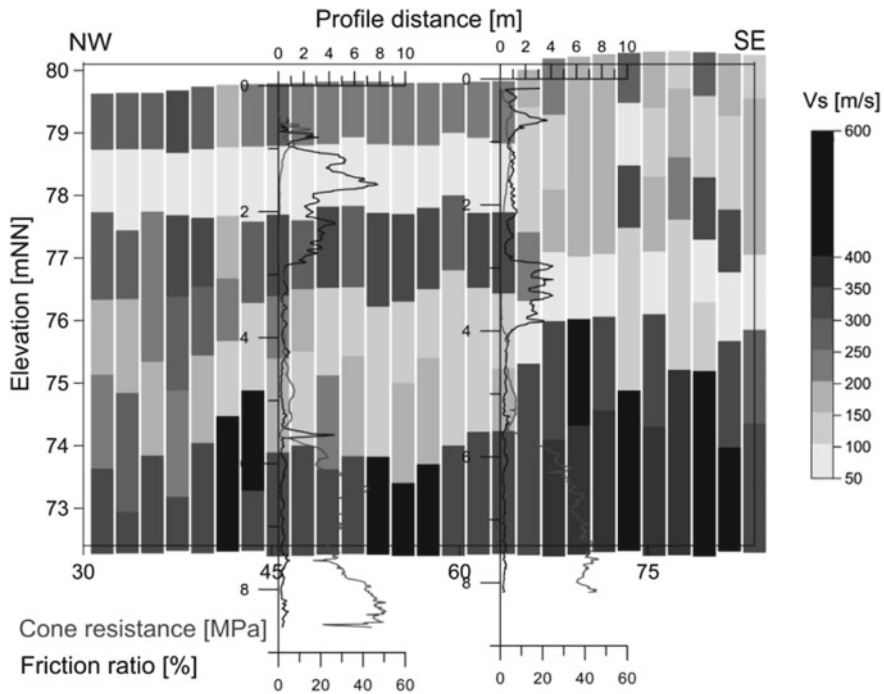


Fig. 6.7 Conjunctural plot of multi-channel analysis of surface waves, S-wave velocity (v_s) in m/s, and DP results (cone penetration testing—CPT: cone resistance and friction ratio) showing variations in near surface sediments of fluvial origin

6.5 SP 4: Instrumentation

6.5.1 State of the Art

Borehole geophones are routinely used for downhole applications. Usually, these are single receiver stations with only three geophone elements in a tri-axial arrangement. Geophone coupling is realized by pneumatic clamping through an air bladder or through a mechanical arm which presses the geophone to the borehole wall. To perform shear wave tomography one needs several 3C stations assembled to a single string to carry out the testing in an efficient way. Multi-station borehole acquisition systems for geotechnical and engineering applications in slim and shallow boreholes are not yet available. The key objective of this subproject was therefore the development of a multi-station borehole acquisition system (MBAS) for efficient recording of S-wave energy in boreholes.

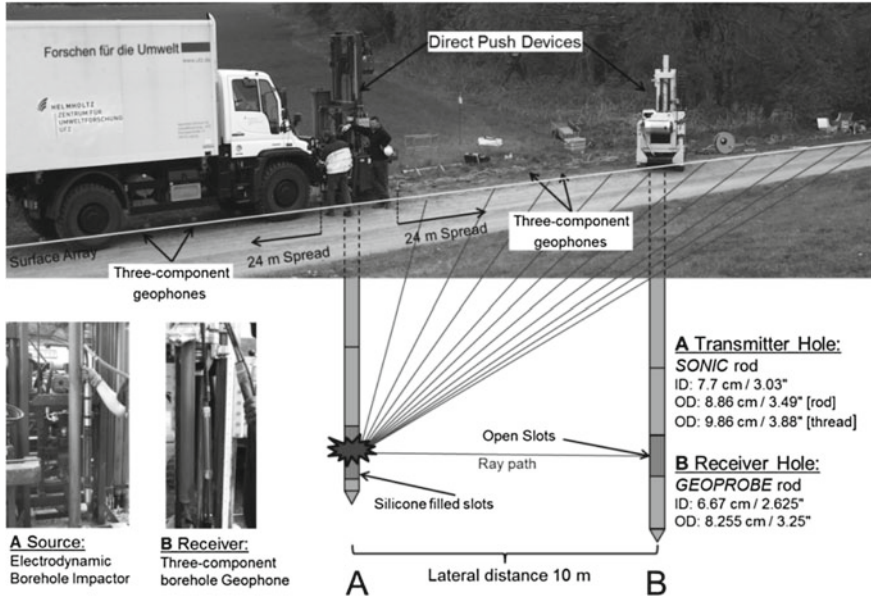


Fig. 6.8 Photograph of experimental setup overlain by conceptual sketch for DP based mobile seismic tomography. The design allows multi-offset reverse VSP with crosshole tomography operating source and borehole geophones in DP rods. These rods are sliced and sealed with synthetic resin or silicone to avoid backfill. For combined P- and S-wave tomography, 3C receivers and a commercial borehole source is used, generating compression and shear wave energy (Paasche et al. 2013)

6.5.2 Conceptual Design

The design of a multi-station borehole system needs to fulfill a few technical requirements. The most important issues are

- Three geophones per station in tri-axial arrangement
- Light weight and easy handling
- Robust coupling mechanism
- 8 or more stations per string for efficiency
- Orientation control of the stations.

In addition to technical requirements also economic aspects have to be considered to build a system on a reasonable price level. For example, a system which allows for an easy addition of stations (seismic channels) would be desirable, since potential users could start with a few stations. Later they could extend the string after their needs and budget.

Typical seismic cables offer 24 seismic channels. Thus, they would be restricted to a maximum of 8 seismic 3C stations. An extension would not be possible in this case. It was therefore decided to consider digital sensors with digital data transmission. This enables easy extension of the number of digital sensors. When using digital

receivers there is no limitation of the number of 3C stations. Furthermore, a cable for digital data transmission is light-weighted, smaller in diameter, and less expensive compared to standard seismic cables. Thus, using digital components would allow a smart design of a multi-station acquisition system by fulfilling the above mentioned general technical requirements.

The clamping mechanism of the borehole stations to the borehole wall is generally a critical technical feature. The clamping mechanism needs to be strong enough to hold the borehole geophone in position once it is clamped. The leading cable from surface needs to be tensionless to avoid mechanical interactions. As spring type clamping will not work in this case also a mechanical clamping mechanism was supposed to be too expensive and error-prone. It was therefore decided to use a pneumatic clamping mechanism, i.e., pneumatic pressure cylinders are employed. When using pneumatic pressure cylinders we can apply a high pressure rate regardless of the depth of the borehole geophones. Bottled compressed air and a simple ON/OFF valve at a pre-defined pressure level can be used to couple and decouple the borehole geophones.

The alignment of the different borehole stations with respect to each other is another critical issue to be addressed. The proper identification of S-waves requires the orientation of the sensors with respect to the strike direction of the seismic source to receive the maximum wave amplitude. Usually, orientation can be measured by using a magnetic compass. However, orientation can also be controlled if the stations are connected to each other with the same orientation. Then the orientation of the entire string could be controlled from the surface by using a hydraulic hose. Advantageously, hydraulic hoses can be coiled up on a drum but they are inflexible and stiff against torsion. This makes it feasible to rotate the downhole array to any desired direction. Therefore, we decided to use a hydraulic hose to connect the single stations as well as to connect the stations to the surface. The digital transmission cable as well as air pressure supply run within the hydraulic hose. Thus, all cables are inside the hose which offers an ideal protection against cable damages.

Digitizing seismic signals has some great advantages compared to analogue signal transmission. The crosstalk between wires is minimized to almost zero as the digitization starts right after the sensor. Slim cables with 4–6 wires only can be used instead of the big and heavy cables required for analogue transmission. Analogue standard cables are limited with regard to the number of wires they have. When using digital data transmission new channels can be easily connected. The only requirement is the assignment of a new ID to them so that they can be identified by the main digital unit. The considered design is sketched in Fig. 6.9.

Components for digitization of the seismic signals were developed in cooperation with the Italian company Micromed. This company is specialized in designing medical equipment for scanning bodies and do have long term experiences in digitizing electrical signals at lowest voltage levels. Micromed also started to make digital seismic equipment over the past years. Thus, it was agreed to develop and re-design existing digital boards to meet the requirements for borehole surveys. Mainly, the sampling rate, the dynamic range as well as stacking and triggering options needed to be modified. Major technical specifications are given in Table 6.1.

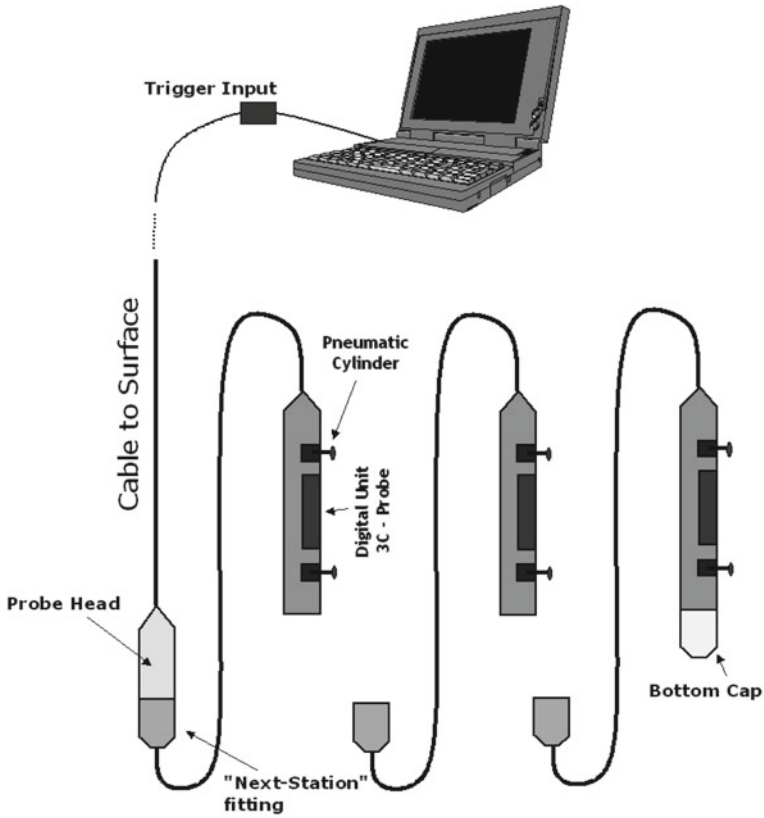


Fig. 6.9 Schematic sketch of the multi-station borehole acquisition system

Table 6.1 Technical specification of the digital multi-station borehole acquisition units

Specification	Realization
Weight	3 kg per station
Voltage	3.3 V (PC USB interface)
Geophones	SM11 (30 Hz)
Seismic channels	3 geophones per station
A/D conversion	24 bit @ 128 Hz
Sample rate	256, 512, 1024, 2048, 4096, 8192, 16384, 32768 Hz
Stacking	Plus/minus option on every stack
Trigger	TTL or channel

6.5.3 Field Testing

A field experiment has been conducted in November 2012 at the test site for Technical Safety (TTS) of the Federal Institute for Materials Research and Testing (BAM) in

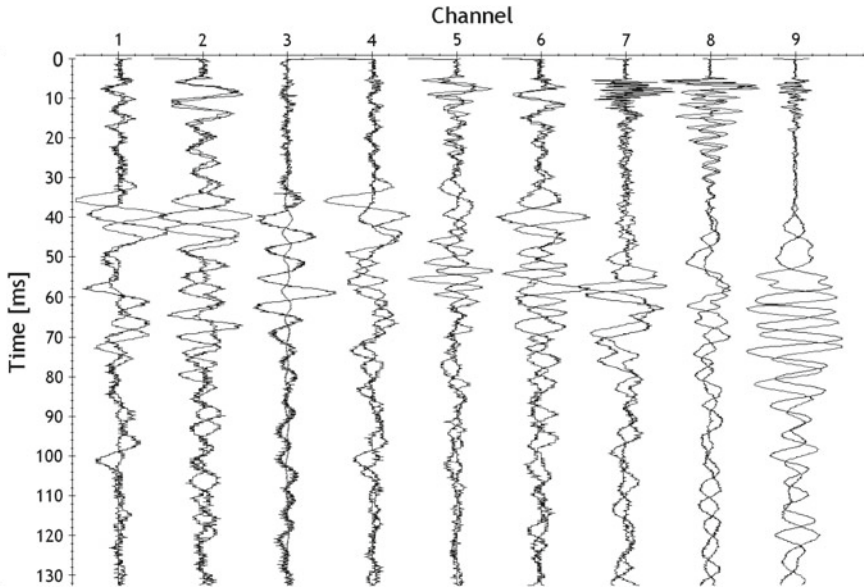


Fig. 6.10 Example record of the MBAS field experiment at the Horstwalde test site

Horstwalde, located approximately 50 km south of Berlin. The test was carried out as a crosshole test with boreholes separated around 5 m. Borehole BL2/08 was used as the receiver borehole and the MBAS prototype was placed at depth ranging from 10.5 to 22 m. Station spacing of the three-station MBAS was 2 m. The source borehole was made by sonic drilling as described under SP1 (see Sect. 6.2.1). Inside the borehole the BIS-SH shear wave source was placed to generate horizontally polarized S-waves. The sampling rate of the MBAS was set to 8 kHz and recording length was 250 ms. An example shot of the survey is shown in Fig. 6.10. Nine channels are displayed whereas CH1 to CH3 belong to the bottom station, CH4 to CH6 to the middle station, and CH7 to CH9 to the upper station. The S-wave and P-wave arrivals are clearly visible. The P-wave arrives at approximately 3 ms and the S-wave arrives at about 30 ms.

6.5.4 Results and Conclusions

A digital multi-station borehole acquisition system was built as a prototype system consisting of three 3C stations. The MBAS is fully digital and comes with a direct USB connection, i.e., no seismograph is needed. The MBAS can be oriented from the surface using a hydraulic hose which is stiff against rotation but can be coiled up on a drum for transportation. The system capacity in terms of digital seismic channels

is almost unlimited. Anyhow, due to the station weight of approximately 3 kg only a limited number of stations could be manageable.

The system has been tested at different field sites and proven to be reliable. Results from the Horstwalde test site show excellent seismic data quality and clear S-wave arrivals.

6.6 Conclusions

Near surface P- and S-wave tomography has the potential to enhance geotechnical site characterization. Within the MuSaWa project we developed highly mobile P- and S-wave tomographic acquisition technologies solely using DP technology instead of boreholes. This allows for highly flexible acquisition of local-scale and high resolution crosshole seismic tomographic data sets at irregular DP injection locations. A newly developed modular multi-station acquisition system allows for efficient acquisition of seismic crosshole tomographic data. Full digitization of the system guarantees high signal quality and easy operation, i.e., without additional use of a seismograph. DP technology has been employed to advance ground-truthing of seismic tomographic data. For example, a new soil color sensor allows for *in situ* high resolution assessment of sediment stratigraphy. Processed soil color logging data improve interpretation of seismic velocity tomograms. Furthermore, DP logging data support the setup of optimal model parameterizations essential for an efficient fully non-linear inversion of P- and S-wave tomographic data sets. We used particle swarm optimization to realize a joint global inversion of various crosshole tomographic traveltimes data sets. The resultant ensembles of acceptable velocity models fitting the underlying data equally well have been used for further geotechnical site characterization and quantitative model uncertainty appraisal. Full H/V(f, z) inversion of seismic energy recorded at the surface and in boreholes as well as the combination of active and passive surface wave experiments enables a more accurate assessment of regional S-wave velocity distributions. This approach covers exploration depths beyond standard near surface active seismic tomography.

Acknowledgments The project MuSaWa is part of the R&D programme GEOTECHNOLOGIEN and is funded by the German Ministry of Education and Research, grant 03G0745.

References

- Atkinson JH (2000) Non-linear soil stiffness in routine design. *Geotechnique* 50:487–508
- Bensen GD, Ritzwoller MH, Barmin MP, Levshin AL, Lin F, Moschetti MP, Shapiro NM, Yang Y (2007) Processing seismic ambient noise data to obtain reliable broad-band surface wave dispersion measurements. *Geophys J Int* 169:1239–1260
- Boschetti F, Dentith MC, List RD (1996) Inversion of seismic refraction data using genetic algorithms. *Geophysics* 61:1715–1727

- Dietrich P, Leven C (2006) Direct push-technologies. In: Kirsch R (ed) *Groundwater geophysics: a tool for hydrogeology*. Springer, Heidelberg
- Fahay M (1998) Deformation and in situ stress stress measurements: geotechnical site characterization. In: *Proceedings of the 1st international conference on site characterization*, vol 1, pp 49–68
- Hannemann K, Papazakos C, Ohrnberger M, Savvaidis A, Anthzmidis M, Lontsi AM (2013) 3D shallow structure from high-frequency ambient noise tomography: new results for the Mygdonian basin-Euroseistest area. *J Geophys Res* (Submitted). Northern Greece
- Hausmann J, Dietrich P, Vienken T, Werban U (2013a) Enhanced direct push based characterization of the near surface using in-situ gained soil colours. In: *Proceedings AquaConSoil 2013*
- Hausmann J, Steinel H, Kreck M, Werban U, Vienken T, Dietrich P (2013b) Two-dimensional geomorphological characterization of a filled abandoned meander using geophysical methods and soil sampling. *Geomorphology* 201:335–343
- Kennedy J, Eberhart RC (1995) Particle swarm optimization. In: *Proceedings of the IEEE international joint conference on neural networks*, 1942–1948
- Lehmann B (2007) *Seismic traveltime tomography for engineering and exploration applications*. EAGE Publications, Houten
- Lontsi AM, Ohrnberger M, Krüger F, Rumpf M, Hausmann J (2013) Sediment deposit characterization using active and passive seismic surface wave data. In: *Proceedings of the 4th international geoscience student conference*, Berlin
- Lunne T, Robertson PK, Powell JJM (1997) *Cone penetration testing in geotechnical practice*. Taylor & Francis, London
- Paasche H, Ohrnberger M, Werban U, Fechner T, Tronicke J, Krüger F, Dietrich P (2011) Multi-scale S-wave tomography for exploration and risk assessment of development sites (MuSaWa). In: Münch U (ed) *Tomography of the Earth's crust - from geophysical sounding to real-time monitoring*, Geotechnologien Science Report 18. Koordinierungsbüro Geotechnologien, Potsdam
- Paasche H, Rumpf M, Hausmann J, Fechner T, Werban U, Tronicke J, Dietrich P (2013) Advances in acquisition and processing of near-surface seismic tomographic data for geotechnical site assessment. *First Break* 31:59–65
- Paasche H, Tronicke J (2013) Global joint inversion of tomographic data - appraisal of model reconstruction ambiguity. In: *Proceedings of the 19th meeting of environmental and engineering geophysics - near surface geoscience 2013*, WES2b09
- Paasche H, Werban U, Dietrich P (2009) Near-surface seismic traveltime tomography using a direct-push source and surface-planted geophones. *Geophysics* 74:G17–G25
- Park CB, Miller RD, Xia J (1999) Multi-channel analysis of surface waves. *Geophysics* 64:800–808
- O'Connell DRH, Turner JP (2011) Interferometric multichannel analysis of surface waves (IMASW). *Bull Seismol Soc Am* 101:2122–2141
- Robertson PK (1990) Soil classification using the cone penetration test. *Can Geotech J* 27:151–158
- Robertson PK, Sasitharan S, Cunning JC, Segs DC (1995) Shear-wave velocity to evaluate in-situ state of Ottawa sand. *J Geotech Eng* 121:262–273
- Rumpf M, Tronicke J (2014) Predicting 2D geotechnical parameter fields in near-surface sedimentary environments. *J Appl Geophys* 101:95–107
- Sanchez-Sesma FJ, Rodriguez M, Iturraran-Viveros U, Luzon F, Campillo M, Margerin L, Garcia-Jerez A, Suarez M, Santoyo MA, Rodriguez-Castellanos A (2011) A theory for microtremor H/V spectral ratio: application for a layered medium. *Geophys J Int* 186:221–225
- Sen MK, Stoffa PL (1995) *Global optimization methods in geophysical inversion*. Elsevier, The Netherlands
- Steinel H, Hausmann J, Werban U, Dietrich P (2013) Reliability of MASW profiling in near-surface applications. *Near Surf Geophys* (Submitted)
- Tronicke J, Paasche H, Böniger U (2011) Joint global inversion of GPR and P-wave seismic traveltimes using particle swarm optimization. In: *Proceedings of the 6th international workshop on advanced ground penetrating radar (IWAGPR)*

- Troncke J, Paasche H, Böniger U (2012) Crosshole travelttime tomography using particle swarm optimization: a near-surface field example. *Geophysics* 77:R19–R32
- Vasco DW, Peterson JE, Majer EL (1996) Nonuniqueness in travelttime tomography: ensemble inference and cluster analysis. *Geophysics* 61:1209–1227
- Wathelet M (2008) An improved neighborhood algorithm: parameter conditions and dynamic scaling. *Geophys Res Lett* 35:L09301
- Weber Z (2000) Seismic travelttime tomography: a simulated annealing approach. *Phys Earth Planet Inter* 119:149–159

Chapter 7

Seismic Tomography and Monitoring in Underground Structures: Developments in the Freiberg Reiche Zeche Underground Lab (Freiberg, Germany) and Their Application in Underground Construction (SOUND)

Stefan Lüth, Thomas Bohlen, Rüdiger Giese, Sven Heider, Silke Hock, Stefan Jetschny, Ulrich Polom, Sonja Wadas and Aissa Rechlin

Abstract The construction of large tunnels and underground infrastructures faces increasingly large dimensions and complex geological conditions. Under these conditions, exploration techniques are needed which enable for a detection of potentially hazardous structures during construction. Seismic sensors, integrated into rock anchors, and small seismic signal sources using defined pneumatic impulses or sweep signals generated by magnetostrictive actuators are the components of an exploration system which can be easily integrated into different types of underground excavation work and which can also be deployed for the long-term monitoring of already existing tunnels or caverns. However, for a continuous acquisition of seismic signals during tunnel excavation, the strong and broadband signal generated by a tunnel boring machine (TBM) may be used as a continuously operating source. Within the collaborative project SOUND, the seismic equipment at the Underground Lab of the Reiche Zeche Research Mine in Freiberg (Germany) has been used for a tomographic monitoring study during the excavation of an inclined gallery. A synthetic, but realistic seismic data set was simulated using a randomly heterogeneous velocity model which can be regarded as a realistic prototype of the velocity distribution in

S. Lüth (✉) · R. Giese
GFZ German Research Centre for Geosciences, Potsdam, Germany
e-mail: slueht@gfz-potsdam.de

T. Bohlen · S. Heider
Karlsruhe Institute for Technology (KIT), Karlsruhe, Germany

S. Hock
Regierungspräsidium Freiburg, Freiburg, Germany

S. Jetschny
Petroleum Geo-Services (PGS), Oslo, Norway

U. Polom · S. Wadas
Leibniz Institute for Applied Geophysics (LIAG), Hannover, Germany

A. Rechlin
TU Berlin, Berlin, Germany

the real Gneiss block. The simulated acquisition geometry has been derived from the actual source and receiver point distribution in the Underground Laboratory. It can be shown that the analysis of the modelled seismic data by full waveform inversion (FWI) was able to reveal the lateral heterogeneity of the velocity model with significantly higher resolution compared to traveltimes tomography of the direct P-wave arrivals. The analysis of field data from the Underground Laboratory has shown that there are complex interactions in close vicinity to the receiver location, and before FWI can be applied to this real data set, source and receiver dependant signatures need to be removed by inversion and deconvolution. A further field experiment, performed during gallery excavation in the Underground Laboratory, has shown that the setup of seismic receivers in rock anchors and a sparse array of adaptive vibro-sources is able to detect subtle changes in seismic wave propagation related to stress changes due to the excavation of an inclined gallery. After the deployment in the Underground Laboratory, a field survey was carried out on a tunnel construction site. A broadband seismic data set, using the tunnel boring machine could be acquired providing a basis for high resolution imaging of structures ahead of the construction site and geotechnical characterization of the imaged volume.

7.1 Introduction

Tunnelling and underground construction have been dynamically growing engineering fields in the past decades. Tunnels and underground structures, such as caverns, are currently under construction or being planned which are characterized by increasing dimensions. As an example, the Gotthard Base Tunnel, which is scheduled to become available for public use in 2016, consists of two tubes of 57 km length each (Alptansit 2013). The tunnel's transect runs through a geologically complex area characterized by rock mass units of highly variable stability (Loew et al. 2000). Underground construction under such conditions poses particular challenges for the exploration before and during excavation. Additionally, an increasing demand for long-term safety of the construction, especially for traffic infrastructure, requires monitoring solutions providing data on potentially dangerous changes in the stability of the rock masses supporting the tunnel (Lang et al. 2009).

In order to support excavation in complex geological settings, seismic exploration was performed on the construction site of Gotthard Base Tunnel using a system of seismic receivers in rock anchors and seismic source signals generated with explosives (Dickmann and Sander 1996). At a later stage of the project, seismic surveys were performed along a gallery in order to explore the rock mass quality for the *Multifunktionsstelle* (MFS) Faïdo, a cavern along the Base Tunnel with large diameter. Here, a system consisting of a pneumatic hammer as a seismic source and rock anchors as seismic receivers was applied (Giese et al. 2006).

The seismic exploration systems used here consist of mobile components which are typically deployed on construction sites for specific campaigns covering a small portion of the construction project. There is currently only one seismic exploration

system available which is integrated in the cutter head of tunnel boring machines (TBM) and which is mainly applicable in soft soil tunnelling in water saturated underground (Kneib et al. 2000).

As an alternative to seismic surveys along the tunnel construction site using mobile sources or explosives, the vibrations generated by the cutter head of a TBM may be used as a seismic signal. In this scenario, a continuous exploration ahead of the construction is possible which potentially can provide enhanced predictions for fault zones, fractured rock mass units or other risks for the construction. This approach has been described as *Tunnel Seismic While Drilling* (Petronio and Poletto 2002; Brückl et al. 2008). Previous pilot surveys were performed using an acquisition scheme inspired by the *Seismic While Drilling* method applied during the drilling of boreholes (Poletto and Miranda 2004). This means that, while the source (the drill-bit, or the cutter head of a TBM) is approaching the object of investigation, seismic receivers are positioned typically at a few hundred metres distance from the source (and the rock mass under investigation) resulting in a relatively low dominant frequency in the acquired seismic signals.

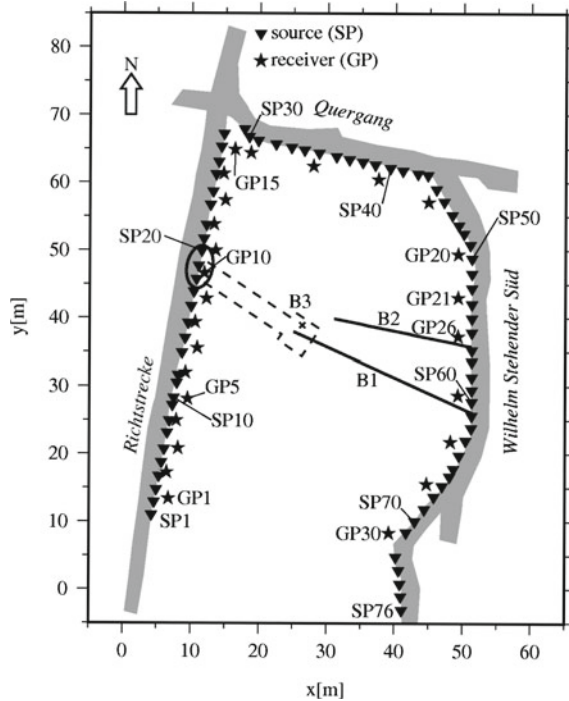
In the study presented here, we make use of the enhanced flexibility in the design of seismic acquisition by the use of seismic receivers integrated in (removable) rock anchors. This allows for previously unreached high-frequency (and thus high resolution) data acquisition. The technology is applied in the GFZ-Underground Lab in the research and education mine *Reiche Zeche* in Freiberg in order to investigate its potential for monitoring rock mass units, and in an active tunnel excavation in order to investigate its applicability for exploration while tunnelling. The field work is complemented by investigations on the Full Waveform Inversion of tomographic data acquired under the very specific conditions of underground construction. The feasibility of tomographic inversion is shown using synthetic seismic data, and the specific challenges of field data acquired in the underground are discussed.

7.2 Infrastructure at the GFZ-Underground Lab

The GFZ-Underground Lab is situated 150 m below surface on the first floor in the research and education mine *Reiche Zeche* of the Technical University of Freiberg in Germany. The *Reiche Zeche* is located in the eastern part of the *Erzgebirge* Mountains within the *Innerer Freiburger Gneis* (interior *Freiberger* gneiss), an augen-structured, high-grade biotite gneiss (Sebastian 2013). In the mine silver, lead and zinc were mined from the middle of the 14th century until 1969. During the 1980s the mine was reconstructed and prepared for research and educational purposes.

Surrounded by three galleries, the measuring site of the GFZ-Underground Lab (GFZ-ULab) comprises a gneiss block of 50 m width and 80 m length (Fig. 7.1). Two horizontal 8 1/2" boreholes (B1 and B2) of 30 and 20 m length were drilled into the measuring plane. In 2011 the GFZ-ULab was extended by an incline with a dip of 40° and a cubic shaped chamber with 5 m edge length 10 m above the galleries. From

Fig. 7.1 Top view of the GFZ-ULab, the seismic receiver locations are marked by stars, the source locations by inverted triangles. The encircled source locations (SP18-SP20) and receiver location (GP10) get lost due to excavation of incline and chamber. The *dashed line* marks the projection of incline and chamber into the measuring plane and the *x* depicts the penetration point of the vertical borehole B3 (Krauß 2013)



there a 70 m 8 1/2'' vertical borehole (B3) was drilled through the gneiss block. All boreholes are open and completely cored.

For the transportation of equipment all galleries and the incline are equipped with rail tracks. A winch can pull material up- and downward the incline or move borehole probes in the vertical borehole, respectively. The GFZ-ULab also comprises a workshop with telephone and internet connections.

For data recording up to thirty-five 3-component (3C) geophone anchors can be mounted along the galleries in one and two meter deep boreholes with a distance of 4–9 m from each other (Fig. 7.1). These receivers are connected either with wireless data loggers or cables to transmit the data to a host computer for data quality control and preliminary processing.

7.3 Seismic Experiments: Source and Receiver System for Underground Surveys

The GFZ runs the underground test site in order to examine new seismic exploration technologies for tunneling and borehole drilling as well as for monitoring techniques of underground constructions. Different imaging techniques like 3-component Kirchhoff-Migration or Fresnel-Volume-Migration are tested and modified with

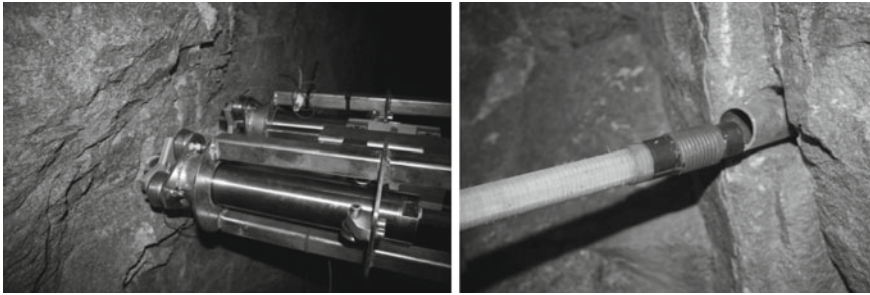


Fig. 7.2 Vibrator source (*left*) and geophone-anchor receiver (*right*) applied during tomographic measurements in April 2012. The vibrator source comprises two magnetostrictive actuators with a spacing of 28 cm. The receiver anchor in the right picture has a thread-shaped head comprising the three 1C-geophones in axial, vertical and horizontal direction. The receiver anchor is to be screwed into the respective threaded tube which is glued into a borehole. The geophones have always the same orientation and the same coupling conditions

respect to their capability to resolve small-scale structures within the gneiss block. The galleries also act as potential seismic reflectors for the seismic imaging. The major challenge of seismic imaging in the underground is the spatial ambiguity of the recorded wave field due to limited aperture of seismic source and receiver survey geometry.

Since 2009, a further focus of investigation has been on tomographic inversion techniques, e.g. the application of attenuation tomography (Krauß 2013) and the full waveform inversion method (Heider et al. 2012). The task is to detect and to locate changes of rock conditions while drilling and construction works within the GFZ-ULab have been undertaken. An alternative approach to identify changes of rock condition is the application of coda wave interferometry (Sens-Schönfelder et al. 2011).

The lab is also used to test newly developed seismic system components, e.g. receivers and sources. Different geophones, piezoelectric sensors and optical receivers were tested and compared with respect to their signal amplitude, signal phase characteristics and signal-to-noise ratio. Other objectives of these measurements were to study the influence of near surface conditions, different glues as well as mechanical coupling techniques on the signal quality on the gallery surfaces and in boreholes. Finally, a removable mechanical coupling system for 3-component receivers in boreholes was developed, successfully tested and installed at the GFZ-ULab. This is the patent-registered ISIS (Integrated Seismic Imaging System)-geophone anchor system (Borm et al. 2007) ensuring a high repeatability of seismic measurements. The receiver system consists of a tube which is glued in boreholes by a two-component-epoxy-resin and a removable geophone anchor rod (Fig. 7.2 right). The tube is equipped with a thread at the interior end into which the thread shaped head of the geophone anchor can be screwed. This ensures reproducible coupling of the three orthogonally assembled geophones. GS14-L3 geophones with a resonance frequency of 28 Hz are used as seismic sensors for the ISIS receiver anchors.

GFZ-developed pneumatically driven impact hammers and magnetostrictive vibrators (partially in collaboration with Leibniz Institute for Applied Geophysics, Hannover), and these were successfully tested as seismic sources. The impact hammer incorporates a pneumatic cylinder. The power for the impacts is supplied by pressurized air accelerating a moving mass of 5 kg. Each impact takes 1 ms and is triggered by a Programmable Logic Controller. The hammer can shoot with 5 s minimal interval. The hammer source is pre-stressed to the rock surface to achieve a good coupling. It can be operated in all directions. It is mounted either directly on a TBM or other machinery. In crystalline rocks the hammer transmits pulses with frequencies up to 2000 Hz. The small error in triggering time of less than 0.1 ms allows together with the reliable repeatability of the transmitted signals the application of vertical data stacking to improve signal-to-noise ratio. The pneumatic hammer was successfully applied during tomographic measurements in the Gotthard Base Tunnel, Switzerland (Giese et al. 2006).

For more than 10 years magnetostrictive actuators have been in use as seismic sources at the GFZ. The magnetostrictive actuators use the ferromagnetic alloy Terfenol-D composed of Terbium, Iron, and Dysprosium (produced by Etrema Products Inc.) which changes its shape in a magnetic field. The vibrator source applied for the tomographic measurements in the GFZ-ULab consists of two actuators (Fig. 7.2). Each actuator has a diameter of 63.5 mm and a length of 380 mm. Its weight is 5.6 kg. The actuators are manufactured to perform as synchronously as possible. To ensure the constructive interference of both actuator signals a real-time control system defines amplitude and phase of the source signals using the registrations of piezoelectric sensors integrated in the coupling stamps. For each sweep the source signal (pilot signal) given by the control device is stored and later used for correlation of the raw data. For hard rock applications exploration distances of about one hundred meters can be achieved operating with three seconds linear frequency sweeps in the frequency range 100–3000 Hz.

Major progress during the development of the control technique for the magnetostrictive actuators has allowed the simultaneous control of signal amplitudes and phases of up to four vibrators. Based on this technique a prototype of a phased array borehole source has been developed and tested in two horizontal boreholes of the GFZ-ULab (Jaksch et al. 2010).

7.4 Full Waveform Inversion of Vibroseis Data Acquired in the GFZ-ULab: Synthetic Modelling and Challenges of Real Data

7.4.1 Motivation

Using the infrastructure at the GFZ-ULab, multi-component vibroseis measurements were performed in order to explore the potential of adjoint time-domain Full

Waveform Inversion (FWI) in crystalline rock. The FWI is an iterative minimization method to reduce the difference between computed and observed wavefields. FWI has the potential to use the full information content of multi-component seismograms and leads to a significantly higher resolution of elastic rock properties. The challenges in the GFZ Underground Lab are (1) the pre-processing and incorporation of the vibroseis data into the FWI workflow and (2) strong small-scale medium heterogeneities within the crystalline rock mass, especially close to the receivers.

Nowadays, FWI is becoming an established method in both science and industry to recover highly resolved velocity models of the subsurface. However, most of the published applications until today apply acoustic FWI for marine environments with mostly layered sedimentary structures of moderate heterogeneity and excellent coupling of marine sources and receivers (Virieux and Operto 2009). Here, first attempts are shown applying elastic FWI to multi-component vibroseis land data acquired in a highly heterogeneous crystalline environment. Vibroseis sources allow for a regulation of excited frequencies and energy which is quite crucial for FWI where especially low frequencies are of importance to avoid the method to get trapped into a local minimum. Furthermore, multi-component receivers may allow for a better discrimination between P- and S-waves and inherently contain information on the angles of incidence.

In this report, we first present a synthetic study to demonstrate the improved resolution of FWI for crystalline rocks. We then describe a deconvolution method to obtain the transfer functions for each source and each receiver. This turned out to be an important pre-processing step for a successful application of FWI in underground crystalline environments.

7.4.2 The FWI Method

FWI aims to minimize the misfit between modelled and observed seismograms. This can be implemented efficiently using a conjugate gradient approach (Tarantola 1984; Mora 1987). The adjoint-state method enables to calculate the gradient of the misfit function as zero-lag cross-correlation between a forward propagated wavefield and a wavefield propagated back from the receivers into the medium. The time-domain 2-D elastic FWI code developed by Köhn (2011) is used, which is available under the terms of GNU GPL at <http://www.opentoast.de>. For the inversion of crystalline host rock vibroseis data this code was further enhanced by implementing different misfit definitions and especially a source wavelet inversion. The source wavelets are estimated by a stabilized deconvolution of the recorded data with the simulated data for the current subsurface model.

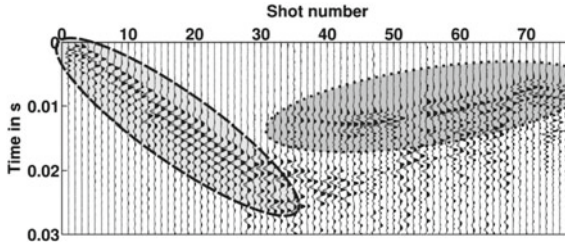


Fig. 7.3 Correlograms of the X-component of a common receiver gather (CRG) for Receiver 1 (GP1 Fig. 7.1). The traces are normalized. The dominant wave type is the tunnel-surface wave for shot numbers below 28 (highlighted by a *dashed ellipse*). Shot numbers above 36 show the transmitted P-wave as first arrival (highlighted with a *dotted ellipse*)

7.4.3 Synthetic Case Study

To explore the possible resolution of FWI in the Freiberg underground environment, the FWI workflow is first tested with synthetic data. This simulated scenario is very close to the real measurements in the GFZ-Underground Lab. 76 shot positions with an average spacing of 2 m and 30 receiver positions around the three galleries were simulated (Fig. 7.1). Because of the almost plane transmission geometry of sources and receivers, the 2-D elastic FWI method was chosen.

To get a better understanding of the involved wavefields, in Fig. 7.3 trace-normalized correlograms of a common receiver gather (CRG) for Receiver 1 (GP1 in Fig. 7.1) in Fig. 7.3 are shown. The dominant wave type recorded close to the source is the tunnel-surface wave. For the shots on the opposite side of the *Freiberger Gneis* the first arrivals mainly represent the direct P-wave. For shot numbers 36 to 41 and particularly 51 to 54, due to the radiation pattern of the vibro-source, enhanced shear-wave amplitudes were recorded by receiver 1, and therefore, due to trace normalization, apparently weaker direct P-wave arrivals were observed from these shotpoint locations.

Using the 2-D elastic forward modelling performed during the FWI, the tunnel surface wave could not be simulated properly (Jetschny et al. 2010). We thus restricted the FWI to the directly transmitted P-waves highlighted in Fig. 7.3. A time window around the direct P-wave was applied in order to suppress later phases. Additionally, traces were normalized to their maximum amplitude before being fed into the FWI (Sheng et al. 2006).

The *Freiberger* Greygneiss exhibits heterogeneities on all scales and can be best approximated by a so-called random medium model. We chose a correlation length of 10 m and a Gaussian velocity distribution with a standard deviation of 5 %, and an average P-wave velocity of 6000 m/s (Kneib 1995). The S-wave velocity model is calculated via $v_s \approx v_p/\sqrt{3}$. The density model was kept constant at 2550 kg/m³. The starting model was obtained by traveltime tomography of the transmitted P-waves. The model update was only allowed within the gneiss block.

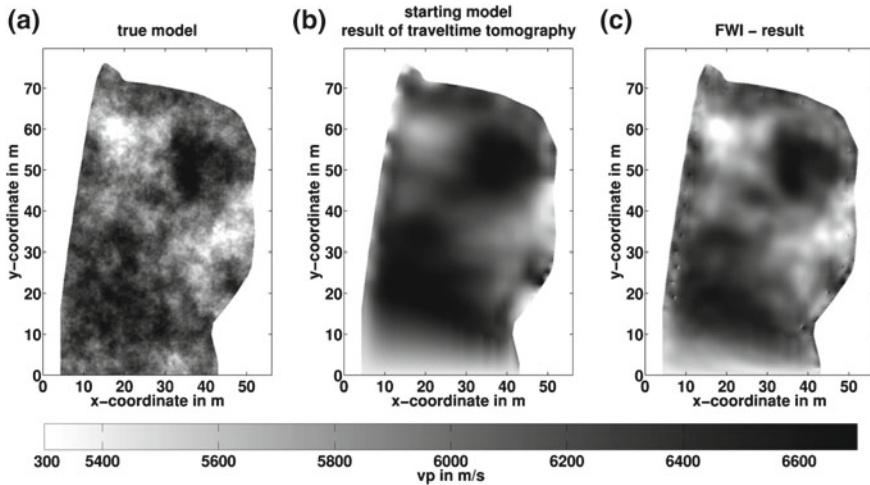


Fig. 7.4 Synthetic case study. Comparison of P-wave velocity models. **a** True model: Random media model which simulates the crystalline host rock. **b** Starting model derived from a first arrival traveltimes tomography. **c** Elastic FWI result using a Klauder wavelet below 750 Hz

In our first synthetic study we used a Klauder wavelet as the source time function extracted from the field data and filtered it with a Butterworth lowpass filter of 750 Hz. The required 74 iterations of the FWI took 12 h on 96 cores.

In Fig. 7.4 the true model, the starting model obtained by a traveltimes tomography, and the FWI result are compared. Note the significantly increased resolution of the model obtained by the FWI.

7.4.4 Field Data Application and Its Challenges

In the synthetic example, the source signal was assumed to be known and a perfect coupling of sources and receivers was postulated. Further, no unknown small-scale heterogeneities (fractures, tunnel surface topography) in the vicinity of the sources and receivers were taken into account. These assumptions are invalid for real field measurements. Especially at the receivers a site response which differs significantly for each receiver location can be observed. Previous studies and test measurements revealed that the receiver coupling was likely caused by small-scale heterogeneities such as fractures or local tunnel wall topography in the immediate vicinity of the receivers (Maurer et al. 2011). Each three component geophone was mounted on a 1 or 2 m long standard rock anchor that is drilled into the formation. During the drilling of the borehole, small-scale fractures around the anchor and the geophone at their tips may be generated. The drastic effect of the small-scale heterogeneities close to the receivers on the recorded transmitted P-waveforms can be studied in Fig. 7.5a.

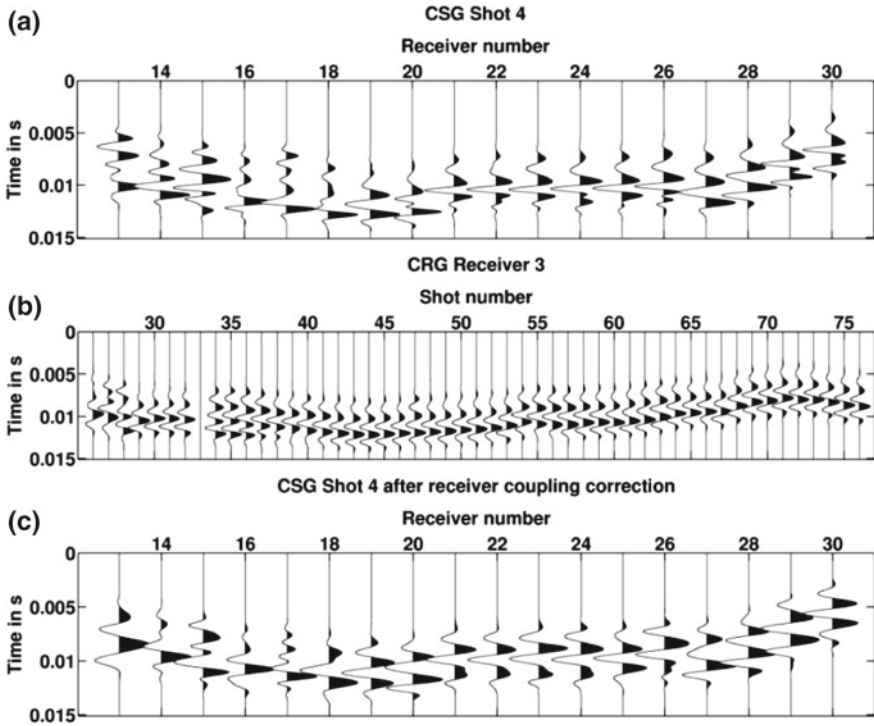


Fig. 7.5 **a** Exemplary Common Shot Gather (CSG) and **b** Common Receiver Gather (CRG) of the correlated vibroseis field data. **c** Same CSG as in **a** after the correction of the receiver coupling

Note that the site effect is mainly observed on the receiver side, i.e. in the common shot gathers. The common receiver gather shows relatively coherent P-wave forms for each shot indicating a good reproducibility of the vibroseis source for different shot locations (Fig. 7.5b).

From Fig. 7.5 it is obvious that an inversion and correction of the receiver coupling is required for FWI. The approach is similar to iterative source time function deconvolution introduced by Pratt (1999) for common-shot gathers which is generally required in field data applications. Here the deconvolution approach is applied to common-receiver gather to remove the effects of small-scale heterogeneities close to the receivers (Maurer et al. 2011). In this approach the least squares misfit function for each frequency w in the Fourier-domain

$$s(w) = \frac{\mathbf{u}^t \cdot \mathbf{d}^{conj}}{\alpha + \mathbf{u}^t \cdot \mathbf{u}^{conj}} \quad (7.1)$$

is minimized, where vector \mathbf{u} denotes the synthetic data and the vector \mathbf{d} the field data of a common-receiver gather. The superscript t is the transpose operator and

conj means the complex conjugated. α is a water-level parameter which is necessary for a stable deconvolution to avoid small values in the denominator.

The gained filter functions for the receivers are then convolved with the field data (Fig. 7.5c) in the time domain. In contrast to a source time function inversion, the field data is fitted to the synthetic data because the synthetics are free of any receiver effects. In Fig. 7.5c the same common shot gather (CSG) as in Fig. 7.5a is shown after the receiver coupling correction. The coherence of the waveforms has been improved and the receiver coupling effect is eliminated.

7.5 Monitoring of Excavation Using a Permanent Seismic System Installation

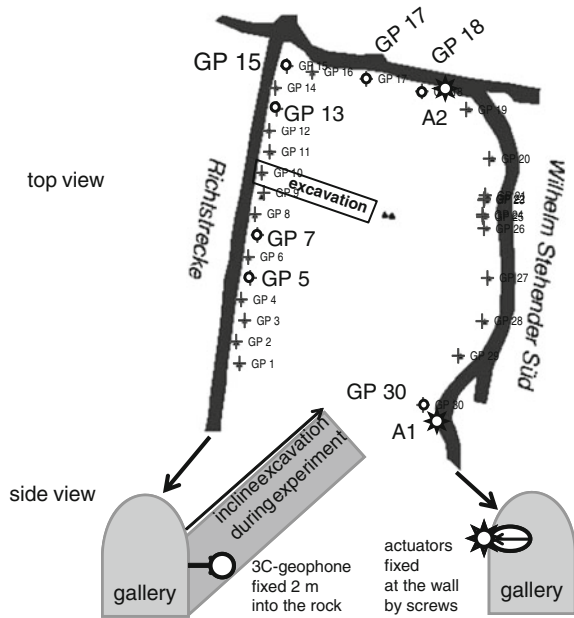
During the excavation of the incline at the GFZ-ULab, a tomographic monitoring setup was installed in the galleries to enable a seismic time-lapse observation of the excavation process and its influence on seismic wave propagation between the galleries. The aims of this experiment were to evaluate the influences to the seismic signals due to the excavation process and to test the signal repeatability of the system components for time-lapse applications. It was an initial pre-experiment to adapt the system components for an automated long-term monitoring of the structure integrity of underground constructions.

The setup consisted of seven 3C-geophone anchors, four installed in the western gallery (*Richtstrecke*), 2 installed in the northern gallery, one installed in the eastern gallery (*Wilhelm Stehender Süd*), and 2 vibrator sources installed in the northern and eastern galleries, respectively (Fig. 7.6).

One geophone anchor was positioned close to each source position to enable a near-field monitoring of the source signals. The setup remained fixed during the excavation work, and the vibrator units were fixed by screws at the rock wall. The operation direction of the sources was arranged perpendicular to the rock surface in order to act as a vertical single force.

Prior to the excavation start, one measurement cycle was acquired as a reference (baseline) recording. During the incline excavation work from March to November 2011, 12 measurement cycles were acquired in intervals of nearly three weeks using the same geometry and recording parameters. Additionally, a final measurement cycle was carried out in July 2012 in order to detect possible long time changes in the rock mass after the excavation work. During each cycle, a fixed recording sequence was applied, consisting of 6 different source signal types which were repeated ten times each to evaluate the signal reproducibility within each cycle. Additionally, two different source control algorithms were applied for each source signal. The whole recording sequence was applied to both vibrator units sequentially. The sources could remain fixed on site during the whole time-lapse experiment. The receivers and the electric connections of the recording system needed to be installed and uninstalled for each cycle to prevent system damages during the excavation work.

Fig. 7.6 Top view of the seismic monitoring setup in the GFZ-ULab used during the incline excavation process. The seven chosen 3C-geophone anchor positions (GP) from the available set (crosses) from the available set (crosses) are marked by circles, vibrator positions (A1, A2) are marked by stars. The excavation inclined by 40° upward, leaving the plane of receivers and sources towards east and not affecting most of the direct ray paths



After vibroseis correlation using the pilot source signal, sorting to geophone components, and data quality inspection, data processing was carried out by calculating the recording differences to the reference measurement since no travelt ime influence could be observed. Data changes during the time-lapse sequence were mainly focused on amplitude changes for the shear wave part of the recordings. To improve the imaging, a bandpass filter was applied to enhance the frequency part below 900 Hz. An example of the difference data is shown in Fig. 7.7 for the North-South receiver component at geophone anchor position GP5 for the seismic source A1, which generated a linear frequency modulated sinusoidal signal (sweep) of 300–3000 Hz of 1.45 s duration for this cycle part.

The result of all 3C-signals received during the experiment part using the source signal shown in Fig. 7.7 is sketched in Fig. 7.8. Most of the signals emitted by source A1 and received by the geophones GP5, GP7, and GP13 (western gallery—*Richtstrecke*) and geophone GP17 (northern gallery) had an amplitude response during excavation, while most of the signals from source A2 had no response on these geophones. All signals received by geophone GP15 provided no information. Geophones GP18 and GP30 were used for short-distance source control monitoring only and are not implemented in the image.

Even though the ray paths from source A1 to receiver GP5 and GP7 were not affected by the excavation (Fig. 7.6), the data of GP5 IT (component in gallery direction) had a significant amplitude increase up to a factor of 6 during the whole time lapse sequence. The amplitude of GP5 RT (component radial to gallery direction) increased by up to a factor of 7.5. The average amplitude increase for all responding

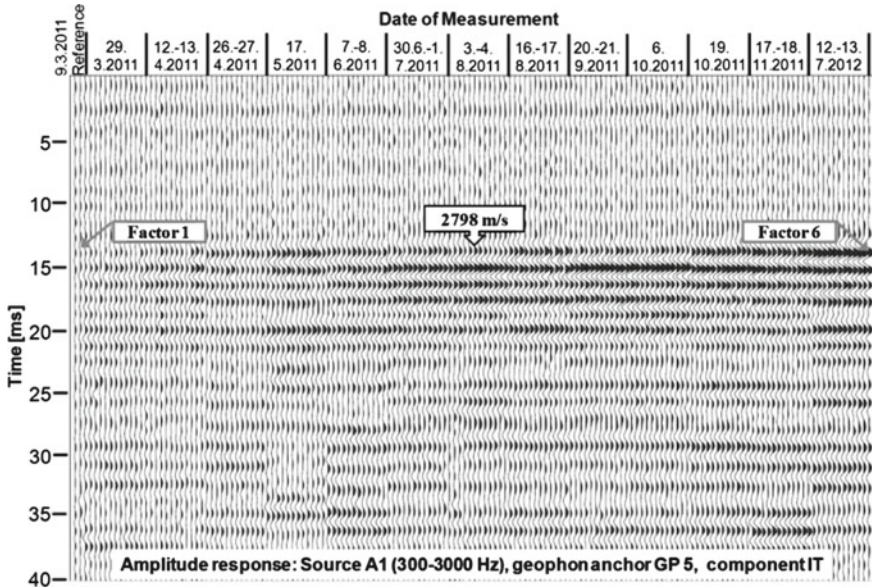


Fig. 7.7 Example of observed amplitude differences with respect to the reference recording (left-most trace) during the excavation process. Time-lapse recording increased from left to right, ten traces were recorded at each measurement cycle to verify the system reproducibility. Since absolute amplitudes decreased over the time-lapse sequence, relative amplitudes with respect to the reference increased. The calculated velocity of nearly 2800 m/s indicates clearly shear wave signal propagation. The IT component is shown (IT: in gallery direction)

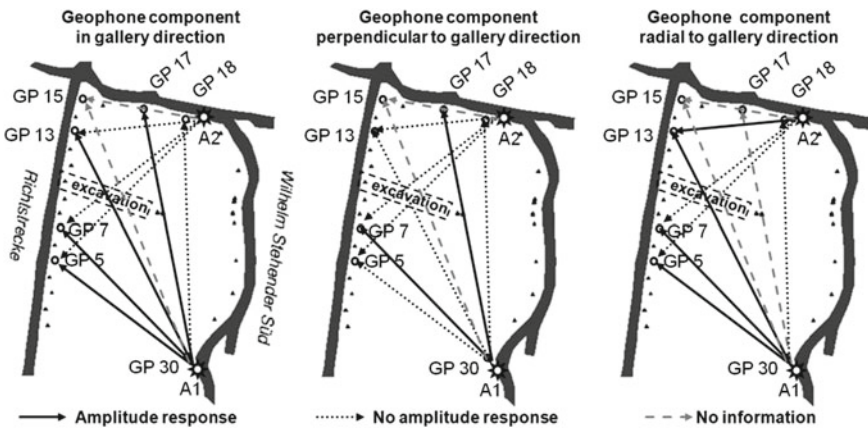


Fig. 7.8 Over all result for the tomographic ray paths of the experiment. Most of the signals emitted by source A1 achieved an amplitude response during excavation, while most of the source A2 signals had no amplitude response. All signals received by geophone GP15 gave no information. For discussion and interpretation see text

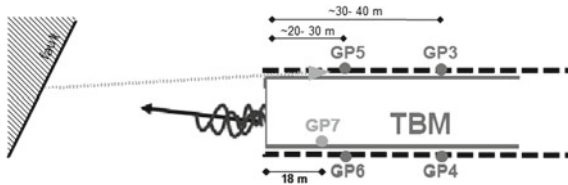


Fig. 7.9 Sketch of wave propagation during TBM advance (to the *left* side) due to TBM noise generation with the field setup in Spain (modified after Jetschny et al. 2010)

components from both sources sums up to a factor of 4.2. Signals emitted by source A2 had only a response on one component channel of the receiver setup, whereas signals emitted by source A1 had a response on nine component channels.

This increasing amplitude difference is interpreted to be caused by the increased scattering within the rock mass due to the excavation work. The distribution of amplitude response shows a complex pattern. Some ray paths passing the excavation zone are not affected, while others not passing the excavation zone are. The observation of recordings from source A1 being affected while source A2 recordings being mostly unaffected may indicate that the excavation of the incline has resulted in induced micro-cracks mainly in the southern part of the monitored rock mass. Previous seismic tomography experiments performed on the site have identified rather high P-wave velocities in the northern part of the monitored area (~ 6 km/s), and rather low P-wave velocities in the southern part (5–5.5 km/s, e.g., Heider et al. 2012). The monitored rock mass is lithologically rather homogeneous. Varying seismic velocities in a homogeneous rock mass are indicative for varying mechanical strength (Barton 2006). The drill-and-blast excavation of the incline may have increased the length and aperture of some of the micro-cracks and fractures in the rather weak rock mass in the southern part of the monitored area, and the northern half seems to have been less affected by the excavation works. Some inconsistency with this interpretation remains for the responses of GP5 and GP7 (vertical component, perpendicular to gallery) and source A1, for which there is no straightforward interpretation available. The results verify in principle that the system can be used to detect structural integrity changes of the rock mass surrounding underground constructions.

7.6 Application of the Seismic Monitoring System in Tunnel Construction

Tunnel Seismic While Drilling is derived from seismic while drilling in boreholes. Figure 7.9 shows the principle of the wavefield propagation together with the field setup used in this project.

In autumn 2012 a survey in Spain in co-operation with Dragados S.A. (Spain) was carried out for recording the seismic wavefield excited primarily by the cutter wheel of a TBM. In this pilot seismic tunnel survey for a feasibility study, the

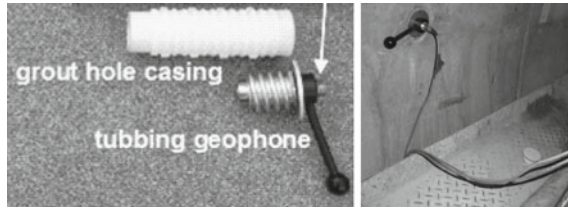


Fig. 7.10 For seismic measurements the tubbing geophone (*left* picture) is screwed into a grout hole casing of a tubbing segment. The *arrow* indicates the orientation mark that is used for the “horizontal” components (perpendicular to the axis) of the tubbing geophone. The *right* picture shows a real installation

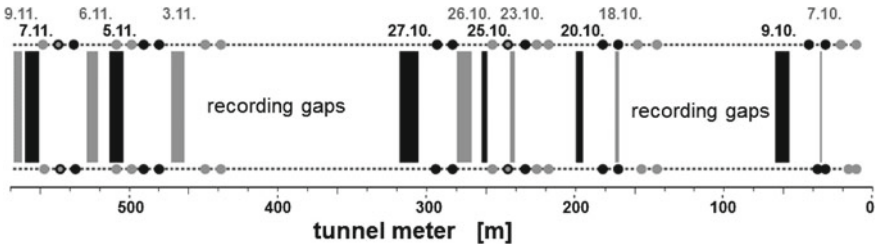
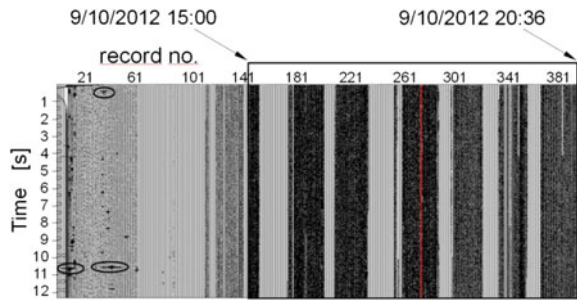


Fig. 7.11 TBM advance and according position of the installed field setup. The *dots* mark receiver positions and *bars* indicate the TBM advance during one acquisition shift. The numbers on the top indicate the date of the respective acquisition shift

ISIS-based hardware and a conventional recording unit for high resolution acquisition were used. Figure 7.10 shows the 3C-tubbing geophone—constructed by the GFZ for use on TBMs with segment lining—consisting of three geophones with 28 Hz eigenfrequency like the ISIS geophone anchor. This is an addition to the ISIS hardware.

The main setup consisted of five receiver positions (GP): 4 tubbing geophones (GP3-GP6 in Fig. 7.9) for recording the seismic wavefield and one triaxial accelerometer for recording the pilot signal (GP7 in Fig. 7.9). The accelerometer was permanently installed on a non-rotating part of the main TBM-bearing during the whole survey. At the start of each recording shift two tubbing geophones were deployed approximately 20 m behind the cutter head (GP5 and GP6 in Fig. 7.9), into segment linings and remained their till the end of the recording shift. At 10–13 m distance from GP5 and GP6 two further tubbing geophones were deployed (GP3 and GP4 in Fig. 4.1). Figure 7.10 (right) illustrates a tubbing geophone position. 5041 records with a length of 12.288 s per record were collected. The duration of one recording cycle was between 45 and 60 s, including data storage and initializing the next recording cycle. Therefore, data records cover 20–27 % of a continuous advance period. Figure 7.11 shows the positions of the main setup through the whole survey and in addition the TBM advance. In total there were around 77 m TBM advance during 13 acquisition shifts with an average of 7–8 m during an acquisition shift (on 6 days) and a maximum advance of 11.5 m in one shift.

Fig. 7.12 Data example for the acquisition period 4–9 October 2012 for the pilot sensor (IT component (along the tunnel axis)) on GP7



The recording gaps were due to regular and irregular maintenance stops as well as partly fast TBM advance while the acquisition team was not on site. Due to logistic reasons the survey could only be carried out in a 1-shift operation with 2 persons and therefore it was not possible to cover 100% of the 7 days and 24 h per day operation mode on the construction site.

Figure 7.12 shows a data example of the triaxial accelerometer. The TBM advance is clearly distinguishable from inactive TBM times. Giese et al. (2013) showed that with this acquisition setup in the neighbourhood of the cutter head a frequency range of approximately 200–600 Hz could be obtained for the seismic exploration signal. This is significantly higher compared to previous approaches to *Tunnel Seismic While Drilling* (e.g. approximately 40–100 Hz according to Poletto and Petronio (2006)) and shows that this setup is capable of acquiring high-resolution data as a prerequisite for a high resolution exploration during tunnel excavation. During this project, the first semi-continuous passive data from an active tunnel excavation have been acquired which can be used as a basis for future development of an appropriate correlation algorithm to extract Green's Functions out of the recorded time series. These may then be interpreted using the imaging algorithms implemented within the underground exploration system ISIS (Giese et al. 2006, 2013).

7.7 Summary and Conclusions

Geophysical exploration in underground construction still is a challenging field with the need for further methodological and technological adaptation to the specific tasks posed by tunnel or cavern excavation and by the operation of these structures. The efforts made during this project for acquiring realistic geophysical data on a construction site shows, however, that integrating a geophysical pilot survey into active tunnel excavation is a highly complex task. Space is limited, in the underground, and in particular on a TBM. Thus, testing of different acquisition scenarios and acquiring data under various environmental conditions is highly restricted by logistical factors, bearing a high risk of spending personnel and financial resources but being provided with rather limited field data.

These observations show that for the development of efficient and reliable sub-surface exploration, underground laboratories are of significant value as these enable for data acquisition under much less restricted logistical conditions. For underground tomographic exploration and monitoring, field work and numerical modelling have therefore been focusing on the research and education mine *Reiche Zeche* in Freiberg. Within this study, previously unprecedented monitoring data during active excavation works have been collected and first approaches for the interpretation of these innovative acquisition approaches were developed.

Tomographic inversion of simulated data using a realistic rock mass model with realistic statistical properties shows the general applicability of Full Waveform Inversion (FWI) in terms of imaging heterogeneities at very high resolution. Crucial steps towards a successful application of FWI to underground seismic prediction were described. With a synthetic study that simulates a real multi-component vibroseis measurement, the improved resolution of FWI compared to the classical traveltimes tomography has been demonstrated. The P-waveforms of the correlated vibroseis field data are significantly influenced by individual unknown medium heterogeneities at the receiver locations which can be successfully corrected by a deconvolution. This is a crucial pre-processing step for future FWI applications.

Field data have been acquired in the underground laboratory (GFZ-ULab), which are useful for high resolution imaging of the rock mass surrounded by the galleries. Here, the analysis of the field data has shown that there are complex interactions in close vicinity to the receiver location. Before FWI can be applied to this data, source and receiver dependant signatures need to be removed by inversion and deconvolution.

Conventional tomographic investigations typically rely on a large amount of source and receiver locations distributed as much as possible with large spatial aperture around the object under investigation. Opposite to that, for a monitoring setup, long-term observation periods and the need for highly time-efficient data evaluation require a rather sparse network of permanently installed measuring equipment. Based on this consideration, a monitoring survey has been performed in the GFZ-ULab using two sources and seven receivers. The survey consists of a baseline and thirteen repeat observations showing time-lapse effects on several source-receiver pairs triggered by the excavation of an incline and a cubic chamber in the underground laboratory. The time-lapse effects can be mainly described as amplitude variations with time (with decreasing amplitudes of the dominating direct shear wave in time). Traveltimes variations, which are mostly used for interpreting monitoring surveys, did not occur to a significant amount, but a complex pattern of amplitude variations indicating enhanced shear-wave scattering and attenuation has been identified. The technical feasibility of monitoring underground structures is assured by a high degree of source signal repeatability and stable conditions at the receiver locations. For the interpretation of this monitoring data, approaches are needed which are able to consider rather sparse acquisition geometries, and to detect and quantify critical variations based on the full wavefield rather than considering seismic traveltimes alone.

Acknowledgments This project was funded by the German Ministry for Education and Research (BMBF) in the framework of the GEOTECHNOLOGIEN programme (reference numbers 03G0738A, 03G0738B, 03G0738C). We are grateful for constructive remarks and discussions in preparation of the field survey by Dr. N. Pralle (Züblin AG) and for providing us access to a tunnel construction site and intensive logistical support by Dragados S.A. (Spain).

References

- Alptransit Gotthard Base Tunnel, <http://www.alptransit.ch>, Aug 2013
- Barton N (2006) Rock quality, seismic velocity, attenuation and anisotropy. Taylor and Francis, London, p 729, ISBN: 0-415-39441-4
- Born G, Giese R, Otto P, Maushake B, Paul R (2007) Verankerungseinrichtung für eine Sensoreinrichtung zur Erfassung von seismischen Signalen in geologischen Strukturen oder Bauwerken. Patent DE 10 2006 007 474.2, published 30 Aug 2007
- Brückl E, Chwatal W, Mertl S, Radinger A (2008) Exploration ahead of a tunnel face by TSWD - tunnel seismic while drilling. *Geomech Tunn* 1(5):460–465
- Dickmann T, Sander BK (1996) Drivage-concurrent tunnel seismic prediction (TSP). *Felsbau* 14:406–411
- Giese R, Dickmann Th, Eppler Th, Lüth S (2006) Seismic tomography to investigate the tunnel surroundings of the Side Gallery West of the multifunctional station Faido. In: Löw S (ed) *Geologie und Geotechnik der Basistunnels am Gotthard und am Lötschberg*, Tagungsband zum Symposium Geologie Alptransit Zürich, pp 145–154, vdf Hochschulverlag der ETH (2006)
- Giese R, Hock S, Krüger K, Lüth S, Martin Diaz E (2013) Seismic prediction on tunnel boring machines - comparison of active seismic sources and drilling noise measurements. In: *EURO:TUN 2013, 3rd international conference on computational methods in tunnelling and subsurface engineering, extended abstracts (2013)*
- Heider S, Jetschny S, Bohlen T, Giese R (2012) Towards an application of an elastic full waveform inversion (FWI) for a measurement below ground in a crystalline environment. In: *SEG technical program expanded abstracts*, pp 1–5
- Jaksch K, Giese R, Kopf M, Mikulla S (2010) Seismic prediction while drilling (SPWD): looking ahead of the drill bit by application of phased array technology. *Sci Drilling* 9:41–44
- Jetschny S, Bohlen T, De Nil D (2010) On the propagation characteristics of tunnel surface-waves for seismic prediction. *Geophys Prospect* 58:245–256
- Kneib G (1995) The statistical nature of the upper continental crystalline crust derived from in situ seismic measurements. *GJI* 122:594–616
- Kneib G, Kassel A, Lorenz K (2000) Automatic seismic prediction ahead of the tunnel boring machine. *First Break* 18:295–302. doi:10.1046/j.1365-2397.2000.00079.x
- Köhn D (2011) Time domain 2-D elastic full waveform tomography. Dissertation, Christian-Albrechts-Universität zu Kiel
- Krauß F (2013) Seismic attenuation tomography in the education and research mine “Reiche Zeche” and at the GFZ-Underground-Lab”. Master Thesis, Freiberg
- Lang D, Lindholm C, Polom U (2009) THEAM - tunnel health monitoring using active seismics. In: *Subsea tunnels, Norwegian Tunnelling Society Publication Nr. 18*, pp 91–96
- Loew S, Ziegler H-J, Keller F (2000) Alptransit: engineering geology of the world’s longest tunnel system. In: *GeoEng2000, An international conference on geotechnical and geological engineering, volume 1: invited papers*, Technomic Publishing Co., In. Lancaster & Basel, pp 927–937
- Maurer H, Greenhalgh SA, Manukyan E, Marelli S, Green AG (2011) Receiver coupling effects in seismic waveform inversions. *Geophysics* 77(1):R57–R63
- Mora P (1987) Nonlinear two-dimensional elastic inversion of multioffset data. *Geophysics* 52(9):1211–1228

- Petronio L, Poletto F (2002) Seismic-while-drilling by using tunnel boring machine noise. *Geophysics* 67(6):1798–1809
- Poletto F, Miranda F (2004) Seismic while drilling: fundamentals of drill-bit seismic for exploration. In: *Handbook of geophysical exploration: seismic exploration*. Elsevier, Amsterdam, p 546
- Poletto F, Petronio L (2006) Seismic interferometry with TBM source of transmitted and reflected waves. *Geophysics* 71:185–193
- Pratt RG (1999) Seismic waveform inversion in the frequency domain Part 1: theory and verification in a physical scale model. *Geophysics* 64(3):888–901
- Sebastian U (2013) *Die Geologie des Erzgebirges*. Springer Spektrum, Berlin
- Sens-Schönfelder C, Ballhause T, Rechlin A, Pomponi E, Niederleithinger E, Giese R (2011) Determining material changes on the centimeter and meter scale with diffuse elastic waves, AGU, Poster S31C–2265
- Sheng J, Leeds A, Buddensiek M, Schuster GT (2006) Early arrival waveform tomography on near-surface refraction data. *Geophysics* 71:U47–U57
- Tarantola A (1984) Inversion of seismic reflection data in the acoustic approximation. *Geophysics* 49:1259–1266
- Virieux J, Operto S (2009) An overview of full-waveform inversion in exploration geophysics. *Geophysics* 74(6):WCC1–WCC26

Chapter 8

Toolbox for Applied Seismic Tomography (TOAST)

Thomas Forbriger, Michael Auras, Filiz Bilgili, Thomas Bohlen, Simone Butzer, Sandra Christen, Luigia Cristiano, Wolfgang Friederich, Rüdiger Giese, Lisa Groos, Heiner Igel, Florian Köllner, Rolf Krompholz, Stefan Lüth, Stefan Mauerberger, Thomas Meier, Ilaria Mosca, Dirk Niehoff, Heike Richter, Martin Schäfer, Andreas Schuck, Florian Schumacher, Karin Sigloch, Mario Vormbaum and Frank Wuttke

Abstract TOAST (Toolbox for Applied Seismic Tomography) makes methods of full-waveform inversion of elastic waves available for the practitioner. The inversion of complete seismograms is an utmost ambitious and powerful technology. One of its strengths is the enormously increased imaging-resolution since it is able to resolve structures smaller than the seismic wave length. Further it is sensitive to material properties like density and dissipation which are hardly accessible through

T. Forbriger (✉) · T. Bohlen · S. Butzer · L. Groos · M. Schäfer
Karlsruhe Institute of Technology (KIT), Karlsruhe, Germany
e-mail: thomas.forbriger@kit.edu

M. Auras
Institut für Steinkonservierung e.V. Mainz, Mainz, Germany

F. Bilgili · S. Christen · L. Cristiano · T. Meier · F. Wuttke
Christian-Albrechts-Universität zu Kiel (CAU), Kiel, Germany

W. Friederich · F. Schumacher
Ruhr-University Bochum (RUB), Bochum, Germany

R. Giese · S. Lüth · H. Richter
Helmholtz Centre Potsdam (GFZ), Potsdam, Germany

H. Igel · S. Mauerberger · I. Mosca · K. Sigloch
Ludwig-Maximilians-University (LMU), Munich, Germany

F. Köllner · A. Schuck · M. Vormbaum
Geophysik und Geotechnik Leipzig GmbH (GGL), Leipzig, Germany

R. Krompholz
Geotron Elektronik (GEOTRON), Pirna, Germany

D. Niehoff
Dornburger Zement GmbH and Co. KG, Dorndorf-Stednitz, Germany

conventional techniques. Within the TOAST project algorithms available in academia were collected, improved, and prepared for application to field recordings. Different inversion strategies were implemented (global search, conjugate gradient, waveform sensitivity kernels) and computer programs for imaging the subsurface in 1D, 2D, and 3D were developed. The underlying algorithms for the correct numerical simulation of physical wave propagation have thoroughly been tested for artefacts. In parallel these techniques were tested in application to waveform data. They proved their potential in application to synthetic data, shallow-seismic surface waves from field recordings, and microseismic and ultrasonic data from material testing. This provided valuable insight to the demands on seismic observation equipment (repeatability, waveform reproduction, survey layout) and inversion strategies (initial models, regularization, alternative misfit definitions, etc.). The developed software programs, results of benchmark tests, and field-cases are published online by the OpenTOAST.de initiative.

8.1 Introduction

Full-waveform inversion (FWI) is a leading edge technique to exploit the full signal content of seismic data. It promises sub-wavelength resolution, high performance in resolving P- and S-wave velocity as well as sensitivity to variations in mass density. In particular for surface wave studies, where conventional methods require lateral homogeneity of the structure under investigation, FWI opens a new window to subsurface imaging. The computational demands for FWI are extraordinary and require state-of-the-art equipment and large computer clusters in the case of 3D application. Meanwhile a variety of implementations are developed in academic environments. Their potential is mainly demonstrated on synthetic data. The TOAST project pursues the goal to make these implementations available to a broader community as well as to end-users.

We established a unique knowledge base through a fertile collaboration of universities (Karlsruhe Institute of Technology [KIT], Ruhr-University Bochum [RUB], Christian-Albrechts-Universität zu Kiel [CAU], and Ludwig-Maximilians-University Munich [LMU]), the Helmholtz Centre Potsdam (GFZ), and commercial companies (Geophysik und Geotechnik Leipzig GmbH [GGL] and Geotron Elektronik [GEOTRON]). Contributions from wave propagation and inverse theory, numerical programming, IT management, field experience in shallow-seismics as well as ultrasonics and microseismics on application targets were successfully brought together.

In the current contribution we present some selected results of the joint project. We feature three different approaches to FWI. The adjoint method currently is a widespread approach, since it is of outstanding numerical efficiency. The computation of waveform kernels is much more demanding but offers improved convergence and the potential for resolution analysis. If the parameter space for subsurface models can be kept small, as is the case in material testing, global search algorithms can explore the

full non-uniqueness of the inverse problem. The aim of TOAST is not only to demonstrate the fitness of these approaches by application to synthetic data. We long for the successful inversion of field data. In field laboratories on the shallow-seismic and the ultrasonic (material testing) scale we recorded waveform data. The field laboratories not only produced challenges for the FWI but also many insights in properties of seismic sources (partly developed within the project), appropriate surveying and new insights to seismic properties of the different materials under investigation. The final products of the project in terms of computer code, benchmark data, technical definitions, and recommendations we share with a broader community through the web portal OpenTOAST (<http://www.opentoast.de>). A prerequisite for this is the resolution of licensing issues and basic documentation. The TOAST members hope that this initiative will remain prosperous after the end of the funding period.

The scientific results of the joint project go beyond this brief contribution. They will be published in separate research papers within the near future (Butzer et al. 2013; Forbriger et al. submitted; Groos et al. in prep; Krauss et al. submitted; Kurzmann et al. 2013; Mosca et al. submitted; Schäfer et al. submitted). Three dissertations use TOAST software for the FWI of reflected acoustic waves (Kurzmann 2012; Przebindowska 2013) as well as surface waves (Groos 2013). Further dissertations are in preparation in the context of TOAST.

8.2 Full-Waveform Inversion with the Adjoint Method

Full-waveform inversion (FWI) aims to minimize the misfit between modeled and observed seismograms. This can be implemented efficiently using a conjugate gradient approach (Tarantola 1988; Mora 1987). The adjoint-state method enables to calculate the gradient of the misfit function as zero-lag cross-correlation between a forward propagated wavefield and a wavefield propagated back from the receivers into the medium. Hereby the explicit calculation of the Fréchet derivatives can be avoided.

We use the time-domain 2D elastic FWI code developed by Köhn (2011), which is available under the terms of GNU GPL at <http://www.opentoast.de>. For the inversion of shallow-seismic field data this code was further enhanced by implementing different misfit definitions, source wavelet inversion and viscoelasticity.

Time domain FWI requires the storage of wavefields of the whole time series for gradient calculations. By contrast, in the frequency domain only few discrete frequencies can be sufficient for the gradient calculations, known as single frequency inversion (Sirgue and Pratt 2004). As the wavefield needs to be stored only for these frequencies, storage costs decrease dramatically. In our 3D FWI implementation we therefore adopted the approach suggested by Sirgue et al. (2008). This is a combination of forward modeling in the time domain and inversion in the frequency domain and offers an optimal approach to minimize storage needs and runtime. Using discrete Fourier transformations the wavefields can be transformed from time into frequency domain on the fly. The gradients are then calculated as multiplications of forward and

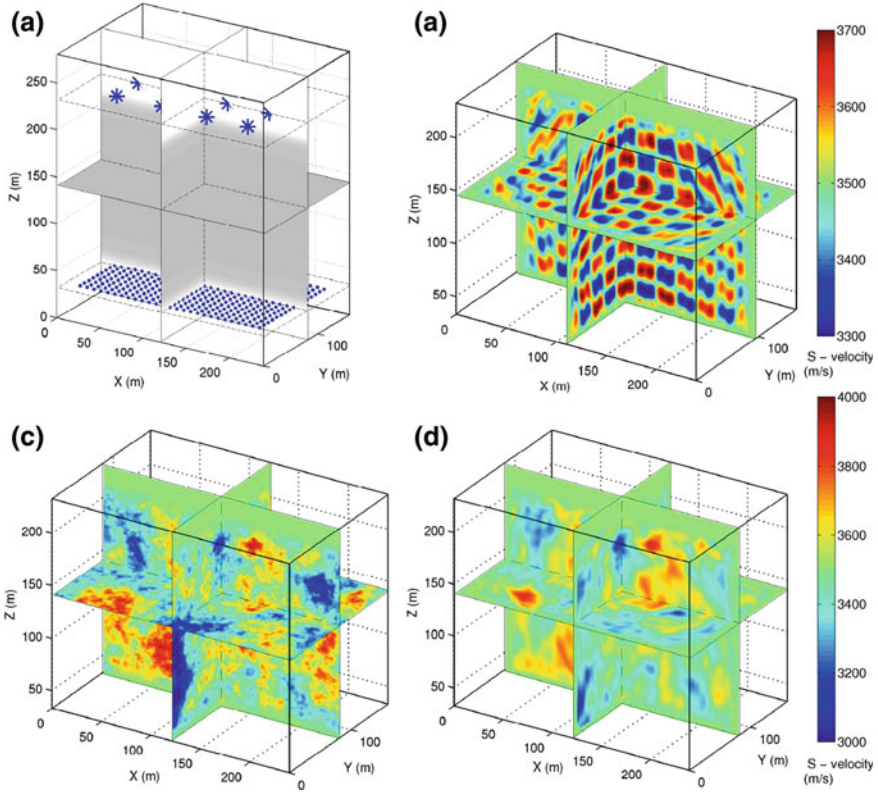


Fig. 8.1 Inversion results of 3D FWI for S-velocity: **a** 3D acquisition geometry with sources (*) and receivers (+), **b** inversion result checkerboard ($\pm 5\%$ variation), **c** real model random medium and **d** random medium inversion result

conjugate backpropagated wavefields in the frequency domain. This approach additionally enables to increase the frequency during inversion without further effort. Starting from sufficiently low frequencies is extremely important to decrease the ambiguity of the inverse problem (e.g. Sirgue and Pratt 2004).

The modeling of two and three-dimensional wavefields is performed with a time-domain elastic finite-difference code based on the velocity stress formulation on a staggered grid (Bohlen 2002). The code is heavily parallelized and thus enables a very efficient and fast calculation of the wavefields.

8.2.1 3D Elastic Full-Waveform Inversion

Here we present two inversion tests for v_p and v_s using homogeneous starting models with $v_p = 6300$ m/s, $v_s = 3500$ m/s and $\rho = 2800$ kg/m³. Figure 8.1 shows results

for v_s only. The inverted P-wave velocity models are much smoother due to their larger wavelengths. Figure 8.1a shows the acquisition geometry, consisting of 12 sources and 416 receivers in transmission geometry.

A resolution study was performed, using a checkerboard with 5% velocity variation and 20m edge length. Frequencies were increased from 140 to 240Hz. The result is shown in Fig. 8.1b. The alternating cubes are well reconstructed, except at the boundaries. The sharp contrast between the cubes could not be resolved and requires the use of higher frequencies.

In a second inversion test, we inverted data of a random medium model, described by an exponential autocorrelation function in space. The real shear wave velocity model is plotted in Fig. 8.1c. The model represents a crystalline rock environment. The S-velocity result is shown in Fig. 8.1d. The inversion method could successfully recover the differently sized 3D random medium structures down to the scale of a wavelength. Higher frequencies would be required to reconstruct smaller features. Similar to the resolution test, we find that the resolution of the result decreases towards model boundaries, where wavepath coverage is less.

8.2.2 2D Elastic Full-Waveform Inversion

We apply a 2D FWI to shallow-seismic Rayleigh waves. Shallow-seismic Rayleigh waves can be easily excited by a hammer blow on the surface and have a high sensitivity to the shear wave velocity in the first meters of the subsurface. We apply FWI to a field dataset acquired on a test site of the TOAST field laboratory at Rheinstetten near Karlsruhe (Germany). The subsurface consists of layered fluvial sediments. Figure 8.2 displays the inversion results. The data misfit is significantly decreased during the inversion. Furthermore, the S-wave velocity model still corresponds to a predominantly depth dependent structure even though this is not enforced in the inversion by regularization. Although the changes in the S-wave velocity model are small, these changes have a strong influence on the wavefields which confirms the high sensitivity of Rayleigh waves to the S-wave velocity model of the shallow subsurface.

8.3 Full-Waveform Inversion and Sensitivity Analysis Using Waveform Sensitivity Kernels

We derive waveform sensitivity kernels from Born scattering theory, for use in an iterative full-waveform inversion procedure that tries to explain the full information content of measured seismic waveforms by inhomogeneities of the structural elastic earth model. Additionally, the sensitivity kernels may be used to follow various strategies of seismic sensitivity and resolution analysis.

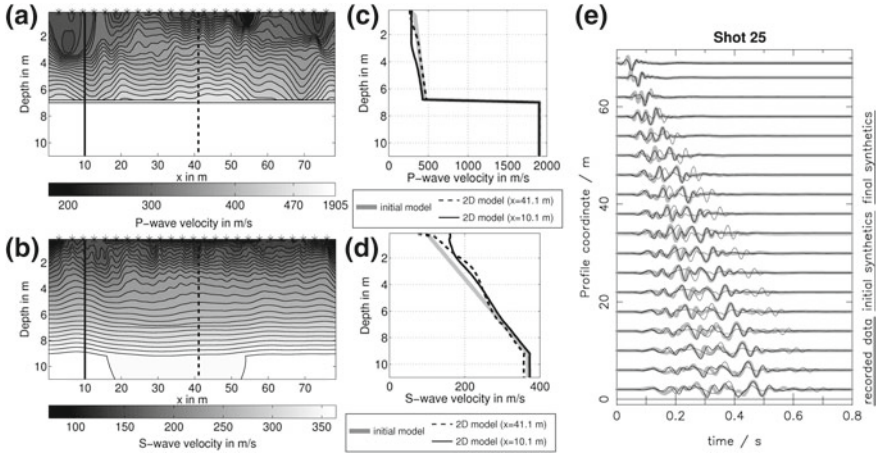


Fig. 8.2 2D subsurface model obtained by FWI. **a** displays the P-wave velocity model and **b** the S-wave velocity model. The stars mark the source positions. **c** and **d** shows the corresponding vertical velocity profiles in comparison to the initial model. **e** displays vertical displacement seismograms for shot 25 ($x = 77.0$ m) in the frequency band between 5 and 70 Hz. Recorded data are displayed by the thick gray line, seismograms calculated with the initial model are displayed by the thin gray line and seismograms calculated with the 2D model are displayed in black. Each trace is normalized to its maximum amplitude

8.3.1 Waveform Sensitivity Kernels

In the context of Born scattering, we may derive the following expression of the scattered displacement field $\delta \mathbf{u}$, starting of with the elastodynamic equation in the frequency domain and using Betti's theorem and the reciprocity property of Green functions

$$\delta u_n(\mathbf{r}) = \int_{\Omega} \left[\delta \rho G_{in}(\mathbf{r}_s, \mathbf{r}) \omega^2 u_i(\mathbf{r}_s) - \delta c_{ijkl} \partial_j G_{in}(\mathbf{r}_s, \mathbf{r}) \partial_l u_k(\mathbf{r}_s) \right] d^3 \mathbf{r}_s \quad (8.1)$$

where $G_{in}(\mathbf{r}_s, \mathbf{r})$ denotes the i^{th} displacement component at \mathbf{r}_s for a delta force in n -direction at \mathbf{r} , ρ and c_{ijkl} denote density and tensor of linear elasticity and leading δ indicates the perturbed/scattered property. Einstein summation convention is assumed and integration is done over the whole volume of interest Ω , where perturbed boundaries, hence contributions by surface integrals, are omitted.

For a specific linear elastic parametrization of N parameters p_1, \dots, p_N , the integrand in Eq. (8.1) may be linearly rearranged to yield

$$\delta u_n(\mathbf{r}) = \int_{\Omega} \left[\delta p_1 K_{nr}^{p_1}(\mathbf{r}_s) + \dots + \delta p_N K_{nr}^{p_N}(\mathbf{r}_s) \right] d^3 \mathbf{r}_s, \quad (8.2)$$

where the frequency dependent expressions $K_{n\mathbf{r}}^{p_j}(\mathbf{r}_s)$ quantify how the n^{th} component $u_n(\mathbf{r})$ of the displacement spectrum at receiver position \mathbf{r} changes, if model parameter p_j is perturbed by δp_j at scattering point \mathbf{r}_s inside the medium. Hence, we call quantities K *waveform sensitivity kernels*, which by symmetries of tensor c_{ijkl} may be expressed in terms of displacement field \mathbf{u} , Green tensor \mathbf{G} and their strains, respectively.

8.3.2 Software Package ASKI

We developed and implemented the highly modularized software package ASKI—Analysis of Sensitivity and Waveform Inversion—which applies the scattering relation (8.2) to a specific choice of model parameters p_j (e.g. $p_j \in \{\rho, \lambda, \mu\}$, or $p_j \in \{\rho, v_p, v_s\}$). For these parameters, ASKI computes the waveform sensitivity kernels K from synthetic displacement fields, Green tensors and their strains which are calculated by a supported forward method w.r.t. some (possibly already heterogeneous) background model and stored in the frequency domain throughout Ω .

At the moment the 3D spectral element code SPECFEM3D (Tromp et al. 2008) and the 1D semi-analytical code GEMINI (Friederich and Dalkolmo 1995) in both, Cartesian and spherical framework are supported. ASKI can be easily extended to other forward methods.

ASKI discretizes the model space into values p_{js} of the elastic parameters p_j on a set of scatterers Ω_s , which are a disjoint division of the model domain Ω . This way, (8.2) leads to the linear relation

$$\delta u_n(\mathbf{r}) = \sum_s \left[\delta p_{1s} \int_{\Omega_s} K_{n\mathbf{r}}^{p_1} + \dots + \delta p_{Ns} \int_{\Omega_s} K_{n\mathbf{r}}^{p_N} \right], \quad (8.3)$$

assuming the parameter perturbations δp_{js} to be constant throughout scatterer Ω_s .

Using the linear relation (8.3), possibly setting up a linear system of equations for many data, various strategies of sensitivity and resolution analysis, as well as an iterative full-waveform inversion procedure may be followed, as presented in the following.

8.3.3 Iterative Full-Waveform Inversion

The waveform sensitivity kernels can be used to invert structural earth model parameters from a given set of seismic data, taking the full content of information contained in the waveforms into account.

Starting of with some good approximation of the true earth model, we can now iteratively compute waveform sensitivity kernels w.r.t. the currently inverted model

and improve it by inferring parameter perturbations δp_{js} from a linear system of equations, which is established by evaluating Eq. (8.3) on a set of data. The scattered wavefield $\delta u_n(\mathbf{r})$ is computed as the difference of the measured data (interpreted as displacement w.r.t. the perturbed model) and synthetic displacement w.r.t. the currently inverted model.

In order to regularize the inverse problem, we can use low frequency content of data for the first iteration steps and gradually increase the amount of waveform information to higher frequencies as we iterate. Also smoothing constraints, added as additional equations to the linear system, may help to yield sensible physical solutions.

As the steps of forward simulation, i.e. computation of synthetic wavefields, the kernel computation and the actual inversion step are kept completely separate in ASKI, the software is very flexible in terms of using different forward methods or subsets of data and varying the model resolution and intensity of smoothing.

A validation of the iterative full-waveform inversion of ASKI using waveform sensitivity kernels is shown in Fig. 8.3:

In between 12 vertical point sources at the top (yellow) and 12 3-component receivers at the bottom (red), a model inhomogeneity in v_s is placed (of size $48 \times 48 \times 36$ m), as shown in Fig. 8.3a. Simultaneously the isotropic earth model is also perturbed in v_p . Density is kept constant.

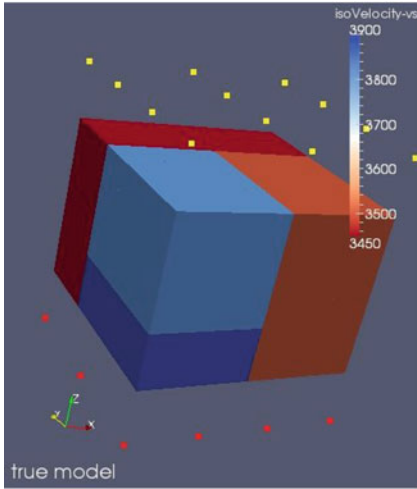
The homogeneous background is used as a starting model Fig. 8.3b. Figure 8.3c, d shows intermediate results of the shear-wave velocity model in the course of the iterative inversion, in which model perturbations were allowed only inside the volume of the true inhomogeneity. v_p was inverted for jointly, but is not shown here.

Note that already after two iterations, the shear-wave velocity model is explained pretty well. Keep in mind, however, the unrealistic conditions of this experiment, assuming no model perturbations outside the known volume of inhomogeneity.

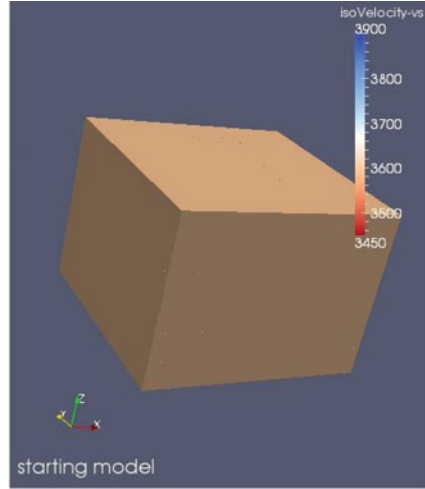
8.3.4 Sensitivity and Resolution Analysis

As the waveform sensitivity kernels quantify how sensitive the particular data are to changes of certain model parameters, they may also be used to estimate the resolving power of a dataset and may even help in active seismic experiments to find an optimal acquisition geometry that resolves the volume of interest best, before actually collecting any data.

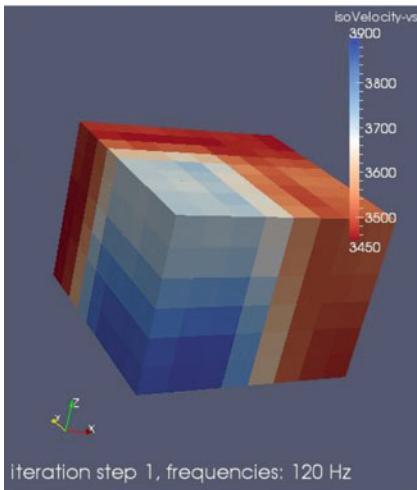
Any sensitivity analysis tools working on the sensitivity matrix, even a full singular value decomposition, may be easily added to ASKI using any modules provided by the ASKI program package.



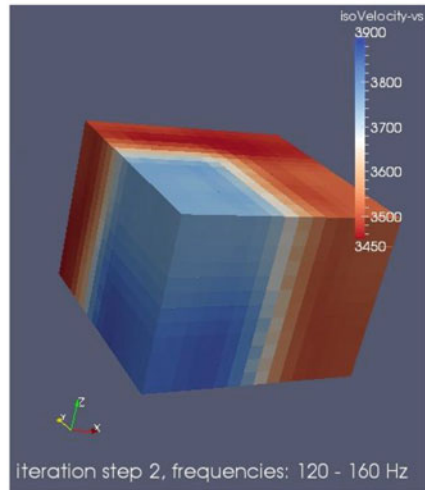
(a) true v_s model



(b) v_s starting model



(c) inverted v_s model after the 1st iteration



(d) inverted v_s model after the 2nd iteration

Fig. 8.3 Validation of ASKI full-waveform kernel inversion. Note that the frequency content of the data as well as the model resolution was increased for the 2nd iteration

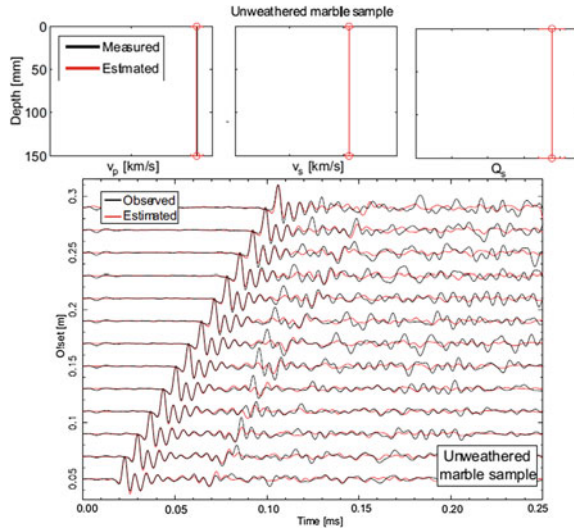
8.4 Full-Waveform Inversion by a Global Search Algorithm Applied to Ultrasonic Data

Non-destructive testing based on ultrasounds allows us to detect, characterize and size discrete flaws in geotechnical and engineering structures and materials. This information is needed to determine whether such flaws can be tolerated in future service. In typical ultrasonic experiments, only the first-arriving P-wave is interpreted, and the remainder of the recorded waveform is neglected. Furthermore, travel-times of first arriving P-waves have limited resolution for the upper centimeters of an object. In contrast, surface measurements are well suited to quantify superficial alterations of material properties, e.g. due to weathering.

In order to characterize well a geotechnical structure, the first step is to benchmark the propagation of ultrasonic surface waves in materials tested with a non-destructive technique. The tremendous potential of ultrasonic surface waves becomes an advantage only if numerical forward modeling tools and spectral analysis are available to describe the waveforms accurately and to distinguish the contribution of surface wave modes. For this reason we compute synthetic full seismograms as well as group and phase velocity spectral analysis for certain synthetic models that resemble structures commonly tested with non-destructive technique (e.g. unweathered and weathered natural stones and concretes and road pavement). They can be end-member models for real structures analysed in field surveys. This synthetic work highlights the fact that even in seemingly simple, multi-layered structures, Rayleigh wavefields of considerable complexity develop. For this reason, not only forward modeling of synthetic seismograms but also spectral analysis of both phase and group velocity are important tools for characterizing these structures (Mosca et al. submitted).

The study of wave propagation for synthetic structures provides an useful background for setting up inverse problem formulations and therefore inferring sub-surface structure from ultrasonic Rayleigh wave measurements. This will entail adopting a proper parameterization (e.g. shear wave velocity, interface thickness and shear quality factor), and efficient solvers for a generally non-linear problem. Unlike in seismological studies where reference models for layered Earth structure have been investigated extensively and are well constrained, at geotechnical scale there is often so little prior information about sub-surface properties that estimating an adequate initial model may represent the largest challenge. In the context of the TOAST project we have developed an inversion strategy based on a Monte Carlo procedure which is already modularized into the basic components of a typical inverse problem (e.g. the forward modeling, the computation of the misfit function in terms of waveform, phase or group velocity dispersion curve). Specifically, the inversion is based on the Neighborhood Algorithm (Sambridge 1999a, b) whose great advantage is the possibility to compute the appraisal problem (i.e. quantitative assessment of uncertainty and resolution) of the estimated solution(s). However, it becomes computationally expensive with increasing the number of model parameters and thus we envision it to be used mainly for estimation of layered structures. This might then serve as starting models for linearized, higher-dimensional inversions in 2D or 3D.

Fig. 8.4 In the *top panel* the estimated model (compressional wave velocity, shear wave velocity and shear quality factor) is displayed together with the associated error-bars, compared with the model a priori known for unweathered marble. In the *bottom panel* seismograms computed for the estimated model and the observed seismograms are compared



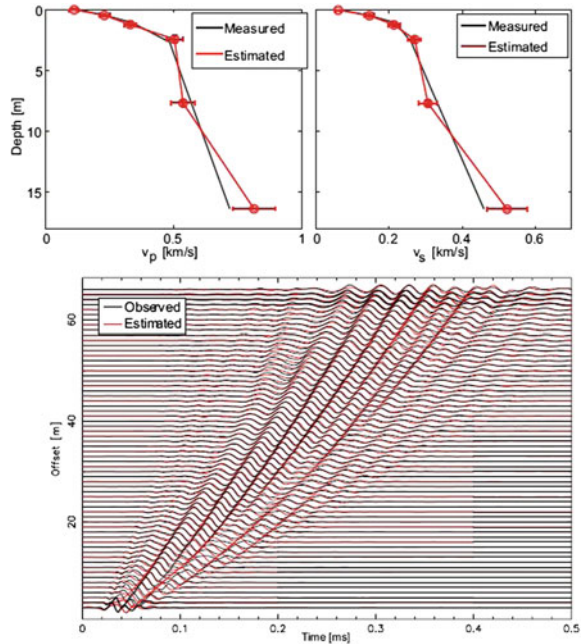
We have applied successfully this inversion scheme to data from material testing, and thus defining seismic properties of models of wavelength from centimetres to meters as a function of depth. We inverted the surface-wave portion of observed seismograms for inferring the shear wave velocity, v_s , and the attenuation parameters, Q_s , of structures. In Fig. 8.4, as an example, we show the results for ultrasonic Rayleigh wave measurements recorded at the surface of an unweathered marble sample.

To test the validity and flexibility of the scheme of our waveform inversion, we inverted also shallow-seismic measurements. An example is displayed in Fig. 8.5.

8.5 The Shallow-Seismic Field Laboratory

A field laboratory was set up to record data on test sites and to develop optimal acquisition strategies and quality control with respect to the subsequent full-waveform inversion (FWI). We selected a test site on the vertical fault system of the southern rim of the Taunus (near Frankfurt on the Main, Hesse, Germany). With preparatory investigations (seismics and DC geoelectrics) we confirmed the predominantly 2D nature of the subsurface. In the northwestern part of the vertical fault sericite-gneiss is met at shallow depth (0.5–2 m), while it is covered by sedimentary layers of up to 6 m thickness southeast of the fault. This is confirmed by Dynamic Probing Light (DPL) investigations and borehole profiles in the near vicinity. Perpendicular to this 2D fault we carried out a shallow-seismic 2D survey in summer of 2011. As sources we used pneumatic impulse hammer, magnetostrictive vibrator and classical hammer blows.

Fig. 8.5 Like Fig. 8.4, but for the shallow-seismic survey at the site of Bietigheim. In the *top panel* the estimated compressional wave velocity, shear wave velocity and thickness of interfaces are displayed together with the known values. In the *lower panel* the synthetic data is compared with the seismograms for the inferred model



We aim to apply FWI to this field dataset. In a first step we use well established first arrival time tomographic methods. This leads to suitable initial models which are essential for successful FWI.

8.5.1 Performance of Different Seismic Sources

Two mechanical seismic sources, the pneumatic impulse hammer and the magnetostrictive vibrator source, were used by GFZ to perform shallow-seismic measurements on the test site. On the vibro source, two actuators are driven synchronously with controlled and amplified frequency sweeps of same amplitude and phase. The head accelerations are detected for control of amplitudes and phases. Within the impulse hammer a pneumatically pre-stressed impact mass is unlatched from its initial position.

The data of the magnetostrictive vibrator source and the impulse hammer were acquired on the main profile. The profile length is about 89m, with 39 vertical-geophones and 50 three-components-geophones at 1m interval. The survey set-up of the receivers was the same for both sources. The shot points were located at the main profile at a 2m interval for the vibrator source and 4m for the impulse source.

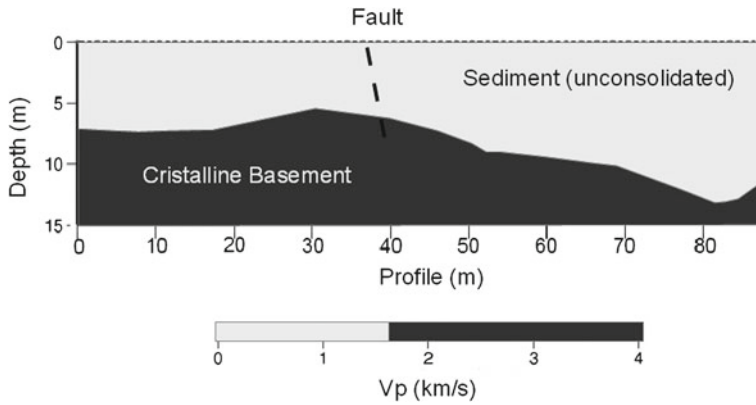


Fig. 8.6 Velocity model as derived from tomographic inversion of the first break traveltimes picked in the data acquired using the magnetostrictive seismic source

8.5.2 Traveltime Tomography of Field Data

A comparison of the data sets acquired using the pneumatic impact hammer and the magnetostrictive vibro source showed that the impact hammer data were strongly dominated by (low frequency, <100 Hz) surface wave signals, whereas the vibro data were dominated by higher frequencies and a broader frequency spectrum consistent with the frequency range of the source sweep. The vibro data do not contain surface wave signals and the first breaks of the P-waves could easily be identified. Therefore, the vibro-seismic data set was used for deriving a P-wave velocity model along the acquisition profile. The traveltime tomography was performed using the FAST package by Zelt and Barton (1998). The resulting final model is shown in Fig. 8.6. The low-velocity sedimentary layer can be clearly separated from the crystalline basement layer below and the varying thickness of the sediment layer on either side of the fault zone in the middle of the profile can be identified.

Vertical and horizontal hammer blows were used to obtain shallow-seismic data at Mammolshain for the inversion of P- and S-wave travel-times. Due to small receiver and shotpoint spacings the geometry of the main seismic profile is suitable for the application of traveltime tomography, which estimates the 2D velocity distribution along the profile. Starting velocity models are separately generated based on this inversion process for P- and S-wave first arrivals. The software Rayfract[®] (Seismic Refraction and Borehole Tomography) uses a 1D gradient initial model which is directly determined from first breaks and further invokes an iterative refinement of this initial 1D velocity model with a 2D WET (Wavepath Eikonal Traveltime) inversion code. This inversion code is based on a finite-difference solution to the Eikonal equation. Traveltimes are corrected for topography and the inversion process is terminated after 20 iterations. The inferred velocity models are displayed in Fig. 8.7. The stratigraphy is simplified by two different colors: The upper light gray repre-

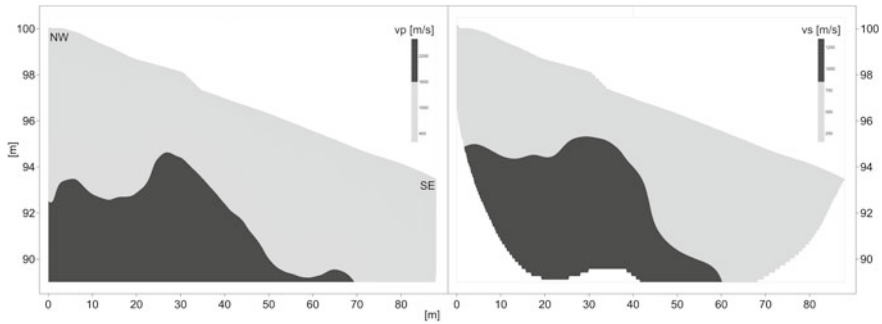


Fig. 8.7 (left) P-wave model and (right) S-wave model as derived from tomographic inversion of first break traveltimes picked in the data acquired using the hammer blow sources. These velocity models are used as initial models for full-waveform inversion. Surface topography was taken into account in this inversion

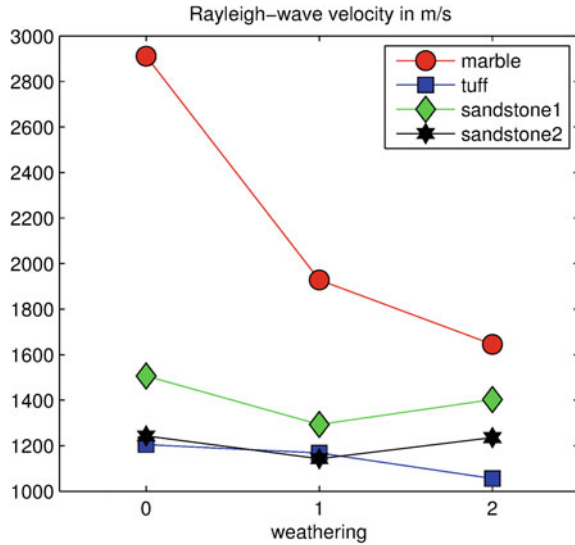
sents a quaternary layer that covers the dark gray part which possibly shapes the bedrock surface consisting of sericite-gneiss. For P-waves a transition velocity of 1600 m/s is chosen whereas a velocity of 850 m/s illustrates the transition zone for the S-wave image. Even though the shape of the bedrock surface seems to vary inconstantly on both sides of the assumed fault, the 2D structure of the subsurface velocity distribution is obvious.

8.6 The Ultrasonics and Microseismic Field Laboratory

On scales of centimeters to decimeters seismic investigations may be applied to non-destructive testing of structures made of natural stone or concrete for example facades, engineering structures, pavements or monuments. Alterations or flaws caused by weathering or repeated usage may be detected by ultrasonic surface measurements along profiles of a length of up to about 30 cm using frequencies between about 5 and 500 kHz. In order to investigate the entire waveform a definite radiation pattern of the transducer and receiver and highly accurate point measurements are needed. In the framework of the project ultrasonic measuring devices well suited for reproducible surface measurements have been developed together with the project partner GEOTRON Elektronik. The equipment is easy to handle allowing for efficient and broadband measurements. Comparison of measured ultrasonic waveforms with synthetics calculated by numerical forward modeling shows that the source may be well approximated by a vertical point force and the receiver record essentially the vertical component of the wavefield (Mosca et al. submitted).

Laboratory experiments. Ultrasonic measurements were carried out before and after two phases of artificial weathering of samples made of natural stones and concrete in order to quantify the effect of weathering on velocities and damping of elastic

Fig. 8.8 Average Rayleigh wave velocities in natural stones before and after two phases of weathering



waves. In addition, 4 samples of concrete made of different recipes were investigated. Figure 8.8 shows the results for Rayleigh wave velocities measured at the surface of the natural stone samples. From the figures it is obvious that weathering of natural stones may result in significant changes in average Rayleigh wave velocities. Interestingly, elastic velocities in marble decrease strongly already after the first phase of weathering and reduce by about 50% after the second phase. Also in tuff the velocities are constantly decreasing in total by about 12%. The behaviour of sandstones differs. After the first phase a decrease of the elastic velocities is observed whereas after the second phase they are increasing again. Very likely this is due to a decrease of porosity by filling of the pore space by clay and sand particles. In contrast, velocities in the concrete samples decrease strongly and monotonously due to weathering.

Field experiments. A number of measurements at real structures have been carried out—more than originally anticipated. Columns made of sandstone were measured at the *Klosterkirche Enkenbach-Alsenborn*. At the *Schlossbrücke, Berlin*, surface measurements were carried out at the statue “Nike bekränzt den Sieger” made of Carrara marble. Roman plaster was investigated at the *Amphitheater Trier*, in the Vomitorium 3 (a former exit). A large number of measurements at different types of damage were carried out at the *Porta Nigra, Trier*. This Roman building is made of sandstone. It is famous for its black crust that is the result of weathering. At the *Tabularium at Campidoglio, Rome*, made of tuff alterations due to weathering were investigated. Roman plaster in the “House of the Tragic Poet” in *Pompeii* was investigated by ultrasonic surface measurements. Finally, at a parking lot of the highway A4 the concrete pavement and a pillar of a bridge crossing the highway A9 were investigated. In all cases accurate and repeatable measurements of ultrasonic

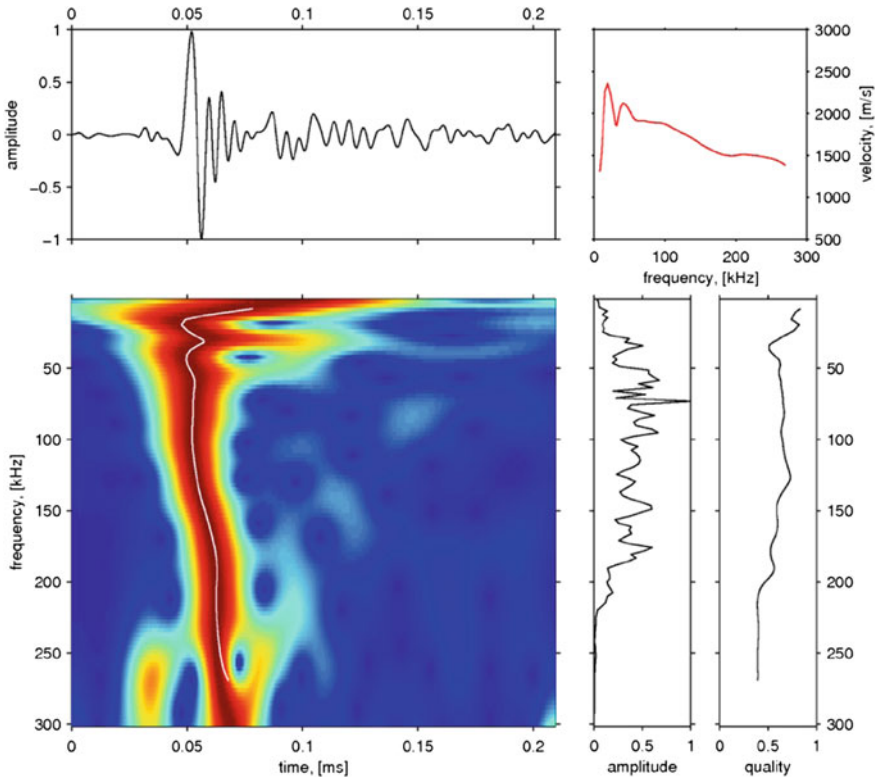


Fig. 8.9 Spectrogram of a waveform measured at Klosterkirche Enkenbach-Alsenborn. (*top left*) Waveform recorded at 12 cm source-receiver distance. (*bottom left*) time-frequency analysis. Red colors indicate high amplitudes. The white line indicates the group travel time of the fundamental Rayleigh mode (*top right*) Group velocity of the fundamental Rayleigh mode. Note the decrease with increasing frequency pointing to superficial softening

waveforms have been obtained. They showed convincingly the potential of surface waveform measurements for the investigation of media properties in the uppermost centimeters. In all cases the waveforms of the Rayleigh fundamental mode are indicative for the changes of media properties with depth. In most of the cases, the velocity is slightly to strongly increasing with depth (Fig. 8.9). In some cases a high velocity crust of altered material has been found. This is e.g. typical for the intact black crust at the Porta Nigra or the Tabularium in Rome. Interestingly, pavement exposed to frequent mechanical load by cars and pillars affected by salty water in winter times showed slightly increased velocities.

Software tools. Various tools for the analysis of ultrasonic waveforms have been developed. This includes tools for the visualization of the waveforms and the determination of wave velocities for waves traveling along the profile. Time-frequency analysis for the determination of Rayleigh wave group velocities (Meier et al. 2004) was adapted to ultrasonic frequencies. This tool proved to be very useful

for the characterization of the waveforms and the detection of superficial changes in material properties. Furthermore, a tool for the linearized full-waveform inversion of ultrasonic surface measurements has been developed. Ultrasonic waveforms are calculated using the Gemini software package (Friederich and Dalkolmo 1995). Waveforms and Rayleigh wave group velocities may be inverted for a 1D model of the uppermost centimeters. The short computation time of only a few minutes on a standard PC ensures the effective applicability to real measurements.

8.7 Toolbox Management

One principal aim of TOAST is the dissemination of software products with all licensing questions resolved. Due to the open and collaborative nature in academics the TOAST toolbox pursues an open-source policy. For distribution the TOAST toolbox bundles components into packages which accomplish both simplicity and flexibility. In the following we describe important licensing issues that were discussed between the TOAST partners and are of broader relevance for open source software distribution projects.

8.7.1 Software Licensing

Licensing is an important tool for setting specific terms on which software may be used, modified or distributed. By mistake, scientists often do not pay much attention to copyright and licensing issues. Making developments available for others is part and parcel in science. In particular, this holds true for reproducibility and the ability to build upon others' work. In fulfilling expectations to distribute and disseminate TOAST related software products appropriate licensing is mandatory. Otherwise exclusive rights are granted to the original work which potentially constitutes copyright infringements.

Software licenses can generally be fit into two categories: Proprietary software or closed source software and free-libre and open source software (FLOSS). Roughly spoken, proprietary licenses are designed with the intent to impose restrictions for modification, sharing, studying or redistribution. Thus, in the following, proprietary licenses are left out. FLOSS on the contrary means liberally licensing to grant users the right to use, copy, study, change, and improve its design through the availability of source code. Because of their open and non-discriminatory nature, FLOSS licenses can simplify development and collaboration which are driving forces in science.

There is a wide variety of liberal licenses which all share the ideas of *open source* and *free software*. Nevertheless, terms and conditions may differ significantly in certain respects and someone should precisely reflect which FLOSS license to choose. In doubt a lawyer should be consulted. The following gives a short introduction to terminology and some selected features often used to describe FLOSS licenses.

Copyleft is a concept to use copyright law to render any modified or extended versions to be considered *free* as well (e.g. GPL).

Share-Alike describes a license which requires any copy or adaptation to be released under the same or a very similar license as the original.

Permissive licenses are a class with minimal requirements on how the software can be redistributed. This is in contrast to *copyleft* and *share-alike*. Examples are MIT and BSD licenses.

Compatible licenses do not contain contradictory requirements which render it impossible to combine projects. For example, including BSD or MIT licensed code into a GPL project is possible but not vice versa.

Linking permissions allow to use and integrate code or libraries into a project without requiring to release the projects entire source code.

Proliferation of FLOSS licenses makes it difficult to choose a particular one coming along with increasing the chance of compatibility issues.

An often used FLOSS license is the GNU General Public License (GPL). If the ideas of *copyleft* and *share-alike* are appealing to a project it is a good choice. The majority of TOAST related software is published under the GPL.

8.7.2 Copyright Assignment

When more than one person is involved or for collaborative and derived works copyright assignment has to be resolved. However, in many jurisdictions copyright can not be transferred i.e. the authorship is not negotiable. In general copyright assignment is a difficult field. A lawyer from the institute's legal department should assist. In case all contribution's and component's licenses are suitable and compatible then there is no reason not to publish under that very license. Broadly spoken, it is the easiest way to agree on the same license for any ingredient throughout the whole package, if possible. Otherwise, it is usually sufficient to collect—what is called—contributor license agreements (CLA). By complying with the CLA each person who works on a project explicitly grants the right to incorporate its contributions.

8.7.3 Software Packaging

Besides licensing, it is very important to distribute scientific codes in a convenient way. From the viewpoint of users the software's usability is a key feature which also concerns the build- and installation process. Most scientists expect programs to run within an hour on commonly used systems. Accordingly, software should be provided as a package.

Providing bare but appropriate licensed source-code is not sufficient for most users. Packaging scientific code must be a trade-off between source-code only and all-round carefree installers. However, for distributing codes non-computer scientists do not want to break down system or software barriers.

As a compromise, for dissemination it is recommended to provide a single tar-archive which includes any ingredient necessary. The following list proposes what a resulting program package should contain. While those guidelines should not be ignored, they are not entirely put into practice by any TOAST related software-suite. To give an example, it depends on the actual project whether a toy-example is included or not.

Source Code: Each package must bring its sources along with any ingredient which is typically not available on the desired system.

License: Every single component in the package as source-code, documentation, examples have to be licensed properly. This also includes code snippets e.g. taken from textbooks.

Readme: By convention, this is the first file users will read. It should provide a first overview on what is contained and whom to ask.

Documentation: It is absolutely inevitable to provide proper and entire documentation on how the program has to be used.

Build Guide: Detailed instructions on how to build executables along with library or software prerequisites should be given.

Version: A widely used naming convention is to start with a stem prefix, followed by a dash followed by a version number.

Build System: To enable users compiling the code it is highly recommended having a *Makefile* to transform sources into executables.

Getting Started: To unburden first steps, a very concise tutorial should be include which might be wrapped around an example.

8.7.4 *The OpenTOAST Initiative*

Throughout the funding period the TOAST project was mentoring various software projects. It was one of the key objectives to monitor and maintain the development process of software suits. As a result a collection of application has been taken together in what is called the TOAST-Toolbox. Codes to be considered have at least to comply with proper licensing and packaging guidelines put in to practice. In fact, actual software packages are made available through the TOAST partners. To provide an overview some selected core applications are listed in Table 8.1.

To preserve TOAST's current status and to offer an open and collaborative platform for applied seismic tomography a successor initiative beyond TOAST's funding period was formed. It is called the *OpenTOAST Initiative* (OTI). It pursues the goal to make actual implementations available throughout a wide academic community as well as end-users. It is OTI's commitment to share not only source code but also software, knowledge, contacts, and data. For further details please visit www.opentoast.de.

Table 8.1 Selected core-applications covered by TOAST with all licensing question resolved, bundled into packages including documentation, build instructions and examples

Name	Description	License
SOFI2D and SOFI3D	A massively parallel finite differences code for modeling 2D and 3D viscoelastic wave propagation in the time domain	GPLv2
Gemini	Software suit to calculate Green's functions for the elastic wave equation in 1D media	GPLv2
TFSsoftware	A collection of tools to process, analyze and asses seismic wavefortn data	Mostly GPL
3DFWI	Finite difference time-frequency doniain 3D elastic full-waveform inversion code using the adjoint method	GPLv2
DENISE	Finite difference time domain 2D elastic full-waveform inversion code using the adjoint method	GPLv2
FW-NA	Framework for probabilistic 1D full-waveform inversion based on neighborhood-algorithm	Proprietary and GPL
SES3D-NT	MPI parallelized 3D waveform modeling code in spherical coordinates covering itnaging capabilities	GPLv3+
ASKI	A higlily modularized program suite for sensitivity analysis and iterative full-waveform inversion	GPLv2

Acknowledgments The project TOAST was funded by the German Federal Ministry of Education and Research (BMBF) within the R&D programme GEOTECHNOLOGIEN (Grant: 03G0752A-F).

References

- Bohlen T (2002) Parallel 3-D viscoelastic finite difference seismic modeling. *Comput Geosci* 28:887–889
- Butzer S, Kurzmann A, Bohlen T (2013) 3D elastic full-waveform inversion of small-scale heterogeneities in transmission geometry. *Geophys Prospect* 61(6):1238–1251. doi:[10.1111/1365-2478.12065](https://doi.org/10.1111/1365-2478.12065)
- Forbriger T, Groos L, Schäfer M (in review) Line-source simulation for shallow-seismic data. Part 1: Theoretical background. *Geophys J Int*
- Friederich W, Dalkolmo J (1995) Complete synthetic seismograms for a spherically symmetric earth by a numerical computation of Green's function in the frequency domain. *Geophys J Int* 122:537–550
- Groos L (2013) 2D Full-waveform inversion of shallow-seismic Rayleigh waves. Dissertation, Karlsruhe Institute of Technology (KIT)
- Groos L, Schäfer M, Forbriger T, Bohlen T (in review) 2D elastic full-waveform inversion of shallow-seismic Rayleigh waves in the presence of attenuation. *Geophysics*

- Köhn D (2011) Time domain 2D elastic full-waveform tomography. Dissertation, Christian-Albrechts-Universität zu Kiel
- Krauss F, Giese R, Alexandrakis C, Buske S (submitted) Seismic travel-time and attenuation tomography to characterize the excavation damaged zone and the surrounding rock mass of a newly excavated ramp and chamber. *Int J Rock Mech Min Sci*
- Kurzmann, A. (2012) Applications of 2D and 3D full-waveform tomography in acoustic and viscoacoustic complex media. Dissertation, Karlsruhe Institute of Technology (KIT)
- Kurzmann A, Przebindowska A, Köhn D, Bohlen T (2013) Acoustic full-waveform tomography in the presence of attenuation: a sensitivity analysis. *Geophys J Int* 195(2):985–1000. doi:[10.1093/gji/ggt305](https://doi.org/10.1093/gji/ggt305)
- Meier T, Dietrich K, Stoeckert B, Hajes HP (2004) 1-dimensional models of the shear-wave velocity for the eastern Mediterranean obtained from the inversion of Rayleigh wave phase velocities and tectonic implications. *Geophys J Int* 156:45–58
- Mora M (1987) Nonlinear two-dimensional elastic inversion of multioffset data. *Geophysics* 52(9):1211–1228
- Mosca I, Meier, T, Sigloch K (submitted) Ultrasonic surface wave propagation in multi-layered structures. *Geophys J Int*
- Przebindowska A. (2013) Acoustic full-waveform inversion of marine reflection seismic data. Dissertation, Karlsruhe Institute of Technology (KIT)
- Sambridge M. (1999a) Geophysical inversion with a neighbourhood algorithms I- searching a parameter space. *Geophys J Int* 138:479–494
- Sambridge M (1999b) Geophysical inversion with a neighbourhood algorithms II- appraising the ensemble. *Geophys J Int* 138:727–746
- Schäfer M, Groos L, Forbriger T, Bohlen T (in review) Line-source simulation for shallow-seismic data. Part 2: Full-waveform inversion - a 2D case study. *Geophys J Int*
- Sirgue L, Etgen J, Albertin U (2008) 3D frequency domain waveform inversion using time domain finite difference methods. In: *Extended Abstracts, 70th EAGE meeting, Rome, Italy, F022*
- Sirgue L, Pratt RG (2004) Efficient waveform inversion and imaging: a strategy for selecting temporal frequencies. *Geophysics* 69(1):231–248
- Tarantola A (1988) Theoretical background for the inversion of seismic waveforms, including elasticity and attenuation. *Pure Appl Geophys* 128(1/2):365–399
- Tromp J, Komatitsch D, Liu Q (2008) Spectral-element and adjoint methods in seismology. *Commun Comput Phys* 3(1):1–32
- Zelt CA, Barton PJ (1998) 3D seismic refraction tomography: a comparison of two methods applied to data from the Faeroe Basin. *J Geophys Res* 103:7187–7210

Chapter 9

Tomographic Methods in Hydrogeology

Olaf A. Cirpka, Carsten Leven, Ronnie Schwede, Kennedy Doro, Peter Bastian, Olaf Ippisch, Ole Klein and Arno Patzelt

Abstract The extraction of groundwater for drinking water purposes is one of the most important uses of the natural subsurface. Sustainable management of groundwater resources requires detailed knowledge of the hydraulic properties within the subsurface. Typically, these properties are not directly accessible. The evaluation of hydraulic properties therefore requires hydraulic stimuli of the subsurface (e.g., injection and extraction of groundwater, tracer tests, etc.) with subsequent data analysis. In this context, tomographic techniques and inversion strategies originally derived for geophysical surveying can be transferred to hydraulic applications. In addition, geophysical techniques may be used to monitor hydraulic tests. The latter requires fully coupled hydrogeophysical inversion strategies, accounting for the entire process chain from hydraulic properties via flow and transport to the application of the geophysical surveying techniques. The project “Tomographic methods in hydrogeology” focuses on the development of a geostatistical inversion method for transient tomographic data of multiple hydraulic investigation techniques, the model-based optimal design of tomographic surveys, and the development of experimental techniques and equipment for an efficient execution of tomographic surveys in a hydrogeological context using the model-based design and providing data for the inversion. In this chapter we will show selected examples of the project’s outcome. The examples include developments related to the joint geostatistical inversion of tomographic data sets, its efficient parallelization, and its application to a 3D-inversion of tomographic

O. A. Cirpka (✉) · C. Leven · R. Schwede · K. Doro
University of Tübingen, Center for Applied Geoscience, Tübingen, Germany
e-mail: olaf.cirpka@uni-tuebingen.de

C. Leven
e-mail: carsten.leven-pfister@uni-tuebingen.de

P. Bastian · O. Ippisch · O. Klein
Interdisciplinary Center for Scientific Computing, University of Heidelberg,
Heidelberg, Germany

A. Patzelt
Terrana Geophysik Dr. A.Patzelt und Partner, Mössingen, Germany

thermal tracer tests. Furthermore we present a method for solving the inversion of transient tomographic data sets which usually suffer from high computational efforts. Related to the acquisition of tomographic data sets, we also discuss the development of tracer-tomographic methods using heat as tracer.

9.1 Introduction

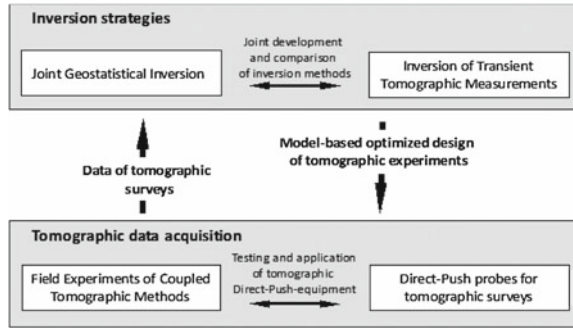
The natural subsurface is characterized by high spatial variability. This has direct consequences on the management of shallow aquifers used for the provision of drinking water and other purposes. The spatial variability of hydraulic conductivity causes solute transport to be non-uniform which impedes the assessment and remediation of contaminated aquifers and causes uncertainty in risk assessment and design of protective measures. Therefore the comprehensive assessment of hydraulic properties of the subsurface and their spatial variability is mandatory for management and protection of groundwater resources.

The project *Tomographic Methods in Hydrogeology* deals with the acquisition and inversion of hydraulic data, obtained in hydrogeological field studies using tomographic layouts. The main objective is the development of coupled tomographic surveying and inversion strategies, combining hydraulic and geophysical measurements to obtain three-dimensional distributions of hydraulic aquifer properties. This involves (1) the development of experimental methods and assessment strategies in the field, and (2) the development of fully coupled hydrogeophysical inversion methods using high-performance computing methods to be implemented in the software package DUNE, a leading platform for parallel solution of partial differential equations. In the project, we also use numerical models for designing the experiments, and the experimental data will be inverted by the new inversion codes developed in the project. The interplay between experimental and numerical studies facilitates jointly optimizing the experimental strategy and the numerical inversion. Figure 9.1 gives an overview of the structure of the project with its experimental and numerical work packages. More specifically, the following objectives are addressed in the framework of the project.

9.1.1 Joint Inversion of Multiple Data Sets

For joint inversion of multiple data types, different hydrogeological data sets are considered: (1) hydraulic tests in tomographic arrays, (2) direct measurements of hydraulic conductivity, (3) temperature measurement in experiments, in which heat is used as tracer in tomographic setups, and (4) data from the geoelectrical monitoring of salt-tracer tests. The combination of several investigation techniques depending quantitatively on the distribution of hydraulic conductivity improves the resolution

Fig. 9.1 Structure of the project “Tomographic methods in Hydrogeology”



and decreases the uncertainty in the three-dimensional estimation of hydraulic subsurface properties.

9.1.2 Three-Dimensional, Fully Coupled Inversion on Parallel Computers

A three-dimensional, fully coupled hydrogeophysical inversion on parallel computers is developed and implemented in the software package DUNE which includes efficient parallel discretization methods and solvers for partial differential equations. Also, a modular approach is used so that combinations of different data sets and types can be analyzed.

9.1.3 Model-Based Optimal Design of Tomographic Field Surveys

The expected data worth of a particular tomographic field set up can be quantified by the expected reduction of conditional uncertainty (Cirpka et al. 2004). This metric can be used to choose the best set up of several candidates and to optimize the experimental setup (e.g. location of probes, pumping rates or other continuous design parameters) by automatic maximization routines.

9.1.4 Development and Test of Coupled Tomographic Assessment Strategies in the Field

The tomographic assessment strategy includes different tomographic approaches (e.g. hydraulic and tracer tomography) that are applied at the test site Lauswiesen of University of Tübingen and are developed to reliable and applicable field techniques. Data from previous studies are used for the design of experiments and are partly

included in the inversion process. In particular, a method for heat-tracer tomography is developed as a ready-to-use tomographic field technique. The field studies also include pumping tests based hydraulic tomography, and geoelectrical monitoring of salt tracer tests with three-dimensional electrode arrays.

9.1.5 Development of Direct-Push Probes for Three-Dimensional Tomographic Surveying

Geoelectrical monitoring of salt-tracer tests often requires the installation of vertical electrodes directly in the aquifer to improve the measurement resolution. Rather than installing additional observation wells and equipping them with probes, we use probes that can be easily installed into the subsurface with simple direct-push techniques and which can be re-used after retrieval. This is especially important as often the retrieval of in-situ installation is required after termination of an investigation. For this purpose, a modular technique is developed which is easy to install and to be retrieved from the subsurface. The probes are applied in the field experiments at the Lauswiesen test site and contribute to the integrated tomographic assessment strategy.

In the following sections we present selected examples of the project's outcome. The examples include developments related to the joint geostatistical inversion of tomographic data sets, its efficient parallelization, and its application to a 3-D inversion of tomographic thermal tracer tests. Furthermore, we present a method for inverting transient tomographic data sets which usually suffer from high computational effort. Related to the acquisition of tomographic data sets, we also show development of tracer-tomographic method for which we use heat as tracer.

9.2 Efficient Parallelization of Geostatistical Inversion Using the Quasi-Linear Approach

In hydrogeology, inverse modeling is used to infer the spatial distribution of hydraulic conductivity from indirect measurements, such as hydraulic heads or concentrations. In three-dimensional applications, this may result in millions of hydraulic-conductivity values that have to be estimated and correspondingly large groundwater flow problems have to be solved. The associated high demands with respect to computational power and memory make the application of high-performance computing techniques necessary. In the study presented here; we show the implementation of efficient parallel methods for geostatistical inversion to infer the spatial distribution of hydraulic conductivity of an artificial test case. For this purpose, all quantities that depend directly or indirectly on hydraulic conductivity may be used in the inversion procedure, which may include direct estimates of hydraulic conductivity (e.g., from

grain-size analysis), hydraulic heads, and solute concentrations from tracer tests. In this study, we only consider the inversion of hydraulic heads, but the same general inversion strategy can be applied to other types of data as well (see e.g. Cirpka and Kitanidis 2000; Nowak and Cirpka 2006; Li et al. 2005, 2007, 2008; Schwede and Cirpka 2009; Pollock and Cirpka 2010).

The general objective of our approach is to obtain the hydraulic conductivity field as a continuous spatial field. Upon discretization, this leads to as many discrete parameter values as elements of the grid, which is typically a number much higher than the number of the measurements available. The inversion problem is therefore mathematically ill posed. For regularization, we use geostatistical prior knowledge by assuming that the parameter field is a random, auto-correlated space variable with certain spatial correlation structure (Matheron 1971). In this context, inversion becomes (geo)statistical conditioning. Various versions of geostatistical inversion exist, differing, among others, in the exact representation of the generated fields, the approach of minimizing the objective function, and the question whether only a smooth best estimate is sought for or multiple conditional realizations (Sahuquillo et al. 1992; Gómez-Hernández et al. 1997; RamaRao et al. 1995; Bennett 1992; Valstar et al. 2004; Kitanidis 1995; McLaughlin and Townley 1996; Yeh et al. 1996; Hernandez et al. 2006). Only few studies exist using methods of parallel computation in the context of geostatistical inversion (e.g. Berg and Illman 2011; Doherty 2010a, b; Hunt et al. 2010; Fienen et al. 2011).

Here we present a quasi-linear geostatistical approach based on that of Kitanidis (1995) as inverse kernel, using extensions and modifications, e.g. from Nowak and Cirpka (2004) and Sun and Yeh (1990) to make the scheme more stable and efficient. The theory of the geostatistical framework, the inversion method, and the approach for the evaluation of the sensitivity matrix and for an efficient matrix multiplication is presented in detail in Schwede et al. (2012).

In recent years, parallel computing has become increasingly important in the numerical solution of partial differential equations arising in many fields of computational physics, including flow and transport in porous media. In the example presented here, we show the possibilities for parallelization of geostatistical inversion on mid-range and large computer clusters. The software framework “Distributed Unified Numerics Environment”—DUNE (Bastian et al. 2008a, b), is used to implement a parallelized geostatistical inversion environment in C++.

9.2.1 Parallelizing the Quasi-Linear Geostatistical Inverse Approach

Given a sequential implementation of the quasi-linear geostatistical inverse approach, the question arises which parts can be parallelized. The computation of sensitivities for different measurements may easily be parallelized, because the individual sensitivities are independent from each other. Each of these computations requires the

solution of an adjoint problem. On a second level, the solution of the adjoint and forward problem can be parallelized using domain decomposition techniques (Smith et al. 1996).

In the two-level parallelization approach for the computation of sensitivities, the total number of available processors is split into processor groups. The adjoint problems are distributed among the processor groups such that each processor group uses domain decomposition for the solution of (at least) one adjoint problem. A further improvement in performance can be reached by optimizing the parallelization of the fast Fourier Transformation which is used for efficient matrix multiplication according to the domain decomposition applied for solving the partial differential equations. Also, we use the parallel AMG preconditioner available in the software framework DUNE with the implemented Overlapping Schwarz Method for domain decomposition (Blatt 2010).

9.2.2 Implementation and Computational Examples

The software framework DUNE (Bastian et al. 2008a, b) provides an easy access to different grids and facilitates the implementation of various finite element schemes with different shape functions. For the example presented here, we use the continuous Galerkin method with bilinear finite elements on a regular cuboidal grid, and for implementing efficient parallel programs, the Message Passing Interface (MPI Forum 2009) with its high flexibility and scalability. For the calculation of matrix–vector multiplications, we use the FFT software library Fastest Fourier Transform in the West (FFTW) (Frigo and Johnson 2005).

In our geostatistical inversion scheme two parallelization levels are used: In an iterative framework, the current parameter estimate is used to evaluate the hydraulic head field throughout the domain in the forward problem. The fastest way to solve the forward problem is to use domain decomposition with all available processors. The output of the forward model includes the simulation results corresponding to the measurements, but the full forward solution is needed in the evaluation of the sensitivity fields. The latter also requires the solution of one adjoint problem per measurement, which is done independently from the forward solution. For the calculation of the adjoint problems, all available processors are split into multiple processor groups. Each processor group calculates the adjoint states using domain decomposition and evaluates the sensitivities for the measurements. Parallel matrix–vector multiplications are required for the updating step of the parameter estimate. A detailed and complete description of the implementation can be found in Schwede et al. (2012).

We tested our inversion scheme with an artificially generated hydraulic log-conductivity field (Fig. 9.2), which was used to solve for the true hydraulic head field and to retrieve 36 hydraulic conductivity measurements and 36 head measurements taken at the same locations which were perturbed to account for measurement errors. The total calculation time for a complete inversion is shown in Fig. 9.2c for different total processor and processor group numbers. It clearly shows that an addi-

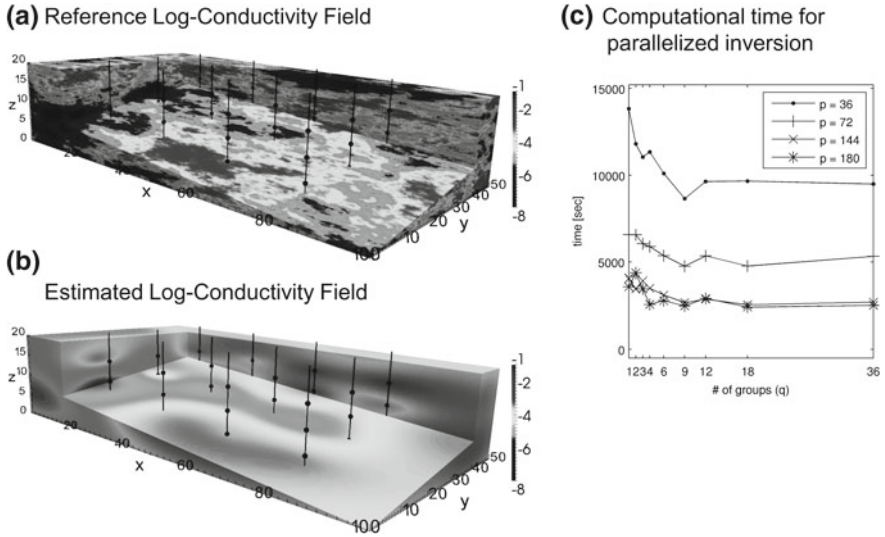


Fig. 9.2 Artificial test case with “true” **a** and estimated hydraulic log-conductivity field **b** in [log K in m/s]. The *black lines* indicate observation wells and the *black dots* are the measurement locations. Computational time of a complete inversion **c** in the two-level parallelized quasi-linear geostatistical approach: For a series of different numbers of processors p , the plots show the computational time as a function of the number of processor groups q reserved for the computation of sensitivities. From: Schwede et al. (2012)

tional speed-up can be achieved for a fixed number of processors when sensitivities are calculated in parallel (i.e. $q > 1$). This speed-up can nearly be up to a factor of two. Even for the other case, where the number of processors is larger than 36, the results show that adding parallel computation of sensitivities to domain decomposition pays off. Independent from the degree of parallelization, all calculations resulted in the same parameter estimates. Figure 9.3 shows the result of our estimation in comparison to the true parameter field. The main patterns of high and low hydraulic conductivity are clearly revealed. Even though, we only presented results for inverting hydraulic-head measurements, the scheme also allows including other types of measurements, such as solute concentrations (e.g., Nowak and Cirpka 2006; Schwede and Cirpka 2009) or geophysical monitoring data obtained during hydraulic tests (e.g., Pollock and Cirpka 2010) that are related to hydraulic conductivity in a known way. For further aspects on efficient parallelization of geostatistical inversion we refer to Schwede et al. (2012).

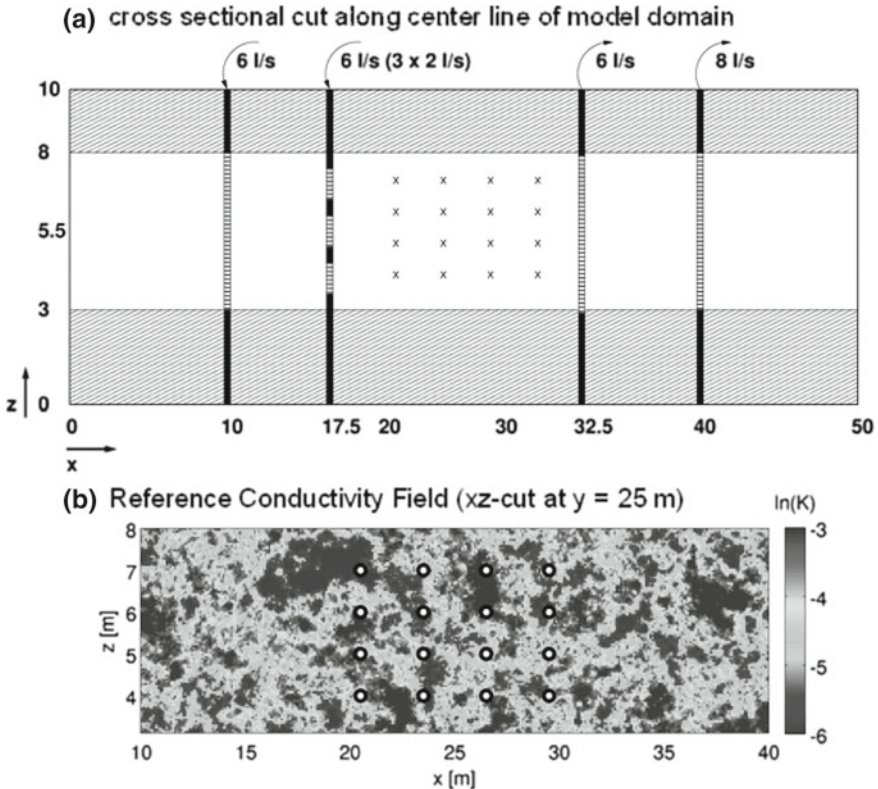


Fig. 9.3 a Schematic cross sectional cut along the *center line* of the modeled domain. Shown is the configuration with four wells (two injection and two extractions wells) and the screened sections in the *inner injection well* with 3×2 l/s. b 2-D view of the vertical cut along $y = 25$ meters of reference conductivity field (*circles* are measurement location)

9.3 Three-Dimensional Field Scale Geostatistical Inversion Using Tomographic Thermal Tracer Test Data

With the groundwater flow equation being a diffusion equation, high resolution in inverting head data can only be achieved when considering many pumping and observation wells, which may be costly. Other types of measurements, mainly tracer test data, depend on hydraulic conductivity in a different way than hydraulic head measurements. This implies that the same set of wells can be used for different measurement types with different information content. In previous studies, temporal moments of solute-tracer data were considered for this purpose, either measured directly or using geoelectrical monitoring (Cirpka and Kitanidis 2000; Nowak and Cirpka 2006; Pollock and Cirpka 2008, 2010, 2012). These studies were restricted to two-dimensional laboratory setups, whereas in the example presented here, we

focus on a three-dimensional analysis. For the synthetic field test case we present an approach relying on two injection-observation-well doublets to create a stable flow field by an outer well pair and an investigation zone by an inner well pair, in which the tracer test is applied. This scheme has the advantage, that leakage of the tracer into the environment and the influence of changes of outer hydraulic boundaries can be minimized. For the tracer test, the use of heat as a tracer is considered because temperature changes can be very easily measured in-situ at a very large number of locations. Also, the high thermal diffusivity allows a faster repetition of thermal tests because the signal disappears faster than a comparable solute signal. This, however, also poses the problem that the intended thermal signal disappears over wide distances.

In the synthetic study presented in the following, we show the value of tracer arrival-time data obtained in tomographic heat-tracer tests for the assessment of hydraulic conductivity and compare it to the value of head measurements from hydraulic tomography. The synthetic test case resembles field investigations and is also aiming at guiding experiments. The well setup and the geometry of the investigation domain are chosen as realistic as possible in order to test which quality of inversion results is possible under realistic conditions.

For the inversion of the synthetic test case we use the quasi-linear geostatistical approach for inversion scheme as described in the previous section and in Schwede et al. (2012). For large parts of the code we rely on the modular toolbox DUNE (Bastian et al. 2008a, b), especially on the module PDELab for solving partial differential equations using domain-decomposition techniques. The governing equations are discretized by the standard Finite Element Method with bilinear, conforming elements on a regular cuboidal. The calculation of huge matrix-vector multiplications was realized by circulant embedding in the spectral domain, using the well-known FFTW library (Frigo and Johnson 2005).

The artificial test case analyzed in this study resembles the Lauswiesen test site near Tübingen in Germany (see section on tomographic experiments). Figure 9.3 shows a vertical cross-section through the domain, high-lighting the three layers: the top and bottom layers with low hydraulic conductivity, and the middle layer forming the aquifer under investigation. We assign different deterministic and geostatistical properties based on previous measurements and experiments. Located near the River Neckar, it is often experienced that the direction and strength of ambient groundwater flow is subject to uncontrollable temporal variations driven by river-stage fluctuations. The influence of natural ambient flow on the propagation of the heat tracer plume could be significant if a conventional pumping system of one injection and one extraction well was applied. We therefore adopt the nested treatment cell approach developed for site remediation (Luo et al. 2006), which requires four injection and extraction wells in a row for each test (Fig. 9.3a). The tracer tests are conducted between the two inner wells and by the nested-cell approach leaking of the tracer into natural ambient flow can be prevented.

In the test case presented here, four injection/extraction wells were used as shown in Fig. 9.3a. The injection of the heated water is injected in steady state flow fields in different intervals as indicated by the screened sections in Fig. 9.3a. The hydraulic and

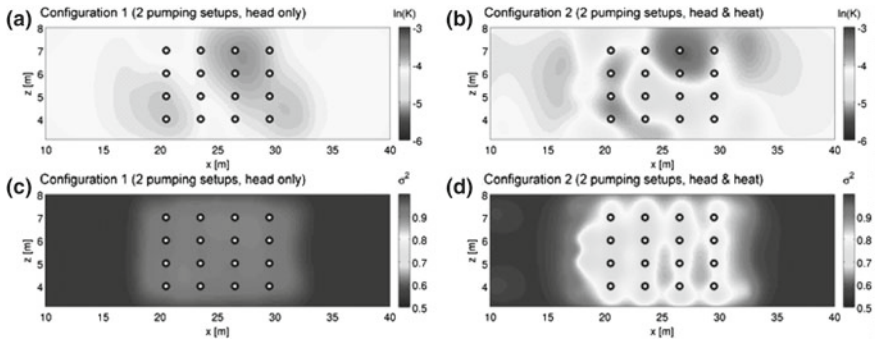


Fig. 9.4 Vertical cross-sections ($y = 25$ m) of the estimated log-hydraulic conductivity fields (**a** and **b**) and corresponding estimation variance (**c** and **d**) obtained by geostatistical inversion of configuration 1 (2 pumping setups with 128 hydraulic head measurements) and of configuration 2 (2 pumping setups with 128 hydraulic head measurements and 128 mean arrival time of a thermal tracer test signal)

thermal tracer tests are simulated for both possible directions, i.e. with and against the ambient flow direction. In the inversion we investigate two configurations: In configuration 1 only head measurements are used from two tomographic pumping setup: one with pumping in flow direction, the other one with pumping perpendicular to the main groundwater flow. Configuration 2 has the same pumping setup but in addition to measurements of hydraulic head also those of mean arrival time of the thermal signal are used. In every configuration a total number of 50 million parameters needed to be estimated. The reference conductivity field used to generate all synthetic measurements is shown in Fig. 9.3b with a 2-D view of the vertical cut along $y = 25$ m. The results of the 3-D geostatistical inversions are presented for the same cross-section in Fig. 9.4a, b, and the corresponding estimation variance for the section is visualized in Fig. 9.4c, d. The results along other cross-sections look similar. Comparing the estimation results to the reference field, it can be concluded that the quasi-linear geostatistical approach is able to recover some features of the reference field. The estimations using only hydraulic head data (Fig. 9.4a) show very smooth estimates which re-cover only basic features of the underlying reference field.

Adding the arrival times of the thermal signal leads to a significant improvement of the estimate. Figure 9.4c shows the estimated conductivity field for configuration 2. It is already visually clear that more details are recovered than in the corresponding head inversion. The estimation variance illustrated in Fig. 9.4d is significantly reduced with a clear trend: At small distances to the injection wells (left and bottom of Fig. 9.4d), the reduction is bigger than further away from these wells, which can be explained by the asymmetric sensitivity pattern of travel-time measurements. The thermal tracer-test arrival times are much more affected by hydraulic conductivity upstream than downstream of the observation point, leading to overlapping sensitivities at the upstream side of the domain. This behavior is in agreement with similar

findings obtained for solute-tracer arrival times (Cirpka and Kitanidis 2000; Nowak and Cirpka 2006; Pollock and Cirpka 2008, 2010, 2012) and is discussed in further detail in Schwede et al. (2014) based on more configurations.

With this example we can clearly show that it is valuable to use different measurement types when identifying the hydraulic conductivity distribution of an aquifer by geostatistical inversion. This is especially relevant for the analysis of field data, where in most cases the number of observation wells is a limiting factor. For a given number of measurement locations, combining different measurement types with different sensitivity patterns improves the resolution of the estimate and reduces the uncertainty as it is demonstrated for the combination of hydraulic-head measurements with measurements of the mean arrival time of thermal signals obtained during tomographic heat-tracer tests.

9.4 Inversion of Transient Tomographic Measurements

Gradient-based inversion schemes of high-resolution parameter fields Y have been successfully applied in a variety of hydrogeological settings (Castaings et al. 2009; Michalak and Kitanidis 2004). The main constraint, however, is still the available computational power and its efficient use. Most inversion codes are either restricted to steady-state flow or relatively few observations. Even with steady-state groundwater flow, a dense grid of observations z typically leads to a time to solution measured in days or weeks (Nowak and Cirpka 2006). Transient PDEs take significantly more time to solve than their steady-state counterparts, and when computation time rises linearly with the number of measurements to be inverted geostatistical inversion quickly becomes unfeasible. This dependency is caused by the need of gradient-based schemes to compute the sensitivity matrix $H_z := \partial z / \partial Y$, which is a linearization of the forward model $F(z)$. This is a $n_Y \times n_z$ matrix, where n_Y is the number of parameters and n_z is the number of observations. Therefore the effort for the full assembly of H_z is $O(n_Y^2)$ using naive numerical differentiation or $O(n_Y n_z)$ using backward sensitivity analysis, i.e. adjoint state theory (Sun and Yeh 1990). There are two reasons to assemble this matrix, the first is the generation of the search direction in Newton-type methods like Gauss-Newton, the second is the establishment of a-posteriori variances for the estimated parameter field, i.e. reliability analysis.

While methods that avoid the explicit assembly of H_z have been known for years (Carrera and Neuman 1986), they normally are not applied due to the high number of iterations they take to convergence, especially for high-resolution parameter fields. We present a modified preconditioned version of this approach, similar to the one in (Tan et al. 2012), not suffering from the slow convergence of older methods. This leads to constant computation time for a wide range of observations and makes high-resolution transient inversion of large data sets feasible. Our code is implemented in the high-performance-computing framework DUNE (Bastian et al. 2004).

Assuming a Gaussian distribution for all relevant parameters Y and observations z one can derive the following objective function, where β is the deterministic part

of Y , Y' its stochastic fluctuation and Q_{pp} the covariance matrix of quantity p :

$$\begin{aligned}
 LY &= L_{\text{reg}}(Y) + L_{\text{cond}}(Y) \quad \text{with} \\
 L_{\text{reg}}(Y) &= \frac{1}{2}(Y')^T Q_{YY}^{-1} Y' \\
 &\quad + \frac{1}{2}(\beta - \beta^*)^T Q_{\beta\beta}^{-1} (\beta - \beta^*) \\
 L_{\text{cond}}(Y) &= \frac{1}{2}(F(Y) - z_m)^T Q_{zz}^{-1} (F(Y) - z_m)
 \end{aligned}$$

Minimization of L can be achieved using a variety of methods, e.g. Gauss-Newton or Levenberg-Marquardt. In addition to the gradient of L ,

$$\begin{aligned}
 \nabla L &= \nabla L_{\text{reg}} + \nabla L_{\text{cond}} \quad \text{with} \\
 \nabla L_{\text{reg}} &= (Y')^T Q_{YY}^{-1} + (\beta - \beta^*)^T Q_{\beta\beta}^{-1} \chi^T \\
 \nabla L_{\text{cond}} &= (F(Y) - z_m)^T Q_{zz}^{-1} H_z
 \end{aligned}$$

these methods require information about the Hessian of L and therefore typically assemble the whole sensitivity matrix H_z . In contrast, the Conjugated Gradient (CG) method only uses the gradient ∇L . There, the matrix H_z only appears in a product with a vector and therefore does not have to be explicitly assembled. The standard method to compute H_z resp. this product is via adjoint-state theory, both due to its efficiency and its accuracy. Assembly of the whole matrix requires solving n_z adjoint equations, one for each observation. The main idea is the reduction of this typically large number of equations to just one combined adjoint that directly computes the product needed. Since the adjoint equations are linear, the superposition principle guaranties that this is possible.

Another computationally expensive operation is the handling of products with Q_{YY}^{-1} in both equations above. This matrix is of dimension $n_Y \times n_z$. Since both Q_{YY} and Q_{YY}^{-1} are dense matrices, the application of standard iterative solvers or direct solvers is impossible even for moderate n_Y , and special solvers based on Fast Fourier Transforms (FFT) are applied (Dietrich and Newsam 1997). Q_{YY}^{-1} in particular is very expensive to compute or use. We solve this through the application of a specific preconditioner, see below.

The computation of ∇L_{reg} therefore is $O(n_Y \log n_Y)$ and that of ∇L_{cond} $O(n_Y)$, giving us a complexity of $O(n_Y \log n_Y)$ for both L and its gradient, independent of the number of observations n_z . The main point remaining is the constant hidden in these complexity estimates, as a theoretically perfectly scaling algorithm is useless if it does not finish in an acceptable time frame.

The number of CG iterations is about an order of magnitude larger than the number of iterations in Quasi-Newton methods even in the case of relatively low-dimensional problems, see Fig. 9.5, left, and the computational cost soon becomes prohibitive. The total number of PDEs to solve, therefore, can exceed those of Quasi-Newton methods

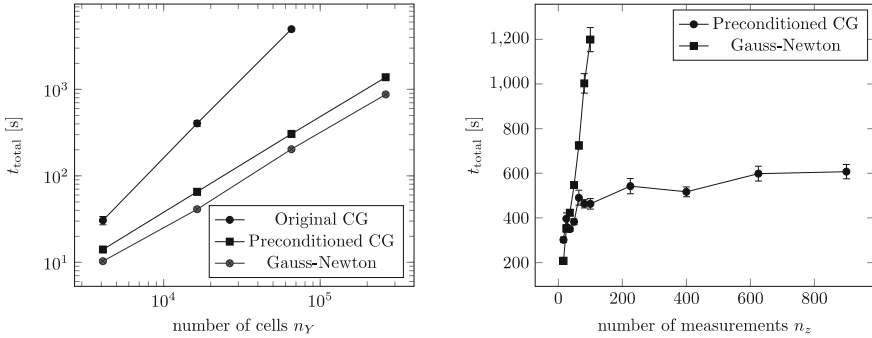


Fig. 9.5 Time to solution for CG, our preconditioned version, and the reference code for different field resolutions (*left*). Time to solution for increasing number of measurements to be inverted (*right*)

by orders of magnitude, even though the number of PDEs per iteration is much lower. The remedy for slow convergence of CG typically is a good preconditioner. Splitting the gradient into its trend and fluctuation parts, analogous to the field Y ,

$$\nabla L = \chi \nabla_{\beta} L + \nabla_{Y'} L,$$

we can use the prior covariance matrix Q_{YY} as a preconditioner for the stochastic part. This preconditioner is relatively cheap, naturally acts as a low-pass filter for spurious oscillations hindering convergence, and can lead to mesh size independent convergence rates for the CG algorithm. The modified step direction becomes

$$\begin{aligned} \Delta Y &= \chi \Delta \beta + \Delta Y' \quad \text{with} \\ \Delta \beta &= -(\nabla_{\beta} L)^T + \beta_{\text{orth}} \\ \Delta Y' &= -Q_{YY}(\nabla_{Y'} L)^T + Y'_{\text{orth}}, \end{aligned}$$

where $Y_{\text{orth}} = \chi \beta_{\text{orth}} + Y'_{\text{orth}}$ is the orthogonalization component of the CG step direction. This is combined with a line search along ΔY to determine an optimal step width α . The method then consists of iteratively setting

$$\begin{aligned} \beta_{\text{new}} &:= \beta_{\text{old}} + \alpha \Delta \beta \\ Y'_{\text{new}} &:= Y'_{\text{old}} + \alpha \Delta Y' \end{aligned}$$

The stochastic part of the step direction is

$$\Delta Y' = -Y'_{\text{old}} - Q_{YY} H_z^T Q_{zz}^{-1} (F(Y_{\text{old}}) - z_m) + Y'_{\text{orth}},$$

and if we know $Q_{YY}^{-1} Y'_{\text{orth}}$, we can compute

$$Q_{YY}^{-1} Y'_{\text{new}} = -\alpha \left(H_z^T Q_{zz}^{-1} (F(Y_{\text{old}}) - z_m) + Q_{YY}^{-1} Y'_{\text{orth}} \right)$$

without applying Q_{YY}^{-1} at all. Starting out with $Y'_0 \equiv 0$, we inductively know $Q_{YY}^{-1} Y'_i$ for all iterates Y_i , as each Y'_i is a linear combination of previous stochastic parts and terms of the form $Q_{YY} \cdot v$. This way, the two multiplications with Q_{YY}^{-1} in the objective function L and its gradient can be replaced by one significantly cheaper multiplication with Q_{YY} . This means that in our case the preconditioner has “negative cost”, i.e. applying it to reduce the number of CG iterations actually makes the iterations faster.

As a practical demonstration Fig. 9.5, left, shows the time needed for inversion of steady-state groundwater flow using head measurements. Flow is simulated in a domain $\Omega = (0, 100)^2$ (in m) with an injection well in the upper part and an extraction well in the lower part of the domain. An array of 4×4 observation wells is installed between them. We generate ten different synthetic fields with identical stochastic properties, calculate the corresponding head measurement values at the observation wells using the groundwater equation, add noise proportional to the measurement error to the data, and start the inversion code. The displayed values are sample-means over the ten realizations with standard error.

In the unpreconditioned case, the number of iterations needed for convergence rises linearly with the number of cells per dimension, while the time per iteration is superlinear in n_Y . The preconditioned CG scheme in contrast shows only a small dependence of the number of iterations on the grid size, and the time per iteration is linear in n_Y . As a result, the preconditioned scheme is of almost optimal complexity, while the original scheme quickly becomes unfeasible.

For comparison, we repeat the inversion with the Gauss-Newton scheme. The number of iterations is independent of the grid size, and the time per iteration is of optimal complexity as in the case of preconditioned CG. While the scheme takes more time per iteration, solving one adjoint equation per observation point, the number of iterations is significantly lower.

The preconditioned CG scheme and the Gauss-Newton algorithm have comparable times to solution for $n_z = 16$. To gauge the influence of the number of observations, we repeat the setup above, replacing the 4×4 measurement grid with $m \times m$ measurement wells, where $m \in \{4, \dots, 10\}$, see Fig. 9.5, right. The Gauss-Newton scheme as expected shows a clear linear trend with regard to $n_z = m^2$. Preconditioned CG shows less pronounced behavior, with a slight increase in both the number of iterations and the total time with increasing n_z . Augmenting the figure with the values for $m \in \{15, 20, 25, 30\}$ displays a constant number of iterations over a wide range, while the total time still exhibits a small dependence on n_z . This is most likely due to the assembly of the right hand side of the combined adjoint equation, a process that is technically first order in n_z but negligible over the range of interest. The time to solution is therefore effectively constant due to the fixed time per iteration and bounded number of iterations.

The properties of the preconditioned CG scheme derived above are independent of the type of measurement and the steady-state or transient nature of the flow field, and therefore also hold for the case of tracer measurements or ERT, where the number

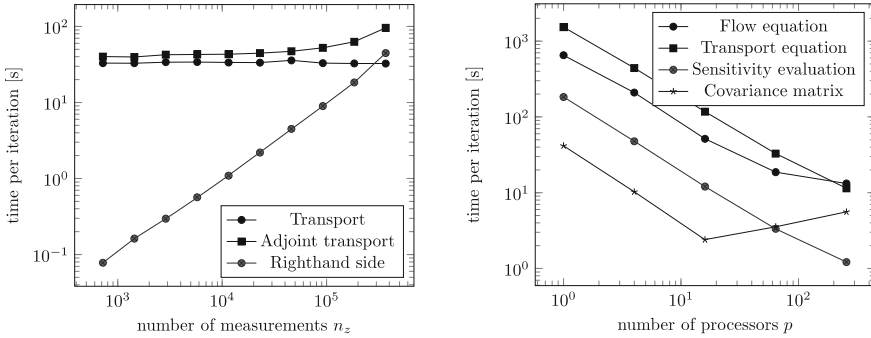


Fig. 9.6 Time per iteration for increasing number of measurements to be inverted (*left*). Time to perform different tasks while run in parallel, $nY = 2562$ (*right*)

of observations goes into the hundreds or even thousands and Newton-type methods are no longer applicable.

As an example, Fig. 9.6, left, shows the time needed to solve the transient transport equation and its adjoint counterpart for large numbers of measurements. In a wide range this time is constant, as the linearly scaling right-hand side of the adjoint equation can be neglected. Figure 9.6, right, shows the scalability of our method under transient conditions. The transport equation and the corresponding calculations scale almost as desired, while the groundwater equation requires an implicit solver, slowing down when the subdomains get too small. The FFTs required for Q_{YY}^{-1} scale very poorly, with the time needed even increasing with more processors used, but this calculation can be avoided using the preconditioner described above.

9.5 Development of an Experimental Tracer-Tomographic Method Using Heat as Tracer

With the recent developments of tomographic aquifer characterization, also new experimental possibilities for tracer testing are possible and required. Hydraulic tomographic testing with the monitoring of changes in hydraulic head has been studied in several experiments (e.g., Bohling 2009; Cardiff and Barrash 2011; Cardiff et al. 2012). The success of such tomographic experiments encourages to extent the approach to tracer testing. However, tracer tomography with the sequential injection of a tracer into an aquifer and the monitoring of the tracer transport at different locations, has so far only been investigated on a theoretical basis (see above) or in laboratory experiments (Yeh and Zhu 2007; Zhu et al. 2009; Illman et al. 2010).

Conducting tracer experiments in tomographic sequence requires the choice of a tracer which can easily be measured at many monitoring points and allows for the repetition of the experiment without the influence of previous test sequences. These challenges led us to explore the development of heat as an active tracer for

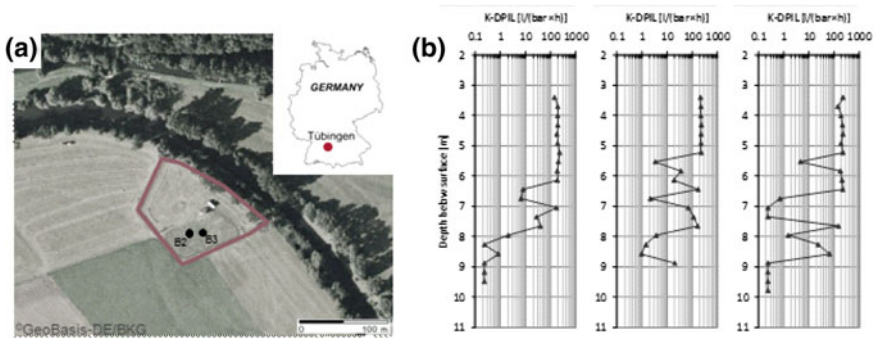


Fig. 9.7 **a** Location of the Lauswiesen test site close to Tübingen. **b** Vertical profiles of relative hydraulic conductivity showing increasing heterogeneity with increasing depth measured by Direct-Push based Injection Logging (Dietrich et al. 2008)

groundwater studies and to extend its use as a tracer for tomographic testing. Active heat tracer testing involves injecting warm or cold water into an aquifer to create a thermal plume which is propagated through the aquifer. Heat as a tracer has already been explored in several other studies, however without addressing tomographic experiments (Constantz et al. 2003; Anderson 2005; Constantz 2008; Hecht-Méndez et al. 2010; Bhaskar et al. 2012; Wagner et al. 2013).

In this section, we present the development of a concept for tomographic heat tracer experiments and show examples of such tests conducted at the Lauswiesen Test Site of the University of Tübingen, Germany (Fig. 9.7a). The site, which is located close to the city of Tübingen at River Neckar, has already been extensively studied and used to develop and test different site characterization techniques (e.g., Sack-Kühner 1996; Riva et al. 2006; Neuman et al. 2007; Riva et al. 2008; Lessoff et al. 2010). The unconfined aquifer consists of an unconsolidated gravel and sand formation with a mean transmissivity of $1.7 \times 10^{-2} \text{m}^2/\text{s}$. The bedrock below 10 m depth consists of a Triassic clay stone formation. Based on previous studies, the aquifer can be divided into two zones: an upper zone ranging from 2–approx. 6 m below ground shows a relatively homogeneous distribution of hydraulic conductivity, while a lower zone ranging from 6 to 10 m below ground is more heterogeneous with a lower average K (Fig. 9.7b). The test site contains several wells which are used for hydrogeological investigation purposes.

The presented experiments have been conducted in June 2012 using well B2 for injection and B3 for extraction while temperature changes were monitored in monitoring wells (Mw and ww-wells) in between wells B2 and B3 (Fig. 9.8a). For the injection, a custom-designed packer system is used which allows injecting water simultaneously at three different levels. To achieve a horizontal tracer injection, the warm water is injected through the middle level, while in the upper and lower interval groundwater with ambient temperature is injected. We utilized a flow-through water heater system to generate warm water with a temperature difference of 10 K over a period of 150 min with an rate of approx. 1 l/s. Throughout the tracer test, the injection

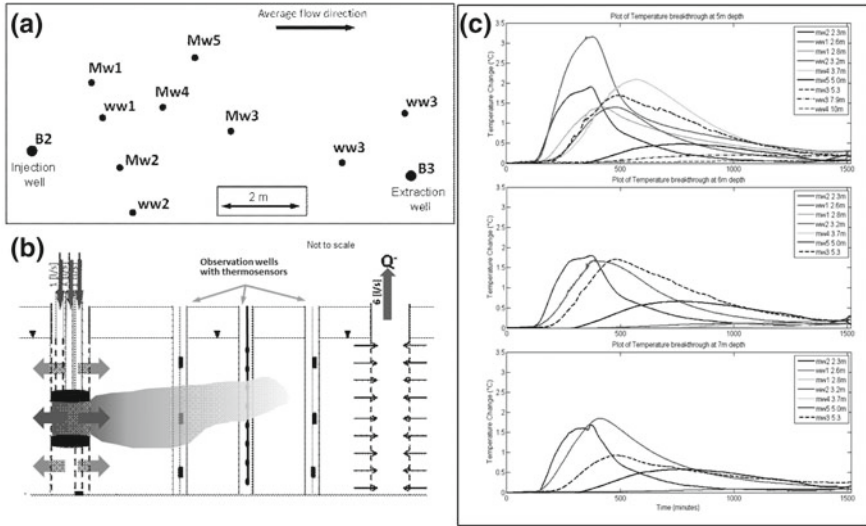


Fig. 9.8 a Layout of the part of the well field used for the tomographic thermal tracer tests conducted in July 2012. b Conceptual design of heat tracer testing technique. c Breakthrough curves at three different levels (top graph: 5 m, middle 6 m, bottom: 7 m) monitored during the tracer injection in the upper most level (4–5 m). All depths are with respect to ground surface

and extraction rates are kept constant with 3 l/s in total for both the injection and the extraction well. The total duration of each tracer test was 36 h. The monitoring of the breakthrough of the heat tracer was done using CTD–Diver (*Schlumberger Water Services*) which were set to log groundwater temperature and pressure every 30 s. To obtain a vertical distribution of temperature, temperature changes in the observation wells at three different levels with the middle level corresponding to the midpoint of tracer injection interval while the upper and lower levels were set at 1 m distance each from the middle level.

By means of the monitored thermal tracer breakthrough curves, with heat injected at different levels of the aquifer, the potential of using heat as a tracer for field application of tracer tomography can be shown (Fig. 9.8c). All experiments show distinct signals with different tracer arrival times and peak temperatures. Assuming faster tracer breakthroughs with higher peak temperatures for those sections of the aquifer with higher hydraulic conductivities, the observed breakthrough behavior is consistent with the earlier delineated hydraulic conductivity structure of the aquifer—as mentioned above. Also, due to the dipole flow field, a strong forced gradient flow field could be established which not only minimizes the effects of changing boundary conditions, but also it results in high advective velocity and ensured that temperature returned to near background value within 36 h after tracer injection, so that repeated tests in relatively short times can be conducted.

Tracer experiments (both heat and salt, the latter being monitored by electrical resistivity tomography) in tomographic settings are currently on the way, and will be inverted by the methods derived within this project in the near future.

Acknowledgments The project “Tomographic Methods in Hydrogeology” is part of the R&D-Programme GEOTECHNOLOGIEN. The project is funded by the German Ministry of Education and Research (BMBF). Additional funding has been provided by the Baden-Württemberg Foundation in the high-performance computing program and the German Academic Exchange Service (DAAD).

References

- Anderson MP (2005) Heat as a ground water tracer. *Ground Water* 43(6):951–968
- Bastian P, Droske M, Engwer C, Klöforn R, Neubauer T, Ohlberger M, Rumpf M (2004) Towards a unified framework for scientific computing. In: *Proceedings of the 15th conference on domain decomposition methods*, edited, pp 167–174, Springer, Berlin
- Bastian P, Blatt M, Dedner A, Engwer C, Kloforn R, Kornhuber R, Ohlberger M, Sander O (2008a) A generic grid interface for parallel and adaptive scientific computing. Part II: implementation and tests in DUNE. *Computing* 82(2–3):121–138
- Bastian P, Blatt M, Dedner A, Engwer C, Kloforn R, Ohlberger M, Sander O (2008b) A generic grid interface for parallel and adaptive scientific computing. Part I: abstract framework. *Computing* 82(2–3):103–119
- Benett AF (1992) *Inverse methods in physical oceanography*. Cambridge University Press, Cambridge
- Berg SJ, Illman WA (2011) Three-dimensional transient hydraulic tomography in a highly heterogeneous glaciofluvial aquifer-aquitard system. *Water Resour Res* 47:W10507
- Bhaskar AS, Harvey JW, Henry EJ (2012) Resolving hyporheic and groundwater components of streambed water flux using heat as a tracer. *Water Resour Res* 48(8):W08524
- Blatt M (2010) A parallel algebraic multigrid method for elliptic problems with highly discontinuous coefficients. <http://www.ub.uni-heidelberg.de/archiv/108565>
- Bohling GC (2009) Sensitivity and resolution of tomographic pumping tests in an alluvial aquifer. *Water Resour Res* 45:W02420
- Cardiff M, Barrash W (2011) 3-D transient hydraulic tomography in unconfined aquifers with fast drainage response. *Water Resour Res* 47(12):W12518
- Cardiff M, Barrash W, Kitanidis PK (2012) A field proof-of-concept of aquifer imaging using 3-D transient hydraulic tomography with modular, temporarily-emplaced equipment. *Water Resour Res* 48(5):W05531
- Carrera J, Neuman SP (1986) Estimation of aquifer parameters under transient and steady-state conditions. 3. Application to synthetic and field data. *Water Resour Res* 22(2):228–242
- Castaings W, Dartus D, Le Dimet FX, Saulnier GM (2009) Sensitivity analysis and parameter estimation for distributed hydrological modeling: potential of variational methods. *Hydrol. Earth Syst Sci* 13(4):503–517
- Cirpka OA, Bürger CM, Nowak W, Finkel M (2004) Uncertainty and data worth analysis for the hydraulic design of funnel-and-gate systems in heterogeneous aquifers. *Water Resour Res* 40(11)
- Cirpka OA, Kitanidis PK (2000) Sensitivities of temporal moments calculated by the adjoint-state method and joint inverting of head and tracer data. *Adv Water Resour* 24(1):89–103
- Constantz J (2008) Heat as a tracer to determine streambed water exchanges. *Water Resour Res* 44:W00D10
- Constantz J, Cox MH, Su GW (2003) Comparison of heat and bromide as ground water tracers near streams. *Ground Water* 41(5):647–656

- Dietrich CR, Newsam GN (1997) Fast and exact simulation of stationary Gaussian processes through circulant embedding of the covariance matrix. *SIAM J Sci Comput* 18(4):1088–1107
- Dietrich P, Butler JJ, Faiss K (2008) A rapid method for hydraulic profiling in unconsolidated formations. *Ground Water* 46(2):323–328
- Doherty J (2010a) Addendum to the PEST manual. Watermark Numerical Computing, Brisbane
- Doherty J (2010b) PEST, model-independent parameter estimation-user manual, 5th edn. Watermark Numerical Computing, Brisbane (with slight additions)
- Fienen MN, Kunicki TC, Kester DE (2011) CloudPEST—a python module for cloud-computing deployment of PEST, a program for parameter estimation. Technical Report. Open-File Report 2011–1062, U.S. Geological Survey
- Frigo M, Johnson SG (2005) The design and implementation of fftw3. *Proc IEEE* 93(2):216–231
- Gómez-Hernández JJ, Sahuquillo A, Capilla JE (1997) Stochastic simulation of transmissivity fields conditional to both transmissivity and piezometric data, 1. Theory. *J.Hydrol* 203(1–4):163–174
- Hecht-Méndez J, Molina-Giraldo N, Blum P, Bayer P (2010) Evaluating MT3DMS for heat transport simulation of closed geothermal systems. *Ground Water* 48(5):741–756
- Hernandez AF, Neuman SP, Guadagnini A, Carrera J (2006) Inverse stochastic moment analysis of steady state flow in randomly heterogeneous media. *Water Resour Res* 42(5):W05425
- Hunt RJ, Luchette J, Schreuder WA, Rumbaugh JO, Doherty J, Tonkin MJ, Rumbaugh DB (2010) Using a cloud to replenish parched groundwater modeling efforts. *Ground Water* 48(3):360–365
- Illman WA, Berg SJ, Liu X, Massi A (2010) Hydraulic/Partitioning tracer tomography for DNAPL source zone characterization: small-scale sandbox experiments. *Environ Sci Technol* 44(22):8609–8614
- Kitanidis PK (1995) Quasi-linear geostatistical theory for inversing. *Water Resour Res* 31(10):2411–2419
- Lessoft SC, Schneidewind U, Leven C, Blum P, Dietrich P, Dagan G (2010) Spatial characterization of the hydraulic conductivity using direct-push injection logging. *Water Resour Res* 46
- Li W, Nowak W, Cirpka OA (2005) Geostatistical inverse modeling of transient pumping tests using temporal moments of drawdown. *Water Resour Res* 41(8):W08403
- Li W, Englert A, Cirpka OA, Vereecken H (2008) Three-dimensional geostatistical inversion of flowmeter and pumping-test data. *Ground Water* 46(2):193–201
- Li W, Englert A, Cirpka OA, Vanderborght J, Vereecken H (2007) 2-D-characterization of hydraulic heterogeneity by multiple pumping tests. *Water Resour Res* 43(4):W04433
- Luo J, Wu W-M, Fienen MN, Jardine PM, Mehlhorn TL, Watson DB, Cirpka OA, Criddle CS, Kitanidis PK (2006) A nested-cell approach for in situ remediation. *Ground Water* 44(2):266–274
- Matheron G (1971) The theory of regionalized variables and its applications. Ecole de Mines, Fontainebleau
- McLaughlin D, Townley L (1996) A reassessment of the groundwater inverse problem. *Water Resour Res* 32(5):1131–1161
- Michalak AM, Kitanidis PK (2004) Estimation of historical groundwater contaminant distribution using the adjoint state method applied to geostatistical inverse modeling. *Water Resour Res* 40(8)
- MPI Forum (2009) The message passing interface (MPI) standard. <http://www.mpi-forum.org/docs/S>
- Neuman SP, Blattstein A, Riva M, Tartakovsky DM, Guadagnini A, Ptak T (2007) Type curve interpretation of late-time pumping test data in randomly heterogeneous aquifers. *Water Resour Res* 43(10)
- Nowak W, Cirpka OA (2004) A modified Levenberg-Marquardt algorithm for quasi-linear geostatistical inversing. *Adv Water Resour* 27(7):737–750
- Nowak W, Cirpka OA (2006) Geostatistical inference of hydraulic conductivity and dispersion coefficients from hydraulic heads and tracer data. *Water Resour Res* 42(8):W08416. doi:08410.01029/02005WR004832
- Pollock D, Cirpka OA (2010) Fully coupled hydrogeophysical inversion of synthetic salt tracer experiments. *Water Resour Res* 46

- Pollock D, Cirpka OA (2012) Fully coupled hydrogeophysical inversion of a laboratory salt tracer experiment monitored by electrical resistivity tomography. *Water Resour Res* 48
- Pollock D, Cirpka OA (2008) Temporal moments in geoelectrical monitoring of salt-tracer experiments. *Water Resour Res* 44(12):W12416
- RamaRao BS, LaVenue AM, deMarsily G, Marietta MG (1995) Pilot point methodology for automated calibration of an ensemble of conditionally simulated transmissivity fields. 1. Theory and computational experiments. *Water Resour Res* 31(3):475–493
- Riva M, Guadagnini L, Guadagnini A, Ptak T, Martac E (2006) Probabilistic study of well capture zones distribution at the Lauswiesen field site. *J Contam Hydrol* 88(1–2):92–118
- Riva M, Guadagnini A, Fernandez-Garcia D, Sanchez-Vila X, Ptak T (2008) Relative importance of geostatistical and transport models in describing heavily tailed breakthrough curves at the Lauswiesen site. *J Contam Hydrol* 101(1–4):1–13
- Sack-Kühner B (1996) Einrichtung des Naturmeßfeldes Lauswiesen Tübingen: Erkundung der hydraulischen Eigenschaften, Charakterisierung der Untergrundheterogenität und Vergleich der Ergebnisse unterschiedlicher Erkundungsverfahren. Lehrstuhl für Angewandte Geologie. Tübingen, Universität Tübingen.
- Sahuquillo A, Capilla J, Gomez-Hernandez J, Andreu J (1992) Conditional simulations of transmissivity fields honoring piezometric data. In: Blain W, Cantera E (eds) *Hydraulic engineering software IV. Fluid Flow Modeling*. Vol 2. Elsevier Applied Science, New Mexico
- Schwede RL, Li W, Leven C, Cirpka OA (2014) Three-dimensional geostatistical inversion of synthetic tomographic pumping and heat-tracer tests using a novel pumping setup. Submitted to *Adv Water Resour* 63:77–90
- Schwede RL, Cirpka OA (2009) Use of steady-state concentration measurements in geostatistical inversion. *Adv Water Resour* 32(4):607–619
- Schwede RL, Ngo A, Bastian P, Ippisch O, Li W, Cirpka OA (2012) Efficient parallelization of geostatistical inversion using the quasi-linear approach. *Comput Geosci* 44:78–85
- Smith B, Bjørsted P, Gropp WD (1996) *Domain decomposition*. Cambridge University Press, Cambridge
- Sun N, Yeh W (1990) Coupled inverse problems in groundwater modeling. 1. Sensitivity analysis and parameter-identification. *Water Resour Res* 26(10):2507–2525
- Tan B-T, Ghattas O, Higdon D (2012) Adaptive hessian-based nonstationary gaussian process response surface method for probability density approximation with application to bayesian solution of large-scale inverse problems. *SIAM J Sci Comput* 34(6):A2837–A2871
- Valstar JR, McLaughlin DB, Stroet CBMT, van Geer FC (2004) A representer based inverse method for groundwater flow and transport applications. *Water Resour Res* 40(5):W05116
- Wagner V, Li T, Bayer P, Leven C, Dietrich P, Blum P (2013) Thermal tracer testing in a heterogeneous sedimentary aquifer: Field experiment and numerical simulation. *Hydrol J*. doi:[10.1007/s10040-013-1059-z](https://doi.org/10.1007/s10040-013-1059-z)
- Yeh TCJ, Jin MH, Hanna S (1996) An iterative stochastic inverse method: conditional effective transmissivity and hydraulic head fields. *Water Resour Res* 32(1):85–92
- Yeh T-CJ, Zhu J (2007) Hydraulic/partitioning tracer tomography for characterization of dense nonaqueous phase liquid source zones. *Water Resour Res* 43(6):W06435
- Zhu J, Cai X, Jim Yeh T-C (2009) Analysis of tracer tomography using temporal moments of tracer breakthrough curves. *Adv Water Resour* 32(3):391–400